University of Southampton

REGENERATION MECHANISM OF ORGANIZED STRUCTURES IN NEAR-WALL TURBULENCE

By

Mirza Faisal Sayeed Baig

Doctor of Philosophy

Supervised by Prof. Sergei I. Chernyshenko

SCHOOL OF ENGINEERING SCIENCES

December 2003

This thesis has been completed as a requirement for a higher degree of the University of Southampton

UNIVERSITY OF SOUTHAMPTON

ABSTRACT

FACULTY OF ENGINEERING

SCHOOL OF ENGINEERING SCIENCES

Doctor of Philosophy

REGENERATION MECHANISMS OF ORGANIZED STRUCTURES IN NEAR-WALL TURBULENCE

by

Mirza Faisal Sayeed Baig

We have performed direct numerical simulations (DNS) of quasi-2D (that is with flow parameters independent of longitudinal coordinate) decaying and forced turbulence and 3D turbulent channel flows in order to ascertain the sustenance mechanism of near-wall turbulence by investigating the mechanism of streak formation. We found the existence of streaks in quasi-2D flows thus demonstrating that contrary to many proposed theories, feedback from longitudinal flow is not necessary for streak formation. Passive scalars having different mean scalar profiles were introduced in forced quasi-2D and 3D turbulent flows in order to compare the streak spacing of the scalars deduced from two-point correlations of DNS results with results obtained theoretically.

It has been found that even for the same vortex structure for all the passive scalars there is a marked variation in streak spacing implying that the preferential streak spacing is not necessarily equal to twice the vortex spacing, as has been suggested by several proposed theories. Moreover, the formation of scalar streaks in a velocity field prescribed as a sum of a mean turbulent velocity profile and random potential perturbations, conclusively supports the fact that organised vortices are not needed for generation of near-wall streaks. It has also been demonstrated that the lift-up mechanism responsible for generation of streaks is also responsible for the cross-flow spacing. The obtained qualitative numerical results are in favour of theory of streak formation based on optimal perturbations (Butler and Farrell, 1993) but at the same time the quantitative agreement is poor. So a modification of the same – Generalized optimal perturbation (Chernyshenko and Baig, 2003) theory has been proposed and it offers significantly better agreement with the DNS results.

ACKNOWLEDGEMENT

First and foremost, I would like to thank my supervisor, Professor Sergei I. Chernyshenko, for his constant assistance and support through every stage of this thesis. His patience and acute analysis of the problem have taught me a great deal, though his sheer brilliance baffled me a lot. I truly hope that many AFM students get the chance to work with Prof. Chernyshenko in the future, and learn from him as I did. A special thanks goes to my co-supervisor Professor Neil D. Sandham. His comments and support in understanding the "numerical code" also helped significantly in producing this document. At the same time, I would like to thank the post-doc research fellows: Dr. Zhiwei Hu and Dr. Mahbubul Alam for helping me understand the intricacies of the "code" and for other useful technical discussions. I would like to acknowledge the financial support via studentship from the School of Engineering Sciences and by the EPSRC grant GR/R27785/01.

My gratitude and love goes out to my family especially my wife and infant daughter Nuha who made a lot of sacrifices for the "Ph.D time". Then I would like to thank my parents who though being sick and old still exhorted me to go 'so far' from home to complete my studies. Finally I would like to thank GOD who made me realize this dream by creating conducive circumstances throughout my stay in U.K.

Contents

List of Tables

List of Figures

Nomenclature

$C_{k,l}$	Complex coefficients
E(k)	Energy spectrum as function of wavenumber
$\bar{u}$, $\bar{v}$, $\bar{w}$	mean velocity components
v', u', w'	components of fluctuation velocity
$2\pi l/L_y, 2\pi k/L_z$	wavenumbers
$Pr = \nu/\chi$	Prandtl number
q^2	$\overline{u_i'u_i'}$, turbulent kinetic energy
q	modified pressure
Q=$\langle v'^2 - w'^2 \rangle$	Difference of Reynolds normal stresses
Re	Reynolds number
Re_τ	$u_\tau^* h^*/\nu$, Wall-friction Reynolds number
$Re_{cf} = V_m Re_\tau$	Cross-flow Reynolds number
S	Source term
$\mathbf{u}$	non-dimensional velocity vector
V_m	root mean square cross-flow velocity
x^+	xu_τ/ν

λ^+	$\lambda u_\tau/\nu$
z^+	$z\, u_\tau/\nu$

Greek Symbols

β	spanwise wavenumber
Δ_{offset}	offset distance of peak from wall
ε_1	Energy transfer rate
ε	$\overline{\nu u'_{i,j} u'_{i,j}}$,dissipation
γ	vector of finite dimension
χ	molecular diffusivity
κ	Eigenvalues; Lagrange multiplier
Λ	circular frequency
λ_y	spanwise wavelength
η	enstrophy transfer rate
ν	kinematic viscosity
ω_f	forcing frequency
ω	non-dimensional vorticity vector
Π	$p + v'^2$, modified pressure
ρ^*	dimensional density
σ	maximum unstable eigenvalues
τ	$\langle v'w' \rangle$,Reynolds shear stress
$\tau_e = q^2/\varepsilon$	Eddy turnover time
τ_w^*	dimensional shear stress

θ	Passive Scalar
u_τ^*	$\sqrt{\tau_w{}^*/\rho^*}$ dimensional wall-friction velocity
$\zeta(z)$	wall-normal forcing function

Acronym

DNS	Direct numerical simulation
GOP	Generalized optimal perturbation
IMSL	Internal Mathematics and Statistics Library
MPI	Message passing interface
OP	Optimal perturbations
PDF	Probability density function
RNSAI	Reynolds normal stress anisotropy instability

Chapter 1

INTRODUCTION

1.1 Genesis of the Problem

Turbulence near walls is a subject of prime technological importance, as well as a fascinating problem from the physical point of view. It is one of the last canonical incompressible turbulent flows that cannot be considered as being completely understood though the structure of near-wall turbulence has been extensively investigated over the past thirty years. Despite the large effort devoted to the subject, the basic self-sustaining mechanism for near-wall turbulence is not well understood. There is no consistent dynamical picture due to lack of understanding of complex interactions between various structures and between the flow in the near-wall region and that in the outer layer. The kinematics of coherent structures have been well characterised [44], but the dynamics of the various mechanisms involved in the regeneration process, including the factors which govern the spanwise spacing of the streaks, have proven extremely difficult to ascertain.

1.1.1 Coherent structures in near-wall turbulence

Theodorsen [62] started the "structural approach" in turbulence by proposing conceptually that the "molecule" of turbulence is a horseshoe-shaped vortex. Townsend [64] supplemented this approach on basis of his two-point correlations by suggesting that dominant near-wall structures are streamwise-oriented vortices. Kline and Runstadler [35] used the hydrogen bubble technique to show that the sublayer streaks exist and have a spanwise streak spacing scale of 100 wall units. Schraub and Kline [51] also found the same streak spacing for both positive and negative pressure-gradient flows. Kim et. al. [30] were able to demonstrate that turbulence production mainly occurs when these streaky structures (primarily low-speed streaks) lift and burst.

Robinson [45] using the Spalarts' [57] low-Reynolds-number boundary layer DNS data noted the presence of near-wall counter-rotating streamwise vortices which are tilted upwards in downstream direction. He hypothesised that these vortices generate cross-flows that create and lift streaks. The lifted low-speed streaks burst and transform into free-shear layers which undergoing some instability generate more vortices. Thus it was conjectured that by these processes self-sustaining cycle of turbulence is ensured. Moreover, it was found that the low-speed streak structures become progressively more broadly spaced and disorganized as we move away from the walls.

This gradual transition from the low-speed streaks near the surface to multiple shape and size vortices farther away suggests that primarily inner streaky structure wall-layer exist simultaneously with an outer-region dominated by vortices of all orientations. It has been observed that for long time intervals of "quiescent periods" the two layers do not interact and then for brief intervals of time strong interaction occurs resulting in localized breakdowns of the low speed streaks: an event which is critical for sustenance of turbulence. This "bursting" of low-speed streaks is characterized by outward ejection of near-wall fluid, often well into the outer-region of the boundary layer [54]. The majority of turbulent kinetic energy and Reynolds stresses are generated during the bursting event [8, 69]. Moreover, the near-wall vorticity that has been generated during the quiescent periods, also gets ejected.

The event of "ejection" is immediately followed by "sweep" event [12] in which high-speed outer-layer fluid swoops down into the wall-layer and the process of development of new streaks ensues. Thus the wall-layer undergoes a spatially random cyclic process of slow streak development, followed by a rapid, strong interaction with the outer region. Some researchers [18],[55] are of the view that large scale outer flow structures are created by coalescence and reconnection of several small-scale active vortical structures. This systematic growth resulting in a "hierarchy" of hairpin vortices has been conceptually idealized by Perry and Chong [41] and observed numerically in DNS of turbulent flows by Zhou et. al. [70].

Turbulent drag reduction can be achieved if the physics of the regenerative mechanism is understood and then will it be possible to disturb the sequence of turbulent near-wall structures, especially by reducing the strength of the streaks so that they result in weaker burst/sweep events.

1.2 Overview of Relevant Literature

The innermost layer, reaching approximately a height of 100 wall units i.e. $z^+ = 100$ on a smooth-wall and including the viscous sublayer, the buffer layer and the inner part of the logarithmic zone, is responsible for most of the production of turbulent energy and is the zone where crucial dynamics responsible for regeneration of turbulence occurs. The experimental presence of streamwise streaks was observed by Kim, Kline and Reynolds [30] which consist of long , $x^+ = 1000$, sinuous arrays of alternating streamwise jets, with an average spanwise wavelength $y^+ = 100$ [52]. The presence of quasi-streamwise vortices and shear layers protruding from the wall have also been documented by various investigators (see ref [3],[28]). These quasi-streamwise vortices are slightly tilted away from the wall and are roughly $x^+ = 200$ long [23]. These vortices might have a longitudinal spacing of $x^+ = 400$ [25] and they merge into disorganised vorticity after leaving the immediate wall neighbourhood [44]. These quasi-streamwise vortices are believed to cause the streaks by advecting the mean velocity gradient [3] and thereby producing turbulent wall drag [39]. In the outer-layer, hairpin like vortices have been visualised experimentally [18] and in numerical simulations [33].

Jimenez and Moin [25] used DNS in turbulent channel flow at $Re's$ (based on channel centreline velocity and halfwidth of the channel) from 2000 to 5000 for streamwise and spanwise periodic boundary conditions. They observed turbulent structures such as sublayer streaks, streamwise vortices, and near-wall shear layers, yet they did not provide a suitable regeneration mechanism for them. Aubry et al. [2] used a dynamical systems approach to study the behaviour of streamwise vortices, but could not ascertain the cause responsible for the origin of these vortices. Vortex formation must recur for turbulence to be sustained, i.e. existing vortices must ensure subsequent vortex regeneration. The numerous proposed regeneration mechanisms, involve either : (i) the direct action (induction) of existing vortices ("parent-offspring" scenarios) or (ii) local recurring instability of a quasi-steady base flow, in which previous vortices play an indirect role in generating an unstable base flow.

In the "parent-offspring" mechanism, it is suggested that there is generation of new vortices near an existing spanwise arch and beside each of the streamwise legs by direct induction [53]. In their model Smith and Walker [53] propose that low-speed streaks are created by the advection of hairpin vortex on wall-region fluid. This process which is a local viscous-surface interaction creates sufficient adverse pressure-gradient at the surface resulting in ejection of portion of the streak which further through inviscid-viscous interaction with the outer-layer fluid results in generation of hairpin vortices. While Smith and Walker propose that hairpin vortex formation mechanism is based on unsteady separation of localized streaks as mentioned above, Zhou et. al.[71] propose that only quasi-streamwise vortices are generated which later by mutual self-induction and viscous reconnection generate offspring heads. Vortex formation is also attributed to 2D Kelvin-Helmholtz type roll up of near-wall streamwise vorticity sheets (see [26]). Brooke and Hanratty [4] proposed a mechanism in which streamwise vortices themselves generate secondary streamwise vorticity by their interaction with the wall, and this vorticity eventually rolls into new streamwise vortices. In their model there is a formation of an opposite-signed vortex underneath an inclined parent vortex. The generation of vorticity is brought about by the vorticity-tilting term, generated by the spanwise inclination of the parent vortex. However, in the numerical experiments performed by Jimenez and Pinelli [27] a transverse free-slip wall, at which $\frac{\partial w}{\partial y}$ =0, was introduced and its effect seen on secondary streamwise vorticity. The findings of these numerical experiments conclusively proved that 'secondary streamwise vorticity' was not responsible for the generation of streamwise vortices.

Of the numerous mechanisms developed to explain near-wall vortex formation, there is considerable disagreement as to the dominant mechanisms of instability and feedback. The various mechanisms include:

1. Direct resonance of oblique modes (Jang, Benney & Gran [22]),
2. Selective amplification (Waleffe et. al. [68]),
3. Lateral instability waves (Jimenez [25]),
4. Centrifugal instability (Sreenivasan, [59]),
5. Shear-driven instability (Hamilton, Kim & Waleffe, [16]) and

6. Streak instability with parent vortex (Swearingen and Blackwelder, [61])
7. Streak instability without any parent vortex (Schoppa & Hussain, [48]).
8. Travelling wave solutions (Waleffe [66]).

The origin of the streamwise vortices was considered by Jang, Benney & Gran [22] using 'direct resonance' theory to explain the observed spanwise spacing of the vortices and the streaks. According to them, this nonlinear mechanism involves algebraic growth of wall-normal vorticity due to vertical velocity generated by nonlinear interaction of oblique vorticity modes. This large wall-normal vorticity ω_z is then oriented in streamwise direction to generate streamwise vortices. Waleffe, Kim & Hamilton [68] challenged this theory by stating that it is the nonlinear interaction of the oblique modes of vertical velocity, rather than wall-normal vorticity oblique modes as required for scale selection in the direct resonance theory. Waleffe *et. al.* [68] also examined the possibility that the spanwise spacing of the streaks is determined by a length scale associated with the thickness of the high-gradient layer of the mean velocity profile. However, this selective amplification mechanism also could not give the correct spacing of the streaks.

Another approach to understanding turbulence regeneration is to assemble various known dynamical processes into a conceptual model which includes some sort of feedback mechanism to close the cycle. Jimenez [25] proposed a model in which lateral instability waves form in regions of large wall-normal vorticity i.e. the interfacial regions of streaks. Streamwise vortices form as this vorticity is tilted into the streamwise direction by the shearing of the main flow. The cycle is closed with the formation of new streaks by the streamwise vortices. Sreenivasan [59] proposed that Görtler, or centrifugal instability mechanism generates streamwise vortices which in turn generate new streaks. According to him, the local concave curvature of near-wall streamlines in x-dependent shear flows can cause generation of near-wall vortices through Taylor-Görtler instability mechanism (see [5]). Even the presence of streamwise undulations in x-dependent shear flows can lead to generation of near-wall vortices through Craik-Leibovich instability [13]. The underlying shortcoming of these instability mechanisms is that namely no instability-generated streamwise vortices can induce unstable base flows with streamline curvature or streamline undulations; hence the necessary feedback mechanism is not evident [49].

Swearingen and Blackwelder [61] suggested that vortex regeneration can occur due to local instability of the spanwise U(y) shear layers flanking low-speed streaks. This streak waviness in (x,y) (or sinuous mode) is apparently induced by vortices advecting upon the streaks. Robinson [45] proposed that lifted low-speed streaks contain a locally unstable wall-normal U(z) profile (or varicose mode) which gives rise to new spanwise "arch" vortices. These "arch" vortices subsequently generate legs or streamwise vortices, which in turn again generate a new unstable streak to close the cycle. Both the above mechanisms relying on sinuous and varicose mode instabilities are x-dependent. It was later found by other researchers that Robinson's mechanism is unlikely to form new arches, since the varicose mode associated to U(z) profile is stable for typical U(y,z) distributions at low *Re* shear flows and hence there would be no generation of hairpin vortices.

Schoppa and Hussain [48] demonstrated via DNS that instability of streaks - without any initial (parent) vortex - directly generates new streamwise vortices, internal shear layers, and arch vortices. They proposed that there is repeated instability of vortex-less streaks left behind by previous streamwise vortices. From their DNS results they show that a new streamwise vortex is created by the instability of a streak, from the wall-normal ω_z vorticity sheet flanking the streak. Subsequently the opposite-signed vortices are stretched by the mean shear, causing them to stack on each other. Then mutual induction of the stacked vortices flattens them into vorticity layers which are then annihilated by viscous cross-diffusion and then the whole process repeats itself. According to Jimenez [24], where further references can be found, the details of this process are still unclear.

Hamilton, Kim & Waleffe [16] and Waleffe [65] studied the vortex regeneration mechanism of near-wall turbulence structures in plane Couette flow with the minimal domain size and *Re* for sustained turbulence. They found a regular quasi-cyclic process of three distinct phases: formation of streaks by streamwise vortices, breakdown of the streaks via its wake-like instability, and regeneration of the streamwise vortices by nonlinear interactions of chaotic flow. The first phase consists of redistribution of streamwise momentum by streamwise rolls. For x-independent flows, the cross-flow velocities that form the streamwise rolls, decouple from streamwise velocity and the rolls decay. But before decaying they induce spanwise modulation of U(z) by redistributing momentum. The slowest decaying rolls have preferential wavelength of 5h, where *h* is the half-channel height.

The typical $U(y,z)$ profile is subject to two dominant types of inflectional instability modes: fundamental sinuous mode with subharmonics and fundamental varicose mode. It is known that fundamental sinuous mode leads to the typical staggered row of vortices [23], while the subharmonic sinucose mode and the fundamental varicose mode, would lead to generation of horseshoe-like structures [1]. The mean shear provides the feedback on streamwise rolls by bringing about non-linear interactions of $e^{\iota\alpha x}$ streak instability modes. Though the study elucidates a detailed dynamics of the coherent structures yet it is not able to explain the effect of large spatio-temporal domain and high Re on the dynamics of coherent structures. All the theories that have been cited above essentially imply 3D mechanism, so that the feedback from longitudinal flow to the cross-flow is crucial.

There are two theories, however, where the streaks are formed from a chaotic background even in the absence of feedback from the longitudinal flow direction. One is the optimal perturbation (OP) theory proposed by Butler and Farrell [7] and the other is Reynolds normal stress anisotropy instability (RNSAI) mechanism by Nikitin and Chernyshenko [38]. In the first mechanism, Butler and Farrell [7],[6] employed a variational approach to find 'optimal' perturbations - perturbations that produce the greatest growth in kinetic energy of the perturbations over a given time - to study streak spacing. In their study, Butler and Farrell calculated the optimal perturbations in a plane channel turbulent flow at a Re=180 (based on channel half-height and wall-friction velocity u_τ). They found that optimal perturbations generate streamwise vortices which in turn generate streaks by lift-up mechanism leading to a significant (by a factor of 235) growth of kinetic energy of the perturbations, but the streak spacing was 540 wall units (instead of being 100 wall units) and the time (scaled by ν/u_τ^2) needed for the energy to attain maximum value turned out to be quite large i.e. 2340 non-dimensional units [6]. But as streak spacing near the wall is of the order of 100 wall units, they suggested an assumption that in reality the perturbations can grow only over a limited time equal to the so-called eddy-turnover time τ_e because after this time the perturbations get disrupted by the turbulent fluctuations. With this additional constraint of eddy turnover time they found that the streak spacing turned out to be approximately 100 wall units, in agreement with experiments.

The other mechanism based on Reynolds normal stress anisotropy instability (RNSAI) by Nikitin & Chernyshenko [38], in contrast to previous work, explains the formation of longitudinal vortices in terms of instability induced by the Reynolds normal stress anisotropy without reference to any other organised structures. In this theory, the natural starting point for the vortex generation/regeneration cycle is just a chaotic motion of the fluid near the wall. Since the wall restricts fluctuations in the direction normal to the wall, there is non-zero difference between normal Reynolds stresses in spanwise and transverse (perpendicular to the wall) directions; in other words, the turbulence is anisotropic. If averaged statistical characteristics do not depend on the spanwise coordinate, the difference in normal stresses can be balanced by a pressure gradient only. If, however, there is a perturbation which is non-uniform in the spanwise direction, non-zero difference in normal stresses inevitably causes fluid motion in the cross-flow plane.

In the case of a cross-flow perturbation whose length scale is much greater than the characteristic length scale of chaotic motion, normal Reynolds stresses are simply advected by the cross-flow motion and this advection of normal stresses results in an instability. Formally, this instability is similar to an instability in a fluid layer heated from below and its generation is due to the persistence over time of the quantity $\frac{\partial^2 <v'^2 - w'^2>}{\partial z^2} < 0$ where z is the wall-normal direction. The z-derivative of Reynolds normal stress distribution plays a role similar to that of the density distribution, with the sign reversed.

This instability has been analysed mathematically using a simple passive-admixture transport equation for the Reynolds-stress perturbations. The calculated eigensolutions describe the longitudinal vortices with spanwise period of 100 wall units.

1.3 Outline of the research

The overall objective of this study is to improve the fundamental understanding of near-wall turbulence which can be used to develop methods of control of turbulent flows especially for drag reduction. The most important aim of our study is to seek out the sustenance mechanism of near-wall turbulence by uncovering the mechanism of streak formation. Initially it was planned to do so by showing the existence of streaks in quasi-2D (that is with flow variables independent of streamwise direction x) turbulent flows (both decaying and forced) thereby excluding several theories that depend on longitudinal feedback, hence leaving two main competitors namely the RNSAI mechanism of Nikitin and Chernyshenko [38] and optimal perturbation theory of Butler and Farrell [7]. This aim was also to let us determine whether even in the absence of vortex stretching, the longitudinal vortices can be created.

It was realised right from the start that to achieve the main aim of this study, a rigorous analytic approach is quite difficult and addition of simplifying assumptions is likely to make the study inconclusive. So it was decided to solve numerically the Navier-Stokes equations using Direct Numerical Simulation (DNS) for incompressible flow in a quasi-2D formulation (gradients of all the dynamical variables in the streamwise direction are zero i.e. $\partial/\partial x = 0$). Since a DNS code for turbulent channel geometry [47] was available, it was decided to modify and use this code to suit our purpose. In quasi-2D case, natural perturbations decay. Therefore, random perturbations have to be introduced externally. Two methods have been considered for introducing external random fluctuating motion in the quasi-2D domain, for the decaying and forced cases, respectively. For the decaying turbulence case, a random velocity spatial distribution was used as the initial condition. As the flow decays and comes to rest coherent organised structures in the form of vortices or their by-products streaks near the walls in the streamwise direction were expected to emerge. For the case of forced quasi-2D turbulence, we examined the motion resulting from the introduction of a randomly fluctuating body force applied to a band of wavenumbers or a single wavenumber at a particular forcing frequency till a statistically stationary state is obtained.

While investigating the formation of coherent structures in quasi-2D domains, we also had the objective to determine the dependence of characteristics of the coherent structures on the parameters of the initial random motion for quasi-2D decaying turbulence and on the forcing parameters for the case of quasi-2D forced turbulence. Regarding this, for the first case we needed to generate the initial random velocity field devoid of any organised structures and also being divergence-free. To this end, two types of initial random velocity were considered: one which generates anisotropic eddies using sinusoidal perturbations covering a range of high wavenumbers and the other which generates isotropic eddies using the concept of Gaussian vortices distributed with a particular probability density function simulating a real turbulent flow. For the forced quasi-2D turbulence case, the statistical properties of the random body force such as its amplitude, its distribution in space, forcing frequency and the wavenumbers excited were expected to significantly influence the results.

The other main objectives were to determine the scalar streak spacings by applying RNSAI mechanism to the case of quasi-2D randomly forced and 3D turbulent channel flows having several passive scalars in the flowfield and compare the results with two-point correlations of DNS and visual observations. Later on we intended to compare results of scalar streak spacings obtained using two-point correlations of DNS results with theoretical predictions of OP theory. To realise these objectives, we conducted numerical experiments for the forced quasi-2D and 3D turbulent channel flows with several passive scalars introduced. The simulation was performed till stationarity was achieved and then higher-order statistics like two-point correlations were gathered for all the dynamical variables. Besides this for each mean scalar profile, wavelengths were computed for which maximum energy growth occurs under the constraint of eddy turnover time based on ideas from OP theory. Finally streak spacing based on wavelengths from OP theory and from RNSAI mechanism were compared with DNS results using two-point velocity and scalar correlations.

We have discussed briefly in the above paragraphs the outline of the research we have pursued in this study, but now we present a succinct summary of aims and objectives that have been realised in this research:

1. By performing numerical experiments in quasi-2D decaying turbulence we have shown that streaks can form even in case when there is no feedback from the longitudinal flow profile, including the streaks, to the cross-flow vortex structure.
2. We have demonstrated that passive scalar streak spacing varies significantly even when the vortical structure generated by the velocity field is fixed. This clearly demonstrates that organised vortices play no direct role in the development of streaks (either velocity or scalar concentration streaks.)
3. It has been shown that vortex regeneration theories which assume the streak spacing being equal to twice the vortex spacing, like, for example, RNSAI, are not able to explain this fact.
4. We have illustrated that the scalar streak spacing strongly depends on the mean profile of the scalar and this behaviour is only described by OP theory. We also found though that in many cases the theoretical prediction of streak spacing by OP differs considerably from DNS results.
5. We expound the fact that scalar streaks can be generated in a random potential velocity field with a mean turbulent velocity profile, thereby strongly corroborating the fact that organized vortices play no significant role and it is the lift-up mechanism [60] which is responsible for formation of streaks as well as their cross-flow spacing.

6. Finally, we provided the DNS data in support of the modification of the OP theory to the Generalized Optimal Perturbation (GOP) theory.

1.4 Outline of the thesis

We close the introduction by outlining the contents of this thesis. The chapters are presented in such a sequence that the emphasis is shifted from background aspects needed to conduct this study starting with introduction to the numerical implementation of the pseudo-spectral code at the beginning to the physical aspects of turbulence regeneration mechanisms at the end of the thesis. Specifically, in chapter 2, we present the mathematical aspects of the tools that have been used in order to achieve the aims of this study. These relate to the numerical model elaborating upon the specifics of the pseudo-spectral code that has been used to solve the Navier-Stokes equations. Besides this a brief introduction as well as numerical implementation of the OP code has been discussed. In chapter 3, we present the numerical experiments concerning simulation of quasi-2D decaying turbulence for two different initial random conditions – one dealing with anisotropic eddy field generation using sinusoidal perturbations while the other pertains to isotropic "random eddy" field generation. The results from both show the formation of near-wall streaks, but no definite conclusion could be reached regarding the regeneration mechanism or the scale selection mechanism.

In chapter 4, we present statistically stationary results of numerical simulation of quasi-2D forced turbulence subjected to divergence-free random forcing which leads to generation of near-wall streaks. The number of near-wall streaks obtained using two-point correlation and visual observations is then compared with theoretical predictions of RNSAI mechanism. The theoretical predictions of RNSAI mechanism are obtained on solving an eigenvalue problem utilising source term obtained from DNS results.

In chapter 5, we present modifications performed on the pseudo-spectral code in order to solve an arbitrary number of passive-admixture equations. We present results relating to quasi-2D forced turbulence simulation with different mean scalar profiles solved simultaneously with the Navier-Stokes equations, which show a significant variation of streak spacing for the scalar variables. In later sections, OP theory is applied to flows with various mean scalar profiles and from this analysis, scalar streak spacings have been computed based on wavelengths for which maximum energy growth occurs over an appropriate turbulent eddy turnover time. The DNS results of two-point correlations for various passive scalars are then compared with theoretical predictions of OP theory and RNSAI mechanism.

In chapter 6, we present results of DNS of 3D turbulent channel flow with eight passive scalar equations solved simultaneously using the modified pseudo-spectral code. A linear combination technique has been employed to generate new scalar profiles that give an order of magnitude variation in streak spacing. These results are then compared with theoretical predictions of OP theory and RNSAI mechanisms and conclusions derived on that basis. Besides this, results are presented related to numerical simulations which show the generation of scalar streaks in a flow having random potential fluctuations. Later on a brief introduction has been given about Generalized Optimal Perturbation (GOP) theory and its theoretical predictions compared with DNS results for the passive scalar mean profiles in appendix A. In chapter 7, a brief discussion about the physical mechanism responsible for variation of streak spacing has been included. Subsequently, an opinion has been proposed on origin of structures in turbulence based on the findings of our results. This is followed by listing of major conclusions and finally suggestions for future work have been proposed. In appendix A we have attached a copy of the manuscript entitled ”The mechanism of streak formation in near-wall turbulence”, which we have submitted for publication to Journal of Fluid Mechanics.

Chapter 2

BACKGROUND

2.1 Introduction

This chapter briefly describes the numerical tools which were made available for this research. For our direct numerical simulations we used the pseudo-spectral channel flow code of Sandham and Howard [47]. The following sections 2.1-2.4 give a brief overview of the numerical model used in this code and its implementation on parallel computers. Further details can be found in Kleiser and Schumann [34] and in the text by Canuto *e*t.al. [9]. A brief background introduction to OP theory is outlined in section 2.5. The mathematical details specific to the numerical OP code written by Prof. Sergei Chernyshenko are given in subsection 2.5.1.

2.2 Governing Equations and the Numerical Approach

The governing equations of incompressible turbulent flow i.e. the continuity equation and the momentum equations, are non-dimensionalized with the channel half-width h^*, and the friction velocity $u_\tau{}^* = \sqrt{\tau_w{}^*/\rho^*}$; where τ_w^* is the wall shear stress and ρ^* is the density. Here asterisks are used to denote dimensional quantities. The Reynolds number is $Re_\tau = u_\tau{}^* h^*/\nu^*$. The non-dimensional quantities are then defined as

$$u_i = u_i^*/u_\tau{}^*, \quad x_i = x_i^*/h^*, \quad p = p^*/(\rho^* u_\tau{}^* u_\tau{}^*), \quad t = t^* u_\tau{}^*/h^* \tag{2.1}$$

The normalised mean pressure gradient for the turbulent plane channel flow obtained using control volume analysis on a fluid element turns out to be $\overline{dP/dx} = -1$.

The *continuity* equation is

$$\nabla \cdot \mathbf{u} = 0 \tag{2.2}$$

while the governing momentum equations, cast in rotational form, are

$$\frac{\partial \mathbf{u}}{\partial t} = \mathbf{u} \times \omega - \nabla q - \mathbf{e_1} \frac{\overline{dP}}{dx} + \frac{1}{Re_\tau} \nabla^2 \mathbf{u} \tag{2.3}$$

where $\mathbf{e_1}$ is the unit vector of x-axis. In the above equations, velocity is denoted by $\mathbf{u}$ and vorticity by ω. The pressure term has been split into mean and fluctuating pressure $p = \bar{P} + p'$ and a modified pressure given as $q = p' + \mathbf{u} \cdot \mathbf{u}/2$. The bold quantities indicate vectors in all the formulations. The coordinates are set as x in the streamwise direction, y in the spanwise direction and z in the wall-normal direction, with the channel walls at $z = \pm 1$. The time advancement uses a compact third-order Runge-Kutta scheme [58] for the convective terms and Crank-Nicolson implicit method for the viscous and pressure terms. The need for implicit treatment of viscous and pressure terms is to avoid extremely small time steps owing to the behaviour of the Chebyshev discretisation in the near-wall region. For each Runge-Kutta substep, the discretised equation can be written as

$$\frac{\mathbf{u}^{n+1} - \mathbf{u}^n}{\Delta t} = a(\mathbf{u} \times \omega)^n + b(\mathbf{u} \times \omega)^{n-1} - \mathbf{e_1} \frac{dP}{dx} - \frac{\nabla q^{n+1} + \nabla q^n}{2} + \frac{\nabla^2 \mathbf{u}^{n+1} + \nabla^2 \mathbf{u}^n}{2Re_\tau} \tag{2.4}$$

where a and b are Runge-Kutta substep coefficients while $n-1$, n and $n+1$ refer to successive substeps. Taking all the terms at $n+1$ substep to the left hand side and then taking Fourier transform in the two periodic directions x and y gives

$$\begin{aligned} \frac{\hat{\mathbf{u}}^{n+1}}{\Delta t} + \frac{\widehat{\nabla q}^{\,n+1}}{2} + \frac{k^2 \hat{\mathbf{u}}^{n+1}}{2Re_\tau} - \frac{\hat{\mathbf{u}}''^{\,n+1}}{2Re_\tau} \quad = \quad & \frac{\hat{\mathbf{u}}^n}{\Delta t} + a(\hat{\mathbf{u}} \times \hat{\omega})^n + b(\hat{\mathbf{u}} \times \hat{\omega})^{n-1} - \mathbf{e_1} \frac{dP}{dx} - \\ & \frac{\widehat{\nabla q}^{\,n}}{2} - \frac{k^2 \hat{\mathbf{u}}^n}{2Re_\tau} + \frac{\hat{\mathbf{u}}''^{\,n}}{2Re_\tau} \end{aligned} \tag{2.5}$$

Here $\hat{\mathbf{u}}$ refers to Fourier-transformed velocity while prime denotes differentiation with respect to z, the wall-normal direction. On multiplying by 2 throughout and putting all the right hand side terms in the residual vector $\hat{\mathbf{R}}$, one gets

$$-\frac{1}{Re_\tau}\hat{\mathbf{u}}'' + \lambda\hat{\mathbf{u}} + \hat{\nabla}\hat{q} = \hat{\mathbf{R}} \tag{2.6}$$

where $\lambda = 2/\Delta t + k^2/Re_\tau$ with $k^2 = k_x^2 + k_y^2$. Here we dropped the superscript $n+1$. The momentum equation in the wall-normal direction can be written as

$$-\frac{1}{Re_\tau}\hat{w}'' + \lambda\hat{w} + \hat{q}' = \hat{R}_z \tag{2.7}$$

Terms on the left-hand side are at time level $n+1$ while terms on the right-hand side are known at time level n and $n-1$. Taking the divergence of the momentum equations, using the Fourier transformed continuity equation

$$ik_x\hat{u} + ik_y\hat{v} + \hat{w}' = 0, \quad \hat{w}'(\pm 1) = 0 \tag{2.8}$$

we can get Poisson equation of the form

$$\hat{q}'' - k^2\hat{q} = \hat{\nabla}.\hat{\mathbf{R}} \tag{2.9}$$

The boundary conditions are $\hat{w}'(\pm 1) = 0$ and no-slip at the walls given as $\hat{u}(\pm1)$=0, $\hat{v}(\pm1)$ =0 and $\hat{w}(\pm1)$ =0. The eqns. (2.7), (2.9) with the boundary conditions constitute a complete set for $\hat{w}$ and $\hat{q}$ and are called 'A-problem'. As there are no boundary conditions for the modified pressure $\hat{q}$, the 'A-problem' is recast into another problem called 'B-problem' such that boundary conditions on $\hat{q}$ are applied at the walls. So the 'B-problem' comprises solution of eqns. (2.7), (2.9) and boundary conditions $\hat{q}(\pm 1) = \hat{q}_\pm$ that are consistent with the conditions $\hat{w}'(\pm 1) = 0$. Let $(\hat{q}_p, \hat{w}_p)$ be the solution of 'B-problem' but with homogeneous Dirichlet boundary conditions on $\hat{q}$. Let $(\hat{q}_+, \hat{w}_+)$ and $(\hat{q}_-, \hat{w}_-)$ be the solutions of the homogeneous B-problems, with boundary conditions $\hat{q}_+(-1) = 0$, $\hat{q}_+(+1) = 1$, and $\hat{q}_-(-1) = 1$, $\hat{q}_1(+1) = 0$, respectively. The solution of the 'A-problem' can be written as

$$\hat{q} = \hat{q}_p + \delta_+\hat{q}_+ + \delta_-\hat{q}_- \tag{2.10}$$

$$\hat{w} = \hat{w}_p + \delta_+\hat{w}_+ + \delta_-\hat{w}_- \tag{2.11}$$

The constants δ_+ and δ_- are found from solution of a 2×2 'influence' matrix, obtained by imposition of $\hat{w}'(\pm 1) = 0$ boundary condition on equation (2.11) at each wall. This gives us the correct pressure boundary condition $\hat{q}(\pm 1) = \delta_\pm$. Hence the solution of the 'B-problem' with correct boundary condition leads to solution of the 'A-problem'.

The next step is to perform Chebyshev-tau discretization of ’B-problem’ in wall-normal direction. The equations for the discretised variables $\tilde{w}$ and $\tilde{q}$ i.e. discrete ’B-problem’ read

$$-\frac{1}{Re_\tau}\tilde{w}_m^{2p} + \lambda\tilde{w}_m + \tilde{q}_m^p = \tilde{R}_{z,m} + \tilde{\tau}_m, \quad \hat{w}(\pm 1) = 0 \tag{2.12}$$

which applies for $m = 0, \dots, N$ and

$$\tilde{q}_m^{2p} - k^2\tilde{q}_m = \imath(k_x\tilde{R}_{x,m} + k_y\tilde{R}_{y,m}) + \tilde{R}^p_{z,m} + \tilde{\tau}^p_m, \quad \hat{q}(\pm 1) = \hat{q}_\pm \tag{2.13}$$

which applies for $m = 0, \dots, N-2$. Exponents p and $2p$ refer to first and second derivatives. Though the tau term $\tilde{\tau}_m$ is zero for $m = 0, \dots, N-2$ modes but we get coupling of eqns. (2.12) and (2.13) through the derivative term $\tilde{\tau}^p_m$. The equations are coupled through the recurrence relation

$$\tilde{\tau}^p_m = \frac{2m'}{c_m}\tilde{\tau}_{m'} \tag{2.14}$$

where m' is equal to N for all odd m and $N-1$ for all even m, and c_m is equal to 2 for $m = 0$ or $m = N$ and equal to 1 otherwise. Kleiser and Schumann [34] further decomposed the discrete ’B-problem’ into ’B1-problem’ and ’B0- problem’. For the ’B1-problem’ all the $\tilde{\tau}_m$ terms are ignored and we get the equations

$$-\frac{1}{Re_\tau}\tilde{w}_m^{2p} + \lambda\tilde{w}_m + \tilde{q}_m^p = \tilde{R}_{z,m}, \quad \hat{w}(\pm 1) = 0, \qquad m = 0, \dots, N-2 \tag{2.15}$$

$$\tilde{q}_m^{2p} - k^2\tilde{q}_m = \imath(k_x\tilde{R}_{x,m} + k_y\tilde{R}_{y,m}) + \tilde{R}^p_{z,m}, \quad \hat{q}(\pm 1) = \hat{q}_\pm, \quad m = 0, \dots, N-2 \tag{2.16}$$

and for the ’B0-problem’

$$-\frac{1}{Re_\tau}\tilde{w}_m^{2p} + \lambda\tilde{w}_m + \tilde{q}_m^p = 0, \qquad m = 0, \dots, N-2 \tag{2.17}$$

$$\tilde{q}_m^{2p} - k^2\tilde{q}_m = \frac{2m'}{c_m}, \qquad m = 0, \dots, N-2 \tag{2.18}$$

The superposition yields

$$\tilde{q}_m = \tilde{q}_{1m} + \tilde{\tau}_{m'}\tilde{q}_{0m} \tag{2.19}$$

$$\tilde{w}_m = \tilde{w}_{1m} + \tilde{\tau}_{(m+1)'}\tilde{w}_{0m} \tag{2.20}$$

where subscripts 0 or 1 refer to the ’B0’ and ’B1’ problems and

$$\tilde{\tau}_m = \frac{\tilde{\tau}_{1,m}}{1 - \tilde{\tau}_{0,m}} \tag{2.21}$$

The solution procedure is to solve the discrete ’B0’ and ’B1’ problems to get $\tilde{\tau}_{0,m}$ and $\tilde{\tau}_{1,m}$, compute the tau term from equation (2.21) and then use eqns. (2.19) and (2.20) to compute $\tilde{w}_m$ and

$\tilde{q}_m$ i.e. solutions with homogeneous boundary conditions on $\tilde{q}$. The constants δ_+ and δ_- can be found by inverting the influence matrix, and the solutions to the homogeneous problem can be added to get the solution $\hat{q}$ and $\hat{w}$. Then we can solve further two more Helmholtz equations to get $\hat{u}$ and $\hat{v}$, so in total 6 Helmholtz or Poisson equations need to be solved, each of which has a quasi-tridiagonal form.

In evaluating the right-hand side of eqn. (2.4), the nonlinear term $\mathbf{u} \times \omega$ must be computed. This is most efficiently done using a pseudospectral transform approach. For practical computations aliasing error will result, due to forming non-linear products when using a finite number of modes. This error can be explicitly eliminated if the '3/2 rule' is used. The implementation of dealiasing involves extending the number of modes by 50% by padding with zeros, transforming to real space using the fast Fourier transform (FFT), computing the nonlinear products in real space, inverse transforming and then truncating the result by dropping the upper-third of the modes. Moreover, the other advantage of dealiasing is that the simulations can be carried out even in under-resolved situations.

2.3 Spatial Derivatives

It is widely known that Fourier spectral methods impose periodic boundary conditions, while Chebyschev methods can be applied to non-periodic boundary conditions. In the Sandham and Howard spectral code [47], Fourier discretization is used for the horizontal planes while the Chebyschev tau method is used for the wall-normal direction to account for the non-periodicity in that direction. As per the details given in Hu et. al. [19], in the horizontal plane, a two-dimensional Fourier transformation (real to complex) from real to wave space is performed in the streamwise direction, followed by a complex to complex Fourier transformation in the spanwise direction. In the streamwise direction, only half the Fourier modes need to be stored due to conjugate symmetry of positive and negative wavenumber modes for real variables. A real quantity $q(x,y)$ is transformed to $\hat{q}(k_x,k_y)$ in discrete Fourier space by the successive operations:

$$\tilde{q}(k_{x_l},y_j) = \frac{1}{N_x}\sum_{i=0}^{N_x-1} q(x_i,y_j)e^{-\imath 2\pi * li/N_x} \tag{2.22}$$

$$\tilde{\tilde{q}}(k_{x_l},k_{y_m}) = \frac{1}{N_y}\sum_{j=0}^{N_y-1} \tilde{q}(k_{x_l},y_j)e^{-\imath 2\pi * mj/N_y} \tag{2.23}$$

where $\imath = \sqrt{-1}$; N_x and N_y are the total number of grid points (both even) in the streamwise and spanwise directions. If uniform grids are used, then

$$x_i = \frac{L_x i}{N_x}, \quad 0 \leq i \leq N_x \tag{2.24}$$

$$y_j = \frac{L_y j}{N_y}, \quad 0 \leq j \leq N_y \tag{2.25}$$

The spatial wavenumbers k_{x_l}, k_{y_m} are given by

$$k_{x_l} = \frac{2\pi l}{L_x} \quad -N_x/2 \leq l \leq N_x/2 \tag{2.26}$$

$$k_{y_m} = \frac{2\pi m}{L_y} \quad -N_y/2 \leq m \leq N_y/2 \tag{2.27}$$

where L_x and L_y are non-dimensional computational box lengths in the streamwise and spanwise directions. Here l and m are number of Fourier modes in streamwise and spanwise directions, respectively. The two-dimensional backward transformation is done with a spanwise complex to complex transformation, followed by a streamwise complex to real transformation

$$\tilde{q}(k_{x_l}, y_j) = \sum_{m=-N_y/2}^{N_y/2} \tilde{\tilde{q}}(k_{x_l}, k_{y_m}) e^{\imath 2\pi * mj/N_y} \tag{2.28}$$

$$q(x_i, y_j) = \tilde{q}(0, y_j) + 2\sum_{l=1}^{N_x/2} q(k_{x_l}, y_j) e^{\imath 2\pi * li/N_x} \tag{2.29}$$

Chebyschev transforms are used for the wall-normal direction:

$$q_m = \sum_{k=0}^{N_z-1} \widetilde{q_m}(z_n) T_k(z_n) \tag{2.30}$$

$$\widetilde{q_m} = \frac{2}{\pi c_k} \int_{-1}^{1} q_m(z_n) T_k(z_n) w(z_n) dz \tag{2.31}$$

Here N_z is the number of wall-normal grid points, while Chebyshev polynomials of first kind $T_k(z_n)$, Chebyshev-Gauss-Lobato coordinates z_n and weights are given as:

$$T_k(z_n) = cos(k \quad arccos(z_n)) \tag{2.32}$$

$$z_n = cos(\frac{\pi n}{N_z}) \tag{2.33}$$

$$w_n = \frac{\pi}{N_z} \quad 1 \leq n \leq N_z - 1$$

$$w_n = \frac{\pi}{2N_z} \quad n = 0, N \tag{2.34}$$

2.4 Implementation on Parallel Computers

The Sandham and Howard [47] code used in the present study is parallel. The domain decomposition technique is employed to divide the domain into blocks where each block is assigned to a certain processor. Hence different modes of Fourier and Chebyshev discretised velocity, modified pressure and vorticity are stored on different processors. In the Fourier space, all the mathematical manipulations on these variables can be performed locally except evaluation of the nonlinear terms. In the pseudospectral approach the nonlinear terms are computed in physical space and for that forward and inverse transforms of the variables need to be performed. Hence information from all the processors is required which means devising an efficient strategy for data transfer between the processors.

The data storage approach is based on data decomposition analogous to slicing a loaf of bread, with each slice stored on one processor. Fourier or Chebyshev transforms in two of the three directions can be performed locally on each processor. However, to perform transformation in the third direction a global transpose needs to be performed. After the transpose, the data is "re-sliced" in a perpendicular direction allowing the transform in the remaining direction to be carried out and the nonlinear terms to be computed.

MPI Library has been used to transfer small chunks of data from each processor in order to perform global transpose. The whole process entails labelling the address of each processor that requires the information, transferring the data, reading it by the receiving processor, and reconstructing the flow field. As the process involves data transfer from all the processors to each single processor, it can lead to choking of the buffer memory on the Myrinet bus especially on Linux clusters. The 'choking' problem can be alleviated by allocating substantial buffer memory to each processor and this approach has been incorporated in the code. The dimension of the arrays used to store flow variables is $(N_x+2)*N_y*(N_z+2)$, but due to dealiasing larger arrays of the size $(3/2N_x+2)*3/2N_y*(3/2N_z+2)$ has been used in the code. Efficient parallelisation [47] requires that $3/2N_z+2$ is close to and less than an integer multiple of the number of processors.

2.5 Optimal Perturbation Theory: Introduction

It is well known from linear algebra that even if all the eigenvalues of a linear system are distinct and lie in the stable zone, inputs to that system may result in an arbitrarily large response if the eigenfunctions are not orthogonal to each other. A matrix or operator whose eigenfunctions are orthogonal is said to be 'normal', like the linear operators that result from linearisation of the governing Navier-Stokes equations for Benard and Taylor-Couette flows. Operators that have non-orthogonal eigenvectors such as those found in flows governed by non self-adjoint differential equations have the property that small perturbations to these flows may be amplified by factors of many thousands, even when all the eigenvalues are in the lower half-plane. This results in an algebraic large growth during the early transient period although decay occurs as time goes on. The essential feature of this nonmodal amplification of perturbations of viscous flows is that it applies to 3D perturbations of the laminar flow field and lays more stress on them in comparison to 2D perturbations of classical hydrodynamic stability theory.

The results of the various investigations of the channel flows suggest that the early transient growth can be extremely large (factors of 20 to 1000) at subcritical values of the Reynolds number when considering optimal growth determined from variational techniques. The discovery that Poiseuille and Couette flows have non-normal operators led to the optimal formulation of the problem as given by Farrell [14], Butler and Farrell [6] and further corroborated by Reddy and Henningson [43]. The optimal perturbation theory considers initial value problem for the linearised Navier-Stokes equations and offers a linear explanation for the ubiquitous presence of streaks in all internal and boundary layer shear flows.

In order to understand the idea of non-normal operators which lead to the algebraic growth we start with linearised Navier-Stokes equations for small perturbations u' in which all the quadratic terms have been neglected. The mean velocity profile **U** is assumed to be the turbulent velocity profile. The linearised Navier-Stokes and continuity equations can be written as:

$$\begin{aligned} \frac{\partial \mathbf{u}'}{\partial t} + \mathbf{U}\cdot\nabla\mathbf{u}' + \mathbf{u}'\cdot\nabla\mathbf{U} &= -\nabla p' + \frac{1}{Re}\nabla^2\mathbf{u}' \\ \nabla\mathbf{u}' &= 0 \end{aligned} \tag{2.35}$$

Assuming normal expansion $u' = e^{\sigma t}\tilde{u}$ reduces the above form to an eigenvalue problem

$$\begin{aligned} \sigma\tilde{\mathbf{u}} + \mathbf{U}\cdot\nabla\tilde{\mathbf{u}} + \tilde{\mathbf{u}}\cdot\nabla\mathbf{U} &= -\nabla\tilde{p} + \frac{1}{Re}\nabla^2\tilde{\mathbf{u}} \\ \nabla\tilde{\mathbf{u}} &= 0 \end{aligned} \tag{2.36}$$

All the solutions of this problem have the real part of σ as negative and hence they decay. So in order to explain the transient growth, let us assume two eigensolutions $\sigma_1 < \sigma_2 < 0$ and that $u' = u'_1 + u'_2$ at t=0. Then $u' \to 0$ as $t \to$. If $\tilde{u}_1 \simeq -\tilde{u}_2$ then $u' \simeq (e^{\sigma_1 t} - e^{\sigma_2 t})\tilde{u}_1$. If $\sigma_1 \neq \sigma_2$ then u' may grow because the exponentials decay at different rates. For this phenomenon to happen the eigenvectors should be non-orthogonal i.e. almost opposite to each other and it has been found generally that eigenvectors of the linearised Navier-Stokes operator are non-orthogonal.

In order to state mathematical formulation of the optimal perturbation theory one has to define a measure of the perturbations $\mathbf{u}'$ using the definition of the norm $||\mathbf{u}'||^2$ as given in eqn. (2.37) i.e. the norm is the kinetic energy of the perturbation and henceforth we will call it as energy norm. The exact formulation of the optimal perturbation problem can be written as: find the initial condition $\mathbf{u}'_{t=0} = \mathbf{u}'_0$ and the corresponding $\mathbf{u}'$ that $||\mathbf{u}'_0|| = 1$ and the $\max_{t>0}||\mathbf{u}'||$ is the largest possible. The energy norm is the perturbation energy density averaged over the entire channel, but for few cases as $u = 0$ at $t = 0$ it basically amounts to the cross-flow perturbation energy density.

$$||\mathbf{u}||^2 = lim_{a,b\to\infty}\frac{1}{ab}\int_{x,y,z=0,0,-1}^{x,y,z=a,b,+1}(u^2+v^2+w^2)dxdydz \tag{2.37}$$

The contributions of cross-flow perturbation energy (v^2+w^2) may become quite small compared to longitudinal kinetic energy u^2 as time progresses i.e for $t > 0$. As eqn. (2.35) is linear, $\mathbf{u}'(t) = A(t)\mathbf{u}'(0)$, where $A(t)$ is a non-normal linear operator depending on time t. The optimal perturbation problem can be formulated as variational problem whose functional is

$$F = (A(t)\mathbf{u}'_0, A(t)\mathbf{u}'_0) + \kappa((\mathbf{u}'_0,\mathbf{u}'_0) - 1) \tag{2.38}$$

Here κ is the Lagrange multiplier for the fixed initial norm. During the numerical implementation, the velocity $\mathbf{u}'_0$ can be represented as a vector γ of finite dimension, which leads to introduction of matrices E_t and E_0 such that $(A(t)u'_0, A(t)u'_0) = \gamma^* E_t\gamma$ and $(u'_0, u'_0) = \gamma^* E_0\gamma$. Here, * denotes transposition. Then the Euler-Lagrange form can be given as

$$E_t\gamma + \kappa E_o\gamma = 0 \tag{2.39}$$

This is a generalized eigenvalue problem whose eigenvalues κ are the ratios of energy at time t to energy at time 0. The governing equation for evolution of longitudinal flow is solved by the eigenfunction expansion approach and the details are given below. The numerical code based on the OP theory was developed by Prof. Sergei Chernyshenko and was validated with the results given in Butler and Farrell [7].

2.5.1 The Governing Equations

It was found by Butler and Farrell [7] that optimal perturbations for plane channel flows are independent of the longitudinal coordinate x. Accordingly, the OP code assumes no streamwise dependence i.e. $\partial/\partial x = 0$. So the governing Navier-Stokes equations (having no dependence on the longitudinal coordinate x) were linearized by neglecting the quadratic terms and the final form of the linearized perturbation equations is given below :

$$\frac{\partial u'}{\partial t} + w'\frac{dU}{dz}(z) = \frac{1}{Re}(\nabla^2 u') \tag{2.40}$$

$$\frac{\partial v'}{\partial t} = -\frac{\partial p'}{\partial y} + \frac{1}{Re}(\nabla^2 v') \tag{2.41}$$

$$\frac{\partial w'}{\partial t} = -\frac{\partial p'}{\partial z} + \frac{1}{Re}(\nabla^2 w') \tag{2.42}$$

$$\frac{\partial v'}{\partial y} + \frac{\partial w'}{\partial z} = 0 \tag{2.43}$$

Here prime quantities denote perturbations of the base flow. These equations (2.41-2.43) can be transformed to linearized vorticity-streamfunction formulation by taking the curl of cross-flow velocity equations to get

$$\frac{\partial \omega'}{\partial t} = \frac{1}{Re}\nabla^2 \omega' \tag{2.44}$$

$$\nabla^2 \psi' = -\omega' \tag{2.45}$$

where $\omega' = \partial w'/\partial y - \partial v'/\partial z$ and $v' = \partial \psi'/\partial z$ and $w' = -\partial \psi'/\partial y$ while the boundary conditions at the two walls are

$$\psi'(\pm 1) = \frac{\partial \psi'}{\partial z}(\pm 1) = 0 \tag{2.46}$$

Assuming

$$\psi' = e^{\imath\alpha y - \Lambda t} f_k(z) \tag{2.47}$$

$$\omega' = e^{\imath\alpha y - \Lambda t}\tilde{\omega}(y,z)$$

the above equations (2.44)-(2.45) can be simplified as

$$\alpha^4 f_k(z) - 2\alpha^2 f_k^{''}(z) + f_k^{''''}(z) = \Lambda(\alpha^2 f_k(z) - f_k^{''}(z)) \tag{2.48}$$

with the boundary conditions

$$f_k(\pm 1) = 0, \qquad \frac{df_k}{dz}(\pm 1) = 0 \tag{2.49}$$

This is a self-adjoint positively determined eigenvalue problem. Here the spanwise wavenumber α is related to non-dimensional spanwise wavelength λ^+ through the relation $\alpha = 2\pi Re/\lambda^+$. Assuming similar spanwise variation as given in eqn. (2.47)

$$\begin{aligned} u' &= e^{\imath\alpha y}\hat{u}(z,t) \\ w' &= e^{\imath\alpha y}\hat{w}(z,t) \\ v' &= e^{\imath\alpha y}\hat{v}(z,t) \end{aligned} \tag{2.50}$$

we get eqn. (2.40) modified as

$$\frac{\partial \hat{u}}{\partial t} + \hat{w}\frac{dU}{dz} = \frac{1}{Re}\left(\frac{\partial^2 \hat{u}}{\partial z^2} - \alpha^2 \hat{u}\right) \tag{2.51}$$

One of the solutions of eqns. (2.44-2.45) can be written as

$$\psi = e^{(-\Lambda t/Re + \imath\alpha y)} f_k(z) \tag{2.52}$$

with the boundary conditions as given in eqn. (2.46).

Equation (2.48) can be solved analytically using Mathematica package. Since it is a fourth-order differential equation we get the general solution as sum of four independent solutions each multiplied by an arbitrary coefficient. The requirement that the solution should satisfy the four boundary conditions gives a homogeneous system of four equations. The eigenvalues Λ can then be calculated by making the determinant of this system equal to zero. This approach leads to a complicated expressions and hence was abandoned in favour of the approach cited below. The new approach consists in finding a solution satisfying only three of the boundary conditions while the eigenvalues Λ are determined from the fourth boundary condition. Finally it was decided to choose two solutions of eqn. (2.48), $f_s(z)$ and $f_a(z)$, satisfying the boundary conditions

$$\begin{aligned} f_s(-1) &= f_s(1) \\ f_s'(-1) &= f_s'(1) = 0 \\ f_a(-1) &= -f_a(1) \\ f_a'(-1) &= f_a'(1) = 0 \end{aligned} \tag{2.53}$$

and having the normalized form

$$f_s = \frac{e^{z\alpha}(-1+e^{2\alpha})\alpha cos(z\beta) + e^{\alpha}(1+e^{2z\alpha})\beta sin(\beta)}{e^{z\alpha}(1+e^{2\alpha})\sqrt{\alpha^2+\beta^2}} \tag{2.54}$$

$$f_a = \frac{e^{\alpha}(-1+e^{2z\alpha})\beta cos(\beta) - e^{z\alpha}(1+e^{2\alpha})\alpha sin(z\beta)}{e^{z\alpha}(1+e^{2\alpha})\sqrt{\alpha^2+\beta^2}} \tag{2.55}$$

where $\beta = \sqrt{\Lambda - \alpha^2}$. Hence the streamfunction solution can now be expressed as

$$\psi = e^{\iota\alpha y - \Lambda t/Re}(sf_s - (1-s)f_a) \tag{2.56}$$

where s is the parameter which is either 0 or 1 depending on whether we want to choose symmetric or anti-symmetric streamfunction variation. Now these functions provide eigenvalues Λ as solutions to $f_s(1) = 0$ and $f_a(1) = 0$. To obtain different eigenvalues from the fourth boundary condition, an iterative numerical procedure was employed with initial approximations for β varying as $0.7\pi, 1.7\pi, \ldots$ for symmetric solutions and $1.3\pi, 2.3\pi, \ldots$ for anti-symmetric solutions. For the initial conditions at $t = 0$, the streamfunctions can be computed for a range of spanwise wavenumbers α and eigenvalues Λ. From these the cross-flow velocity components $\hat{v} = \partial\psi/\partial z = f_k'$ and $\hat{w} = -\partial\psi/\partial y = -\alpha f_k$ can be computed and their squares numerically integrated in the wall-normal direction to get the energy norm.

As the governing source eqn. (2.40) is linear homogeneous partial differential equation (PDE) with homogeneous boundary conditions, use has been made of separation of variables approach on the homogeneous PDE to get the eigenfunctions $\phi_k(z) = sin(k\pi/2(z+1))$ which form a full orthonormal basis. The solution of u can then be expressed as

$$u = \hat{u}_k(t)\int_{-1}^{+1} \hat{w}(z)\frac{dU}{dz}(z)\phi_k(z)dz \tag{2.57}$$

where $\hat{u}_k(t) = Ree^{-(k^2\pi^2/4+\alpha^2)t/Re} - e^{-\Lambda t/Re}/(k^2\pi^2/4+\alpha^2-\Lambda)$. In order to compute the term $\hat{w}(z)\frac{dU}{dz}(z)$, we need to compute the coefficients B_{km} such that

$$f_k(z)\frac{dU}{dz} = \sum_m B_{km}\phi_m(z) \tag{2.58}$$

that is

$$B_{km} = \int_{-1}^{+1} \left[f_k(z) \frac{dU}{dz}(z) \right] \phi_m(z) dz$$

The coefficients B_{km} can be further expanded as

$$B_{km} = \int_{-1}^{+1} \left(f_k(z)(U'(z) - zU'(1))\phi_m(z) \right) dz + U'(1) \int_{-1}^{+1} f_k(z) z \phi_m(z) dz$$

The second integral can be calculated analytically. The first integral involves expanding $f_k(z)$ in $\phi_m(z)$ as $\sum_m f_{km}\phi_m(z)$ and then expanding $(U'(z) - zU'(1))$ in $\phi_m(z)$ to get $\sum_m U'_m \phi_m(z)$. These expansions can be expressed analytically using the integrals of the triple products of eigenfunctions $\phi(z)$

$$\Pi_{klm} = \int_{-1}^{1} \phi_k(z) \times \phi_l(z) \times \phi_m(z) dz$$

Then

$$B_{km} = \sum_{l,n} f_k(z) U'_n \Pi_{lnm} + U'(1) \int_{-1}^{+1} f_k(z) z \phi_m(z) dz$$

The computed values of energy norm at time t are suitably normalized by the energy norm at t=0. So algorithm for computation of eigenvalues κ (which are a measure of ratio of E_t/E_o) involves supplying as input a range of representative times t^+ and a range of spanwise wavenumbers α or wavelengths λ^+. Corresponding to these values a global maximisation is performed to find out the maximal energy growth while the eigenvectors of the code depict the wall-normal variation of the longitudinal velocity u. The numerical analysis of the OP theory as outlined above was carried out by Prof. Sergei Chernyshenko.

Chapter 3

STREAKS IN QUASI-2D TURBULENCE

3.1 Introduction

From the introductory chapter we know that there are several vortex regeneration theories which reportedly explain the mechanism of streak formation and also the streak spacing. In order to seek out the truth, we set out with the aim of showing the presence of streaks in quasi-2D (that is with flow variables independent of streamwise direction x) turbulent flows thereby excluding several theories that rely on longitudinal feedback of the flow. Regarding this, a numerical experiment on quasi-2D decaying turbulent channel flow was devised in which random velocity spatial distribution is used as the initial condition. The details of generation of initial conditions and the corresponding results are given below.

3.2 Generation of Initial Chaotic Velocity Field

In order to perform numerical experiments for a quasi-2D turbulent channel flow having periodic boundary conditions in streamwise x and spanwise y directions, we have assumed zero-gradient

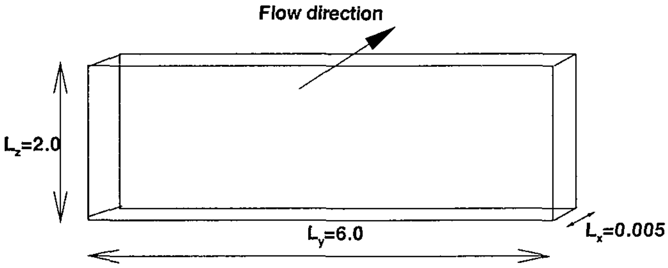

Figure 3.1: Geometry and dimensions of the channel with the flow direction

velocity field in streamwise direction and so the modified continuity equation is

$$\frac{\partial v}{\partial y}+\frac{\partial w}{\partial z}=0 \tag{3.1}$$

Moreover, the modified momentum equations become

$$\frac{\partial u}{\partial t}+v\frac{\partial u}{\partial y}+w\frac{\partial u}{\partial z}=-1+\frac{1}{Re_\tau}\nabla^2 u \tag{3.2}$$

$$\frac{\partial v}{\partial t}+v\frac{\partial v}{\partial y}+w\frac{\partial v}{\partial z}=-\frac{\partial p'}{\partial y}+\frac{1}{Re_\tau}\nabla^2 v \tag{3.3}$$

$$\frac{\partial w}{\partial t}+v\frac{\partial w}{\partial y}+w\frac{\partial w}{\partial z}=-\frac{\partial p'}{\partial z}+\frac{1}{Re_\tau}\nabla^2 w \tag{3.4}$$

where p' is the modified pressure while $\overline{dP/dx}=-1$ is the imposed mean streamwise pressure gradient. From the above equations, it can be seen that the cross-flow equations do not involve the longitudinal velocity u, that is v and w are governed by the 2D continuity and Navier-Stokes equations (3.1), (3.3) and (3.4). However, the evolution of u depends on v and w and is governed by equation (3.2) with a constant source term $\overline{dP/dx}=-1$.

In order to generate the initial conditions, the streamwise component u was chosen to be the mean turbulent streamwise velocity profile with no perturbations, while v and w are given as

$$v,w=Real\sum_{k,l}C_{k,l}e^{\iota(2\pi ky+2\pi lz)} \tag{3.5}$$

where $C_{k,l}$ are complex constants. Here, k and l are the number of modes in spanwise y and wall-normal z directions, respectively. The value of k varies from k_1 to k_2 while the value of l varies from l_1 to l_2. On further simplification we get

$$v, w = Real \sum_{k,l} (C^r_{k,l} + iC^i_{k,l})(\cos(2\pi ky + 2\pi lz) + \imath \sin(2\pi ky + 2\pi lz)) \tag{3.6}$$

or

$$v = \sum_{k,l} (C^{vr}_{k,l} \cos(2\pi ky + 2\pi lz) - C^{vi}_{k,l} \sin(2\pi ky + 2\pi lz)) \tag{3.7}$$

$$w = \sum_{k,l} (C^{wr}_{k,l} \cos(2\pi ky + 2\pi lz) - C^{wi}_{k,l} \sin(2\pi ky + 2\pi lz)) \tag{3.8}$$

As from the continuity equation, $\frac{\partial v}{\partial y} = -\frac{\partial w}{\partial z}$, we get

$$C^{wr}_{k,l} + \imath C^{wi}_{k,l} = -\frac{k}{l}(C^{vr}_{k,l} + \imath C^{vi}_{k,l}) \tag{3.9}$$

In order to obtain a random initial velocity field, we generated random coefficients $C^{vr}_{k,l}$ and $C^{vi}_{k,l}$ using a random number generator based on uniform deviates which lie within a specified amplitude range ($-A/2$ to $A/2$). The amplitude A regulates the strength of cross-flow velocity perturbations. The relationship is given as

$$C^{vr}_{k,l}, C^{vi}_{k,l} = A * (random(seed) - 0.5) \tag{3.10}$$

The choice of number of modes in spanwise and wall-normal directions is dictated by the grid resolution in the cross-flow plane, which in turn is dependent on both the geometrical size and cross-flow Reynolds number, $Re_{cf} = V_m Re_\tau$, where V_m is the normalized root mean square cross-flow velocity. We define V_m as the mean value of the initial velocity magnitude, namely

$$V_m^2 = \frac{1}{L_z L_y} \int_{-1}^{1} \int_{0}^{L_y} (v^2 + w^2) dy dz \tag{3.11}$$

From the previous equations (3.7) and (3.8) it follows that

$$\begin{aligned} V_m^2 &= 1/2 \sum_{k,l} (C^{vr}_{k,l})^2 + (C^{vi}_{k,l})^2 + (C^{wr}_{k,l})^2 + (C^{wi}_{k,l})^2 \\ &= 1/2 \sum_{k,l} (1 + k^2/l^2)((c^{vr}_{k,l})^2 + (C^{vi}_{k,l})^2) \end{aligned} \tag{3.12}$$

Therefore,

$$< V_m^2 > = A^2 \sum_{k,l} (1 + k^2/l^2) \tag{3.13}$$

but V_m^2 can vary from realisation to realisation. The cross-flow Reynolds number can be several times the Re_τ depending upon the amplitude A.

3.3 Formation of Streamwise Vortices and Streaks

The numerical experiments have been performed in a computational box of size L_x=0.005, L_y=6.0 and L_z=2.0 on a grid having 4*384*240 (Δx^+ =0.45, Δy^+ =2.81 and more than 20 grid points below Δz^+ =5.0) nodal points at a Re_τ = 180. The geometry considered is that of a plane channel flow with a short streamwise length $L_x = 0.005$ as shown in Figure 3.1. The short streamwise length is needed in order to satisfy the constraint of maintaining a quasi-2D channel flow i.e. all dynamical variables satisfying $\partial/\partial x = 0$ condition while using a 3D Navier-Stokes spectral code. It was found that this grid was fine enough to resolve modes (k_1 to k_2, l_1 to l_2) varying from 15 to 20 in one period length in both the spanwise and wall-normal direction. The energy was supplied at these higher modes in order to realize the temporal transfer of energy from higher to lower modes. Calculations were made with different amplitudes of the initial velocity perturbation. The numerical experiments were started from A = 0.0001 and it was found that no structures form near the channel walls and it is only once we cross the threshold amplitude value of approximately $A >$ 0.001, we see the formation of weak streak-like structures near the walls. As the threshold value is quite small, the influence of the rounding errors cannot be eliminated.

3.3.1 Visualization

The code has been run for a definite period of non-dimensional time of 0.25 taking the amplitude A = 0.5 as the initial condition. A spanwise averaging has been performed of the velocity components in order to compute fluctuating velocity components (u', v', w') and mean Reynolds normal stresses $\langle v'^2 - w'^2 \rangle$. Since the grid 4*384*240 used for all the simulations is quite fine, all the simulations have been performed on 32 processors of Beowulf Linux cluster 'Iridis' using a parallel code based on MPI protocol [47].

The temporal development of the streaks can be seen from the fluctuating negative streamwise velocity contours as shown in Figures 3.2 corresponding to non-dimensional times t from 0.025 to 0.225.

As can be seen from these figures, the streaks start forming near the walls after a non-dimensional time $t = 0.025$ and by the time $t = 0.125$ they have lifted off and reached a distance of 8% height.

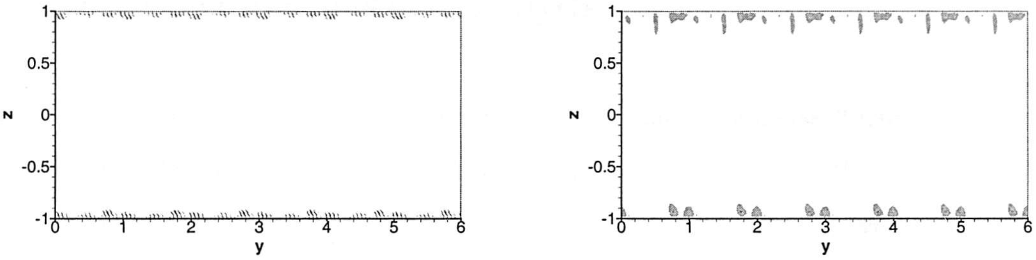

(a) At time instant t=0.025

(b) At time instant t=0.075

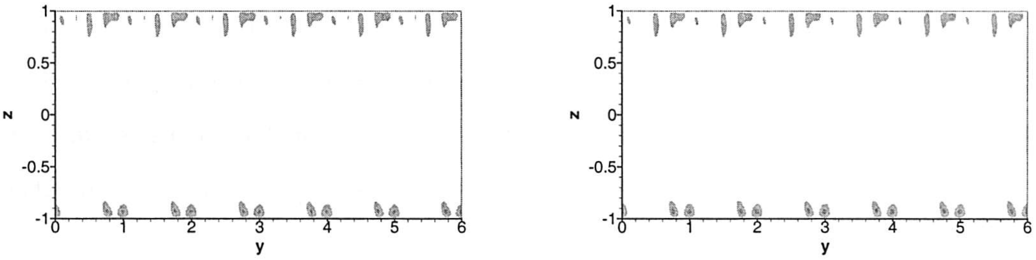

(c) At time instant t=0.125

(d) At time instant t=0.2250

Figure 3.2: Streamwise fluctuating velocity at various time instants. In areas marked black the plotted variables is < 0.25 of its minimum negative value.

The lifting up of the low speed streaks was at the time believed to be due to the longitudinal vortices which can not be visualised due to the strong random fluctuations of the velocity field. It has been found that for all realisations performed approximately 12-15 low-speed streaks form near the walls giving a spanwise spacing of streaks = 0.4. Note that in this numerical experiment the entire flow has a unit period in spanwise y direction due to the way initial condition eq. (3.5) was set.

3.3.2 Spanwise Power Spectral Analysis

Spanwise power spectra of spanwise fluctuating velocity v' and streamwise fluctuating velocity u' have been computed at different time instants (from t = 0.025 to t=0.225) at wall-normal distance of z = 0.1. Figures 3.3 and 3.4 show the spectra of v' and u' at z=0.10. More precisely, v' and u' were represented as $\sum P_n cos(2\pi ny/L_y) + Q_n sin(2\pi ny/L_y)$ and the figures show the plot of $P_n^2 + Q_n^2$ vs numerical wavenumber represented by $k = 2\pi n/L_y$. It is seen from Figures 3.3(a) to 3.3(d) that initially at t= 0.0 the power spectrum for spanwise v' peaks at wavenumbers 90 to 125 (i.e. wavenumbers at which initial energy is supplied) and then with increase in time these peaks diminish while new peaks form at lower wavenumbers i.e. for $k \leq 30$. Results for w' are similar to that for v' and hence are not shown here. Therefore, we can safely infer that an inverse energy cascade is taking place just as expected in 2D flows.

At t=0.125 the cross-flow came almost to rest, as it can be seen by more than two-orders of magnitude drop in kinetic energy of the flow. The inverse energy cascade results in large-scale motion which can consist of chaotic and organised components. At this point it was hypothesised, the organised component, if present, could not be easily seen in the cross-flow field obtained since it is weak as compared to the chaotic component, but the presence of the organised structures in the cross-flow could be noticed by their effect on the longitudinal velocity. Over a long time the chaotic component acts as additional diffusion mechanism, which in fact does not affect u' but the organised structures, owing to their persistent action, do leave their signature in u', as it has already been demonstrated by Figure 3.2. Figures 3.4(a) to 3.4(d) further illustrate this as it can be seen that at t=0.025 peaks in power spectrum of streamwise u' have formed at wavenumbers 90 to 125, which with time show decrease in power while at the same time new peaks form at lower wavenumbers which exhibit increase in power with time. However, such a hypothesis is in contradiction with further results, see chapters 5 and 6.

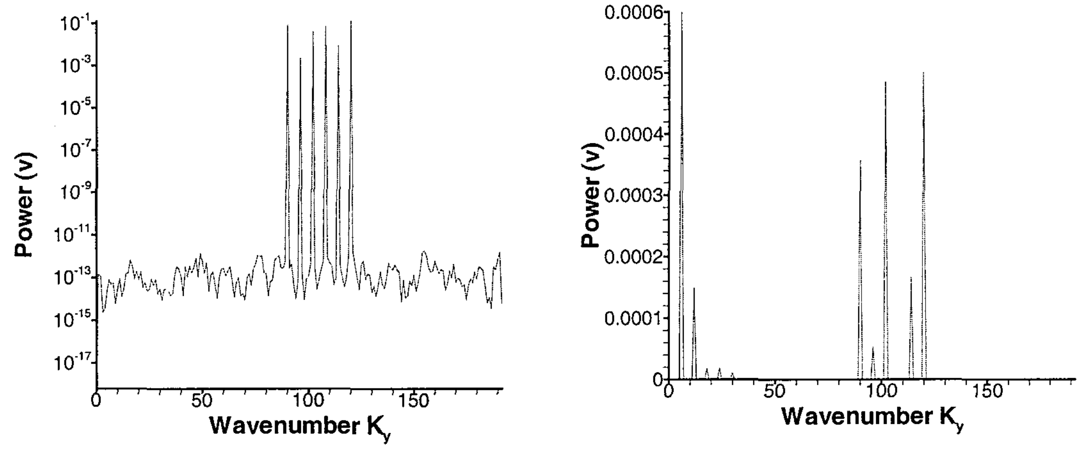

(a) At time instant t=0

(b) At time instant t=0.025

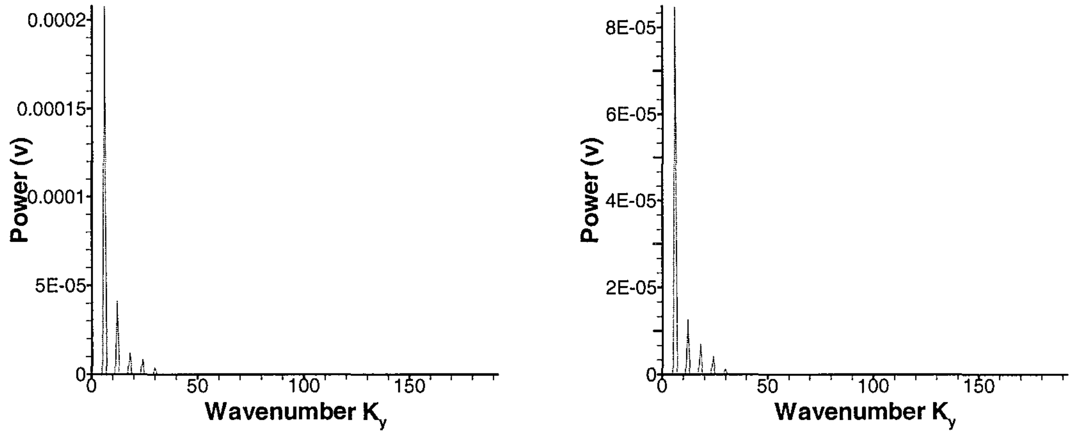

(c) At time instant t=0.125

(d) At time instant t=0.225

Figure 3.3: Power spectrum of spanwise fluctuating velocity v at different time instants

3.3.3 Behaviour of Reynolds Normal Stress Anisotropy

The difference in the Reynolds normal stresses Q= $\langle v'^2 - w'^2 \rangle$ has been computed at different wall-normal distances from the wall. According to RNSAI theory the persistence over time of the quantity $\frac{\partial^2 < v'^2 - w'^2 >}{\partial z^2} < 0$ can be responsible for the instability that causes the formation of the

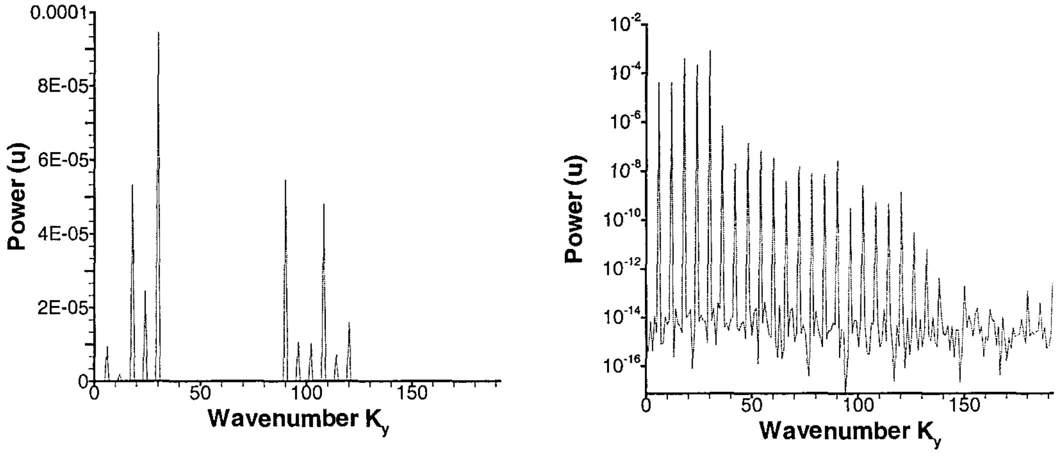

(a) At time instant t=0.025

(b) At time instant t=0.075

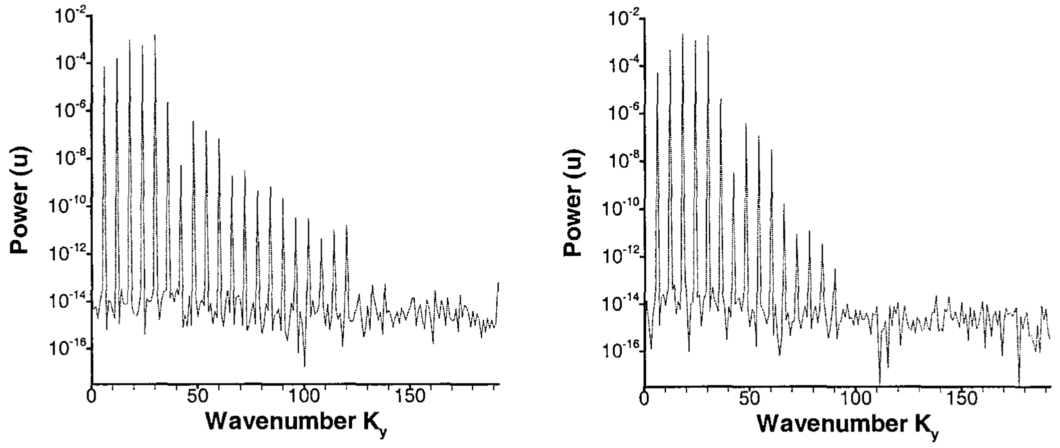

(c) At time instant t=0.125

(d) At time instant t=0.225

Figure 3.4: Power spectrum of streamwise fluctuating velocity u at different time instants

streamwise vortices. The temporal variation of the Reynolds normal stresses can be seen from Figure 3.5 at four different time instants, **especially the persistence of sharp humps near the walls**. The thickness of these layers decreased with time, remaining, however, of the same order of magnitude as the streak spacing. This is in accord with the idea of the Reynolds stress anisotropy induced instability. It can be inferred from the figures that there are strong fluctuations near the centre of the channel, due to strong initial anisotropy. Moreover, it can be seen from the figures that as time advances the magnitude of the Reynolds normal stresses gradually diminish as there is no continual input of energy at lower modes.

3.4 Generation of Isotropic Random Eddy Field

Prescribing an initial velocity field by eqns. (3.7) and (3.8) gives a precise control over its characteristic wavelength, thus allowing to distinguish it clearly from wavelength of organised structures forming later. However, as it can be seen from eqn. (3.9), in this case the initial velocity field is anisotropic from the start. In order to check if similar near-wall organised structures will appear if the only anisotropy in the flow is generated by the wall themselves, an alternative method based on isotropic initial velocity distribution was developed. In order to generate an isotropic but non-homogeneous velocity field for a quasi-2D turbulent channel flow, a random eddy model has been constructed, the details of which are given below. For the numerical experiments in quasi-2D turbulence, we have assumed a zero-gradient velocity field in streamwise direction and so the modified continuity equation and momentum equations are same as eqns. (3.1) to (3.4). The streamwise component u was chosen to be the mean turbulent streamwise velocity profile with no perturbations, while v and w are given as

$$v(y,z) = -\sum_{i=1}^{N} A f_o \frac{(z-z_i)}{a_i^2} f(\tilde{r}) \tag{3.14}$$

$$w(y,z) = \sum_{i=1}^{N} A f_o \frac{(y-y_i)}{a_i^2} f(\tilde{r}) \tag{3.15}$$

where A is the amplitude by which we can increase or decrease the magnitude of the random velocity perturbations, N is the number of generated random eddies, f_o takes ± 1 values alternatively, y_i and z_i are the coordinates of the centre of the eddies, $\tilde{r}$ is given by

$$\tilde{r} = \sqrt{\frac{(z-z_i)^2}{a_i^2} + \frac{(y-y_i)^2}{a_i^2}}$$

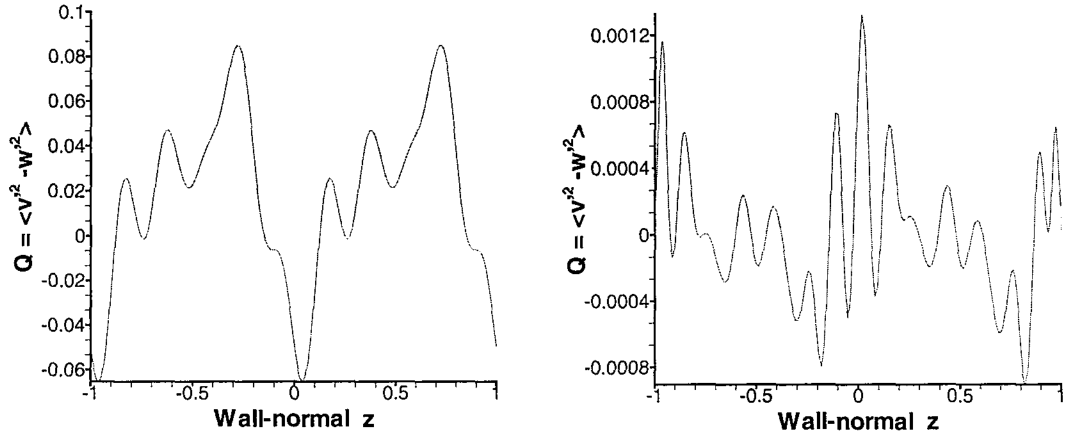

(a) At time instant t=0.0

(b) At time instant t=0.075

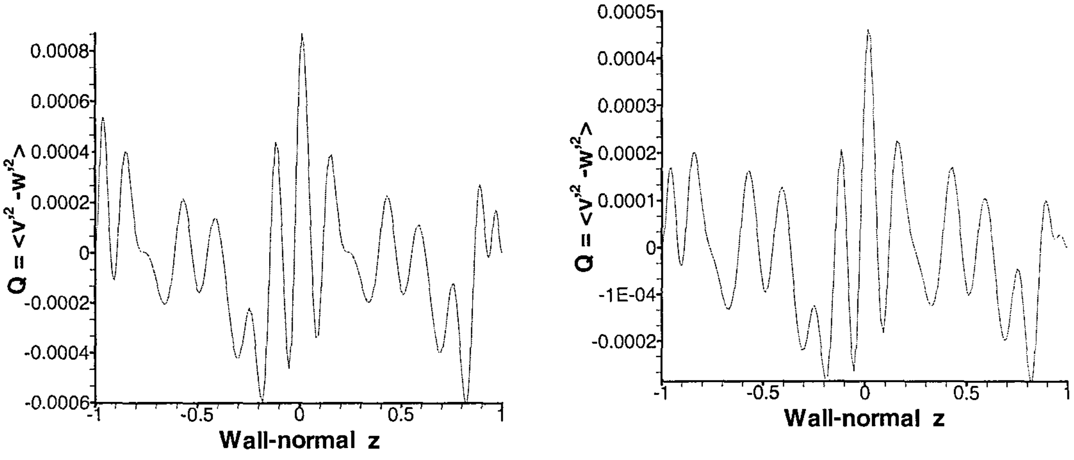

(c) At time instant t=0.125

(d) At time instant t=0.225

Figure 3.5: Temporal variation of Reynolds normal stresses

and

$$f(\tilde{r}) = 0, \quad \tilde{r} \geq 1 \qquad (3.16)$$
$$f(\tilde{r}) = e^{\frac{-1}{(\tilde{r}-1)^2}}, \quad \tilde{r} \leq 1$$

The length scale a_i of the eddies affects the cross-flow velocity field (v,w). To generate an isotropic but non-homogeneous random eddy field, with smaller size eddies concentrated near the wall and comparatively larger eddies near the centre of the channel, we need to vary the length scale a_i as a function of wall-normal coordinate.

In order to have a homogeneous random distribution of eddies in the spanwise direction, we assume $y_i = f(\zeta,\eta) = L_y\zeta$ where L_y is the length in spanwise direction and ζ are the random numbers generated based on uniform deviates which lie within a range of (0 to 1). Similarly, a non-homogeneous random distribution of eddies in wall-normal direction is achieved using $z_i = g(\zeta,\eta) = cos(\pi\eta)$, where η are the random numbers based on uniform deviates which also lie within a range of (0 to 1). As z_i is regulated by a cosine function, we get a larger concentration of eddies near the walls at z = ± 1. The probability density function (PDF) $\rho(y_i,z_i)$ governs the distribution of random eddies in two-dimensional space and is related to the PDF in ζ,η space through the relation ([40])

$$\rho(y_i,z_i) = \tilde{\rho}(\zeta,\eta)J^{-1} = \frac{1}{L_y f'(\eta)} = \frac{1}{L_y \pi sin(\pi\eta)} \qquad (3.17)$$

where J is the Jacobian $\begin{vmatrix} g_\zeta & g_\eta \\ f_\zeta & f_\eta \end{vmatrix}$. This clearly shows that the PDF of eddy distribution peaks near the walls z=$\pm$1.

From the definition of number density, we can relate the mean length scale between randomly distributed eddies l to the number of randomly generated eddies N and the PDF $\rho(y_i,z_i)$ as

$$l = \frac{K}{\sqrt{(\rho(y_i,z_i)N)}} \qquad (3.18)$$

where K is a constant. Making a further assumption, we can take $a_i = l$. The eddies which overlap with the walls are neglected i.e. if $|z_i - 1| \leq a_i$ or $|z_i + 1| \leq a_i$, the corresponding term is not added to eqns. (3.14) and (3.15). Then no-slip boundary conditions are satisfied at the walls for all the velocity components.

3.5 Formation of streamwise vortices and streaks

The numerical experiments have been performed in a computational box of size L_x =0.005, L_y=6.0 and L_z = 2.0 on a grid having 4*480*480 (Δx^+ =0.45, Δy^+=2.25 and more than 30 grid points below Δz^+ =5.0) nodal points at a Re_τ=180.0. The amount of energy supplied using the random eddy model is dependent on the amplitude A and the number of eddies generated N. In prescribing the initial conditions, the Fourier transform was performed on the velocity field eqns. (3.14 -3.15). Fourier modes corresponding to the fifty highest and lowest wavenumbers were excluded. The lower modes were excluded in order that any large-wavelength structures observed were due to an inverse energy cascade only, while higher modes were excluded in order to ensure numerical resolution. Inverse Fourier transformation was then performed. The resulting flowfield did not contain any wavelength above 0.1, while the spanwise length L_y=6.0. The above mentioned process was performed in order to get isotropic eddies in the cross-flow velocity field. The numerical experiments were started from A =0.0001 and it was found that no structures form near the channel walls and it is only once we cross the threshold amplitude value of approximately A $\geq$ 0.002, we see the formation of weak streak-like structures near the walls. As the threshold value is quite small, the role of rounding errors cannot be eliminated.

3.5.1 Visualisation

As per the case of anisotropic runs, for all the simulations only spanwise averaging has been performed in order to compute (u', v' and w') and difference of Reynolds normal stresses $Q =< v'^2 - w'^2 >$. As the grid 4 × 480 × 480 contains nearly 0.92 million points, all the simulations have been performed using 32 processors on Linux Beowulf cluster using a parallel code [47].

The simulations have been performed for a maximum non-dimensional time of 0.4 for an amplitude $A = 4.0$ and number of eddies N =5000 corresponding to a initial cross-flow $Re_{cf} = 305$ based on mean kinetic cross-flow velocity V_m. The temporal development of the streaks can be seen from the fluctuating negative streamwise velocity contours as shown in Figures 3.6(a) to 3.6(d), corresponding to non-dimensional times t from 0.03 to 0.4. It can be seen from these figures, the streaks start forming near the walls after a non-dimensional time $t = 0.03$ and by the time $t = 0.05$ they have lifted off and reached $z = \pm 0.9$. It has been found that for times $t > 0.3$ approximately 12-14 low-speed streaks form near the walls giving a spanwise spacing of streaks = 0.4. This streak spacing is well outside the range of the wavelengths present in the initial conditions.

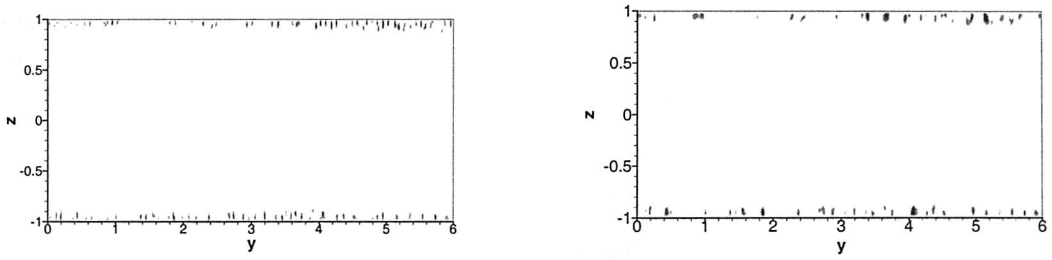

(a) At time instant t=0.05

(b) At time instant t=0.1

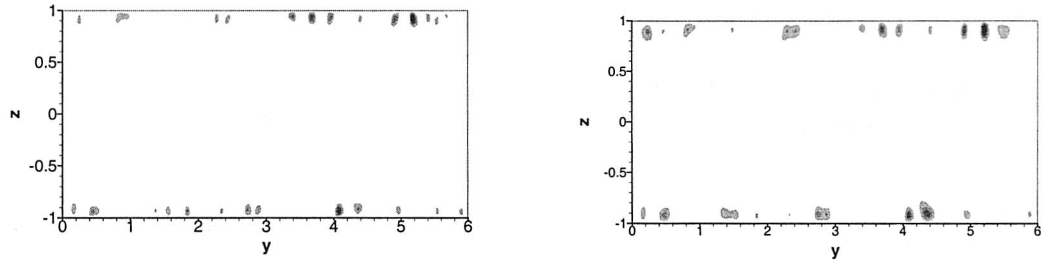

(c) At time instant t=0.2

(d) At time instant t=0.4

Figure 3.6: Streamwise fluctuating velocity at various time instants. In areas marked black the plotted variables is < 0.25 of its minimum negative value.

3.5.2 Spanwise Power Spectral Analysis

Spanwise power spectrums of fluctuating velocities v' and u' have been computed at different time instants (from t=0.0 to t=0.4) at different wall-normal distances as shown in Figures 3.7 and 3.8, respectively. It is seen from Figures 3.7(a) to 3.7(d) that initially at $t = 0.0$, the power spectrum for spanwise fluctuating velocity v' has broad range of power except at lowest and highest fifty wavenumbers and then with increase of time the higher wavenumbers peaks vanish immediately followed by diminishing of power content at lower wavenumbers. From Figures 3.8(a) to 3.8(d), it can be seen that at $t = 0.05$ peaks in power spectrum of fluctuating u' have formed for a broad range of wavenumbers, and with further increase of time a gradual increase in power is seen especially at lower wavenumber i.e. for $k \leq 25$. The evolution of the power spectrums thus shows that there is a shift of energy from high to low wavenumbers due to an inverse energy cascade but there is no selection of particular wavelength during the initial stages. Therefore, the observed behaviour can be described as an initial non-linear inverse energy cascade in the cross-flow, followed by a decay which is most likely governed by linearised equations.

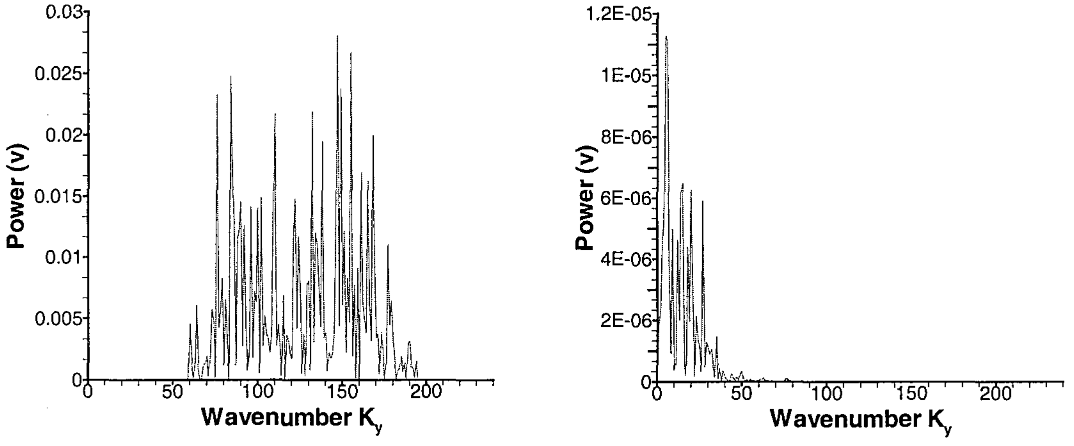

(a) At time instant t=0

(b) At time instant t=0.10

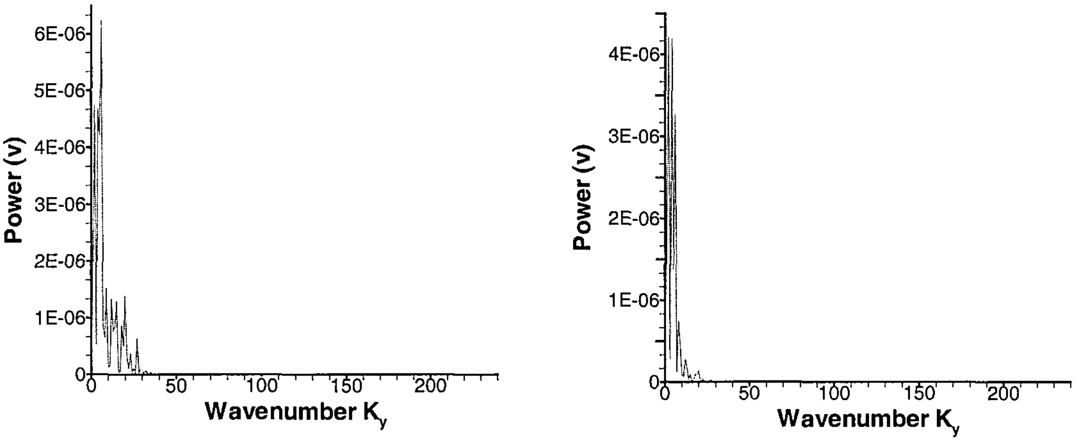

(c) At time instant t=0.20

(d) At time instant t=0.40

Figure 3.7: Power spectrum of spanwise fluctuating velocity v' at different time instants

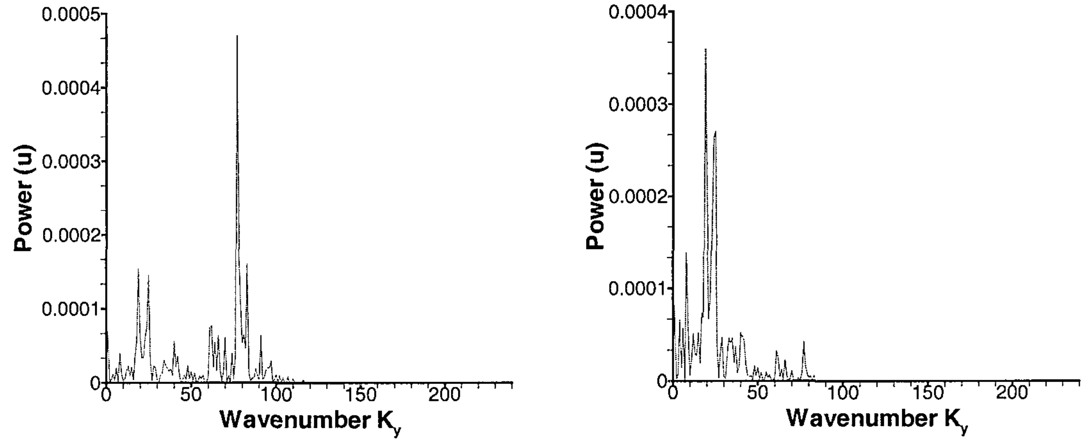

(a) At time instant t=.05

(b) At time instant t=0.10

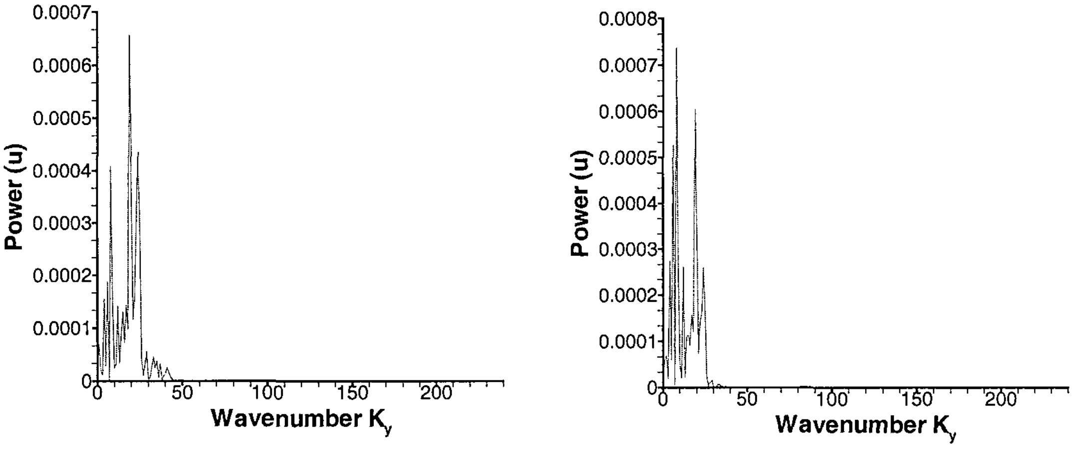

(c) At time instant t=0.20

(d) At time instant t=0.40

Figure 3.8: Power spectrum of streamwise fluctuating velocity u' at different time instants

3.5.3 Behaviour of Reynolds Normal Stress Anisotropy

The profile of difference of Reynolds normal stresses $\langle v'^2 - w'^2 \rangle$ vs z has been computed at different time instances as shown in Figures 3.9(a) to 3.9(d). It can be seen from these figures that the fluctuations near the centre of the channel are comparatively smaller compared to the anisotropic runs. Further, it can be inferred that as time advances the magnitude of Reynolds normal stresses gradually diminishes as there is no continual input of energy at lower modes. Further, it can be seen from the figures that the profile near the walls shows the persistence of the quantity $\frac{\partial^2 < v'^2 - w'^2 >}{\partial z^2} < 0$, which according to RNSAI mechanism is responsible for the generation of longitudinal vortices and consequently the streaks.

3.5.4 Comparison of number of streaks

The number of streaks varying with time, for a fixed spanwise length L_y, were counted for two different realisations of quasi-2D decaying turbulence based on the visualisation of streamwise negative contours above a certain threshold limit, as shown in Figure 3.10. The curves identified as seed 1 and seed 2 in the figure refer to two different realizations of the flow for two different random generator seeds. Moreover, using the optimal wavelengths at different optimal times as given in Figure 3 of paper by Butler and Farrell [7], the number of streaks have been computed for same fixed L_y and the results plotted as shown in Figure 3.10. It can be seen from the figure that there is a good agreement between the two and it seems that optimal perturbations theory might explain the generation of the streaks.

3.6 Summary

From the numerical experiments that have been performed for the random initial velocity fields, the following conclusions can be made:

1. The calculations from the quasi-2D initial value flow show the presence of near-wall streaks, hence streaks can form even in case when there is no feedback from the longitudinal flow profile, to the cross-flow vortex structure.

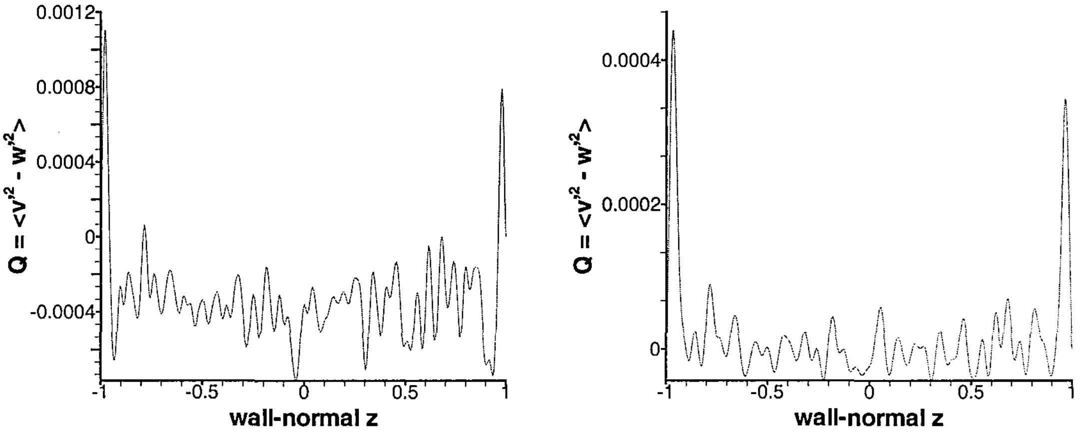

(a) At time instant t=0.05

(b) At time instant t=0.10

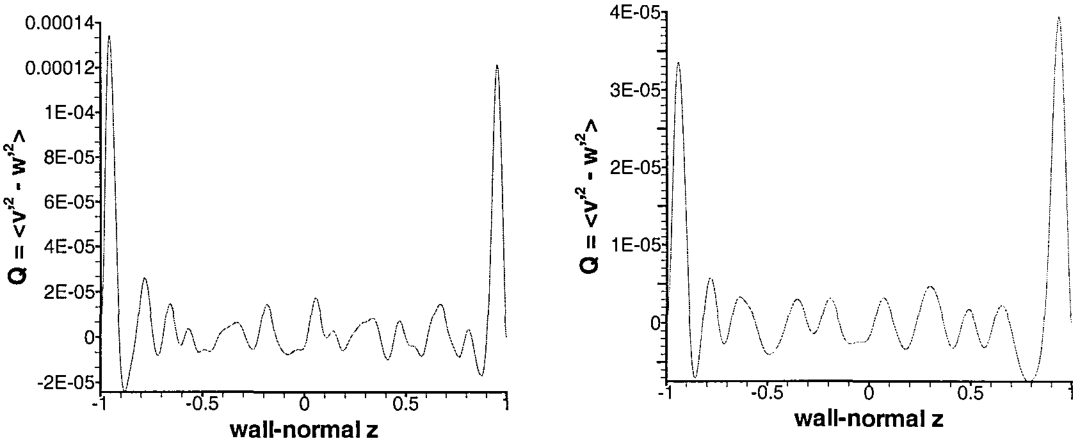

(c) At time instant t=0.20

(d) At time instant t=0.40

Figure 3.9: Temporal variation of Reynolds normal stresses

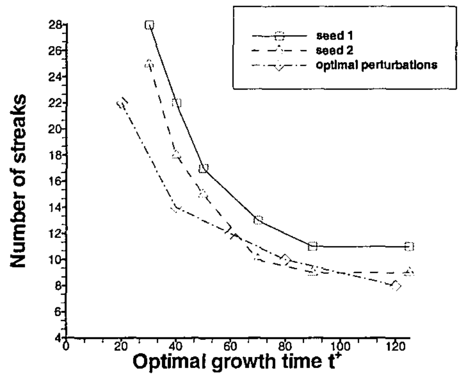

Figure 3.10: Comparison of number of streaks for two different realisations of decaying quasi-2D turbulence with streaks computed based on optimal perturbation theory [7].

2. There is an inverse energy cascade from higher to lower wavenumbers yet it does not lead to any particular scale selection, unlike the non-linear selection mechanism favoured by Nikitin and Chernyshenko theory [38].

3. Near-wall organized structures only form when cross-flow perturbations amplitude exceed a critical threshold value or in other words when Re_{cf} exceeds a critical value, but the influence of rounding errors cannot be fully eliminated especially at low threshold amplitudes.

4. The Reynolds normal stresses exhibit a strong anisotropy near the walls and their profile shows the persistence of the quantity $\frac{\partial^2 < v'^2 - w'^2 >}{\partial z^2} < 0$ which might lead to the formation of an instability akin to RNSA instability. For a quasi-2D decaying turbulence it is not possible to make a comparison with RNSAI theory as the mean flow is time-dependent.

5. The above two points favoured the Nikitin and Chernyshenko theory [38] yet on the basis of the good agreement in number of streaks with time as given by DNS and as inferred using results of optimal perturbation theory (see Figure 3.10), it could not be ruled out that linear mechanism such as optimal perturbation theory might be also responsible for the formation of near-wall organised structures i.e either vortices or streaks.

Chapter 4

STREAKS IN FORCED QUASI-2D TURBULENCE

4.1 Introduction

The physics of 3D turbulence is attributed mainly to the strongly nonlinear term in the Navier-Stokes equations which accounts for the phenomenon of vortex stretching. Going from three dimension to two dimension removes vortex stretching from the Navier-Stokes equation, yet enough nonlinearity remains to produce turbulent behaviour. Despite its apparent simplicity compared with 3D, the 2D turbulence problem has thus far eluded rigorous theoretical interpretation. There is a contradiction between various theories and computer simulations even with respect to simple quantities such as the power spectrum of turbulent velocity fluctuation, $E(k)$. Rutgers (1998) [46] presented first experimental evidence which supports some of the most important theoretical results in 2D turbulence, namely, an inverse energy cascade accompanied by a forward enstrophy cascade.

The theory of 2D turbulence as proposed by Kraichnan (1967) [36], states that if energy is injected into the flow at a particular length scale (l_{inj}), then $E(k)$ will show two distinct power law regions. For k $\leq k_{inj} \equiv 2\pi/l_{inj}$, $E(k) \sim \varepsilon_1^{2/3}k^{-5/3}$, where ε_1 is the energy transfer rate. For k $\geq k_{inj}$, $E(k) \sim \eta^{2/3}k^{-3}$, where η is the enstrophy transfer rate. The inverse energy cascade has been observed in many simulations (e.g. by Frisch and Sulem (1984) [15] and by Smith and Yakhot (1993) [56]). These simulations generally failed to reproduce the forward enstrophy cascade and if they did as in case of Chasnov's (1997) [10] freely decaying 2D turbulence, they failed to abide $E(k) \sim k^{-3}$ but decayed more steeply depending on the initial conditions and simulation methods.

Experiments with flowing soap films have observed the forward enstrophy cascade (Martin et. al. (1998) [37]) in freely decaying 2D turbulence but only recently in experiments performed by Rutgers (1998) [46] on 2D soap films subjected to steady state forcing, both the simultaneous existence of energy and enstrophy cascades have been observed.

4.2 Incorporation of random forcing and its validation

In order to sustain near-wall turbulence, it is sufficient to subject quasi-2D turbulent flows to steady state forcing using random amplitude body force terms in the governing Navier-Stokes equations. To incorporate the random body forces into the mathematical model (as explained in Chapter 2) of the Navier-Stokes solver, there are two possible ways:

1. To add the random body forces with the pressure and viscous terms.
2. To assimilate the random forces with the nonlinear convective terms.

Either one of the methods can be applied and we have preferred the second approach and modified the spectral code [47] accordingly. In order to validate the addition of body force into a steady-state Navier-Stokes solver, we assume a particular analytic velocity distribution and using that we calculate the analytic body forces which we incorporate in the code. Then on execution of the code we should get the numerical velocity field same as what we assumed analytically. For our case, we have taken a velocity distribution that satisfies the no-slip, impermeable boundary conditions at the walls and periodic boundary conditions in the streamwise and spanwise directions. The governing momentum equations with the random body forces are:

$$\frac{\partial \mathbf{u}}{\partial t} = \mathbf{u} \times \omega - \nabla q + \frac{1}{Re_\tau} \nabla^2 \mathbf{u} - \frac{dP}{dx} \mathbf{e}_1 + \mathbf{F} \tag{4.1}$$

where the terms are same as explained in the mathematical model. The divergence of the above equation for steady flow-field gives us the Poisson equation as

$$\nabla^2 p = -\nabla.(\mathbf{u}.\nabla\mathbf{u}) + \nabla.\mathbf{F} \tag{4.2}$$

Assuming a divergence-free body force field we get Poisson equation as

$$\nabla^2 p = -\nabla.(\mathbf{u}.\nabla\mathbf{u}) \tag{4.3}$$

and hence we can compute pressure from it, given a known velocity field. The non-linear convective terms, pressure gradient and viscous terms can also be computed analytically and substituted into the Navier-Stokes equations with the mean pressure-gradient $\overline{dP/dx} = -1$ to get the analytic expressions for the body force. As these body force terms satisfy the divergence-free conditions, they are incorporated into the Navier-Stokes code and time integration performed to get the known velocity field.

In one of the steady-state flowfield case considered for validation use was made of symbolic maths commercial software MAPLE, the velocity field was chosen as (here Re is Reynolds number):

$$u = \frac{Re}{2}(1-z^2) \tag{4.4}$$

$$v = -12(1-z^2)^2\sin(y)z^2 + 3(1-z^2)^2\sin(y) \tag{4.5}$$

$$w = -3(1-z^2)^2\cos(y)z \tag{4.6}$$

The velocity components above satisfy the no-slip and impermeability conditions at the walls. The body force terms computed analytically are:

$$f_x = 3(1-z^2)^2\cos(y)Re \tag{4.7}$$

$$\begin{aligned} f_y = {} & -1/(2Re) * (-8Re\sin(y)\cos(y)e^{2z} - 8Re\sin(y)\cos(y)e^{-2z} + \\ & 12609\sin(y)\cos(y)Re + 1260\cos(y)z^6\sin(y)Re + 8370\cos(y)z^4\sin(y)Re \\ & 25218\cos(y)z^2\sin(y)Re - 4Re\cos(y)^2e^{2z} - 30\sin(y)z^4 + 2Re \quad e^{2z} + \\ & -78\sin(y) + 396z^2\sin(y) + 2Re \quad e^{-2z} - 4Re\cos(y)^2e^{-2z}) \end{aligned}$$

$$\begin{aligned} f_z = {} & 1/(2Re) * (4Re + 16812\cos(y)^2Rez^3 - 12609Rez + 4Re\sin(y)\cos(y)e^{-2z} + \\ & -8\cos(y)^2Ree^{2z} + 132\cos(y)z^3 - 78\cos(y)z - 6\cos(y)z^5 + 360\cos(y)^2Rez^7 \\ & 25218\cos(y)^2Rez + 4Ree^{2z} + 3348\cos(y)^2Rez^5 - 4Ree^{-2z} - 180z^7\Re - \\ & 1674z^5Re - 8406z^3Re + 8\cos(y)^2Ree^{-2z}) \end{aligned} \tag{4.8}$$

After validating for the steady-state velocity field, validation on similar lines was performed for unsteady flow field.

4.3 Generation of Initial conditions and Random forces

Our aim is to attempt generating near-wall longitudinal vortices in quasi-2D flow via the RNSAI mechanism. In order to realise this aim we wish **to generate a difference of Reynolds normal stresses $Q = \langle v'^2 - w'^2 \rangle$ vs z profile which is similar in shape to that obtained from DNS results of 3D channel flow at the same Re**. Specifically we aim to get the distance of peaks from the wall Δ in our Q vs z profile same as that in 3D channel flow profile. In order to do so, we intend to simulate a quasi-2D statistically stationary turbulent channel flow and for that we have to generate a 2D forcing.

For a quasi-2D turbulent channel flow with random 2D forcing, we have assumed that $\partial/\partial x = 0$ for all the dynamical variables. Then the modified continuity equation is

$$\frac{\partial v}{\partial y} + \frac{\partial w}{\partial z} = 0 \tag{4.9}$$

The modified momentum equations become

$$\frac{\partial u}{\partial t} + v\frac{\partial u}{\partial y} + w\frac{\partial u}{\partial z} = \frac{\overline{dP}}{dx} + \frac{1}{Re_\tau}\nabla^2 u + f_x \tag{4.10}$$

$$\frac{\partial v}{\partial t} + v\frac{\partial v}{\partial y} + w\frac{\partial v}{\partial z} = -\frac{\partial p'}{\partial y} + \frac{1}{Re_\tau}\nabla^2 v + f_y \tag{4.11}$$

$$\frac{\partial w}{\partial t} + v\frac{\partial w}{\partial y} + w\frac{\partial w}{\partial z} = -\frac{\partial p'}{\partial z} + \frac{1}{Re_\tau}\nabla^2 w + f_z \tag{4.12}$$

where the mean pressure gradient $\overline{dP}/dx = -1$. The above equations emphasise that the temporal development of velocity field (u, v, w) is only a function of cross-flow coordinates (y, z, t) and random amplitude body forces. For the initial conditions, the streamwise component u was chosen to be the mean turbulent streamwise velocity profile with no perturbations, while v and w are generated using the "random eddy" model as described in section 3.2.

The body forces f_y and f_z in above equations have been chosen such that they have amplitude governed by a random function of certain forcing frequency ω_f in time with a zero mean, a sinusoidal spatial variation of fixed number of modes (l, k) in spanwise and wall-normal directions and a function $\zeta(z)$ controlling near-wall amplitude in wall-normal direction. In order to generate peaked near-wall forcing which reduces to zero towards the centre of the channel, various functions $\zeta(z)$ have been used ranging from approximate Dirac delta to two-hump functions.

4.3.1 Forcing based on approximate Dirac delta functions

Here the function $\zeta(z)$ approximates a delta function centered at z_o with its width controlled by a factor n and is given mathematically as $\zeta(z) = e^{(-.5n^2(z-z_o)^2)}$. It is plotted in Figures 4.1(a) and 4.1(b).

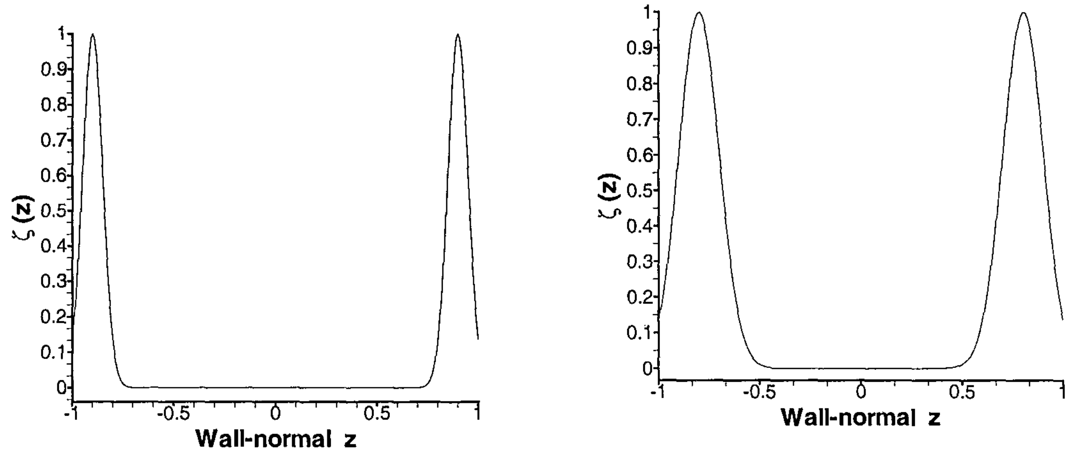

(a) For n=20.0 and z_o=0.9

(b) For n=10 and z_o=0.8

Figure 4.1: Dirac delta function at particular values of exponent n and z_o

The 2D forces are then given as

$$
\begin{aligned}
f_x &= 0.0 && (4.13)\\
f_z &= AF(\omega_f t)\cos(\frac{2\pi l y}{L_y})\zeta(z)\cos(\frac{2\pi k z}{L_z}) &&\\
f_y &= \frac{0.5AF(\omega_f t)(z-z_o)n^2 L_y \sin(\frac{2\pi l y}{L_y})\zeta(z)\cos(\frac{2\pi k z}{L_z})}{\pi l} &&\\
&\quad + \frac{AF(\omega_f t)kL_y \sin(\frac{2\pi k z}{L_z})\zeta(z)\sin(\frac{2\pi l y}{L_y})}{L_z l} && (4.14)
\end{aligned}
$$

on using divergence-free body force condition.

4.3.2 Forcing based on two-hump functions

Here the function $\zeta(z)$ approximates a function which has humps near each wall and is given as $\zeta(z) = a(1 \pm z)Re(Re - (1 \pm z)Re)^n$ where the value of n controls the width of the function i.e. higher the value of n, the smaller the width of the function. For n=8, a should be kept 0.2e-21 so that $\zeta(z)$ =O(1) while for n=4, a should be 0.2e-11. The function $\zeta(z)$ is plotted for different values of exponent n in Figures 4.2(a) to 4.2(b).

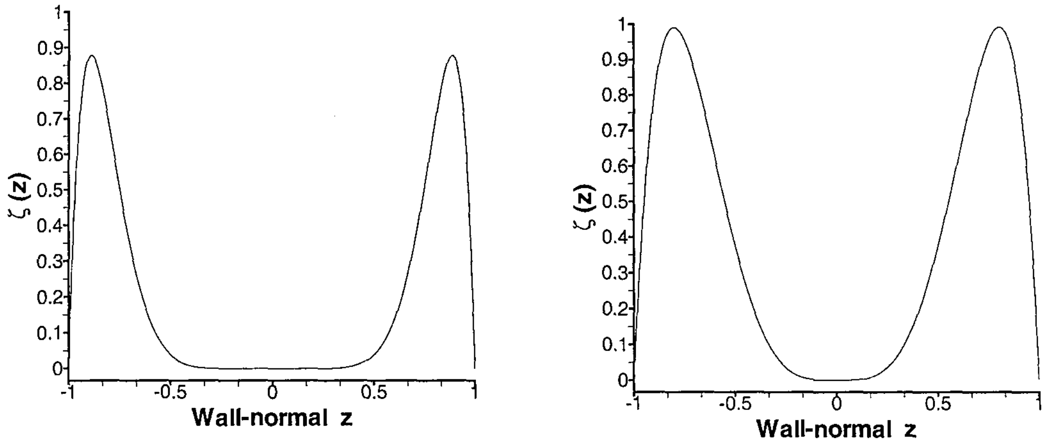

(a) For n=8 (b) For n=4

Figure 4.2: Two-hump function at particular values of exponent n

The 2D forces based on these functions are given as

$$f_x = 0.0 \tag{4.15}$$

$$f_y = AF(\omega_f t)\cos(\frac{2\pi l y}{L_y})\zeta(z)\cos(\frac{2\pi k z}{L_z})$$

$$f_z = \int_{-1}^{z} \frac{-\partial f_y}{\partial y} dz \tag{4.16}$$

4.4 Numerical Simulation

The numerical experiments were carried out by subjecting quasi-2D turbulent flows to statistically steady-state forcing using random amplitude body force terms in the governing Navier-Stokes equations. The results presented below were obtained numerically at Re=360 on a 4 $\times$ 256 $\times$ 160 mesh ($\Delta x^+ = 0.45$, $\Delta y^+ = 8.4$ and 10 grid points below $z^+ = 5.5$) with different number of modes in spanwise l and wall-normal k directions, different values of amplitude A (varying temporally between $-A/2$ and $A/2$) and forcing frequency ω_f in terms of non-dimensional time and different $\zeta(z)$ functions. The wavenumbers $2\pi l/L_y$ and $2\pi k/L_z$ were chosen to be such that the scales excited were much smaller than the large scale structures that form. The important consideration in all these simulations was that if A is made larger than some threshold value then there is a blow-up due to an under-resolved mesh and if A is small then forcing is insufficient to sustain turbulence and the flow returns to laminar state. The forcing has been performed at high frequency ω_f in order to excite small-size eddies that have small time periods of overturning i.e. only small scales have been excited by high frequency forcing.

The simulation for Re =360 has been performed for wall-normal two-hump function with n=8 exponent, fixed spanwise mode l= 55, wall-normal mode k=1, amplitude A = 0.05 and forcing frequency ω_f = 100 in terms of non-dimensional time. For the initial conditions, the mean streamwise velocity u is given by linear profile till $z^+ = 10$ and log-law profile till the centre of the channel, while v' and w' are generated by the "random eddy" model as explained in chapter 2. The forcing of the flow leads to growth of fluctuations in all the dynamical variables and by the time t = 25.0 approximately the flow acquires fully-developed turbulence. The flag is then turned on to perform statistical averaging and the statistics gathered for a very long time till t = 330. Since the flow can be only space-averaged in spanwise direction we have to go for longer time-averaging.

The spatio-temporal variation of the generation, break-up and regeneration of low-speed streaks by visualization of instantaneous u' can be seen in Figures 4.3(a) to 4.3(d) while the temporal variation of the instantaneous Q = $< v'^2 - w'^2 >$ vs z profile can be seen from the Figures 4.4(a) to 4.4(d). From the contour plots of low-speed streaks the number of streaks that can be visualized are approximately 9-10, giving an average value of streak spacing =0.6 for a spanwise length of $L_y = 6.0$. The instantaneous Q in the figures shows a spatio-temporal variation with the values near the wall peaking in time whenever regeneration of streaks occur.

The statistically averaged values of $< v'^2 >$, $< w'^2 >$ and Q=$< v'^2 - w'^2 >$ can be seen in Figures 4.5(a) to 4.5(b). On comparison of Q vs z profile in Figure 4.5(b) with the actual 3D DNS results [19] at same Re=360 it can be seen that the near-wall peak in both the cases form at $\Delta = 0.05$

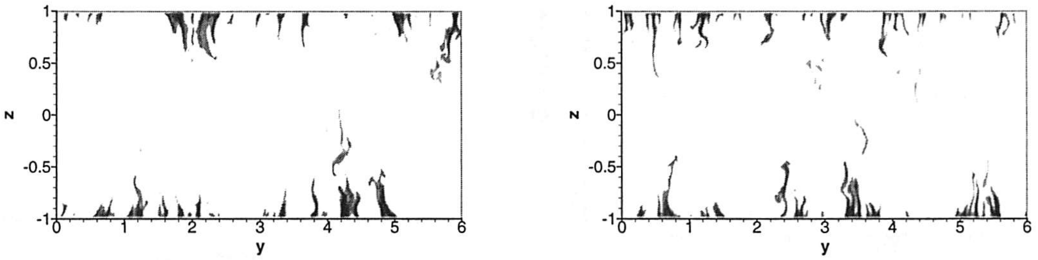

(a) At time t=45.0

(b) At time t =75.0

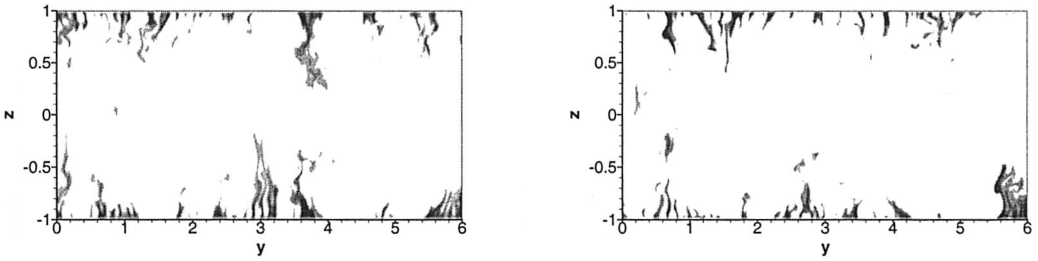

(c) At time t =90.0

(d) At time t =230.0

Figure 4.3: Spatio-temporal variation of negative streamwise velocity fluctuations u'. In areas marked black the plotted variables is < 0.25 of its minimum negative value.

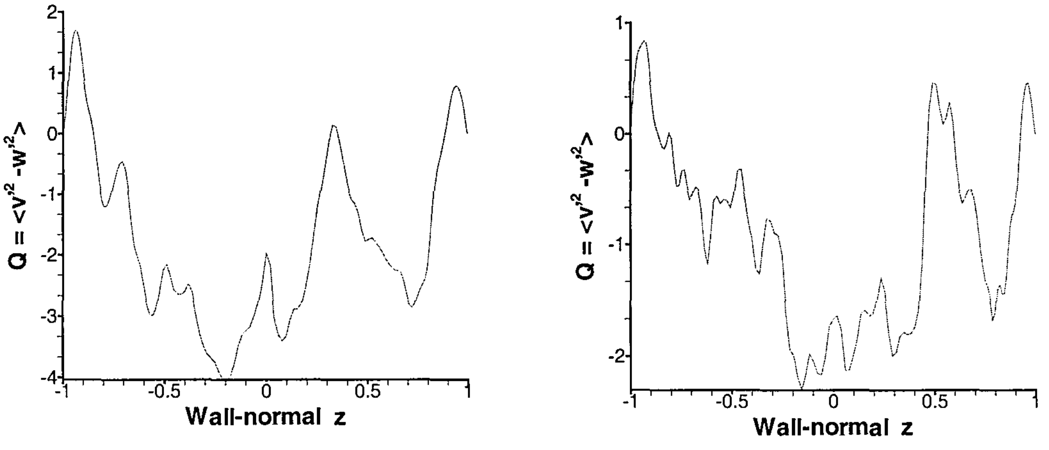

(a) At time t=45.0

(b) At time t =75.0

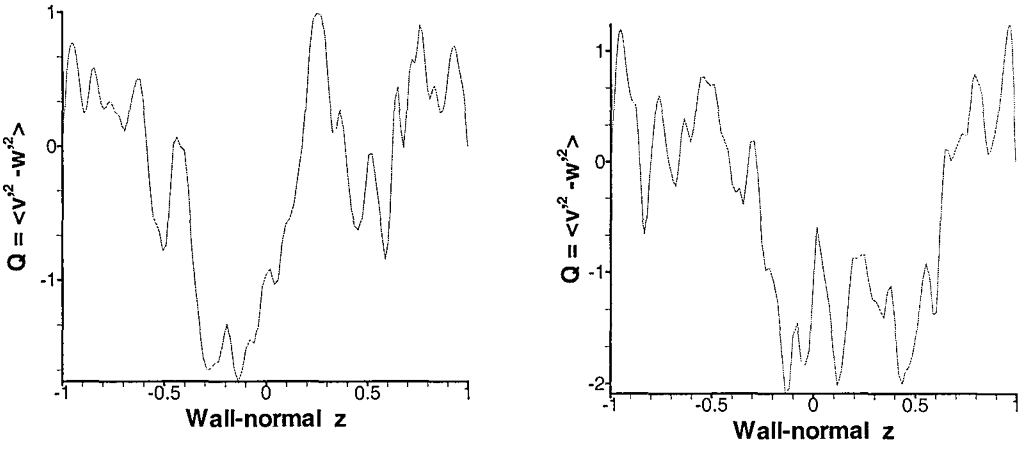

(c) At time t =90.0

(d) At time t =230.0

Figure 4.4: Temporal variation of $Q = < v'^2 - w'^2 >$ vs wall-normal distance z

from the walls. This Δ relates to the characteristic scale of Reynolds stress anisotropy instability responsible for the size of near-wall vortices.

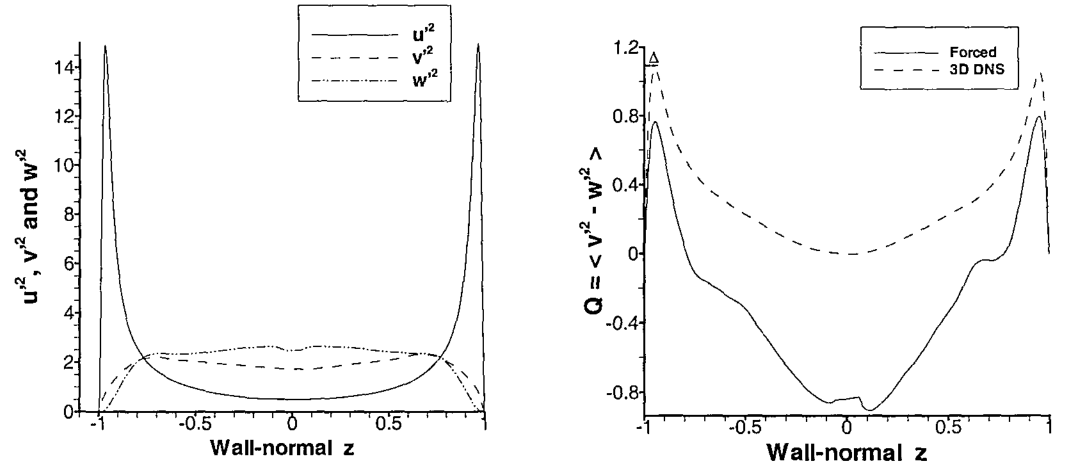

(a) Streamwise, spanwise and wall-normal velocity fluctuations u'^2, v'^2 and w'^2

(b) Reynolds normal stresses difference Q

Figure 4.5: Statistically averaged variation of $\bar{u'}^2$, $\bar{v'}^2$, $\bar{w'}^2$ and Q

The statistically averaged values of $\bar{u}$, $\bar{v}$ and $\bar{w}$ can be seen from the Figure 4.6. From this figure it can be seen that $\bar{v}$ is approximately ± 0.03 while $\bar{w}$ is almost zero. The mean turbulent kinetic energy (TKE) $\overline{u_i'u_i'}$ profile vs z can be seen from Figure 4.6(b) and it shows a peaked variation near the walls due to forcing. The spatial variation of mean turbulent dissipation ε shows as expected, significantly large values in the viscous layer and slightly positive value in the outer region (see Figure 4.6(c)). Mathematically the non-dimensional mean dissipation as used in this study can be expressed as:

$$\begin{aligned}\bar{\varepsilon} = {} & \frac{1}{Re_\tau}\Big(\overline{(\frac{\partial u}{\partial y})^2+(\frac{\partial u}{\partial z})^2+(\frac{\partial v}{\partial x})^2+(\frac{\partial w}{\partial x})^2+(\frac{\partial v}{\partial z})^2+(\frac{\partial w}{\partial y})^2+2(\frac{\partial v}{\partial z}\frac{\partial w}{\partial y}+\frac{\partial u}{\partial y}\frac{\partial v}{\partial x}+\frac{\partial u}{\partial z}\frac{\partial w}{\partial x})} \\ & +2\overline{((\frac{\partial u}{\partial x})^2+(\frac{\partial v}{\partial y})^2+(\frac{\partial w}{\partial z})^2)}-(\overline{(\frac{\partial u}{\partial z})}^2+\overline{(\frac{\partial v}{\partial z})}^2)\Big)\end{aligned}$$

The eddy turnover time which characterises the ratio of TKE/ε shows a profile (see 4.6(d)) which has a step-variation as we proceed from the wall to the centre of the channel. The eddy turnover time increases continuously in the very near-wall region while in the region from z=± 0.9 to 0.8 it shows an undulation and then again starts increasing with a smaller slope in the outer layer region.

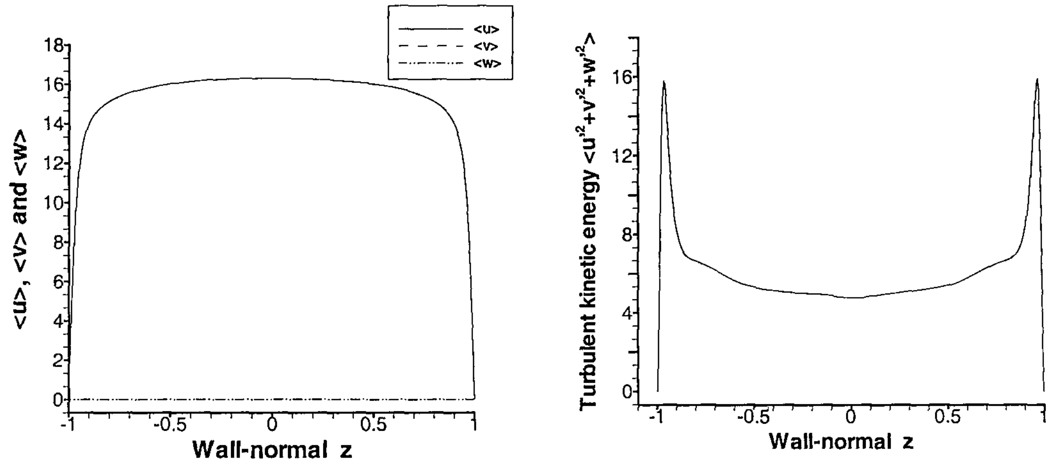

(a) $\bar{u}$, $\bar{v}$ and $\bar{w}$

(b) Mean TKE

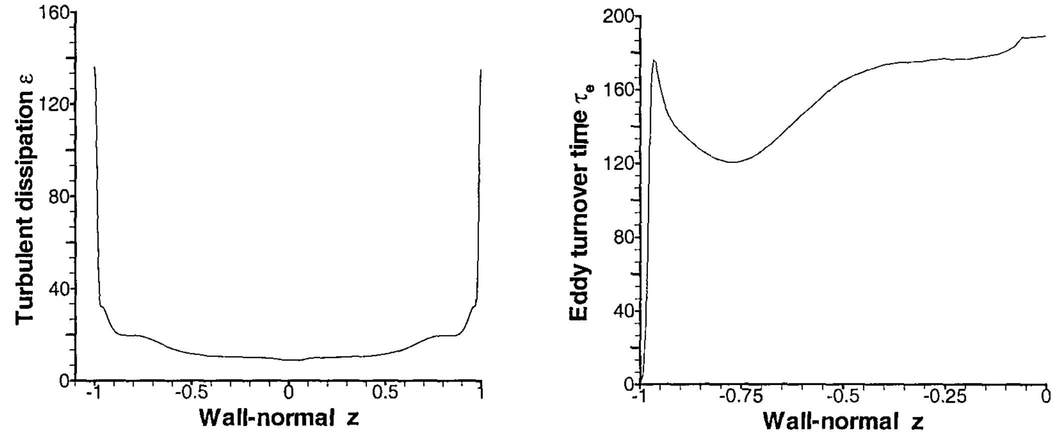

(c) Mean ε

(d) Eddy turnover time

Figure 4.6: Statistically averaged variation of mean velocities, mean TKE, mean ε and eddy turnover time

4.5 Validation of the RNSAI code

Having obtained the statistically averaged Q vs z profile from a quasi-2D randomly forced flow, the next step is to determine the size of near-wall vortices or in other words streak spacing as predicted by the Nikitin and Chernyshenko's RNSAI mechanism [38]. This amounts to the linear stability analysis of the ensemble-averaged two-dimensional Navier-Stokes equations in a cross-flow ($y-z$) plane together with the passive-admixture equation providing the closure for the Reynolds-stress perturbations. As linear stability analysis has been performed in a plane normal to the streamwise direction i.e. in a cross-flow ($y-z$) plane the governing equations do not turn out to be Orr-Sommerfeld equations. The governing two-dimensional Reynolds averaged Navier-Stokes equations in the cross-flow y-z plane are

$$\frac{\partial w}{\partial t}+v\frac{\partial w}{\partial y}+w\frac{\partial w}{\partial z}=-\frac{\partial \Pi}{\partial z}+\frac{1}{Re}\nabla^2 w+\frac{\partial Q}{\partial z}-\frac{\partial \tau}{\partial y} \tag{4.17}$$

$$\frac{\partial v}{\partial t}+v\frac{\partial v}{\partial y}+w\frac{\partial v}{\partial z}=-\frac{\partial \Pi}{\partial y}+\frac{1}{Re}\nabla^2 v-\frac{\partial \tau}{\partial y} \tag{4.18}$$

$$\frac{\partial v}{\partial y}+\frac{\partial w}{\partial z}=0 \tag{4.19}$$

In a laminar flow containing unsteady small perturbations, the instantaneous modified pressure, velocities and Reynolds stresses can be presented as the sum of a base flow and a fluctuating quantity

$$\Pi=\overline{\Pi}+\widetilde{\Pi};\quad v=\bar{v}+\tilde{v};\quad w=\bar{w}+\tilde{w};\quad Q=\overline{Q}+\widetilde{Q};\quad \tau=\bar{\tau}+\tilde{\tau} \tag{4.20}$$

where the bars denote the base flow which obeys the Navier-Stokes equations and tildes denote the perturbations. Here the modified pressure $\Pi=p+\langle v'^2\rangle$, Reynolds normal stress $Q=\langle v'^2-w'^2\rangle$ and Reynolds shear stress $\tau=\langle v'w'\rangle$. Substituting (4.20) into (4.17)-(4.19), neglecting the terms containing products of perturbations and nonlinear convective terms, and subtracting the equations for the base flow gives the resulting linearized perturbation equations in the following form:

$$\frac{\partial \tilde{w}}{\partial t}=-\frac{\partial \widetilde{\Pi}}{\partial z}+\frac{1}{Re}\nabla^2\tilde{w}+\frac{\partial \widetilde{Q}}{\partial z}-\frac{\partial \tilde{\tau}}{\partial y} \tag{4.21}$$

$$\frac{\partial \tilde{v}}{\partial t}=-\frac{\partial \widetilde{\Pi}}{\partial y}+\frac{1}{Re}\nabla^2\tilde{v}-\frac{\partial \tilde{\tau}}{\partial y} \tag{4.22}$$

$$\frac{\partial \tilde{v}}{\partial y}+\frac{\partial \tilde{w}}{\partial z}=0 \tag{4.23}$$

To provide a closure to the above equations (4.21)-(4.23), it is necessary to add equations describing the dynamics of the perturbations of the Reynolds stresses $\widetilde{Q}$ and $\tilde{\tau}$. Nikitin and Chernyshenko

[38] used a phenomenological model in which the Reynolds-stress perturbations are described by the linearised passive-admixture transport equations

$$\frac{\partial \tilde{Q}}{\partial t} + \tilde{w}\frac{dQ}{dz} = \frac{1}{Re}\nabla(E\nabla\tilde{Q}) \tag{4.24}$$

$$\frac{\partial\tilde{\tau}}{\partial t} = \frac{1}{Re}\nabla(F\nabla\tilde{\tau}) \tag{4.25}$$

Here, E=ν_q/ν and F=ν_τ/ν where ν_q and ν_τ are positive diffusion coefficients which are a spatial function of wall-normal coordinate z. As eqn. (4.25) has only damped eigensolutions (see [38]), τ can be eliminated from the solution of the problem. The modified pressure, normal stresses and velocity fluctuations are represented by a harmonic wave of the form

$$(\tilde{\Pi},\tilde{v},\tilde{w},\tilde{Q}) = [\hat{\Pi},\hat{v},\hat{w},\hat{Q}]e^{\imath(\beta y+\Lambda t)} \tag{4.26}$$

where β is the wavenumber in the spanwise y direction and Λ is the circular frequency which, in general, may be complex-valued. The real part of Λ gives the growth/decay rate of the perturbations.

Substituting eqn. (4.26) in the perturbation equations, gives for the case E=1

$$\Lambda\hat{w} = -\frac{\partial\hat{\Pi}}{\partial z} + \frac{1}{Re}(\frac{d^2\hat{w}}{dz^2} - \beta^2\hat{w}) + \frac{d\hat{Q}}{dz} \tag{4.27}$$

$$\Lambda\hat{v} = -\imath\beta\hat{\Pi} + \frac{1}{Re}(\frac{d^2\hat{v}}{dz^2} - \beta^2\hat{v}) \tag{4.28}$$

$$\imath\beta\hat{v} + \frac{d\hat{w}}{dz} = 0 \tag{4.29}$$

$$\Lambda\hat{Q} + \hat{w}\frac{dQ}{dz} = \frac{1}{Re}(\frac{d^2\hat{Q}}{dz^2} - \beta^2\hat{Q}) \tag{4.30}$$

After further modifications which eliminate the $\hat{v}$, one gets

$$\frac{1}{Re}(\frac{\imath}{\beta}\frac{d^4\hat{w}}{dz^4} - 2\beta\imath\frac{d^2\hat{w}}{dz^2} + \imath\beta^3\hat{w}) - \imath\beta\frac{d\hat{Q}}{dz} = \Lambda(\frac{\imath}{\beta}\frac{d^2\hat{w}}{dz^2} - \imath\beta\hat{w}) \tag{4.31}$$

$$\frac{1}{Re}(\beta^2\hat{Q} - \frac{d^2\hat{Q}}{dz^2}) + \hat{w}\frac{dQ}{dz} = -\Lambda\hat{Q} \tag{4.32}$$

The equations (4.31) and (4.32) are 4th and 2nd order ordinary differential equations and hence six boundary conditions are needed, which basically are

$$\hat{w} = \hat{Q} = \frac{d\hat{w}}{dz} = 0 \quad at \quad z = \pm 1 \tag{4.33}$$

resulting in the complex dispersion relation $\Lambda = \Lambda(\beta)$.

The above system of equations has been discretized using both the second-order and fourth-order accurate finite difference schemes. After the discretization, the eqns. (4.31-4.32) along with the boundary conditions (4.33) are formulated as a generalised eigenvalue problem

$$[A][x] = \lambda[B][x] \tag{4.34}$$

where λ are the eigenvalues and [x] is a matrix of discrete eigenfunctions. If N is the number of grid points in the wall-normal direction including the boundary points, then the size of the system matrices [A] and [B] is 2 × N. Moreover, two classes of numerical methods can be followed for computing the eigenvalues: global and local methods. Using a global method we get all the eigenvalues of the system matrix, in exchange for a large computational effort while in a local method, a guess for an eigenvalue is required and only the eigenvalues which lie in the neighbourhood are computed.

We have based our algorithm on a global method and implemented it using the standard eigenvalue solver routines from IMSL package and then performed calculations till we attain grid-independent results. The grid points have been generated in the channel using expansion factor of 1.01 based on geometric series from both the top and bottom walls to the centreline, so that there is a fine clustering of points near both the walls.

In order to validate the developed RNSAI code we have repeated the calculations of Nikitin and Chernyshenko [38]. The analytic function dQ/dz which represents the derivative of difference of Reynolds normal stresses Q with wall-normal distance z proposed by them as approximation to DNS results is

$$\frac{dQ}{dz} = \frac{A}{18} 10^3 \frac{z(18-z)}{(z+10)^3} \left[1 + \left(\frac{z}{30}\right)^4\right]^{-1} \tag{4.35}$$

For medium to high Reynolds numbers A varies from 0.1 to 0.3. We have numerically solved the generalized eigenvalue problem using the eqn. (4.34) for N =241 grid points for A=0.1 and the results are in excellent agreement with Nikitin and Chernyshenko's [38] results as can be seen in Figure 4.7.

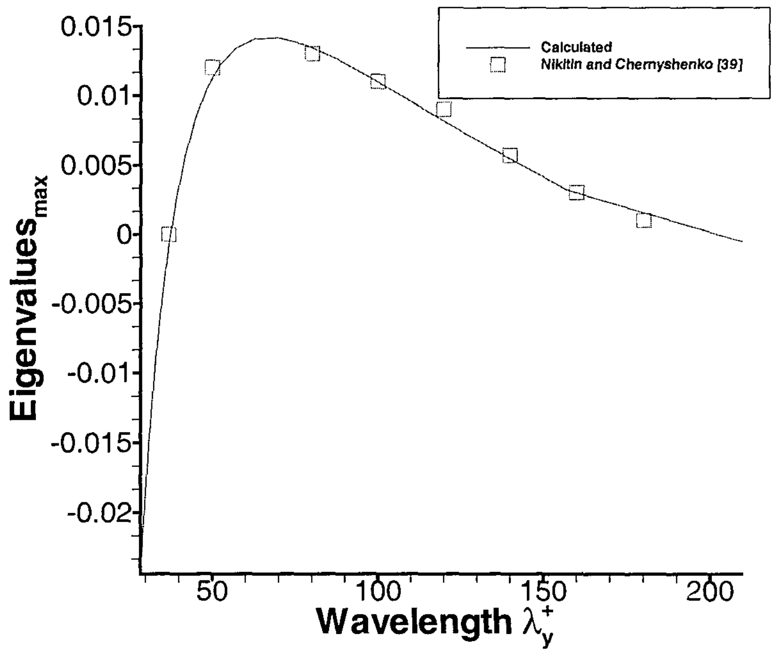

Figure 4.7: Validation of calculated results with results from [38]

4.6 Application of RNSAI to forced quasi-2D flow

From the numerical simulation the details of which were presented in section 4.4, we have extracted a time and space-averaged profile of Reynolds normal stresses Q vs z (see Figure 4.8(a)) and from it we have numerically computed its wall-normal derivative dQ/dz. It can be seen from Figure 4.8(a) that near the wall there are two almost symmetric peaks with wall to peak distance $\Delta_{offset} = 0.05$ which is reasonably good, but Q remained, in contrast to natural 3D flows, far from zero in the centre of the channel. This is believed to be due to insufficient averaging time, since fluctuations of Q in time were large. So a smoothing procedure has been used by which near-wall peaks exponentially decay into constant zero values away from the wall and then a cubic spline interpolation [42] has been used to generate numerical points which are plotted as the new Q vs z profile (see Figure 4.8(b)). The actual Q vs z variation that we get from a 3D DNS [20] has also been computed and plotted as Figure 4.8(c) and a similar value of Δ_{offset} is observed.

Using the profile as shown in Figure 4.8(b) and Re=360 we have run our eigenvalue solver and computed the maximum unstable eigenvalues σ which display the growth rate of streamwise vortices and are plotted as shown in Figure 4.9. As can be seen from the figure we get the maximum

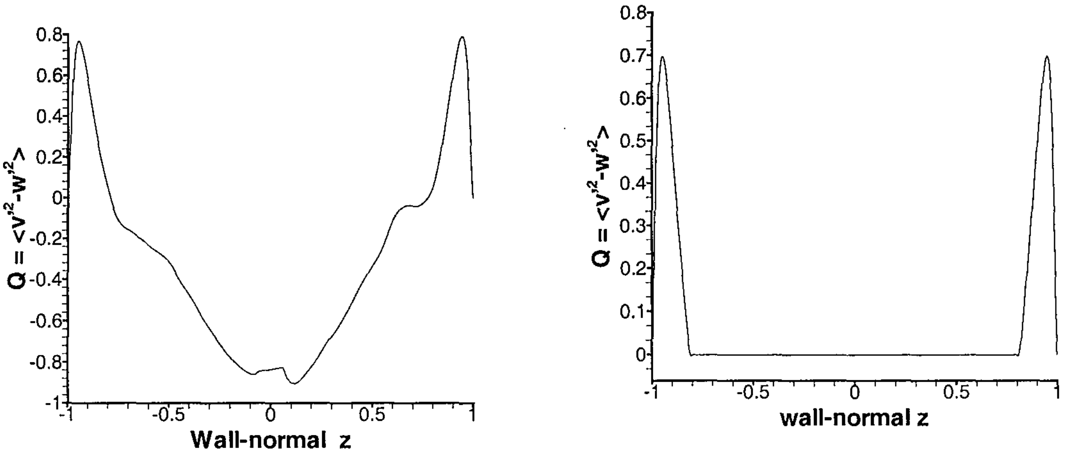

(a) Statistically averaged Q vs z profile

(b) Spline-interpolated Q vs z profile

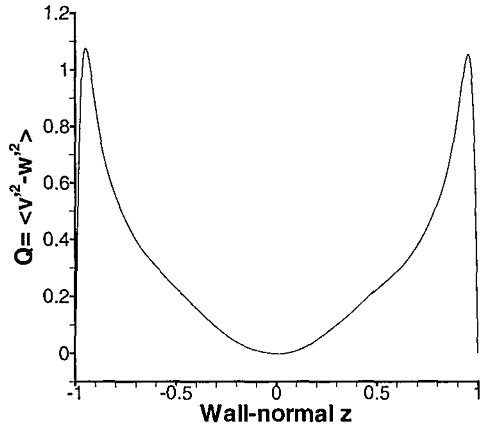

(c) Q vs z profile from a 3D DNS [20]

Figure 4.8: Quasi-2D DNS Statistically averaged, spline-interpolated and 3D DNS [19] Q vs z profile

diameter (size) of the streamwise vortices at λ_y^+ approximately equal to 155 wall units. The wall units are arbitrary units of measure in our quasi-2D flows because in the cross-flow plane the longitudinal flow is of no importance and therefore u_τ is an irrelevant parameter and hence any parameters using u_τ are of no relevance to cross-flow 2D plane. We prefer, however, to use the wall units because they provide a reference frame for comparison of results and also it is a standard practice to measure the streak spacing in wall units. As per the phenomenological model of two streamwise vortices flanking each high or low-speed streaks, we get a streak spacing of 310 wall units and this for our spanwise periodic length $L_y = 6$ and Re = 360, the number of streaks turn out to be 360*6/310 = 6 to 7 which is not consistent with the number of streaks visually observed $\simeq$ 9 to 10 in our randomly-forced quasi-2D calculations. Moreover, the number of streaks computed using two-point streamwise velocity auto-correlations as shown in Figure 5.3(a) turns out to be 360*6/220 $\simeq$ 9 to 10 which is again inconsistent with number of streaks predicted by RNSAI mechanism.

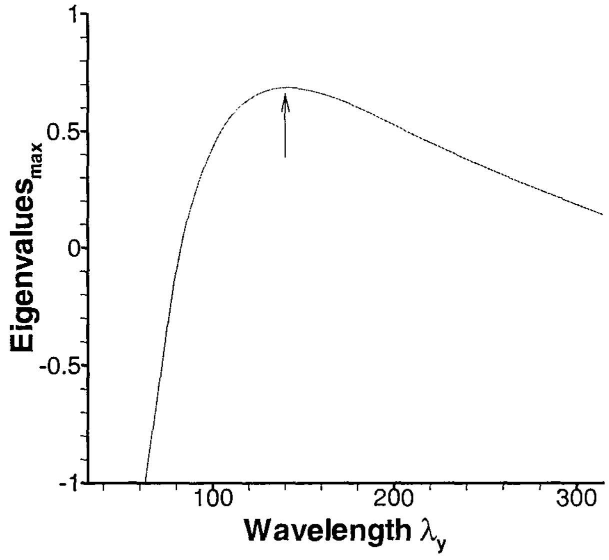

Figure 4.9: Growth rate of streamwise vortices as a function of λ_y, showing the most likely size of vortices

4.7 Conclusions

The quasi-2D forced turbulence calculations were performed to check which of the mechanisms: RNSAI mechanism [38] or OP theory [7] predicts correct streak spacing. It was found that Nikitin and Chernyshenko's RNSAI mechanism gave a streak spacing $\simeq$ 310 wall units or number of streaks $\approx$ 6 to 7 which is not in agreement with number of streaks $\simeq$ 9 to 10 observed visually on basis of threshold cutoff. In order to check the streak spacing based on optimal perturbation theory one of the strategies can be to introduce passive scalars with different mean profiles and then to calculate spacing between the streaks of the scalar using OP theory and compare it with streak spacing as obtained from two-point spanwise correlations of the scalar using DNS results.

Chapter 5

PASSIVE SCALAR STREAKS IN QUASI-2D FORCED TURBULENCE

5.1 Introduction

The findings from the DNS results of naturally decaying quasi-2D turbulence could not with certainty prove that Reynolds stress anisotropy mechanism is responsible for generation of streamwise vortices that in turn generate streaks. Moreover, from those findings it could not be ruled out that optimal perturbations do not have any significant role in generation of near-wall organised structures while at the same time the optimal perturbation results of Butler and Farrell [7] show that the streak spacing agrees with 3D DNS results, if the additional constraint of eddy turnover time is introduced.

In order to further check the optimal perturbation mechanism, we introduce passive scalars in the turbulent flow and calculate streak spacing of the scalars. According to the optimal perturbation theory, the streak spacing for any variable depends on the mean profile of that variable while due to vortex regeneration theories (including RNSAI mechanism [38]), it is not so. Hence a number of passive-scalar admixture equations can be solved alongwith the Navier-Stokes equations with different mean scalar profiles $\Theta_i(z)$ in order to ascertain the dominant theory/mechanism responsible for the observed streak spacing. Regarding this we have modified the pseudo-spectral channel code of [47], in order to solve an arbitrary number of passive-scalar equations.

5.2 Methodology for solution of passive-scalar equations

In order to study streak spacing, it is proposed to solve an advection-diffusion equation with a source term for the continuous distribution of a passive scalar. Consider a continuous distribution $\theta_i(y,z,t)$ of n number of passive scalars in the domain, the transport of which is governed by the advection-diffusion equations

$$\frac{\partial\theta_i}{\partial t} + \mathbf{u}.\nabla\theta_i = \frac{1}{RePr}\nabla^2\theta_i + S_i \tag{5.1}$$

where $Pr = \nu/\chi$ where χ is the molecular diffusivity of the scalar and S_i are the source terms for the passive scalars. The boundary condition for equation (5.1) is given by zero concentration of the scalars on the solid walls $\theta_i(\pm 1) = 0$.

The structure of eqn. (5.1) is very similar to that of the Navier-Stokes equation (2.3). Therefore, the numerical integration of this equation is performed using the techniques described in section 2.2 for solving the Navier-Stokes equations. After discretization in time, the eqn. (5.1) can be modified after multiplication by $2Re$ as

$$\frac{2Re}{\Delta t}\theta_i^{n+1} - \frac{\nabla^2\theta_i^{n+1}}{Pr} = 2Re[-a\mu^n - b\mu^{n-1} + \frac{\theta_i^n}{\Delta t} + \frac{\nabla^2\theta_i^n}{2RePr} + S_i^n] \tag{5.2}$$

where $\mu = \mathbf{u}\cdot\nabla\theta$. Performing Fourier transformation of the variables and their derivatives in homogeneous x and y directions leads to the equations cited below.

$$\begin{aligned}
\mathbf{u}(x,y,z,t) &= \sum_{k_x=-N/2}^{N/2}\sum_{k_y=-N/2}^{N/2} \hat{\mathbf{u}}(z,t)e^{\imath(k_x x+k_y y)} \\
\theta(x,y,z,t) &= \sum_{k_x=-N/2}^{N/2}\sum_{k_y=-N/2}^{N/2} \hat{\theta}(z,t)e^{\imath(k_x x+k_y y)} \\
\mu(x,y,z,t) &= \sum_{k_x=-N/2}^{N/2}\sum_{k_y=-N/2}^{N/2} \hat{\mu}(z,t)e^{\imath(k_x x+k_y y)} \\
\nabla\theta(x,y,z,t) &= \sum_{k_x=-N/2}^{N/2}\sum_{k_y=-N/2}^{N/2} (\imath k_x\hat{\theta}, \imath k_y\hat{\theta}, \hat{\theta}')e^{\imath(k_x x+k_y y)} \\
\nabla^2\theta(x,y,z,t) &= \sum_{k_x=-N/2}^{N/2}\sum_{k_y=-N/2}^{N/2} (\hat{\theta}'' - (k_x^2+k_y^2)\hat{\theta})e^{\imath(k_x x+k_y y)}
\end{aligned} \tag{5.3}$$

Here prime denotes derivative with respect to wall-normal direction z.

The discretisation of eqn. (5.1) after Fourier transformation has been performed in spanwise and streamwise directions is

$$\begin{aligned} \hat{\theta}_i{}''^{n+1} - \left(\frac{2RePr}{\Delta t} + k^2\right)\hat{\theta}_i{}^{n+1} &= 2RePr(a\hat{\mu}^n) + 2RePr(b\hat{\mu}^{n-1}) - \frac{2RePr}{\Delta t}\hat{\theta}_i{}^n \\ &\quad -\hat{\theta}_i{}''^n + k^2\hat{\theta}_i{}^n - 2RePrS^n \qquad (5.4) \end{aligned}$$

The term that is different in the above equation from the momentum equation is the linear convective term $\mu = \mathbf{u} \cdot \nabla\theta = u\partial\theta/\partial x + v\partial\theta/\partial y + w\partial\theta/\partial z$. For this we first converted the scalar θ from real-space to wave-space, computed derivatives in x, y and z directions, extended the number of modes by 50%, transformed the results to real space, computed the products of $u \cdot \nabla\theta$, inverse transformed and then truncated the result by dropping the upper-third of the modes. The evaluation of the linear convective term has been performed in the subroutine CROSSA of the numerical code. The fourth and fifth terms on the right-hand side are Laplacian of θ and have been computed using the procedure similar to that for the Laplacian terms in the scalar momentum equations. After all the terms on the right-hand side of the passive scalar equation have been calculated they are stored in new residual arrays and Runge-Kutta third-order time advancement performed to get the scalar values at new time step. The boundary conditions for the passive scalars are $\theta(\pm 1) = 0$. The initial passive scalar fields have a specified mean profile for each scalar and they remain time-invariant.

For scalar θ_1 we took the source term $S = -1$. Then the only difference between the equations for u and θ_1 is in the term $\partial p'/\partial x$. As in a quasi-2D flow all the streamwise gradients are zero i.e. $\partial/\partial x = 0$, the results for θ_1 must be identical to that of streamwise velocity component u. This gives a validation tool for the whole code. In order to find analytical expression for the mean scalar profile Θ_1 which also holds good for mean streamwise turbulent velocity profile U, curve fitting has been performed on statistically averaged profile of θ_1 as shown in Figure 5.1 and its first wall-normal derivative is given as:

$$\begin{aligned} f(z) &= 0.498(1 + (0.525\frac{Re}{3}(1-z^2)(1+2z^2)(1-e^{(-(1-|z|)Re/39)})^2)^{0.6} - 0.55 \\ \overline{\theta_1}' &= -z \times Re/(1+f(z)) \qquad (5.5) \end{aligned}$$

This is a small modification of the Reynolds-Tiederman profile, see below. In order to obtain different mean profiles for θ_i one has to prescribe different $S_i(z)$, but it is easier to modify the code in such a way that instead of prescribing different source terms $S_i(z)$ one can directly prescribe the mean scalar profile $\Theta_i(z) = \overline{\theta_i}(z)$. Introducing two auxiliary functions,

$$g(z,Re) = 0.5(1 + (0.525\frac{Re}{3}(1-z^2)(1+2z^2)(1-e^{(-(1-|z|)Re/37)})^2)^{0.5} - 0.5$$

(g(z,Re) has been used to generate Reynolds-Tiederman profile, as in Waleffe and Kim [68]) and

$$h(z,d,w) = 150(e^{(-\frac{(-1+d-z)^2}{w^2})} - e^{(-\frac{(-1+d+z)^2}{w^2})})$$

the derivatives of the other seven mean profiles were prescribed as

$$\begin{aligned}
\overline{\theta_2}' &= -z \times Re/(1+g(z)) && (5.6)\\
\overline{\theta_3}' &= h(z,0.20,0.15) && (5.7)\\
\overline{\theta_4}' &= h(z,0.10,0.075) && (5.8)\\
\overline{\theta_5}' &= \overline{\theta_2}' + \overline{\theta_3}' && (5.9)\\
\overline{\theta_6}' &= 1 \times \pi/2 \quad cos(1 \times \pi(1+z)/2) && (5.10)\\
\overline{\theta_7}' &= 3 \times \pi/2 \quad cos(3 \times \pi(1+z)/2) && (5.11)\\
\overline{\theta_8}' &= 5 \times \pi/2 \quad cos(5 \times \pi(1+z)/2) && (5.12)
\end{aligned}$$

The fifth mean profile is a sum of second and third mean scalar profiles. This was used to prove that linear superposition of profiles can be used to generate a new profile whose two-point correlations can be obtained from two-point cross-correlations of the imposed profiles, see below for further details. The source terms in the scalar equations maintain a time-invariant specified mean profile for each scalar θ_i except for the first scalar profile.

5.3 Results

The simulations were performed on a $4 \times 256 \times 160$ mesh ($\Delta x^+ = 0.45$, $\Delta y^+ = 8.4$ and 10 grid points below $z^+ = 5.5$) with spanwise and wall-normal number of modes being 55 and 1, forcing frequency ω_f of 100 in terms of non-dimensional time, amplitude A =0.01 for a two-hump forcing function having an exponent n=8. After a statistically stationary state has been achieved after a non-dimensional time t =25, auto and cross-correlation of each dynamical variable were calculated and time-averaging done for a long time i.e. till t=330.0. As there are 11 variables (3 velocities and

8 passive scalars), 121 spanwise correlations were computed at each third time step (i.e. sampling rate = 3Δt) and time averaging performed. The averaged mean profiles of the streamwise velocity component $\bar{u}$ and mean scalars Θ_i are shown in Figures 5.1(a) to 5.1(c). In figure 5.1(a) the profiles of U and θ_1 lie on each other exactly. It can be easily seen that the slope of the scalar profiles is markedly different from each other which according to optimal perturbation theory [7] might generate markedly different near-wall streaks.

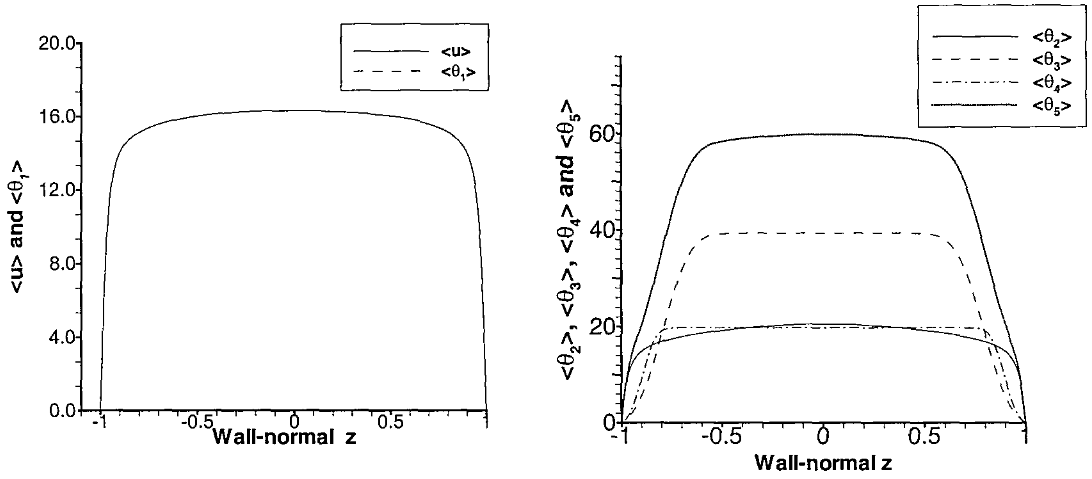

(a) $\bar{u}$ and $\bar{\theta}_1$

(b) $\bar{\theta}_2$, $\bar{\theta}_3$, $\bar{\theta}_4$ and $\bar{\theta}_5$

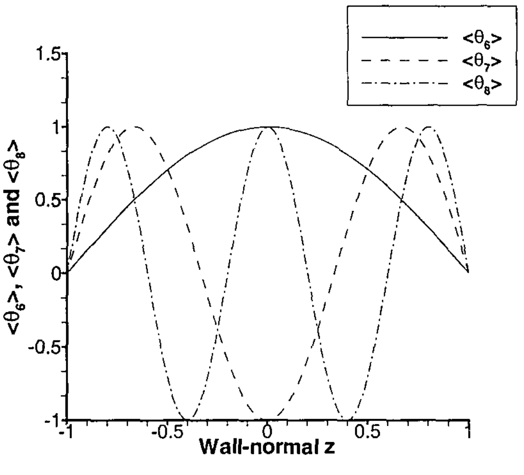

(c) $\bar{\theta}_6$,$\bar{\theta}_7$ and $\bar{\theta}_8$

Figure 5.1: Statistically averaged variation of mean scalar profiles $\bar{\theta}_i$

The proof of the concept of linear superposition of profiles has been validated by taking fifth mean scalar profile Θ_5 as the sum of second and third mean scalar profiles i.e. $\Theta_5 = \Theta_2 + \Theta_3$. Now a two-point correlation of θ_5 with itself gives

$$R_{(\theta_5\theta_5)} = R_{(\theta_2\theta_2)} + R_{(\theta_3\theta_3)} + 2R_{(\theta_3\theta_2)} \tag{5.13}$$

Hence two-point auto-correlation coefficient $R_{\theta_5\theta_5}$ should be sum of cross-correlation coefficients $R_{\theta_2\theta_3}$ and auto-correlations $R_{\theta_3\theta_3}$, $R_{\theta_2\theta_2}$ and the same has been validated by plotting them together in Figure 5.2.

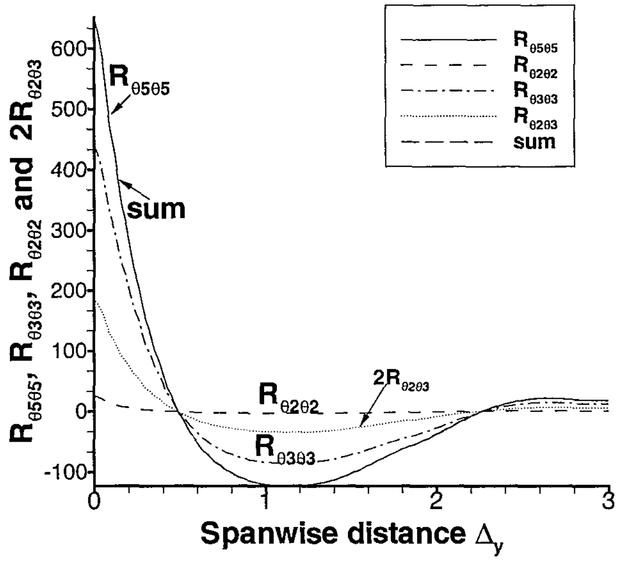

Figure 5.2: Correlation coefficients $R_{\theta_5\theta_5}, R_{\theta_2\theta_2}, R_{\theta_3\theta_3}, 2 \times R_{\theta_3\theta_2}$ and their sum to validate the proof of concept.

As the present computations have a sufficiently fine grid to get a resolution of $\Delta y^+ = 8.4$, two-point correlations can provide quantitative structural information regarding streak spacing in the wall region.

The velocity auto-correlation function $R_{uu}(\Delta, z) = \langle u(x,y,z,t)u(x,y+\Delta,z,t)\rangle$ has a maximum at $\Delta = 0$ and reaches a minimum at a certain value Δ_{min}. Streak spacing can be defined as $2\Delta_{min}$. Similarly, the auto-correlation function for the passive scalars can be used for determining the passive scalar streak spacing. Moreover, spanwise cross-correlations of each dynamical variable with ten other variables were computed and time-averaging performed in order to get a smooth spatial variation. As can be seen from the Figures 5.3 to 5.5 the auto-correlation becomes negative and reaches a minimum at certain spanwise distance Δ_{min}. The separation at which this minimum occurs provides an estimate of the mean separation between the high- and low-speed fluid, and the mean spacing between the streaks should be approximately twice the distance. The presence of the minimum of R_{ww} at $\Delta y^{+} = 35$ is consistent with the existence of streamwise near-wall vortical structures. Twice the separation of minimum R_{ww} corresponds to the mean diameter of the streamwise vortices [33]. The presence of oscillations in Figure 5.3(c) especially their increase in magnitude as one moves out away from wall can be attributed to the external forcing being applied to the flow. Moreover, the increase in magnitude is consistent with the shape of the wall-normal spatial forcing function $\zeta(z)$ which peaks at some distance away from the wall as shown in Figure 4.2.

The streak spacing increases weakly with wall-normal distance for some scalars as can be seen from Figures 5.3 to 5.5 which is consistent with other researchers [33]. Moreover, the streak spacing of the scalars (Θ_1 to Θ_8) as deduced from the two-point correlations can be expressed in spanwise wall units $\lambda_y^{+} = \lambda_y u_\tau / h$ and these values turn out to be 500, 600, 800, 500, 800, 900, 1400 and 700 at a wall-normal distance of $z^{+} = 3.5$.

The time and spanwise-averaged power spectra of velocities taken at different wall-normal distances can be seen from Figures 5.6 to 5.7. It is apparent from these figures that as the distance from the wall increases from $z^{+} = 18$ to $z^{+} = 54$ (z=0.15 from the wall), the power content of the streamwise velocity u' decreases while the power content of the cross-flow velocities v and w increases quite significantly by a factor of two to three times. This implies that the vortices that form in the cross-flow plane have larger kinetic energy as we move away from wall, while the streaks that develop near the wall ($z^{+} = 18$) have higher power content by a factor of two over streaks that occur away from wall at $z^{+} = 54$. The reason why cross-flow vortices have larger kinetic energy as one moves away from wall is possibly due to the nature of applied wall-normal forcing which we know possesses a peak in the vicinity of $z^{+} = 70$.

The spatial variation at non-dimensional time $t = 110.0$ of the streamwise low-speed streaks characterised by negative streamwise velocity fluctuations u' can be seen in Figure 5.8(a). It has been found that there are 9-10 low speed-streaks that can be seen at any time instant in the cross-flow plane if the threshold value of 0.25 of maximum negative values is taken as the cutoff limit. The spatial variation of the first mean scalar Θ_1' is identical to the velocity u' as the governing equations for the two are identical in a quasi-2D flow and hence the streaks observed are almost similar in

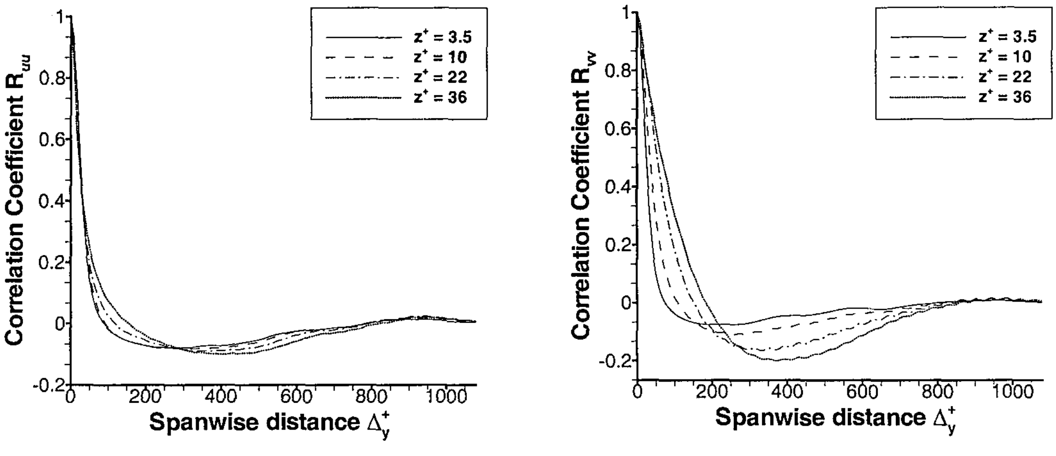

(a) R_{uu}

(b) R_{vv}

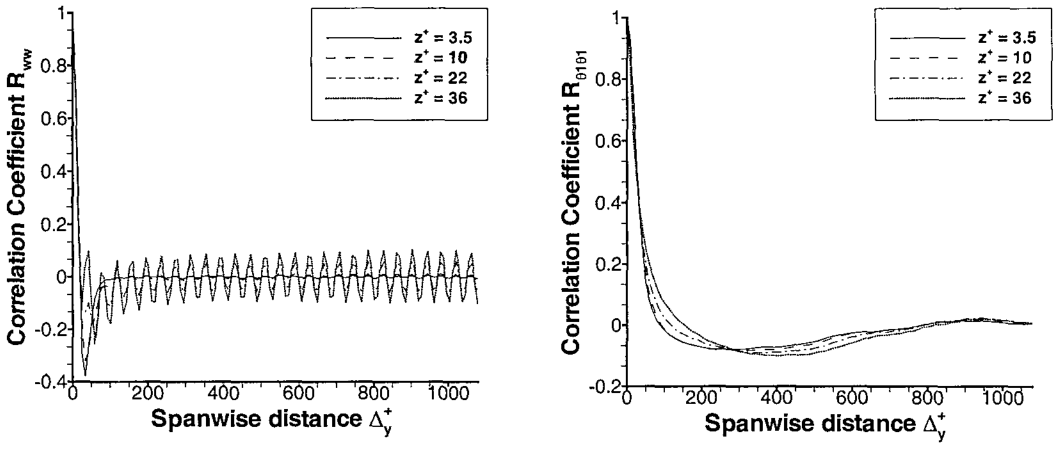

(c) R_{ww}

(d) $R_{\theta_1\theta_1}$

Figure 5.3: Statistically averaged correlation coefficients R_{uu}, R_{vv}, R_{ww} and $R_{\theta_1\theta_1}$ at different wall-normal distances

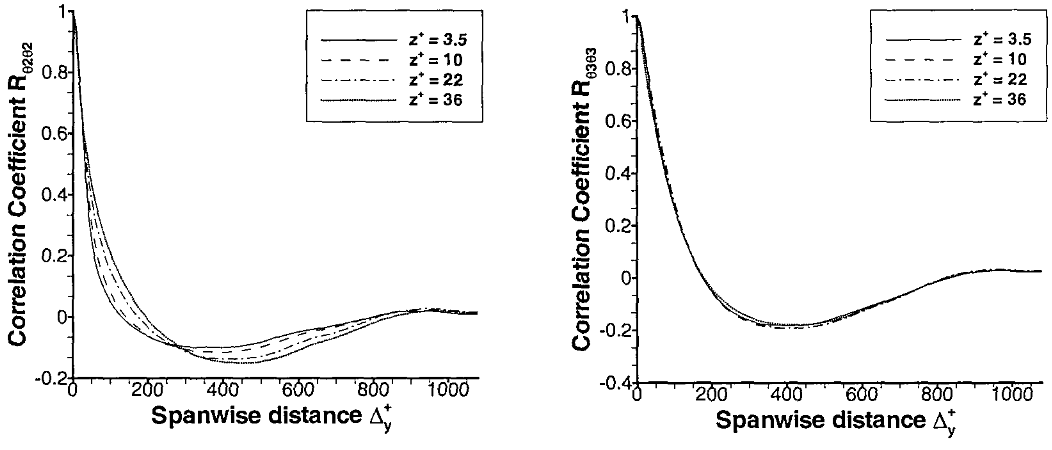

(a) $R_{\theta_2\theta_2}$ (b) $R_{\theta_3\theta_3}$

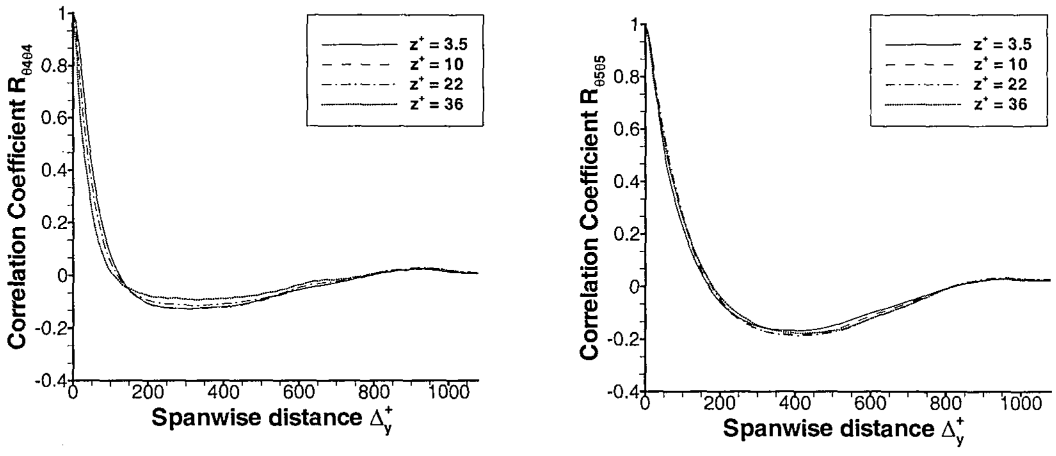

(c) $R_{\theta_4\theta_4}$ (d) $R_{\theta_5\theta_5}$

Figure 5.4: Statistically averaged correlation coefficients $R_{\theta_2\theta_2}$, $R_{\theta_3\theta_3}$, $R_{\theta_4\theta_4}$ and $R_{\theta_5\theta_5}$ at different wall-normal distances

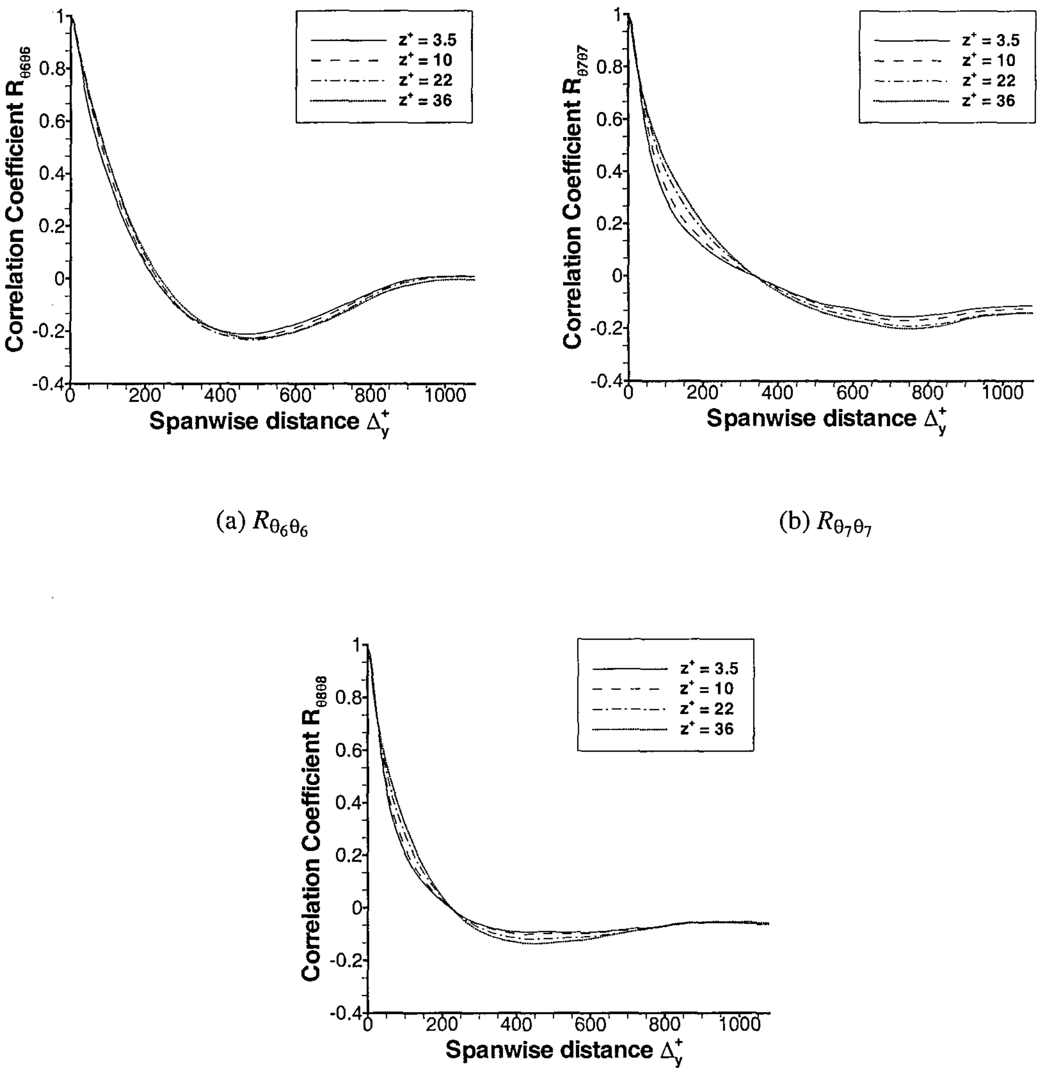

(a) $R_{\theta_6\theta_6}$

(b) $R_{\theta_7\theta_7}$

(c) $R_{\theta_8\theta_8}$

Figure 5.5: Statistically averaged correlation coefficients $R_{\theta_6\theta_6}$, $R_{\theta_7\theta_7}$ and $R_{\theta_8\theta_8}$ at different wall-normal distances

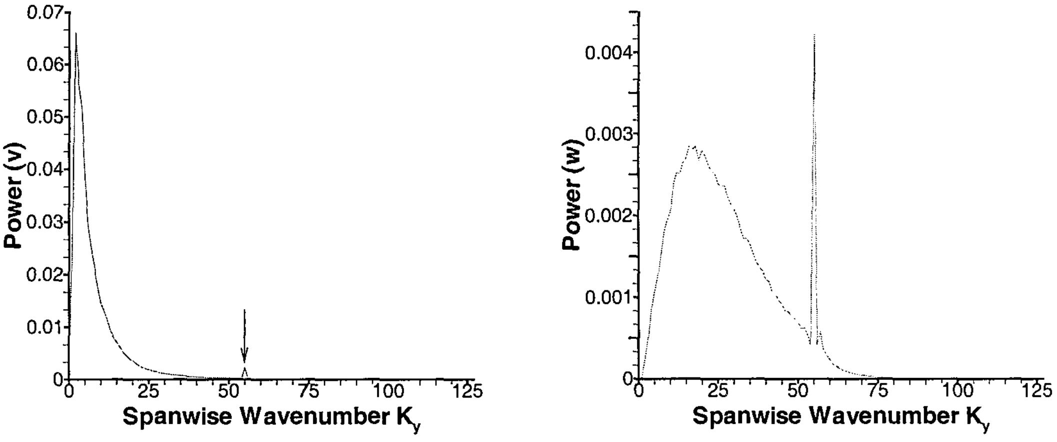

(a) Power (v)

(b) Power (w)

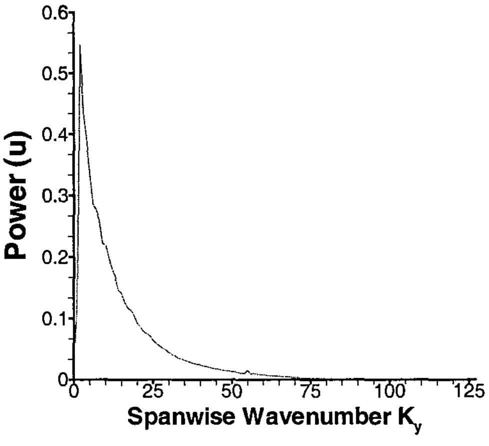

(c) Power (u)

Figure 5.6: Statistically averaged power spectrums of v', w' and u' at a wall-normal distance of $z^+ = 18$

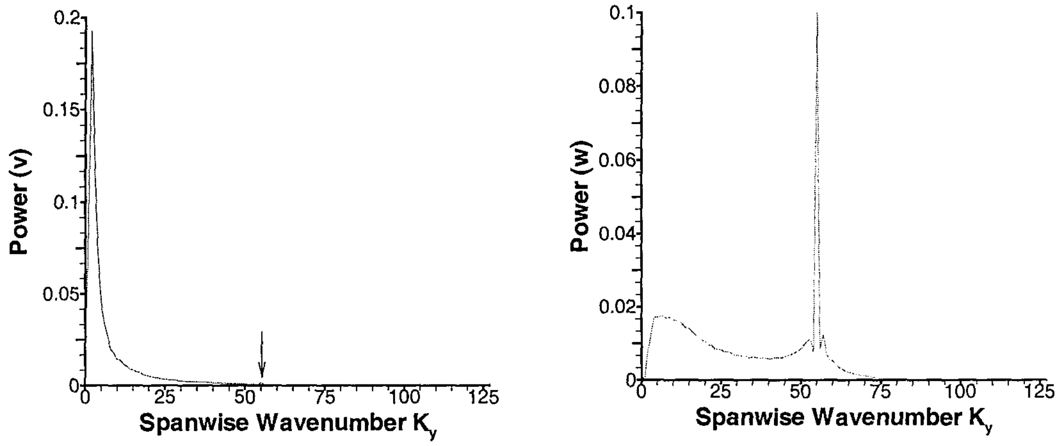

(a) Power (v)

(b) Power (w)

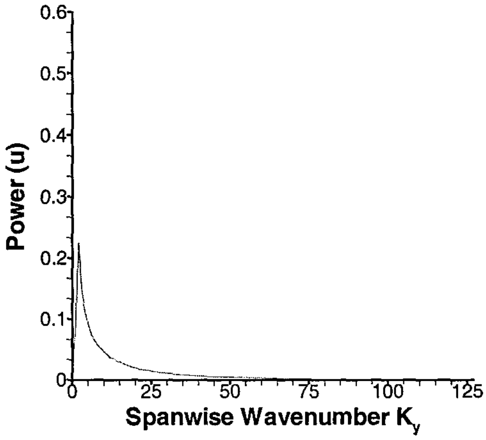

(c) Power (u)

Figure 5.7: Statistically averaged power spectrums of v', w' and u' at a wall-normal distance of $z^+ = 54$

number as well as in shape as can be seen in 5.8(a) and 5.8(b). The second mean scalar profile $\overline{\theta_2}$ is the Reynolds-Tiederman profile chosen by [68] and as its slope is quite similar to the first mean scalar profile, the number of streaks is almost identical as can be seen in 5.8(c).

The third and fourth mean scalar profiles as shown in Figures 5.1(b) have a markedly different slope and the near-wall structures such as low-speed streaks that form are slightly lower in number (3 to 4 streaks) as can be seen in Figures 5.8(d) and 5.9(a). It is important to note that structures that form away from the walls are not being considered as streaks. Similarly for spatial variation of other mean scalar profiles i.e Θ_6 to Θ_8 in Figure 5.9 several structures form near the centre of the channel and few form near the walls and the number of such structures is quite small (1 to 3 streaks). The number of streaks for θ_6 is as low as 2 while for θ_7 we get only 1 streak, thus reinforcing the results of streak spacing obtained from spanwise correlations as shown in Figures 5.5(a) to 5.5(c).

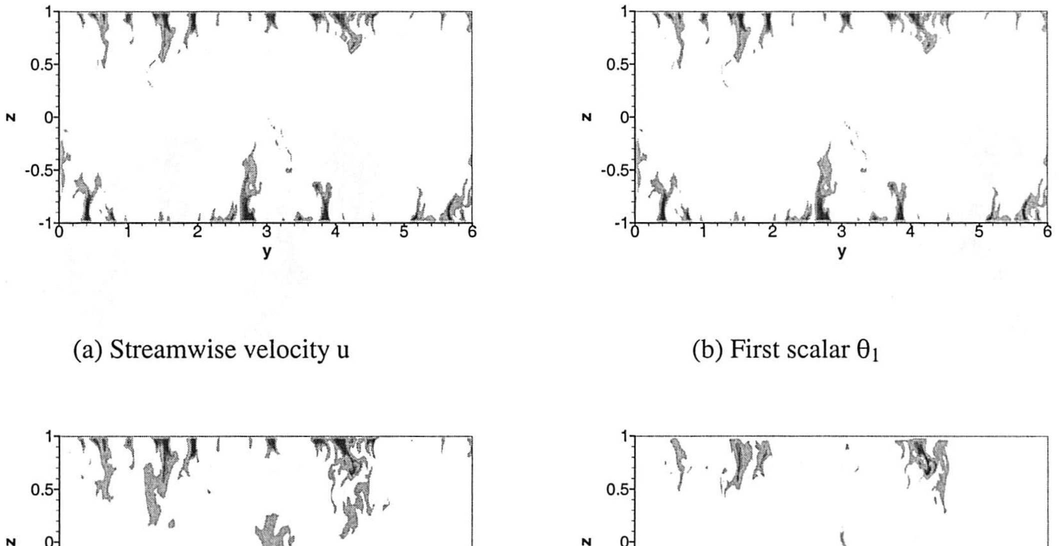

(a) Streamwise velocity u

(b) First scalar θ_1

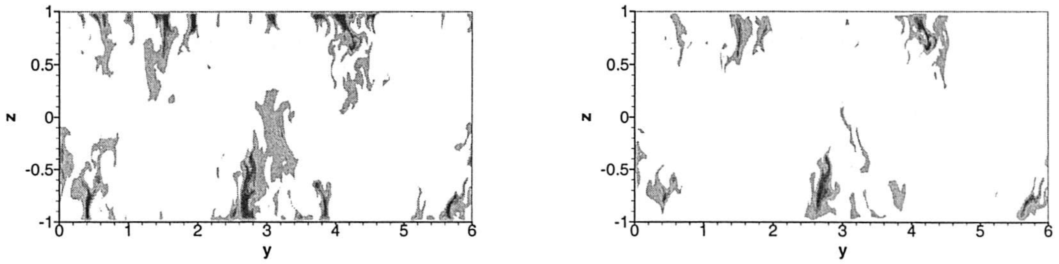

(c) Second scalar θ_2

(d) Third scalar θ_3

Figure 5.8: Spatial cross-flow variation of negative contours of u, θ_1, θ_2 and θ_3 at t=110. In areas marked black the plotted variable is < 0.25 of its minimum negative value.

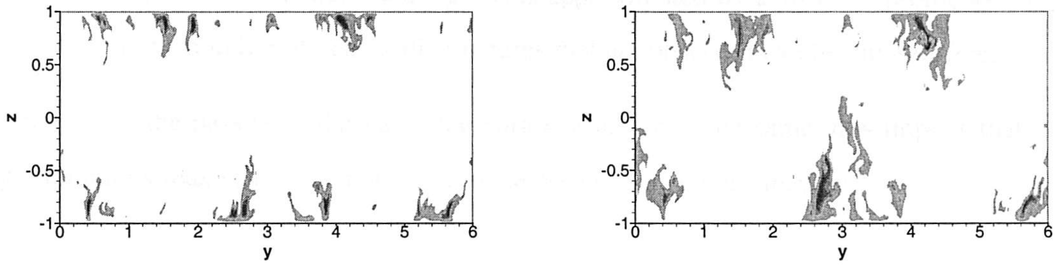

(a) Fourth scalar θ_4

(b) Sixth scalar θ_6

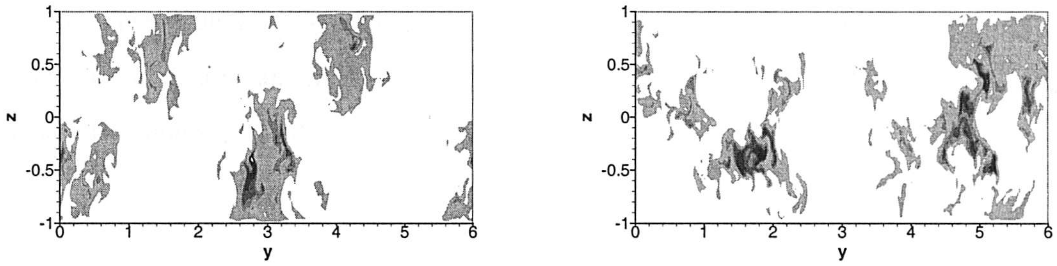

(c) Seventh scalar θ_7

(d) Eighth scalar θ_8

Figure 5.9: Spatial cross-flow variation of negative contours of θ_4, θ_6, θ_7 and θ_8 at t=110. In areas marked black the plotted variable is < 0.25 of its minimum negative value.

5.4 Brief Summary

The above findings can be summarised as follows:

1. If the mean profile of one scalar is approximated by log-law profile from the wall to the centre of the channel, then the number of streaks of that scalar is approximately equal to the number of streaks observed in actual 3D DNS results.
2. If the mean profile of another scalar eg. Θ_3 is approximated by a different profile as stated above, then the number of near-wall structures that are observed can be quite different.
3. Since in all the passive-scalar cases the vortex structure is the same, this implies that the preferential streak spacing is not equal to the preferential vortex spacing.

So we can safely make a deduction that the scalar streak spacing is dependent on scalar mean profile, as it is the case in the optimal perturbation theory. Moreover, the above conclusions clearly exclude the vortex regeneration theories that rely on streak spacing being twice that of vortex spacing. Hence the next logical step in our study is to perform optimal perturbation analysis on the seven independent mean scalar profiles in order to get theoretical scalar streak spacings and then compare the same with DNS results of two-point correlations.

5.5 Theoretical predictions of scalar streak spacing by OP theory

We have computed optimal perturbations for different passive-admixture equations in a turbulent channel flow by assuming the flow can be adequately represented as a laminar flow with different mean scalar profiles as given in section 5.2 for different passive scalars. We can compute maximal energy growths for a range of representative times t^+ and a range of spanwise wavelengths λ^+ using the OP code as explained in section 2.5. Now in order to find which representative time t^+ is optimal time i.e. the time during which the perturbations can grow undisturbed we follow the methodology as proposed by Butler and Farrell [7]. As per Butler and Farrell [7], linear perturbations in laminar flows may grow undisturbed for an unlimited time period but in a turbulent flow the growth is disturbed by small-scale turbulent motions. According to them, the time scale that characterises this disruption is the eddy turnover time τ_e, the ratio of the square of the characteristic turbulent velocity, $q^2 = \overline{u_i u_i}$, to the dissipation rate $\varepsilon = \nu \overline{u_{i,j} u_{i,j}}$ and hence the optimal disturbance development should be limited by a time equal to the eddy turnover time near the wall.

The variation of eddy turnover time as a function of distance from the wall is shown in Figure 4.6(d). This data was obtained from long space-time averaged statistics of our DNS of quasi-2D forced turbulence. From the plot one can easily discern that τ_e first increases linearly outwards from wall and then undergoes an undulation for major portion of buffer layer and after that again starts increasing linearly, albeit with a small slope. Further details regarding how to select the optimal time for any mean scalar or velocity profile are given below.

The first scalar profile is akin to streamwise turbulent velocity profile and the curve fit to this profile is obtained by iteratively changing the coefficients of the Reynolds-Tiederman profile (see eqn. 5.6) till we get the smallest L_2-norm and the profile is then given by eqn. (5.5). For this first mean scalar profile, at five optimization times representative of the eddy turnover times, optimum energy growth has been computed as a function of spanwise wavelength λ_y^+ using the OP code and plotted as shown in Figure 5.11.

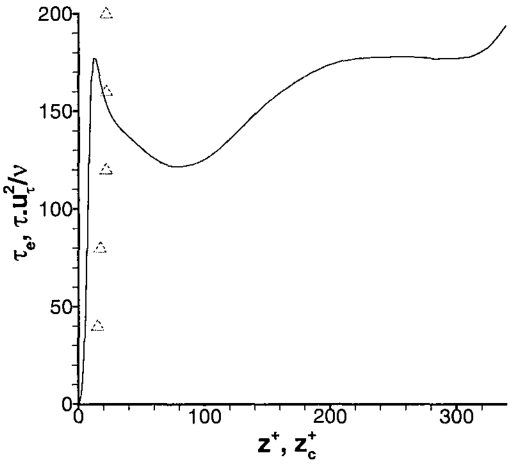

Figure 5.10: Eddy turnover time τ_e versus distance from the wall (—) for quasi-2D randomly forced flow. Also plotted (Δ) is optimal growth time $\tau^+ = \tau u_\tau^2/\nu$ versus location of peak scalar perturbation z_c^+, for the first scalar θ_1.

Corresponding to these optimization times τ^+, wavelengths λ_y^+ can be computed where energy

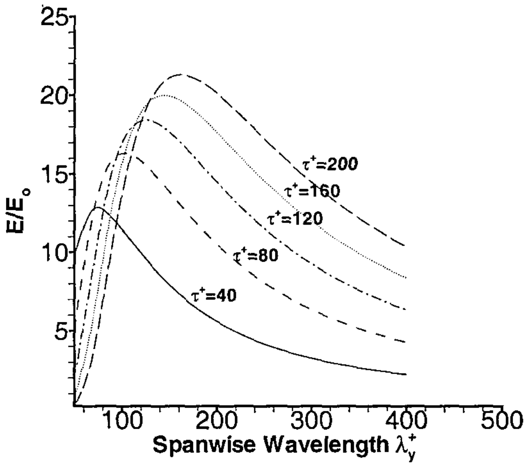

Figure 5.11: Optimal energy growth versus wavelength for optimization times representative of the eddy turnover time for the scalar θ_1.

growth E/E_o maximizes. Knowing τ^+ and λ_y^+ i.e fixing the eigenvalues E/E_o, the corresponding eigenvectors can be computed. The eigenvectors denote the variation of scalar perturbations and from them the wall-normal locations of peak scalar perturbations can be ascertained. These peak scalars corresponding to optimization times of $\tau^+ = 40$, 80, 120, 160 and 200 occur at $z_c^+ = 15$, 17, 20, 22 and 23 respectively and have been plotted as symbols Δ as shown in Figure 5.10.

The optimal time can be determined by comparing $\tau^+ = \tau u_\tau^2/\nu = tRe$ as a function of peak scalar location z_c^+ to eddy turnover time τ_e as function of z^+, as shown in Figure 5.10. Consider the optimal perturbation for τ^+ =200. Figure 5.10 shows that the location of peak scalar streak for this optimal time is z_c^+=23, but the eddy turnover time at z^+=23 is $\tau_e \simeq 160$, so turbulent disruption will not allow the perturbation to reach its full growth. On the other hand, the optimal for τ^+=160 has peak streak velocity at z_c^+=22, where the eddy turnover time is $\tau_e \approx 165$. This perturbation is not highly disrupted over its growth time, although its growth is not as great as that of optimal perturbations with larger τ^+. The best choice of τ^+ occurs near the intersection of these curves corresponding to τ^+ =160. This choice produces spanwise spacing λ_y^+ =140.

The second passive scalar has derivative of mean flow profile as given by eqn. (5.6) and for this profile we get for a range of optimization times varying from $\tau^+ = 40$ to 200, wavelengths λ_y^+ =75, 110, 135, 150 and 165 at which E/E_o peaks. At these specific τ^+ and λ_y^+, we get wall-normal locations of peak scalar perturbations ranging from z_c^+=15 to 29 which have been plotted together with τ_e as a function of distance from the wall in Figure 5.12. For this profile, at five optimization times representative of the eddy turnover times the optimal energy growth has been computed as a function of spanwise wavelength λ_y^+ as shown in Figure 5.13.

The optimization time for this mean flow profile can be determined by comparing τ^+ as a function of peak scalar locations z_c^+ to eddy turnover time τ_e as function of z^+, as shown in Figure 5.12. Similar to the exercise carried out above we find that the best choice of τ^+ occurs near the intersection of the two curves and correspond to τ^+=150 which in turn relates to a optimal spanwise spacing of 140 wall units.

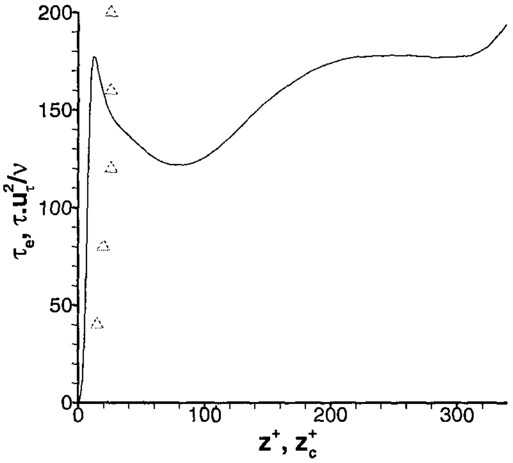

Figure 5.12: Eddy turnover time τ_e versus distance from the wall (—) for quasi-2D randomly forced flow. Also plotted (Δ) is optimal growth time τ^+ versus location of maximum scalar perturbation z_c^+, for the second scalar θ_2.

The third passive scalar has derivative of mean flow profile as given by eqn. (5.7) and for this profile for the range of optimization times τ^+ = 40 to 200, we get wavelengths λ_y^+ =120, 170, 190, 215 and 215 at which E/E_o peak (see Figure 5.15). At these specific τ^+ and λ_y^+ we get wall-normal locations of peak scalar perturbations varying from z_c^+=72 to 78 which have been plotted together with τ_e as a function of distance from the wall in Figure 5.14.

The optimization time for this mean flow profile can be determined by comparing τ^+ as a function of peak scalar location z_c^+ to eddy turnover time τ_e as function of z^+, as shown in Figure 5.14. The best choice of τ^+ occurs near the intersection of the two curves and correspond to τ^+=125 which in turn corresponds to a optimal spanwise spacing of 200.

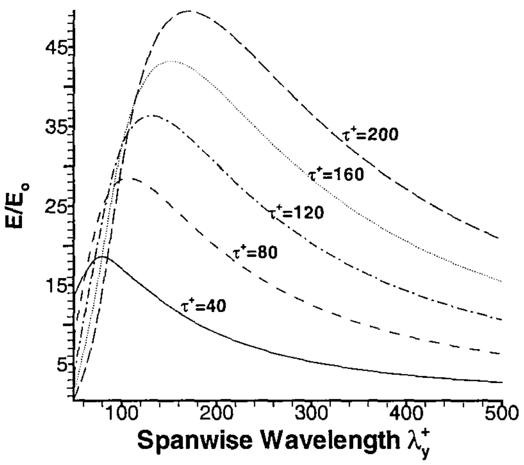

Figure 5.13: Optimal energy growth versus wavelength for optimization times representative of the eddy turnover time near the wall for the scalar θ_2.

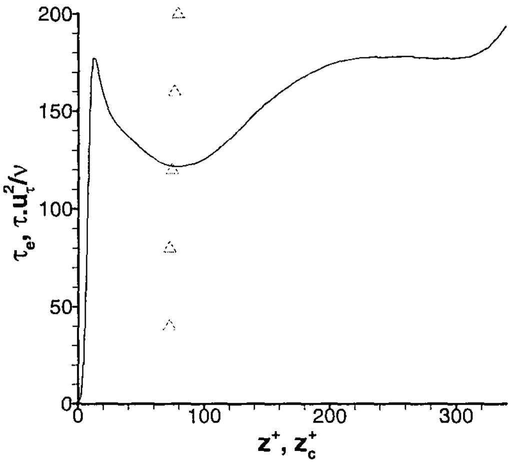

Figure 5.14: Eddy turnover time τ_e versus distance from the wall (—) for quasi-2D randomly forced flow. Also plotted (Δ) is optimal growth time τ^+ versus location of maximum scalar perturbation z_c^+, for the third scalar θ_3.

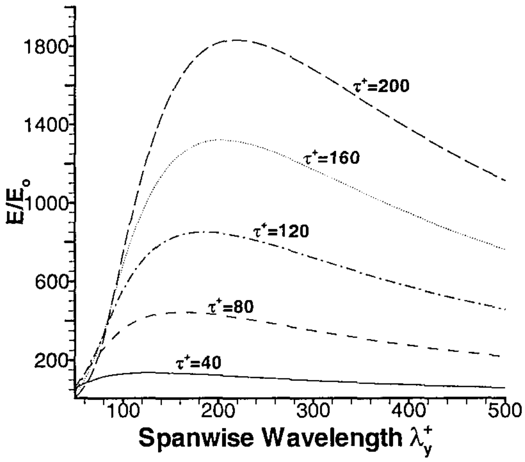

Figure 5.15: Optimal energy growth versus wavelength for optimization times representative of the eddy turnover time for scalar θ_3

The fourth passive scalar has wall-normal derivative of mean flow profile as given by eqn.(5.8) (with different d and w) and for this profile we get for optimization times ranging from $\tau^+ = 40$ to 200, wavelengths λ_y^+=98 to 180 at which maximas of E/E_o occur (see Figure 5.17). At these specific τ^+ and λ_y^+, we get wall-normal locations of peak scalar perturbations varying from z_c^+= 36 to 44 which have been plotted together with τ_e as a function of distance from the wall in Figure 5.16.

The optimization time for this mean flow profile is determined by determining the point of intersection of the two curves as shown in Figure 5.16. The best choice of τ^+ from the figure corresponds to τ^+=135 which gives an optimal spanwise spacing of $\simeq$ 150 wall units.

The fifth passive scalar has wall-normal derivative of mean flow profile given by eqn. (5.9), and is basically a combination of derivatives of second and third scalar mean profiles. For this profile we get for representative optimization times, wavelengths λ_y^+= 120 to 215 at which maximas of E/E_o occur (see Figure 5.19). At these specific τ^+ and λ_y^+, we get wall-normal locations of peak scalar perturbations varying from z_c^+=72 to 76 which have been plotted together with τ_e as a function of distance from the wall in Figure 5.18. It is seen that the optimal time corresponds to τ^+=125 and the corresponding wavelength at which maximum energy growth occurs is $\simeq$ 200 wall units. These values are same as values obtained for third mean scalar profile and so it can be inferred

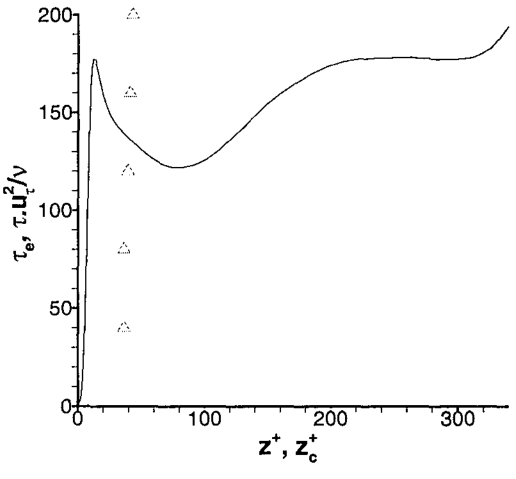

Figure 5.16: Eddy turnover time τ_e versus distance from the wall (—) for quasi-2D randomly forced flow. Also plotted (Δ) is optimal growth time τ^+ versus location of peak scalar perturbation z_c^+, for the fourth scalar θ_4.

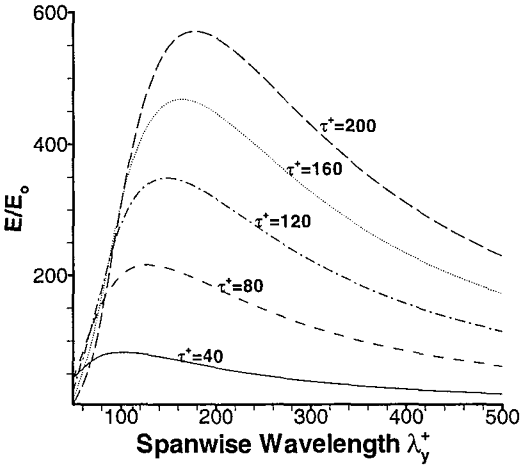

Figure 5.17: Optimal energy growth versus wavelength for optimization times representative of the eddy turnover time near the wall for scalar θ_4.

that similar slope of the mean profile results in no change in spanwise spacing of the streaks.

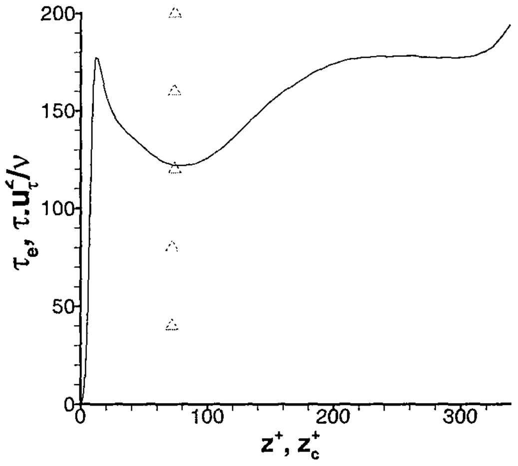

Figure 5.18: Eddy turnover time τ_e versus distance from the wall (—) for quasi-2D randomly forced flow. Also Plotted (Δ) is optimal growth time τ^+ versus location of maximum scalar concentration z_c^+, for the fifth scalar θ_5.

The sixth scalar mean profile as given by eqn. (5.10) is a sinusoidal profile where for the range of optimization times as mentioned above we get a constant spanwise wavelengths $\lambda_y^+ = 400$ for all the representative times, at which the maxima of E/E_o occur (see Figure 5.20). For these specific optimization times and corresponding wavelengths, the wall-normal locations of peak scalar perturbations correspond to z_c^+=135 to 140 which have been plotted together with τ_e as a function of distance from the wall in Figure 5.21. It can be seen from the figure that the two curves intersect at the optimal time corresponding to τ^+=150 which subsequently results in substantially larger spanwise spacing λ_y^+ of 500 wall units.

The seventh scalar mean profile as given by eqn. (5.11) is a three times higher frequency sinusoidal profile compared to sixth mean profile and again for the representative times τ^+ varying from 40 to 200 we get spanwise wavelengths λ_y^+= 320 to 360 at which the maximas of E/E_o occur (see Figure 5.23). For these specific optimization times and corresponding wavelengths, the wall-normal locations of peak scalar concentrations correspond to z_c^+ = 240 to 245. These have been plotted together with τ_e as a function of distance from the wall in Figure 5.22. It can be seen from the figure that as peak scalar locations are 240 wall units, the corresponding near-wall optimal vortices are bigger hence we get corresponding larger spanwise streak spacing of approximately

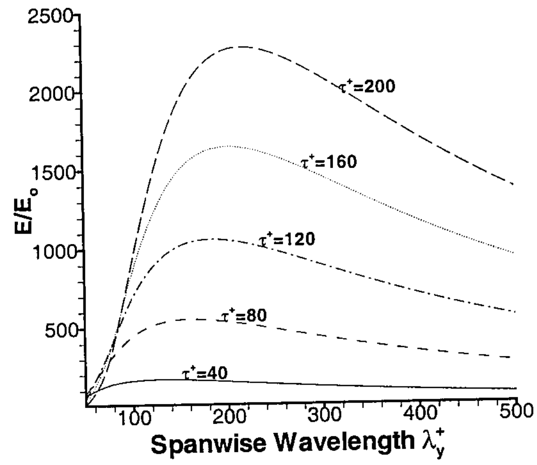

Figure 5.19: Optimal energy growth versus wavelength for optimization times representative of the eddy turnover time near the wall for scalar θ_5.

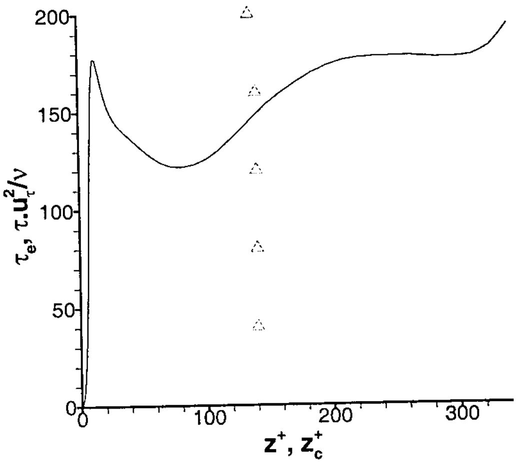

Figure 5.20: Eddy turnover time τ_e versus distance from the wall (—) for quasi-2D randomly forced flow. Also plotted (Δ) is optimal growth time τ^+ versus location of maximum scalar perturbation z_c^+, for the sixth scalar θ_6.

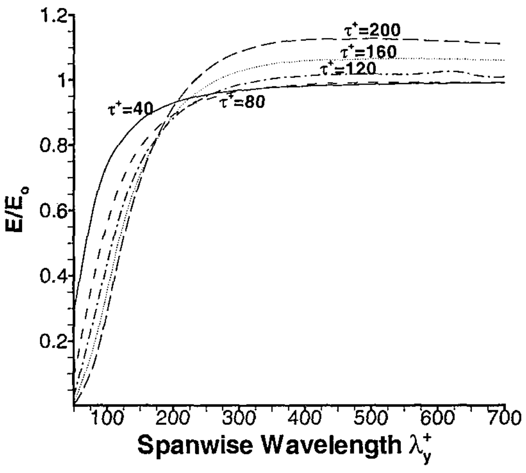

Figure 5.21: Optimal energy growth versus wavelength for optimization times representative of the eddy turnover time near the wall for scalar θ_6.

360 wall units.

The eighth scalar mean profile as given by eqn. (5.12) is a still higher frequency sinusoidal profile, where for similar optimization times as mentioned above we get spanwise wavelengths λ_y^+ ranging from 290 to 350 wall units at which the maximas of E/E_o occur (see Figure 5.24). Due to the larger spanwise wavelengths, the wall-normal locations of peak scalar perturbations also correspond to larger values i.e. z_c^+=285. These have been plotted together with τ_e as a function of distance from the wall in Figure 5.25. It can be seen from the figure that the optimal time is $\tau^+ = 175$ which results in larger λ_y^+ of 380 wall units.

The Table 5.1 shows the optimization times and wavelengths that have been computed corresponding to optimal energy growth for different mean scalar profiles.

The optimal times, respresentative of eddy turnover time, that can be inferred from Figures 5.10 to 5.24 for different mean scalar profiles θ_1 to θ_8 are τ^+ = 160, 150, 125, 135, 125, 150, 175 and 175. These optimization times correspond to optimal wavelengths, representative of streak spacing, λ_y^+ = 140, 140, 200, 150, 200, 500, 360 and 380 wall units. Now the streak spacing of scalars for θ_1 to θ_8 that have been deduced from two-point correlations (at wall-normal height $z^+ = 3.5$) as shown in Figures 5.3 to 5.4 are λ_y^+ = 500, 700, 800, 600, 800, 900, 1500 and 1000 wall units. The results mentioned above are tabulated in Table 5.2.

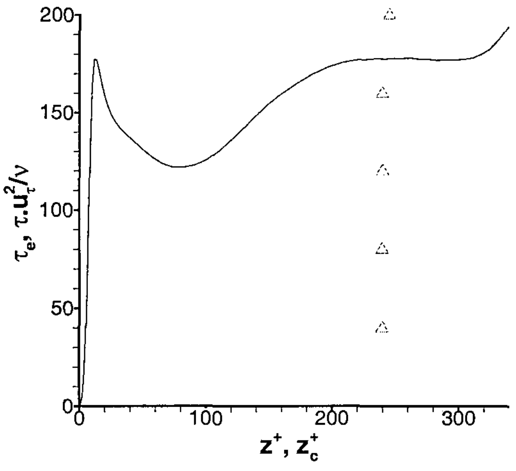

Figure 5.22: Eddy turnover time τ_e versus distance from the wall (—) for quasi-2D randomly forced flow. Also plotted (Δ) is optimal growth time τ^+ versus location of maximum scalar perturbation z_c^+, for the seventh scalar θ_7.

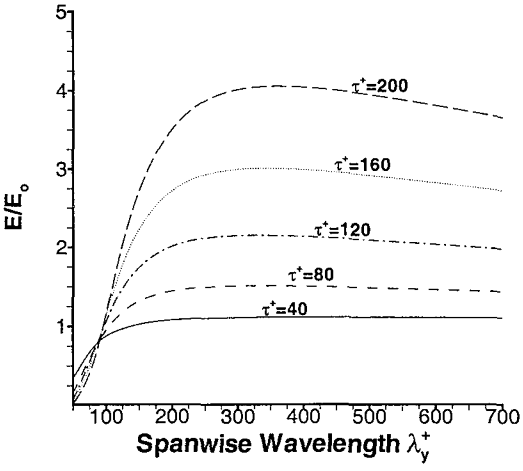

Figure 5.23: Optimal energy growth versus wavelength for optimization times representative of the eddy turnover time near the wall for scalar θ_7.

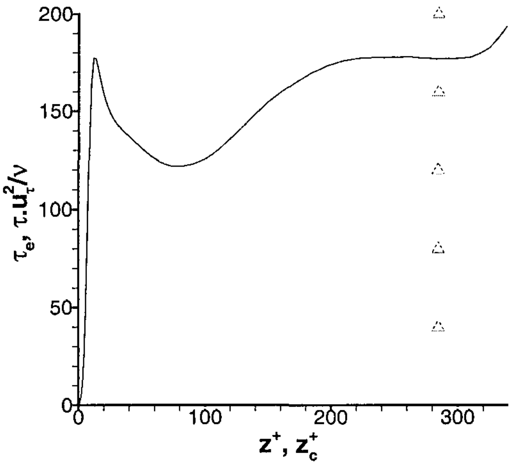

Figure 5.24: Eddy turnover time τ_e versus distance from the wall (—) for quasi-2D randomly forced flow. Also plotted (Δ) is optimal growth time τ^+ versus location of peak scalar perturbation z_c^+, for the eighth scalar θ_8.

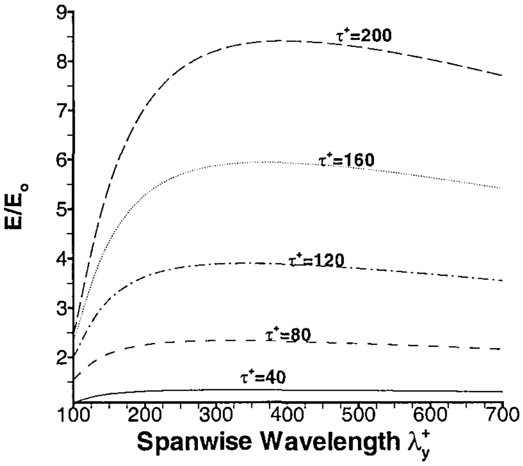

Figure 5.25: Optimal energy growth versus wavelength for optimization times representative of the eddy turnover time near the wall for scalar θ_8.

Scalar	optimization time range	optimal wavelength range	Peak scalar location z_c^+	optimal τ^+	optimal λ_y^+
θ_1	40-200	70-160	15-22	160	140
θ_2	40-200	75-165	15-29	150	140
θ_3	40-200	120-215	72-78	125	200
θ_4	40-200	100-180	36-44	135	150
θ_5	40-200	120-215	72-76	125	200
θ_6	40-200	450-550	135-140	150	500
θ_7	40-200	360-400	240	175	360
θ_8	40-200	340-420	285	175	380

Table 5.1: Representative times and wavelength ranges corresponding to maximum energy growth for various mean scalar profiles. Also shown are the locations of peak scalar perturbations z_c^+ for different optimization times τ^+. Last two columns show the most optimal times τ^+ on basis of eddy turnover time and corresponding optimal wavelengths λ_y^+ representative of streak spacing.

5.6 Linear combination of mean scalar profiles

The above results show that for the mean scalar profiles considered above the streak spacing varies from 500 to 1500 wall units. Additional new mean profiles Θ_{ni} were generated as combinations of the above six basic mean scalar profiles (Θ_2, Θ_3, Θ_4, Θ_6, Θ_7 and Θ_8). Since the equations for the passive scalar are linear, a linear combination of several solutions is a solution. If $\theta = \sum_{i=1}^{i=n} X_i\theta_i$ then the averaged profile of the passive scalar is

$$\bar{\theta} = \langle\theta\rangle = \sum_{i=1}^{i=n} X_i\langle\theta_i\rangle = \sum_{i=1}^{i=n} X_i\bar{\theta}_i \tag{5.14}$$

The two-point autocorrelation function for the new profiles can be calculated as

$$R_{\theta,\theta}(\Delta) = \sum_{i=1,j=1}^{i=1n,j=n} X_iX_jR_{\theta_i,\theta_j}(\Delta) \tag{5.15}$$

Therefore, by solving simultaneously several passive scalar equations with different source terms and calculating the cross-correlations $R_{\theta_i\theta_j}(\Delta)$ we can easily calculate the auto-correlation and hence the streak spacing, provided we know the vector of coefficients X_i. Thus we sought for such a vector $(X_1,\ldots,X_n)$ of unit length that the corresponding auto-correlation function is as small as

Scalar	Streak spacing DNS at z^+=3.5	Streak spacing Nikitin and Chernyshenko [38]	Streak spacing Butler and Farrell [7]
θ_1	500	310	140
θ_2	700	310	140
θ_3	800	310	200
θ_4	600	310	150
θ_5	800	310	200
θ_6	900	310	500
θ_7	1500	310	360
θ_8	1000	310	380

Table 5.2: Comparison of streak spacing from DNS results of two-point correlations of randomly forced quasi-2D turbulence, from RNSAI mechanism and from OP theory.

possible at the specific value of $\Delta = \Delta_0$. For this first we have to normalise the auto-correlation function (5.15) by $R_{\theta\theta}(0)$ and then seek for $\Delta = \Delta_0$ at which the minima of this function appears. This leads to a minimisation problem for the functional

$$\sum_{i=1,j=1}^{i=n,j=n} X_iX_j(R_{\theta_i,\theta_j}(\Delta_0)) - \lambda\left(\sum_{i=1,j=1}^{i=n,j=n} X_iX_jR_{\theta_i,\theta_j}(0) - 1\right) \to min \tag{5.16}$$

Here λ is the Lagrange multiplier for the condition that $(X_1,\ldots,X_n)$ has a unit length. The above formulation can be recast to a standard linear eigenvalue problem. The eigenvalues of the above optimization problem provide minimum values of $R_{\theta_i\theta_i}(\Delta_0)$ while the eigenvectors $\bar{X}$ provide the coefficients of the new mean scalar profile Θ_n. It is found during this process of linear combination that the minimum of the auto-correlation function does not exactly coincide with Δ_0, but in practice Δ_0 and Δ_{min} turn out be close within a reasonable range of Δ_0. The computed eigenvectors for the five new mean scalar profiles have been tabulated in Table 5.3. Out of the six eigenvalues we always chose the one giving the smallest value of $R_{\theta\theta}(\Delta_0)$ and its corresponding eigenvectors were selected. The cross-correlations values that have been used in the computations were calculated at a distance $z^+ = 3.5$ from the wall. Using this modified technique five new mean scalar profiles, which we denote $\Theta_{n1},\ldots,\Theta_{n5}$ have been computed.

The location of the first minima Δ_0 for these five new profiles varies from 0.123, 0.295, 0.652, 1.31 and 2.10 giving a corresponding streak spacing λ_y^+= 85, 210, 470, 945 and 1515 wall units.

mean scalar	X_1	X_2	X_3	X_4	X_5	X_6
Θ_{n1}	0.09507	0.001095	0.002242	-0.98364	-0.142724	-0.055096
Θ_{n2}	-0.02708	-0.02732	0.05651	0.98226	0.16869	0.045099
Θ_{n3}	0.05671	0.034597	-0.067894	0.71535	0.62507	0.29754
Θ_{n4}	-0.01010	0.00223	0.04096	0.72825	-0.47060	-0.49637
Θ_{n5}	0.012068	0.014927	-0.025696	0.44900	-0.68640	0.57115

Table 5.3: Eigenvectors of the new mean scalar profiles computed using linear combination technique.

The two-point autocorrelations of the five new profiles can be seen from Figure 5.26. The shape of the new five mean scalar profiles Θ_{ni} which have increasing two-point correlations can be seen in Figure 5.27.

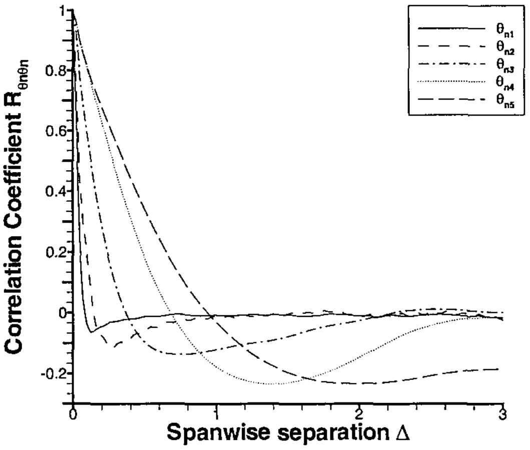

Figure 5.26: Wall-normal variation of two-point auto-correlation coefficients $R_{\theta_{n1}\theta_{n1}}(\Delta)$, $R_{\theta_{n2}\theta_{n2}}(\Delta)$, $R_{\theta_{n3}\theta_{n3}}(\Delta)$, $R_{\theta_{n4}\theta_{n4}}(\Delta)$ and $R_{\theta_{n5}\theta_{n5}}(\Delta)$ for the new five profiles.

For the first new mean scalar profile its derivative (as required by the OP theory) can be determined using derivatives of six mean scalar profiles together with the relevant coefficients obtained through eigenvectors $\bar{X}$ of the minimisation problem. For this profile for the range of representative times varying from τ^+ = 40 to 200, we get wavelengths λ_y^+ =60, 110, 120, 120 and 120 at which E/E_o peak (see Figure 5.28). At these specific τ^+ and λ_y^+, we get wall-normal locations of peak scalar perturbations as z_c^+=12 to 22 which have been plotted together with τ_e as a function of distance z^+ from the wall in Figure 5.29. It can be found from Figure 5.29 that the optimal time

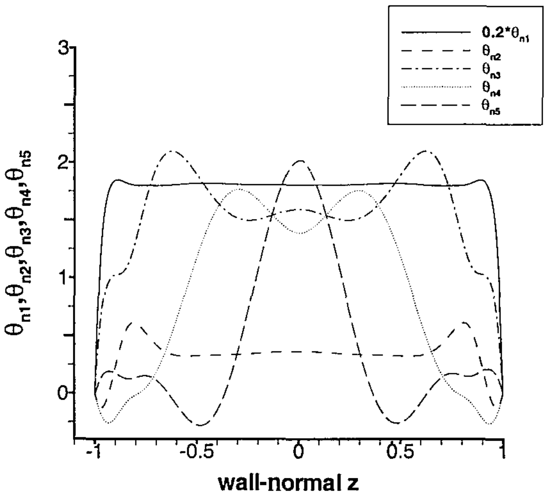

Figure 5.27: Wall-normal variation of new profiles θ_{n1}, θ_{n2}, θ_{n3}, θ_{n4} and θ_{n5}.

corresponds to τ^+=160 and corresponding wavelength at which optimal energy growth occurs is $\simeq$ 120 wall units.

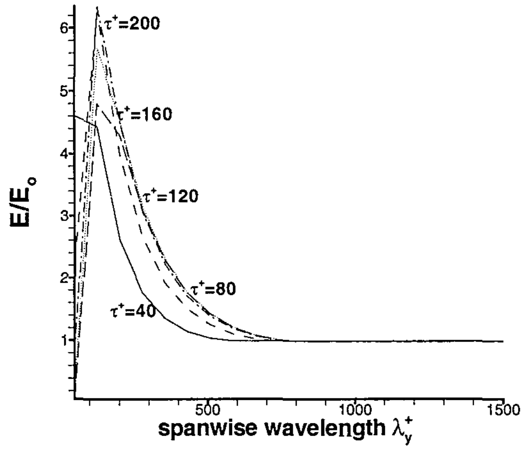

Figure 5.28: Optimal energy growth versus wavelength for optimization times representative of the eddy turnover time near the wall for scalar θ_{n1}.

The second new scalar profile can be constructed using the derivatives of the six basic mean profiles together with the coefficients obtained as eigensolution of the minimisation problem. For this profile for the range of optimization times varying from τ^+ = 40 to 200 in steps of 40, we get wavelengths λ_y^+ =180, 180, 190, 200 and 200 at which E/E_o peaks (see Figure 5.30). At these specific τ^+ and λ_y^+, we get wall-normal locations of peak scalar perturbations z_c^+ ranging from 38

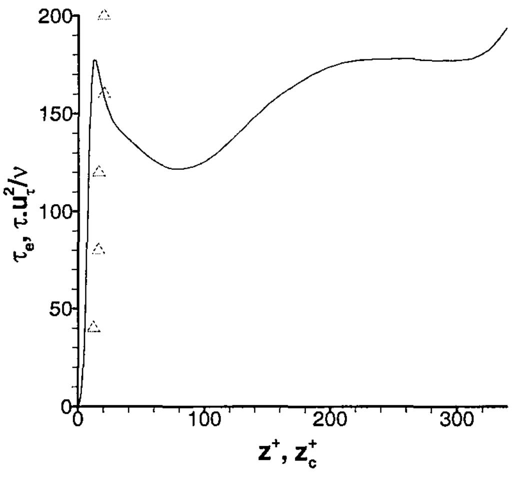

Figure 5.29: Eddy turnover time τ_e versus distance from the wall (—) for quasi-2D randomly forced flow. Also plotted (Δ) is optimal growth time τ^+ versus location of peak scalar perturbation z_c^+, for the new scalar θ_{n1}.

to 40 wall units which have been plotted together with τ_e as a function of distance from the wall in Figure 5.31. From the figure one can easily ascertain that the optimal time corresponds to τ^+=140 and the corresponding wavelength at which optimal energy growth occurs is $\simeq$ 200 wall units.

The third new scalar mean profile for the similar optimization times as mentioned above has spanwise wavelengths λ_y^+ ranging from 200 to 220 wall units at which the maximas of E/E_o occur (see Figure 5.32). For these specific optimization times and corresponding wavelengths, the wall-normal locations of peak scalar perturbations correspond to z_c^+= 80 which have been plotted together with τ_e as a function of distance from the wall in Figure 5.33. The corresponding optimal time is τ^+ =120 and the resulting optimal streak spacing is λ_y^+=220 wall units.

The fourth new scalar mean profile for the optimization times τ^+ ranging from 40 to 200 has spanwise wavelengths λ_y^+ varying between 220 to 280 wall units at which the maximas of E/E_o occur (see Figure 5.34). For these specific optimization times and corresponding wavelengths, the wall-normal locations of peak scalar perturbations correspond to z_c^+=160 which have been plotted together with τ_e as a function of distance from the wall in Figure 5.35. The corresponding optimal time is τ^+ =160 and the resulting optimal streak spacing is λ_y^+=280 wall units.

For the fifth new passive scalar profile, we get for the range of optimization times τ^+ = 40 to 200,

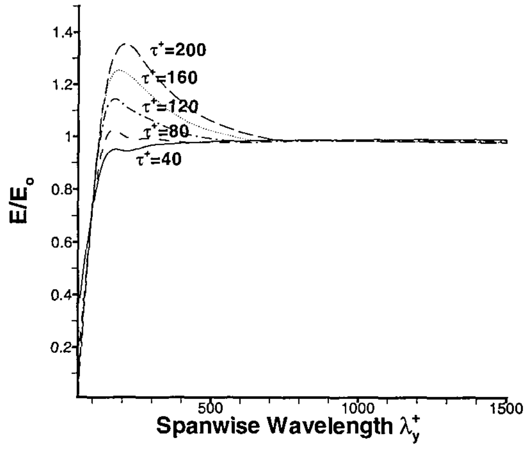

Figure 5.30: Optimal energy growth versus wavelength for optimization times representative of the eddy turnover time near the wall for scalar θ_{n2}.

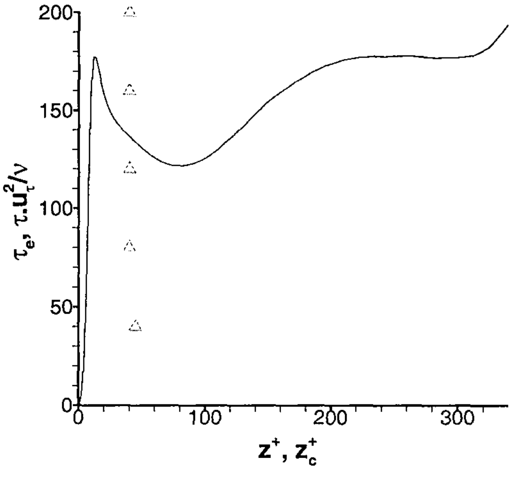

Figure 5.31: Eddy turnover time τ_e versus distance from the wall (—) for quasi-2D randomly forced flow. Also plotted (Δ) is optimal growth time τ^+ versus location of peak scalar concentration z_c^+, for the new scalar θ_{n2}.

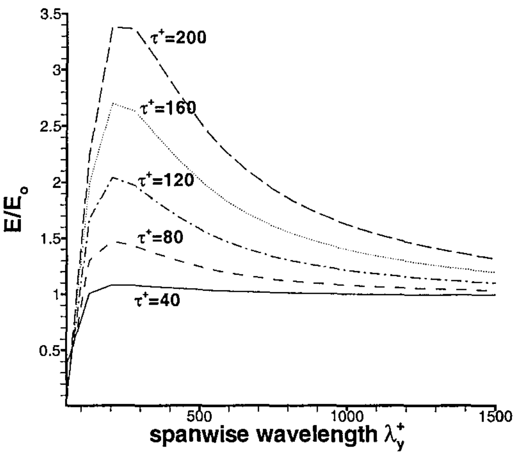

Figure 5.32: Optimal energy growth versus wavelength for optimization times representative of the eddy turnover time near the wall for scalar θ_{n3}.

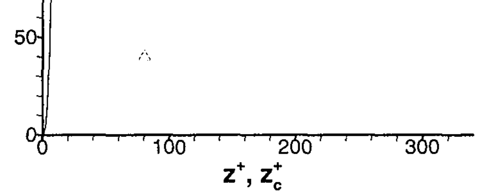

Figure 5.33: Eddy turnover time τ_e versus distance from the wall (—) for quasi-2D randomly forced flow. Also plotted (Δ) is optimal growth time τ^+ versus location of maximum scalar concentration z_c^+, for the new scalar θ_{n3}.

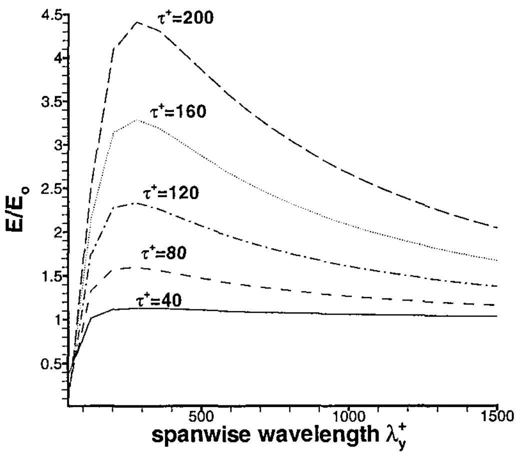

Figure 5.34: Optimal energy growth versus wavelength for optimization times representative of the eddy turnover time near the wall for scalar θ_{n4}.

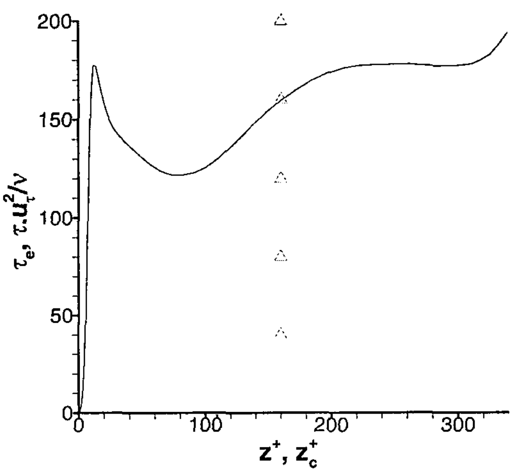

Figure 5.35: Eddy turnover time τ_e versus distance from the wall (—) for 2D randomly forced flow. Also plotted (Δ) is optimal growth time τ^+ versus location of maximum scalar concentration z_c^+, for the new scalar θ_{n4}.

wavelengths λ_y^+= 280 to 350 at which maximas of E/E_o occur as can be seen from Figure 5.36. At these specific τ^+ and λ_y^+, we get wall-normal locations of peak scalar perturbations as z_c^+=280 which have been plotted together with τ_e as a function of distance from the wall in Figure 5.37. It is seen that the optimal time corresponds to τ^+=175 and corresponding wavelength (i.e. streak spacing) at which optimal energy growth occurs is $\simeq$ 350 wall units.

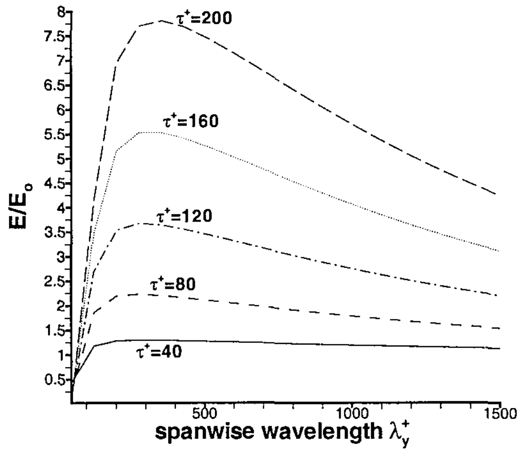

Figure 5.36: Optimal energy growth versus wavelength for optimization times representative of the eddy turnover time near the wall for scalar θ_{n5}.

The optimal times representative of eddy turnover time, that can be inferred from Figures 5.28 to 5.37 for different new mean scalar profiles θ_{n1} to θ_{n5} are namely τ^+ = 160, 140, 120, 160 and 175. These optimization times correspond to optimal wavelengths, representative of streak spacing, λ_y^+ = 120, 200, 220, 280 and 350 wall units. But the streak spacing of scalars for θ_{n1} to θ_{n5} that have been deduced from two-point correlations (at wall-normal height $z^+ = 10$) as shown in Figure 5.27 are λ_y^+ = 90, 210, 470, 945 and 1515 wall units. The results mentioned above are tabulated in Table 5.4 and a graphical visualisation of the same can be seen from Figure 5.38.

The spatial visualisation of low-speed streaks for new profiles θ_{n1} to θ_{n5} can be seen in Figures 5.39 to 5.40. It can be seen from the figures that as two-point autocorrelation increases from λ_y^+ = 90 to 1515 the number of streaks decreases from almost 20 to just 1.

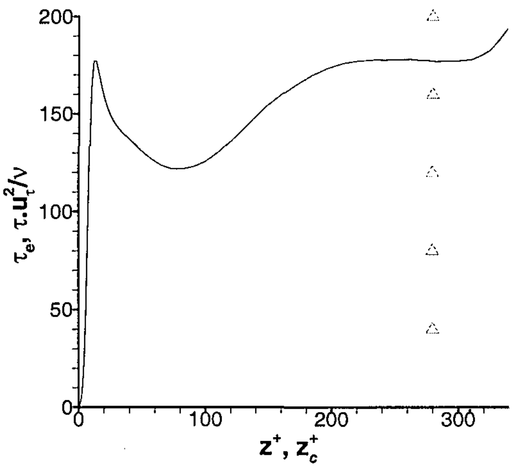

Figure 5.37: Eddy turnover time τ_e versus distance from the wall (—) for quasi-2D randomly forced flow. Also plotted (Δ) is optimal growth time τ^+ versus location of peak scalar concentration z_c^+, for the new scalar θ_{n5}.

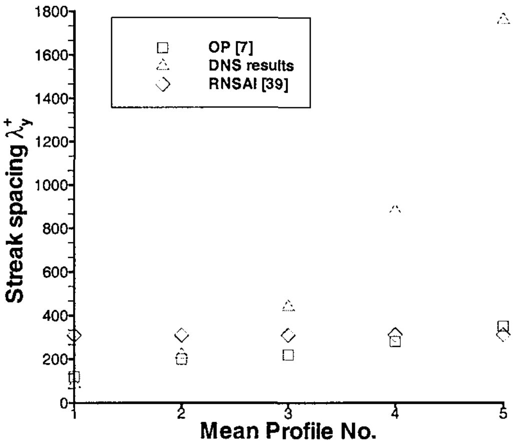

Figure 5.38: Comparison of streak spacing as computed using DNS of quasi-2D forced turbulence, RNSAI mechanism [38] and OP theory [7].

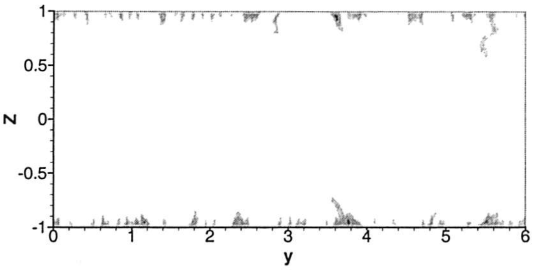

(a) For λ_y^+=90

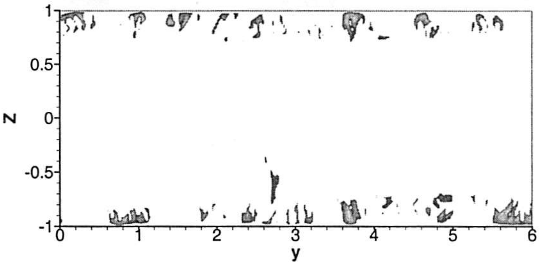

(b) For λ_y^+=210

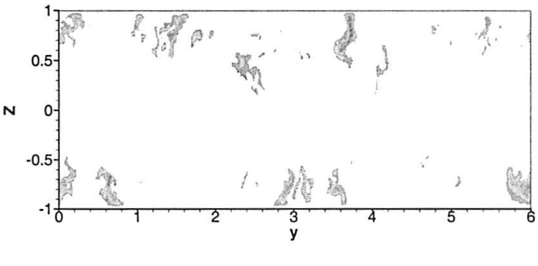

(c) For λ_y^+=470

Figure 5.39: Spatial variation of negative passive scalar concentrations θ'_{ni} for new scalar profiles θ_{n1}, θ_{n2} and θ_{n3}. In areas marked black the plotted variable is < 0.25 of its minimum negative value.

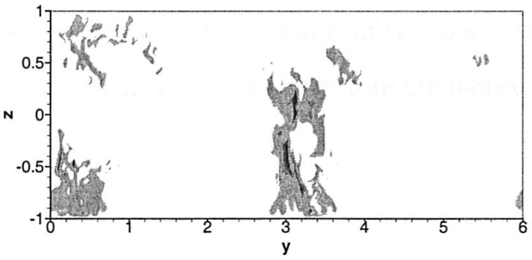

(a) For λ_y^+=945

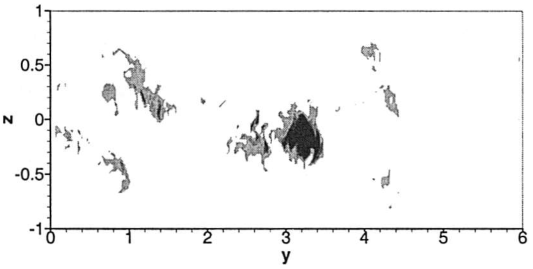

(b) For λ_y^+=1515

Figure 5.40: Spatial variation of negative passive scalar concentrations θ'_{ni} for new scalar profiles θ_{n4} and θ_{n5}. In areas marked black the plotted variable is < 0.25 of its minimum negative value.

Scalar	Streak spacing DNS	Streak spacing RNSAI [38]	Streak spacing OP theory [7]
θ_{n1}	90	310	120
θ_{n2}	210	310	200
θ_{n3}	470	310	220
θ_{n4}	945	310	280
θ_{n5}	1515	310	350

Table 5.4: Comparison of streak spacing from DNS results of two-point correlations of randomly forced quasi-2D turbulence, from RNSAI mechanism and from OP theory.

5.7 Conclusions

In light of the above results the following conclusions can be drawn:

1. The RNSAI mechanism [38] yields a constant streak spacing and thus is not likely the candidate which can explain the variation of streak spacing with different mean scalar profiles. Theories which assume the streak spacing being equal to twice the vortex spacing and that includes all the vortex regeneration theories, cannot explain this fact.

2. The streak spacings for different scalar profiles obtained on basis of DNS results from two-point correlation differ considerably from streak spacings obtained using theoretical predictions of OP theory. So qualitatively there is a similarity between DNS results and results of OP theory but quantitatively it is not so.

3. The major finding of the above numerical experimentation is that a new theory needs to be proposed which incorporates the elements of OP theory but should give better quantitative predictions.

Chapter 6

PASSIVE SCALAR STREAKS IN 3D TURBULENT CHANNEL FLOWS

6.1 Introduction

The conclusions of the previous study of quasi-2D forced turbulence with the passive scalars clearly showed that there can be an order of magnitude change in streak spacing of the scalars even when the vortical structure of the flow is held fixed. Moreover, the findings of the nonmodal analysis based on optimal perturbation theory explicitly favour the view that the streak spacing depends on the mean velocity profile. Therefore, the next logical step is to check whether for 3D turbulent flows the variation of the mean profile strongly affects the streak spacing even when the vortex structure (created by the velocity field) is held fixed. In order to achieve this goal, we intend to work again with passive scalars so that mean velocity profile is held constant while the mean scalar profiles are altered.

DNS with passive scalars was first performed by Kim and Moin [32] and as they had mean scalar profile similar to that of mean velocity profile, the scalar streaks that developed had almost same streak spacing as that of velocity streaks. Kasagi, Tomita and Kuroda [29] also found the existence of temperature streaks in their DNS study when they considered temperature as the passive scalar by neglecting the buoyancy effects. They came to the conclusion that velocity and temperature fluctuations had a close correlation especially in the near-wall region. In order to study streak spacing of the scalars, a similar procedure as described in chapter 5 has been followed for 3D turbulent channel flows and we have solved several convection-diffusion equations each having a different source term in order to regulate the distribution of a passive scalar. The governing equation for the passive scalars is

$$\frac{\partial \theta_i}{\partial t} + \mathbf{u}.\nabla\theta_i = \frac{1}{RePr}\nabla^2\theta_i + S_i(z) \tag{6.1}$$

where the source terms $S_i(z)$ describe a given rate of production of the passive scalar. The passive scalars can be considered as chemical species being produced due to a chemical reaction (the source). The Prandtl (or Schmidt) numbers for the passive scalars is taken as unity. The boundary condition for equation (6.1) is given by zero concentration of passive scalars at the solid walls.

$$\theta_i(\pm 1) = 0$$

The initial passive scalar fields have a specified mean profile for each scalar and we have solved eight passive-scalar equations simultaneously with the Navier-Stokes equations in our simulation and each solution will then correspond to exactly the same vortex structure. This allows one to isolate the influence of the shape of the mean profile on the streak spacing. Out of the eight scalar mean profiles, one profile Θ_5 (as mentioned in chapter 5) is a linear combination of others and is used for validation purposes. Therefore, the results are for seven independent scalar mean profiles or basic profiles. We have taken for the first scalar profile the source term $S_1(z) = -1$ and hence the equations for u and θ_1 only differ in the term $\partial p'/\partial x$. The next three profiles have their shapes defined via their derivatives with respect to z and are expressed mathematically by eqns. (5.6-5.8) while mean scalar profiles Θ_6 to Θ_8 are trigonometric functions given by eqns. (5.10-5.12).

6.2 Numerical Simulation

The calculations were performed at $Re_\tau = 360$ in a computational box of the size $L_x \times L_y \times L_z = 6 \times 3 \times 2$ using 64 complex Fourier modes in spanwise y and streamwise x directions and 160 Chebyshev modes in the wall-normal z direction. The smallest scales that can be resolved are $\Delta x^+ = 16.8$, $\Delta y^+ = 8.4$ and $\Delta z^+ = 0.07$. The validation of the modified pseudo-spectral code [47] was performed on the same lines as has been mentioned in chapter 4 to ensure the reliability of the results. The eight passive scalar equations were solved simultaneously with the Navier-Stokes equations. Regarding the initial conditions, the mean streamwise velocity u is given by linear profile till $z^+ = 10$ and log-law profile till the centre of the channel, while v' and w' are generated by the "random eddy" model as explained in chapter 3. The three-dimensionality in the run sets in due to inherent instability of the flow. The initial conditions for all the passive scalars except the first scalar were the prescribed mean scalar profiles. The mean pressure gradient $\overline{dP}/dx$ is explicitly prescribed to be -1. As the simulation progresses all the flowfield soon becomes spatio-temporally chaotic and by the time $t = 12.0$ approximately the flow becomes fully-developed turbulent channel flow. The flag is then turned on to perform statistical averaging and the statistics gathered with time and space-averaging performed in streamwise and spanwise directions till $t =$ 39.7

The statistically averaged values of $\langle v'^2 \rangle$, $\langle w'^2 \rangle$ and Q=$\langle v'^2 - w'^2 \rangle$ can be seen in Figures 6.1(a) to 6.1(b). These results are well in consonance with DNS results of Hu and Sandham [20] [21] who performed their simulation at the same Re=360 but in a larger computational box. The statistically averaged values of $\bar{u}$, $\bar{v}$ and $\bar{w}$ can be seen from the Figure 6.2(a). Though it is not clearly seen in the figure it is found that $\bar{v}$ is approximately ± 0.03 while $\bar{w}$ is of the order of 10^{-7}. The mean turbulent kinetic energy TKE $\overline{u_i'u_i'}$ vs z profile can be seen from Figure 6.2(b) and it shows a peaked variation near the walls which gradually reduces to small value at the centre of the channel. The spatial variation of mean turbulent dissipation ε (see section 4.4) shows its confinement to the viscous layer as can be seen from Figure 6.2(c). The eddy turnover time which characterises the ratio of TKE/ε shows a profile (see 6.2(d)) which has a monotonic increase as we proceed from the wall to the centre of the channel. The eddy turnover time has largest positive slope in the very near-wall region while the slope becomes smaller as we proceed to the outer region.

The first mean scalar $\Theta_1 = \overline{\theta_1}$ is such that the source term $S = -1$ and then the only difference between the equations for u and Θ_1 is in the term $\partial p'/\partial x$. Calculations show that this term is insignificant. The mean value of θ_1 is only different by 2.9% at the channel symmetry plane with the mean value of u. In order to find an analytical expression for Θ_1, curve fitting has been performed on statistically averaged profile of Θ_1 by iteratively changing the coefficients of the Reynolds-Tiederman profile (see $g(z, Re)$ in eqn.(5.6)) till we get minimum L_2 norm for Θ_1 data

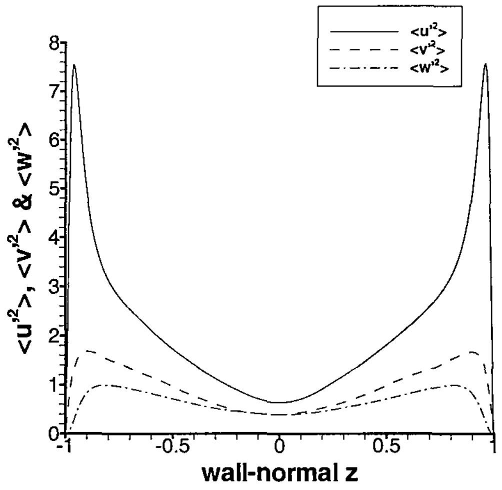

(a) Streamwise, spanwise and wall-normal velocity fluctuations $\bar{u'^2}$, $\bar{v'^2}$ and $\bar{w'^2}$

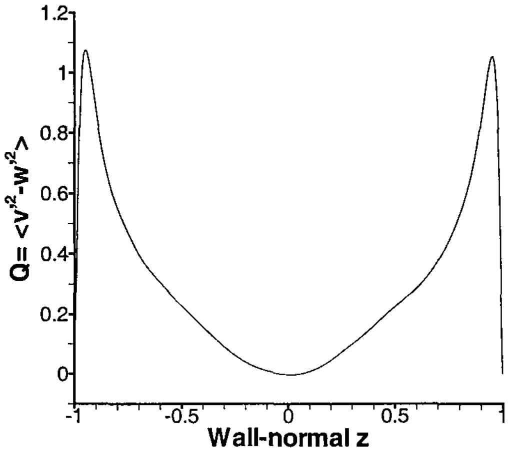

(b) Reynolds normal stresses difference Q

Figure 6.1: Statistically averaged variation of $\bar{u'^2}$, $\bar{v'^2}$, $\bar{w'^2}$ and Q

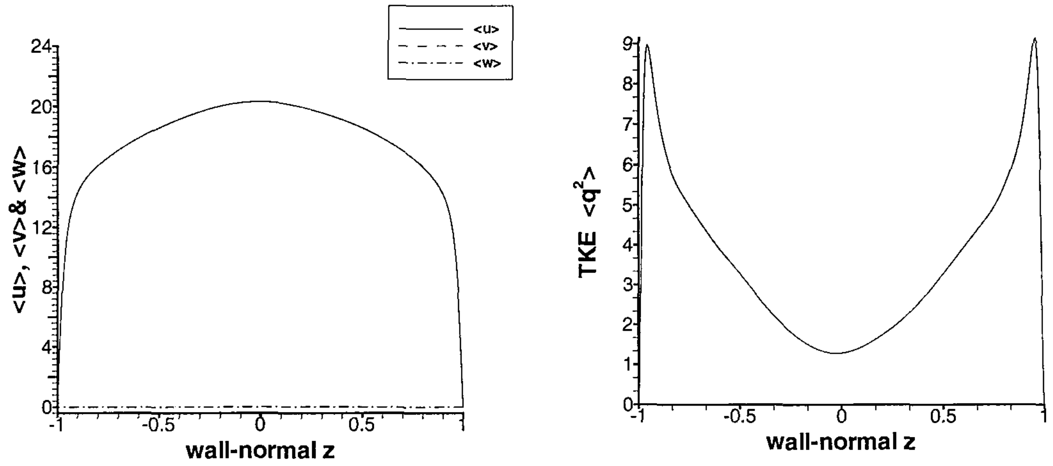

(a) $\bar{u}$, $\bar{v}$ and $\bar{w}$

(b) Mean TKE

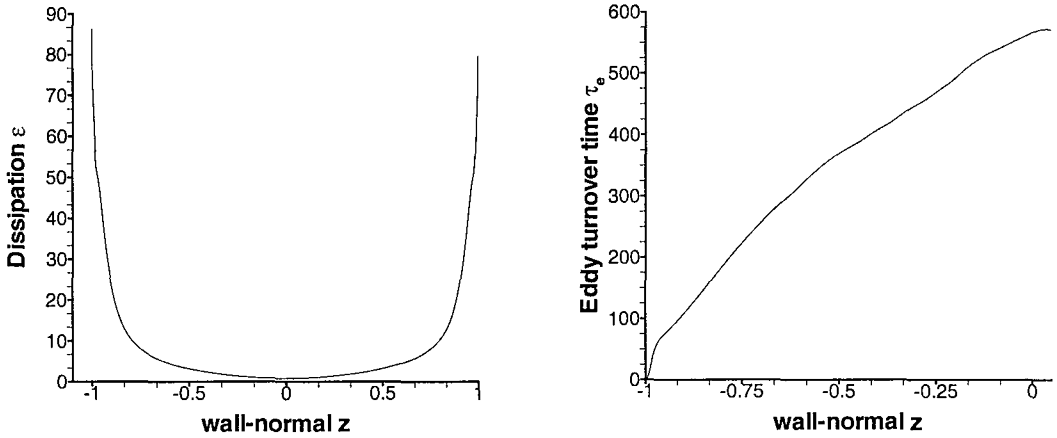

(c) Mean ε

(d) Eddy turnover time

Figure 6.2: Statistically averaged variation of mean velocities, mean TKE, mean ε and eddy turnover time

points. The first wall-normal derivative of Θ_1 profile is then found to be:

$$\begin{aligned} \overline{\theta_1}' &= -z \times Re/(1+f(z)) \\ f(z) &= 0.498(1+(0.525\frac{Re}{3}(1-z^2)(1+2z^2)(1-e^{(-(1-|z|)Re/39)})^2)^{0.6}-0.55 \end{aligned} \tag{6.2}$$

The profiles we have used have been defined via their derivatives with respect to z, because these derivatives are needed by OP theory. The other seven mean scalar profiles (from Θ_2 to Θ_8) have been defined by their derivatives as given in eqns. (5.6-5.12) and the shape of the profiles is same as shown in Figures 5.1(b) and 5.1(c). The two-point spanwise auto-correlation of the velocity components and passive scalars at different wall-normal distances ranging from $z^+ = 3.5$ to 36 can be seen from Figures 6.3 to 6.5. The spanwise spacing λ_y^+ of the velocity streaks (u primarily) and scalar streaks (Θ_1 to Θ_8, excluding 'proof of concept' profile Θ_5) as deduced from the two-point correlations turn out to be 110, 110,115, 560, 500, 600, 520 and 600+ wall units at a wall-normal distance of $z^+ = 3.5$. It is quite difficult to find the actual minima for the multiple frequency sinusoidal profiles as there seem to be 2-3 minimas in two-point correlations (see Figure 6.5). The spanwise streak spacing of 110 wall units for velocity streaks is consistent with results of other researchers [19]. As Θ_1 profile is almost similar to the mean velocity turbulent profile, the streak spacing of passive scalar θ_1 turns out to be same as that of velocity streaks. The second scalar mean profile is given by Reynolds-Tiederman profile [68] and as it follows closely the mean turbulent velocity profile U, it is not surprising that streak spacing for the second scalar θ_2 turns out be 115 wall units. This result is again in agreement with the basic idea of OP theory that similar shaped profiles should yield similar streak spacings.

As the mean scalar profiles Θ_3 to Θ_8 are markedly different in shape we get a wide variation of streak spacing even though the vortex structure generated by the velocity field is held fixed. This wide variation of streak spacing is also apparent on visualization of the velocity as well as passive scalar low-speed streaks as has been shown in Figures 6.6 and 6.7. It is seen that the number of streaks (approximately 9-10) for streamwise velocity profile U and for the first two mean scalars Θ_1 and Θ_2 is consistent with the streak spacing of approximately 110 wall units and the size of computational box in spanwise direction of 1080 wall units. The number of streaks for scalars θ_3 to θ_7 varies from 2 to 3, thus reinforcing the results of streak spacing obtained from spanwise correlations as shown in Figures 6.4 and 6.5.

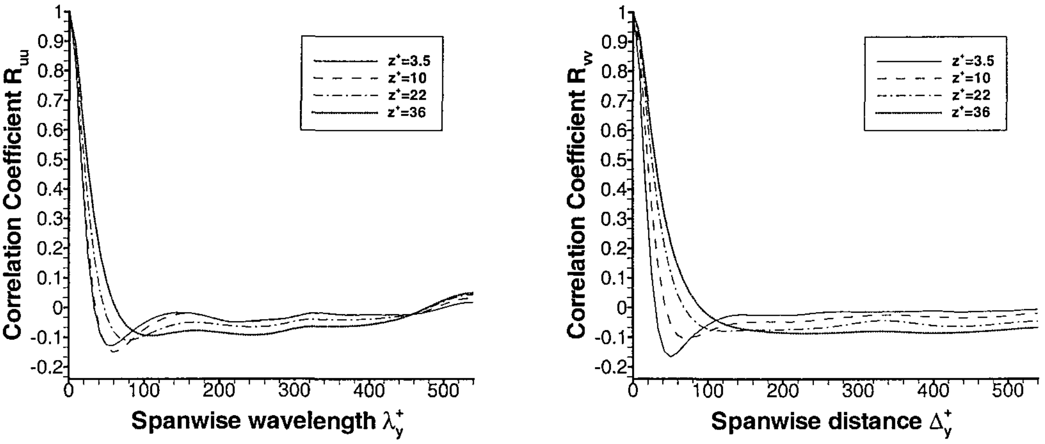

(a) R_{uu}

(b) R_{vv}

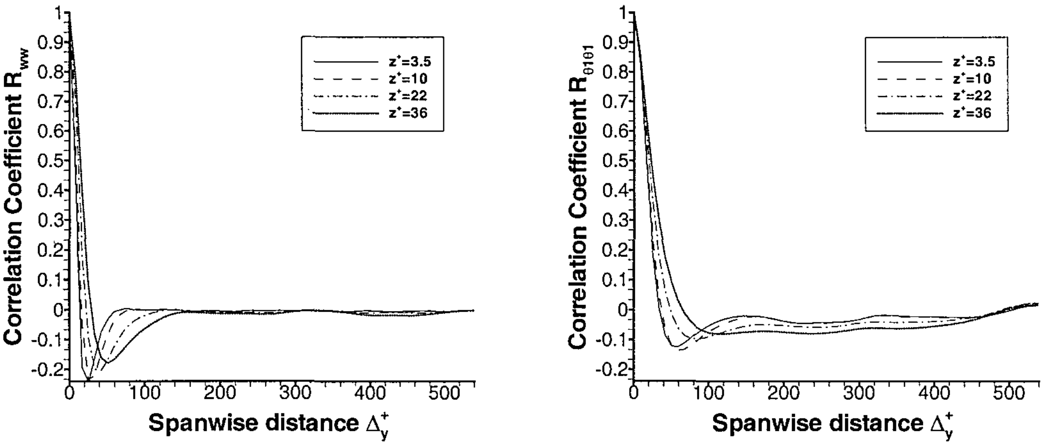

(c) R_{ww}

(d) $R_{\theta_1\theta_1}$

Figure 6.3: Statistically averaged correlation coefficients R_{uu}, R_{vv}, R_{ww} and $R_{\theta_1\theta_1}$ at different wall-normal distances

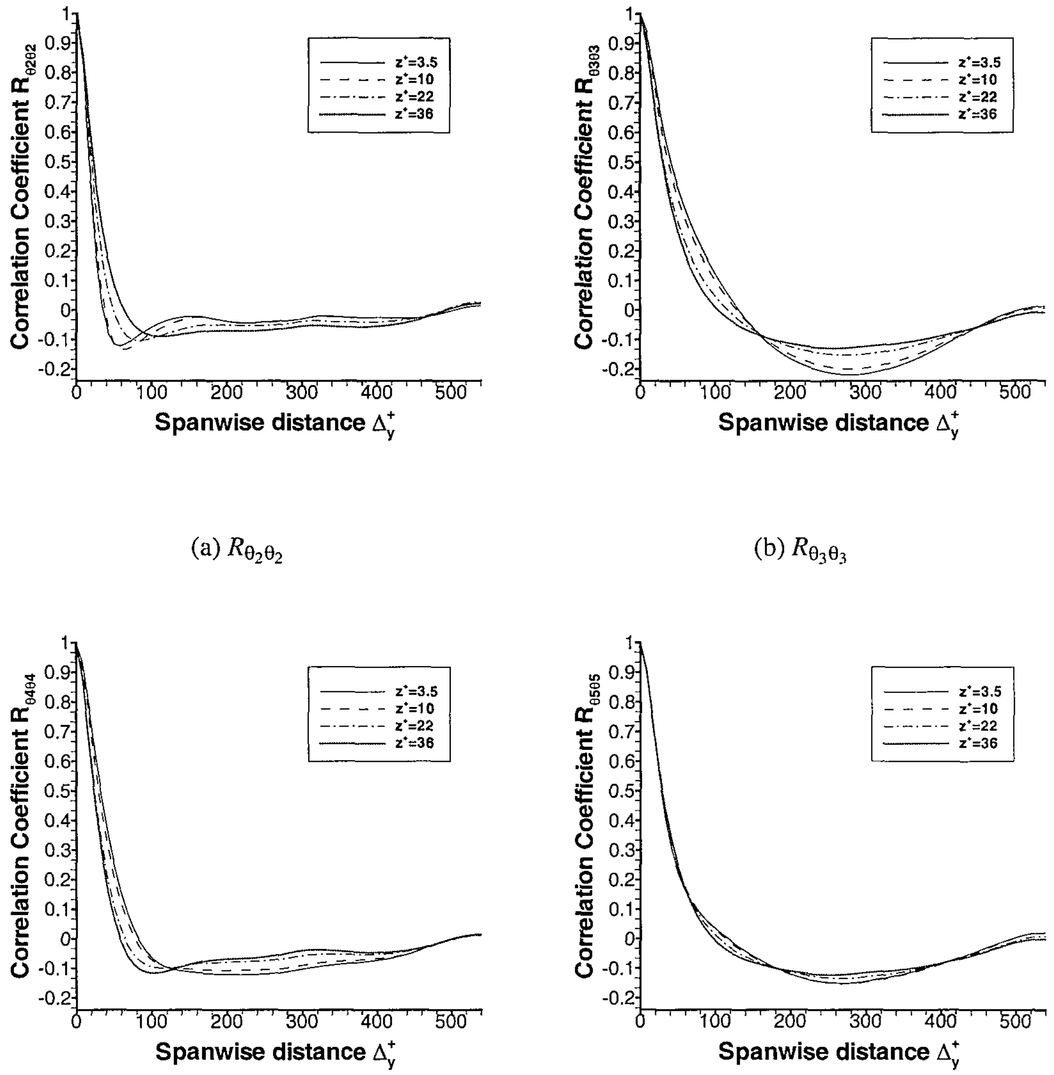

(a) $R_{\theta_2\theta_2}$

(b) $R_{\theta_3\theta_3}$

(c) $R_{\theta_4\theta_4}$

(d) $R_{\theta_5\theta_5}$

Figure 6.4: Statistically averaged correlation coefficients $R_{\theta_2\theta_2}$, $R_{\theta_3\theta_3}$, $R_{\theta_4\theta_4}$ and $R_{\theta_5\theta_5}$ at different wall-normal distances

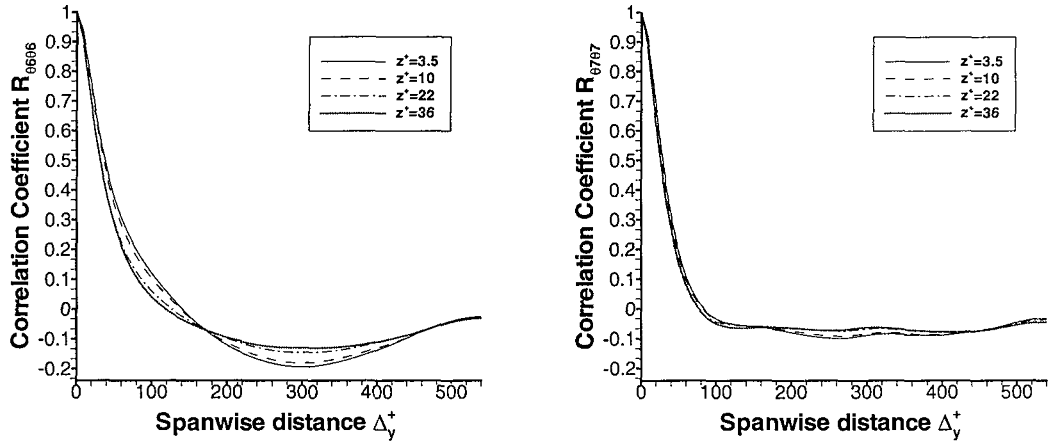

(a) $R_{\theta_6\theta_6}$

(b) $R_{\theta_7\theta_7}$

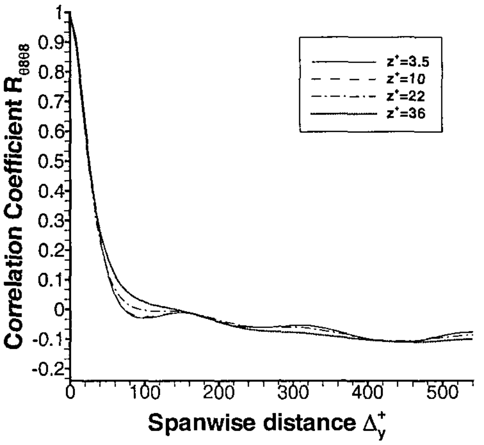

(c) $R_{\theta_8\theta_8}$

Figure 6.5: Statistically averaged correlation coefficients $R_{\theta_6\theta_6}$, $R_{\theta_7\theta_7}$ and $R_{\theta_8\theta_8}$ at different wall-normal distances

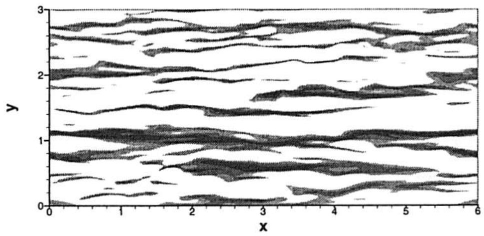

(a) Streamwise velocity u

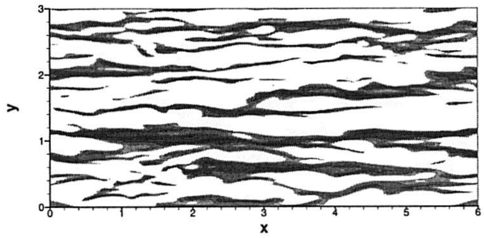

(b) First scalar θ_1

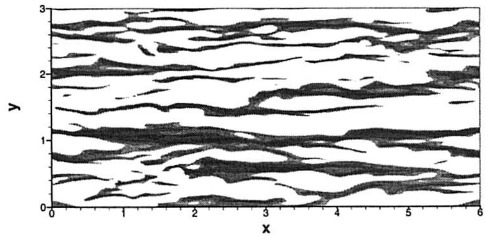

(c) Second scalar θ_2

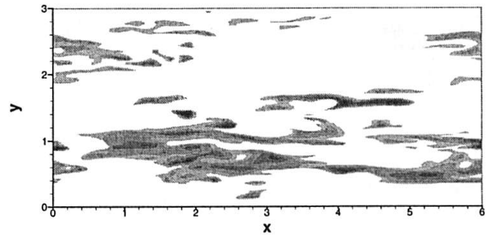

(d) Third scalar θ_3

Figure 6.6: Spatial variation of negative contours of u, θ_1, θ_2 and θ_3 showing low-speed velocity and scalar streaks at $z^+ = 5.6$. The areas marked black are < 0.25 of minimum negative values of the variables.

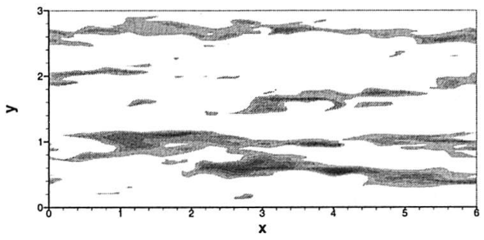

(a) Fourth scalar θ_4

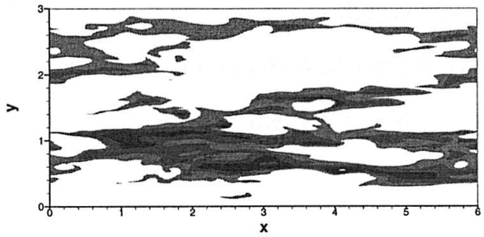

(b) Sixth scalar θ_6

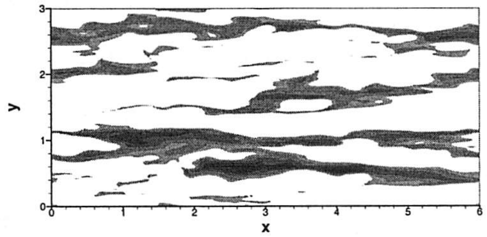

(c) Seventh scalar θ_7

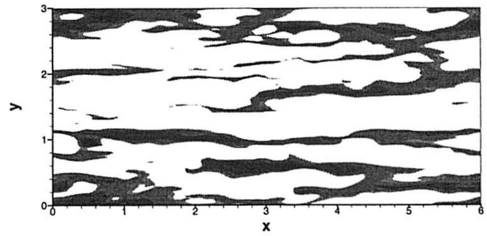

(d) Eighth scalar θ_8

Figure 6.7: Spatial variation of negative contours of θ_4, θ_6, θ_7 and θ_8 showing low-speed scalar streaks at $z^+ = 5.6$. The areas marked black are < 0.25 of minimum negative values of the variables.

6.3 Linear combination of basic mean profiles

The above results show that for the mean scalar profiles considered above the streak spacing varies from 110 to 600 wall units. We generated additional new mean profiles Θ_{ni} from linear combination of the above six basic mean scalar profiles (Θ_2, Θ_3, Θ_4, Θ_6, Θ_7 and Θ_8). This was achieved by following the analysis mentioned in section 5.7 but with slight modifications. The modifications were introduced because for certain values of Δ_0 the minimisation problem becomes ill-posed. The ill-posed nature of the problem is caused due to the ill-conditioning of the coefficient matrix A, which in turn happens due to linear dependencies of the six basic mean scalar profiles. One of the ways to overcome this problem is to introduce some kind of regularisation technique such as Tikhonov regularisation [63, 17]. This changes the functional introduced earlier in section 5.7 to a new form given below:

$$\sum_{i=1,j=1}^{i=n,j=n} X_iX_j(R_{\theta_i,\theta_j}(\Delta_0)+r\delta_{i,j}) - \lambda\left(\sum_{i=1,j=1}^{i=n,j=n} X_iX_jR_{\theta_i,\theta_j}(0)-1\right) \rightarrow min \qquad (6.3)$$

where r is the regularisation parameter and n is the number of basic mean scalar profiles, n = 6. The regularisation parameters and the computed eigenvectors for the new seven profiles have been tabulated in Table 6.1. The cross-correlations values that have been used in the computations were calculated at a distance $z^+ = 22.3$ from the wall. Out of the six eigenvalues we always chose the one giving the smallest value of $R_{\theta\theta}(\Delta_0)$. Using this modified technique seven new mean scalar profiles, which we denote $\Theta_{3D1}, \ldots, \Theta_{3D7}$ were computed.

mean scalar	r	X_1	X_2	X_3	X_4	X_5	X_6
Θ_{3D1}	0.1	0.9452	0.03027	0.3191	0.003794	-0.03407	-0.05132
Θ_{3D2}	0.1	-0.9841	0.1426	0.04708	-0.0007388	-0.08993	-0.03150
Θ_{3D3}	0.01	-0.3198	-0.1153	0.7649	-0.1601	0.5173	0.07813
Θ_{3D4}	0.001	0.1415	-0.07865	-0.07077	0.3237	-0.8607	-0.3522
Θ_{3D5}	0.1	-0.07543	-0.8645	0.4305	0.02091	-0.1787	0.1709
Θ_{3D6}	0.0025	-0.03643	-0.03295	0.002782	-0.2214	0.9641	0.1380
Θ_{3D7}	0.001	-0.006337	-0.02004	0.005644	-0.1841	0.9090	-0.3733

Table 6.1: Regularisation parameter r and eigenvectors of the new mean scalar profiles computed using linear combination technique.

Seven new profiles have been computed using this technique with location of the first minima Δ_{min} varying from 0.118, 0.140, 0.515, 0.772, 0.795, 0.937 and 1.5 giving a corresponding streak spacing $\lambda_y^+ = 85, 100, 370, 555, 570, 675$ and 1080 wall units at a wall-normal distance of $z^+ = 5.6$. The two-point auto-correlations of the seven new profiles at $z^+ = 5.6$ can be seen from Figure 6.8. For the last profile it is evident that the streak spacing exceeds the spanwise computational box size of 1080 wall units. The variation of the auto-correlation function with wall-normal distance is quite substantial for some profiles as can be seen from Figure 6.9 at $z^+ = 22.3$. For all the new scalar mean profiles, except Θ_{3D3}, Θ_{3D4} and Θ_{3D5} the streak spacing increases as the distance from the wall increases and the new streak spacings are 100,135, 200, 505, 570, 710 and 1080 wall units at $z^+ = 22.3$.

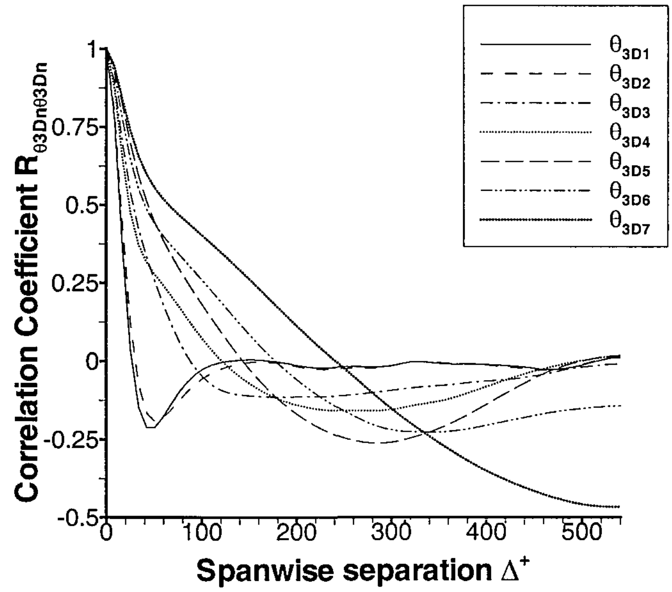

Figure 6.8: Wall-normal variation of two-point auto-correlation coefficients $R_{\theta_{3D1},\theta_{3D1}}$, $R_{\theta_{3D2},\theta_{3D2}}$, $R_{\theta_{3D3},\theta_{3D3}}$, $R_{\theta_{3D4},\theta_{3D4}}$, $R_{\theta_{3D5},\theta_{3D5}}$,$R_{\theta_{3D6},\theta_{3D6}}$ and $R_{\theta_{3D7},\theta_{3D7}}$ for the new profiles at $z^+ = 5.6$.

It can be seen from the Figure 6.10 that for the mean profile Θ_{3D1} which is similar in slope to the mean turbulent velocity profile as shown in Figure 6.2(a), the two-point correlation gives a minimum at $\Delta^+ = 42$ thus yielding a streak spacing of 85 wall units. This streak spacing is consistent with number of streaks seen on instantaneous visualization of negative fluctuating scalar θ'_{3D1} at $z^+ = 5.6$ as shown in the figures. The black areas in all the following figures correspond to regions in $z^+ = 5.6$ plane where the values for θ were below the threshold values which in turn were so adjusted that visually the area of dark region was approximately the same in all figures.

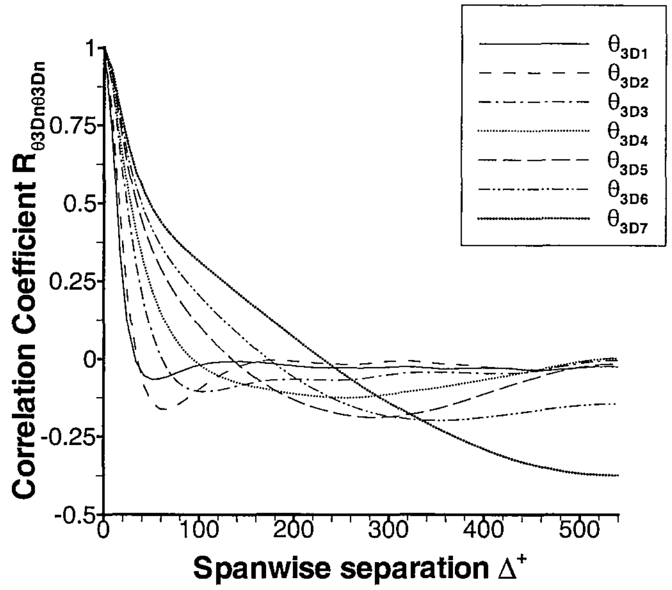

Figure 6.9: Wall-normal variation of two-point auto-correlation coefficients $R_{\theta_{3D1},\theta_{3D1}}$, $R_{\theta_{3D2},\theta_{3D2}}$, $R_{\theta_{3D3},\theta_{3D3}}$, $R_{\theta_{3D4},\theta_{3D4}}$, $R_{\theta_{3D5},\theta_{3D5}}$,$R_{\theta_{3D6},\theta_{3D6}}$ and $R_{\theta_{3D7},\theta_{3D7}}$ for the new profiles at $z^+ = 22.3$.

The threshold values were respectively 15, 16, 4.5, 5, 3.6, 0.7 and 1.5 percent of the scalar minimal instantaneous value in that plane.

Figure 6.11 shows that as the mean profile Θ_{3D2} is changed slightly so that its peaks shift away from the walls towards the channel centre, the two-point correlation changes slightly giving a new streak spacing of 100 wall units at wall-normal distance of $z^+ = 5.6$. The number and pattern of streaks as seen in this figure is quite similar to that obtained for the profile Θ_{3D1}.

Figure 6.12 shows the mean profile Θ_{3D3} where the peaks have shifted further away from the walls towards the channel centre causing the minima of the two-point correlation to change significantly. The streak spacing obtained with this profile is 370 wall units. This results in a significant change in the streak spacing as can be seen visually from the accompanying figure.

Further variation of the mean profile leads to Θ_{3D4} (see Figure 6.13) which has got further shifting of "shear zone" away from the walls. This profile leads to streak spacing $\lambda_{streak} = 555$ wall units i.e. presence of two streaks in the spanwise box length of 1080 wall units and the same can be visualised in the accompanying figure.

The mean profile Θ_{3D5} (see Figure 6.14) has got further "shear shift" as compared to the previous

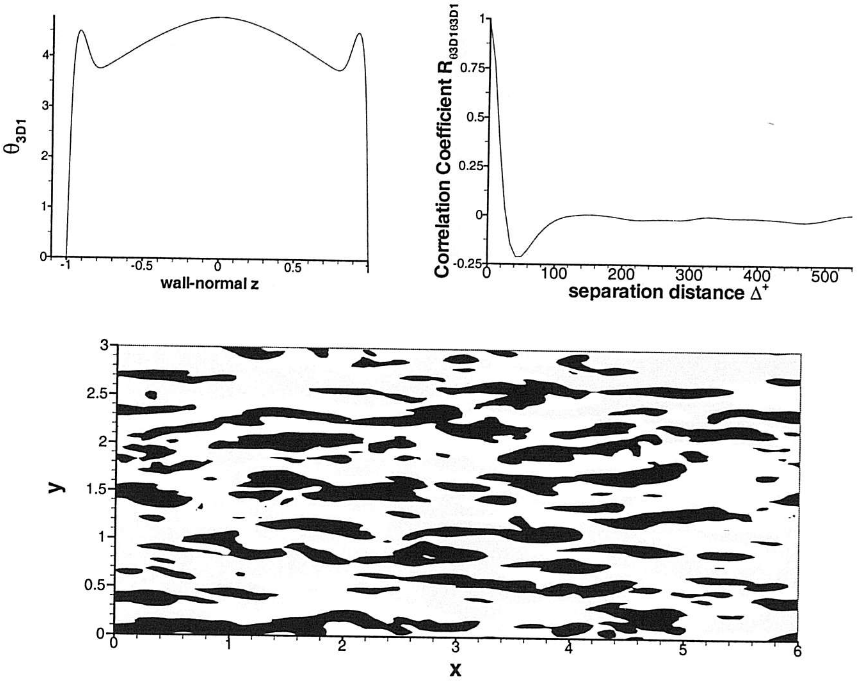

Figure 6.10: Mean profile Θ_{3D1}, it auto-correlation function and fluctuating scalar θ'_{3D1} low-value streaks at $z^+ = 5.6$.

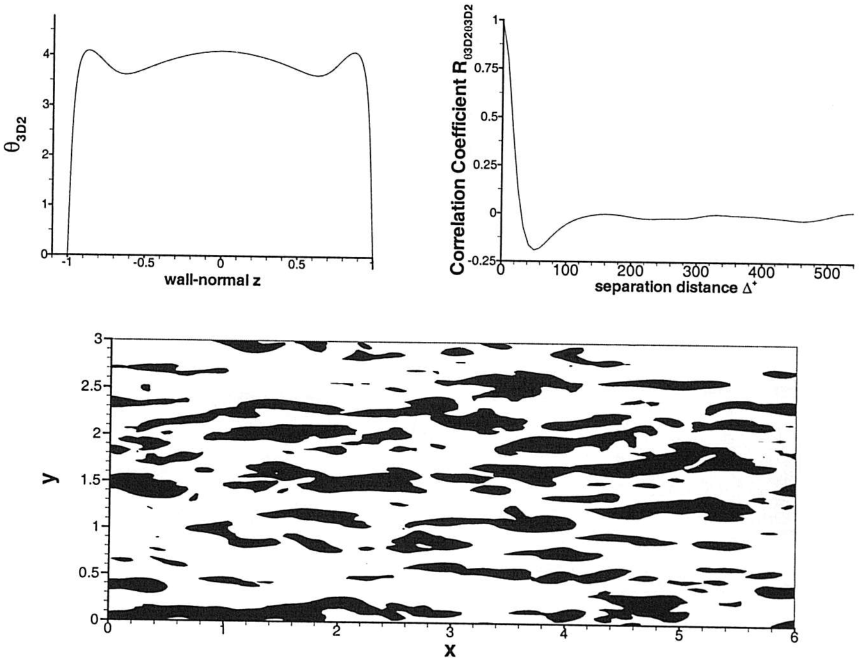

Figure 6.11: Mean profile Θ_{3D2}, it auto-correlation function and fluctuating scalar θ'_{3D2} low-value streaks at $z^+ = 5.6$.

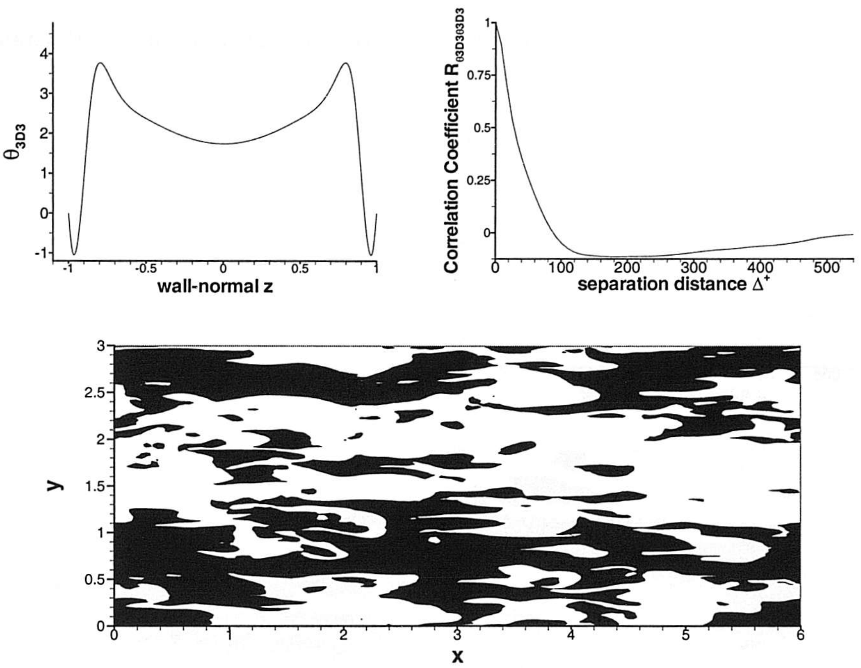

Figure 6.12: Mean profile Θ_{3D3}, it auto-correlation function and fluctuating scalar θ'_{3D3} low-value streaks at $z^+ = 5.6$.

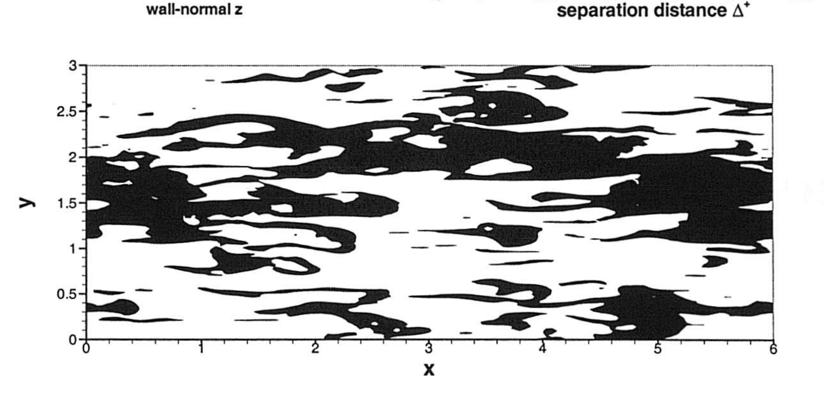

Figure 6.13: Mean profile Θ_{3D4}, it auto-correlation function and fluctuating scalar θ'_{3D4} low-value streaks at $z^+ = 5.6$.

profile. This profile leads to a streak spacing of $\lambda_{streak} = 570$ wall units i.e. primarily two streaks in the spanwise box and the instantaneous visualization of streak picture confirms the view.

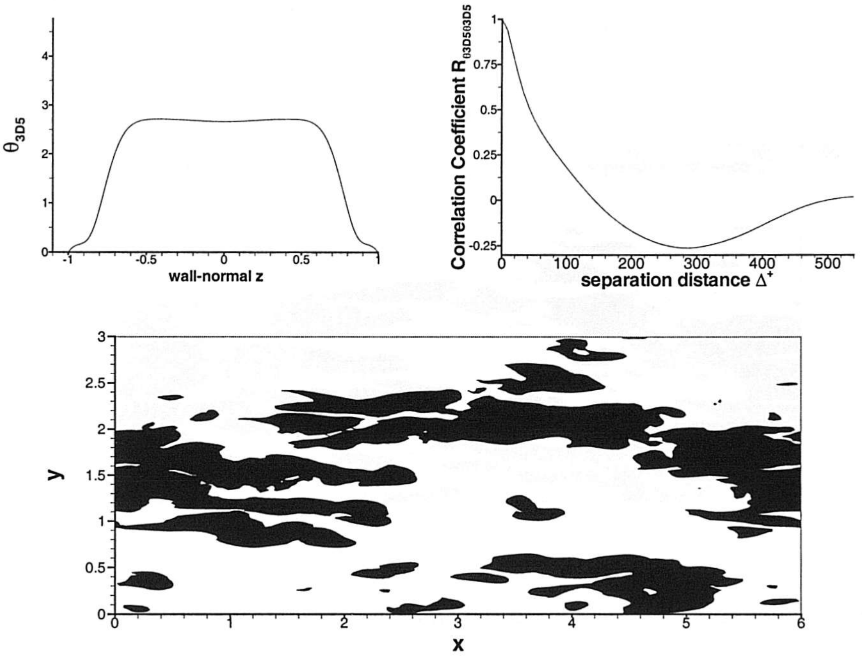

Figure 6.14: Mean profile Θ_{3D5}, it auto-correlation function and fluctuating scalar θ'_{3D5} low-value streaks at $z^+ = 5.6$.

Finally we have chosen the mean profiles Θ_{3D6} and Θ_{3D7} which have got the shear profiles significantly shifted away from the walls and hence the auto-correlation functions give λ_{streak} of 675 and 1080 wall units, respectively. This results in a single broad streak in the computational box and the same is apparent on visualization of the negative scalar concentration in the Figures 6.15 and 6.16.

6.4 Theoretical predictions from RNSAI and OP mechanisms

Due to our statistically averaged Q vs z profile being slightly different from the Q vs z profile of Nikitin and Chernyshenko [38] case, we had to repeat the analysis [38] of applying RNSAI mechanism to 3D turbulent channel flows. We have used the statistically averaged Q vs z profile (see

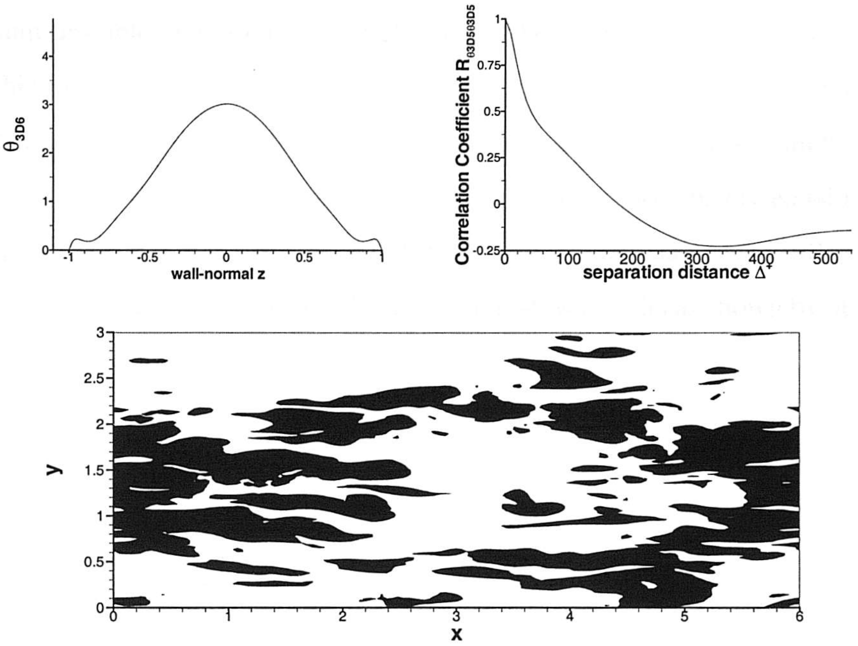

Figure 6.15: Mean profile Θ_{3D6}, it auto-correlation function and fluctuating scalar θ'_{3D6} low-value streaks at $z^+ = 5.6$.

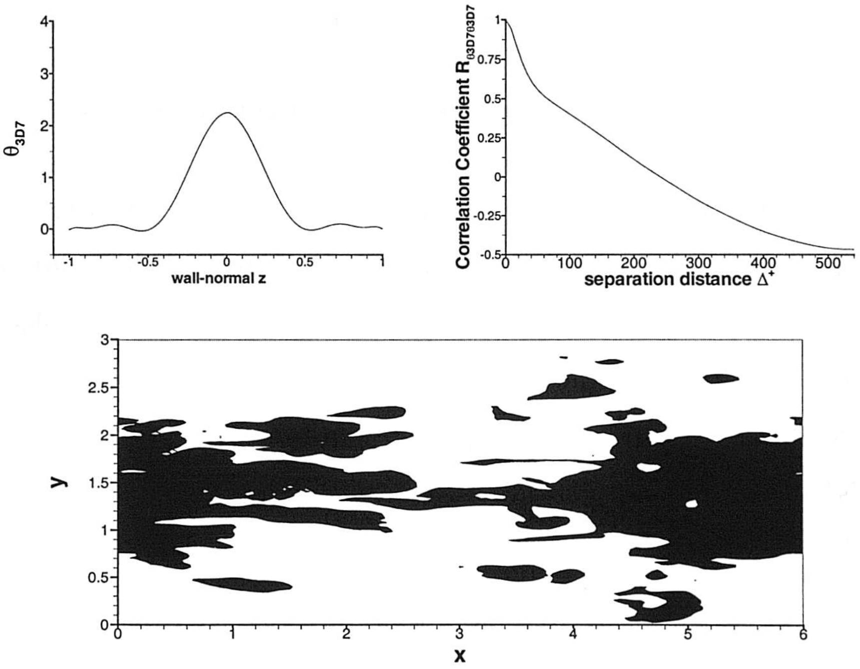

Figure 6.16: Mean profile Θ_{3D7}, it auto-correlation function and fluctuating scalar θ'_{3D7} low-value streaks at $z^+ = 5.6$.

Figure 6.1(b)) from DNS results, with the eigenvalue solver (see details in section 4.4) to compute the maximum unstable eigenvalues σ which display the growth rate of streamwise vortices, the twice of which yields the velocity (and hence all the scalars) streak spacing. Figure 6.17 exhibits the unstable eigenvalues as function of spanwise wavelength λ_y^+ and hence from this figure we can get the maximum size (diameter) of the streamwise vortices approximately equal to 70 wall units or streak spacing as 140 wall units. The value of 140 wall units is not too different with streak spacing of 100 wall units with standard deviation of ± 40 wall units as shown by other researchers [52].

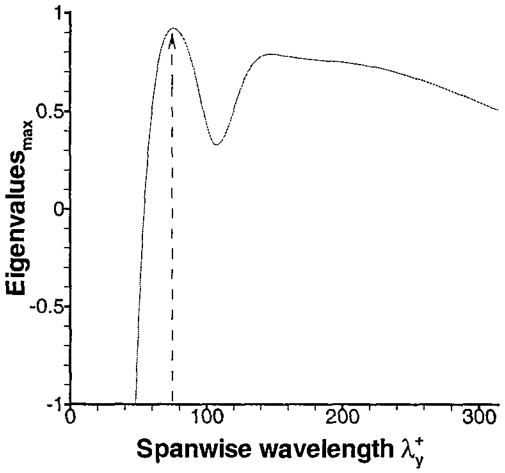

Figure 6.17: Growth rate of vortices as a function of spanwise wavelength λ_y^+.

We have computed optimal perturbations for seven basic mean scalar profiles in a 3D turbulent channel flow following the methodology outlined in section 5.5. As the analysis is similar to that given in chapter 5 except that the range of optimal times representative of eddy turnover time is now much larger i.e. from 40 to 600 due to a different eddy turnover time τ_e vs z plot, we are citing the results in a tabular format without presenting the figures for each basic mean scalar profile. The Table 6.2 shows the range of optimization times and wavelengths that have been computed corresponding to optimal energy growth for seven basic mean scalar profiles.

For the first new mean scalar profile Θ_{3D1} its derivative (as required by the OP theory) can be determined using derivatives of six basic mean scalar profiles (Θ_2 to Θ_8 excluding Θ_5) together with the relevant coefficients obtained through eigenvectors $\bar{X}$ of the minimisation problem. For this profile we get for the range of optimization times varying from $\tau^+ = 40$ to 600, wavelengths

Scalar	optimization time range	optimal wavelength range	Peak scalar location z_c^+	optimal τ^+	optimal λ_y^+
θ_1	40-400	75-250	15-43	75	95
θ_2	40-200	75-175	15-29	80	100
θ_3	40-400	125-280	75-80	200	230
θ_4	40-400	100-230	36-43	120	150
θ_6	40-600	425-450	130-145	310	420
θ_7	40-600	320-530	240-250	480	500
θ_8	40-600	335-570	290	520	530

Table 6.2: Representative times and wavelength ranges corresponding to maximum energy growth for basic mean scalar profiles. Also shown are the locations of peak scalar perturbations z_c^+ for different optimization times τ^+. Last two columns show the most optimal times τ^+ on basis of eddy turnover time and corresponding optimal wavelengths λ_y^+ representative of streak spacing.

λ_y^+ varying from 80 to 450 at which E/E_o peak (see Figure 6.18). At these specific τ^+ and λ_y^+, we get wall-normal locations of peak scalar perturbations as z_c^+=13 to 160 which have been plotted together with τ_e as a function of distance z^+ from the wall in Figure 6.19. It can be found from Figure 6.19 that the optimal time corresponds to τ^+=70 and corresponding wavelength at which optimal energy growth occurs is $\simeq$ 90 wall units.

The second new mean scalar profile Θ_{3D2} can be constructed similarly by the linear combination technique described above. For this profile we get for the range of optimization times varying from τ^+ = 40 to 600, wavelengths λ_y^+ varying from 80 to 350 at which E/E_o peaks (see Figure 6.20). At these specific τ^+ and λ_y^+, we get wall-normal locations of peak scalar perturbations z_c^+ ranging from 13 to 90 wall units which have been plotted together with τ_e as a function of distance from the wall in Figure 6.21. From the figure one can easily ascertain that the optimal time corresponds to τ^+=80 and the corresponding wavelength at which optimal energy growth occurs is $\simeq$ 100 wall units.

The third new scalar mean profile for the similar optimization times as mentioned above has spanwise wavelengths λ_y^+ ranging from 100 to 220 wall units at which the maximas of E/E_o occur (see Figure 6.22). For these specific optimization times and corresponding wavelengths, the wall-

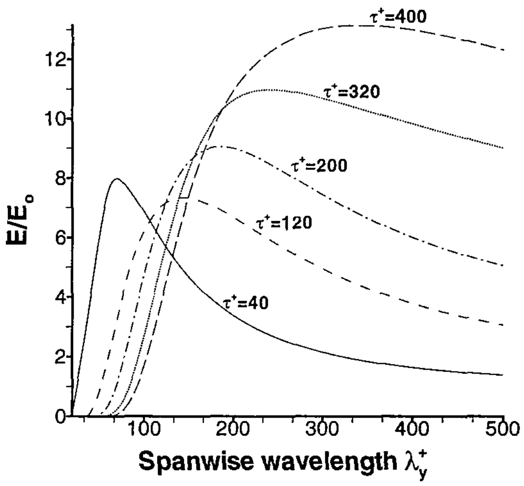

Figure 6.18: Optimal energy growth versus wavelength for optimization times representative of the eddy turnover time near the wall for scalar θ_{3D1}.

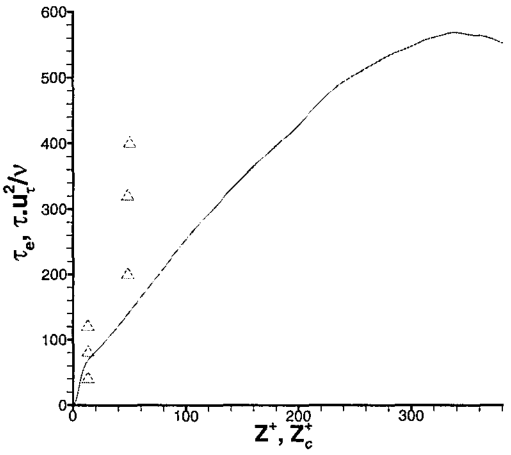

Figure 6.19: Eddy turnover time τ_e versus distance from the wall (—) for 3D turbulent channel flow. Also plotted (Δ) is optimal growth time τ^+ versus location of peak scalar perturbation z_c^+, for the new scalar θ_{3D1}.

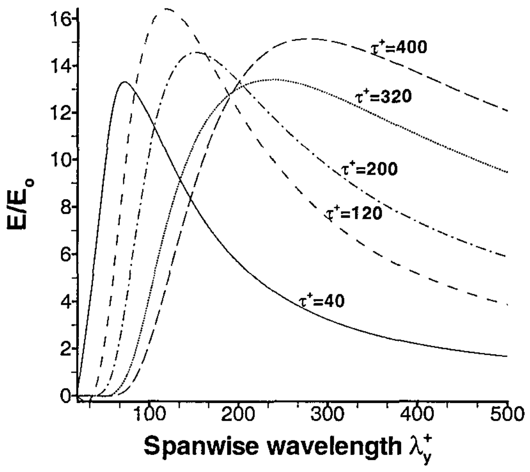

Figure 6.20: Optimal energy growth versus wavelength for optimization times representative of the eddy turnover time near the wall for scalar θ_{3D2}.

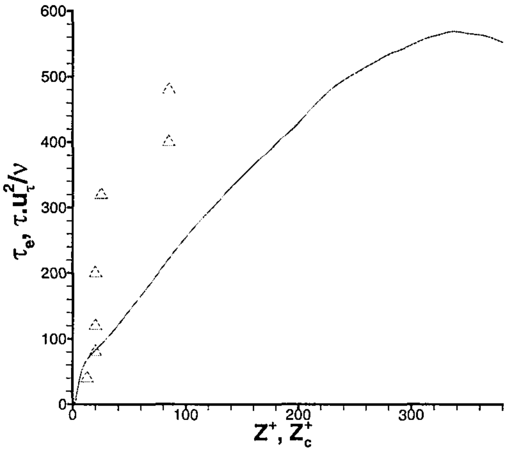

Figure 6.21: Eddy turnover time τ_e versus distance from the wall (—) for 3D turbulent channel flow. Also plotted (Δ) is optimal growth time τ^+ versus location of peak scalar concentration z_c^+, for the new scalar θ_{3D2}.

normal locations of peak scalar perturbations correspond to $z_c^+ = 36$ to 43 which have been plotted together with τ_e as a function of distance from the wall in Figure 6.23. The corresponding optimal time is $\tau^+ = 125$ and the resulting optimal streak spacing is $\lambda_y^+ = 150$ wall units.

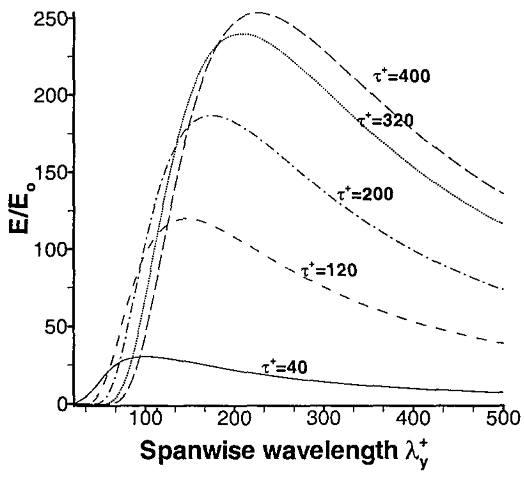

Figure 6.22: Optimal energy growth versus wavelength for optimization times representative of the eddy turnover time near the wall for scalar θ_{3D3}.

The fourth new scalar mean profile for the optimization times τ^+ ranging from 40 to 400 has spanwise wavelengths λ_y^+ varying between 120 to 260 wall units at which the maximas of E/E_o occur (see Figure 6.24). For these specific optimization times and corresponding wavelengths, the wall-normal locations of peak scalar perturbations correspond to $z_c^+ = 50$ to 60 which have been plotted together with τ_e as a function of distance from the wall in Figure 6.25. The corresponding optimal time is $\tau^+ = 160$ and the resulting optimal streak spacing is $\lambda_y^+ = 190$ wall units.

For the fifth new passive scalar profile, we get for optimization times varying from $\tau^+ = 40$ to 400, wavelengths $\lambda_y^+ = 130$ to 280 at which maximas of E/E_o occur as can be seen from Figure 6.26. At these specific τ^+ and λ_y^+, we get wall-normal locations of peak scalar perturbations as $z_c^+ = 80$ to 85 which have been plotted together with τ_e as a function of distance from the wall in Figure 6.27. It is seen that the optimal time corresponds to $\tau^+ = 220$ and corresponding wavelength (i.e. streak spacing) at which optimal energy growth occurs is $\simeq 240$ wall units.

For the sixth new passive mean scalar profile Θ_{3D6}, we get for optimization times ranging from $\tau^+ = 40$ to 600, wavelengths λ_y^+ varying from 300 to 480 at which maximas of E/E_o occur as can be seen from Figure 6.28. At these specific τ^+ and λ_y^+ we get wall-normal locations of peak

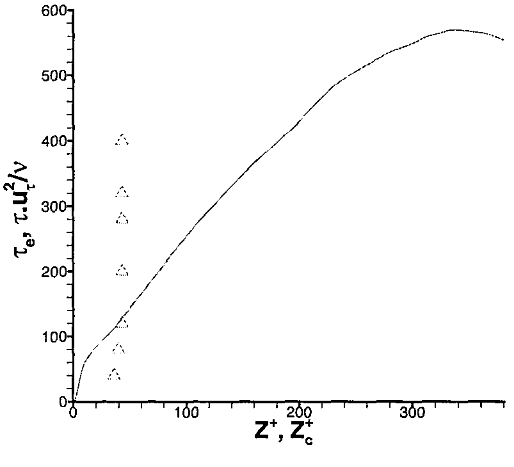

Figure 6.23: Eddy turnover time τ_e versus distance from the wall (—) for 3D turbulent channel flow. Also plotted (Δ) is optimal growth time τ^+ versus location of maximum scalar concentration z_c^+, for the new scalar θ_{3D3}.

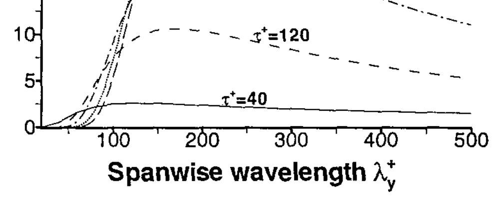

Figure 6.24: Optimal energy growth versus wavelength for optimization times representative of the eddy turnover time near the wall for scalar θ_{3D4}.

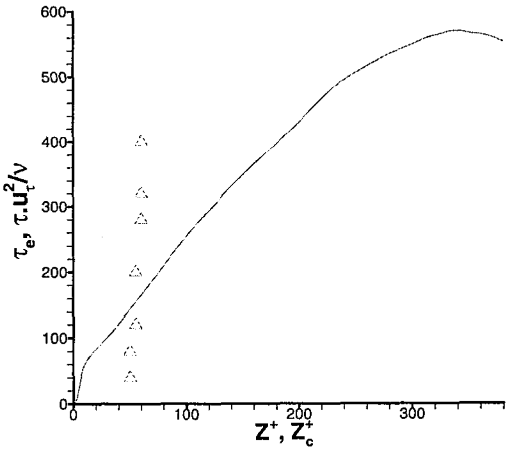

Figure 6.25: Eddy turnover time τ_e versus distance from the wall (—) for 3D turbulent channel flow. Also plotted (Δ) is optimal growth time τ^+ versus location of maximum scalar concentration z_c^+, for the new scalar θ_{3D4}.

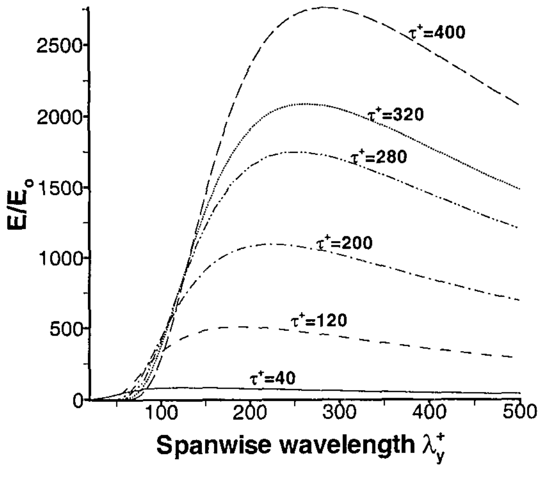

Figure 6.26: Optimal energy growth versus wavelength for optimization times representative of the eddy turnover time near the wall for scalar θ_{3D5}.

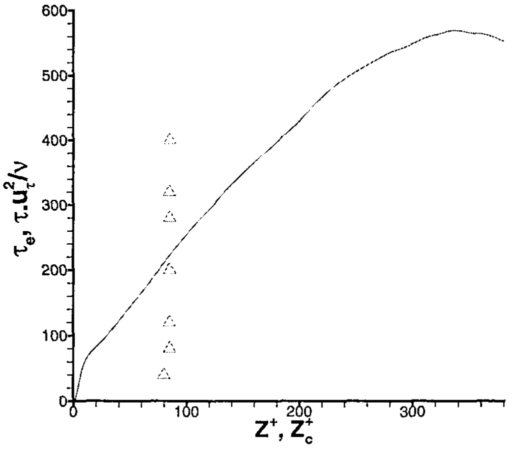

Figure 6.27: Eddy turnover time τ_e versus distance from the wall (—) for 3D turbulent channel flow. Also plotted (Δ) is optimal growth time τ^+ versus location of peak scalar concentration z_c^+, for the new scalar θ_{3D5}.

scalar perturbations as z_c^+=200 to 210 which have been plotted together with τ_e as a function of distance from the wall in Figure 6.29. It is seen that the optimal time corresponds to τ^+=440 and corresponding wavelength (i.e. streak spacing) at which optimal energy growth occurs is $\simeq$ 450 wall units.

Finally for the last seventh mean scalar profile θ_{3D7}, we get for optimization times τ^+ = 40 to 600, wavelengths λ_y^+ varying from 270 to 510 at which maximas of E/E_o occur as can be seen from Figure 6.30. At these specific τ^+ and λ_y^+, we get wall-normal locations of peak scalar perturbations as z_c^+=275 which have been plotted together with τ_e as a function of distance from the wall in Figure 6.31. It is seen that the optimal time corresponds to τ^+=530 and corresponding wavelength (i.e. streak spacing) at which optimal energy growth occurs is $\simeq$ 490 wall units.

The optimal times representative of eddy turnover time, that can be inferred from Figures 6.18 to 6.31 for different new mean scalar profiles θ_{3D1} to θ_{3D7} are namely τ^+ = 70, 80, 125, 160, 220, 440 and 530. These optimization times correspond to optimal wavelengths, representative of streak spacing, λ_y^+ = 90, 100, 150, 190, 240, 450 and 490 wall units. The tabulated comparsion between streak spacings as found from DNS results at $z^+ = 5.6$ with theoretical predictions of RNSAI and OP theory is given below in Table 6.3.

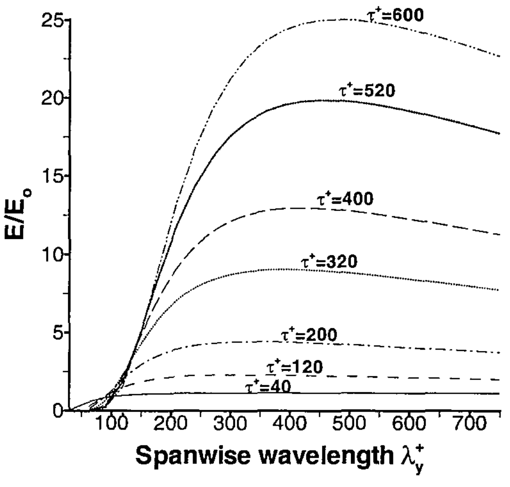

Figure 6.28: Optimal energy growth versus wavelength for optimization times representative of the eddy turnover time near the wall for scalar θ_{3D6}.

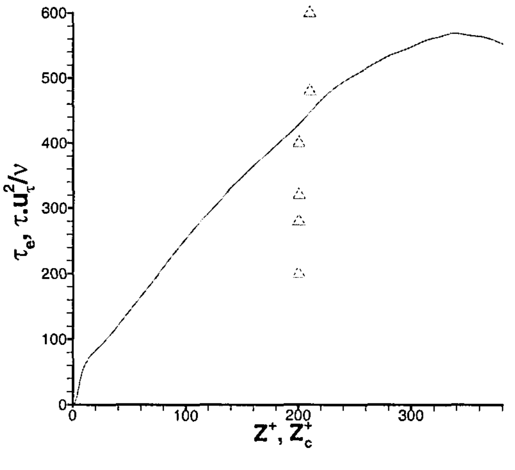

Figure 6.29: Eddy turnover time τ_e versus distance from the wall (—) for 3D turbulent channel flow. Also plotted (Δ) is optimal growth time τ^+ versus location of peak scalar concentration z_c^+, for the new scalar θ_{3D6}.

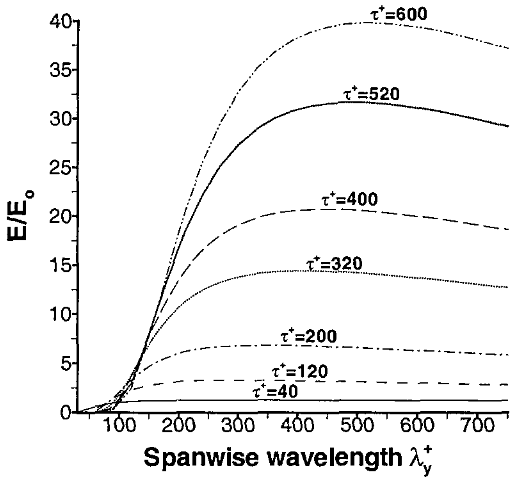

Figure 6.30: Optimal energy growth versus wavelength for optimization times representative of the eddy turnover time near the wall for scalar θ_{3D7}.

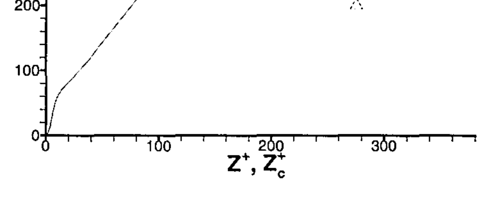

Figure 6.31: Eddy turnover time τ_e versus distance from the wall (—) for 3D turbulent channel flow. Also plotted (Δ) is optimal growth time τ^+ versus location of peak scalar concentration z_c^+, for the new scalar θ_{3D7}.

Scalars	Streak spacing, wall units		
	DNS	RNSAI	OP
θ_1	110	140	95
θ_2	115	140	100
θ_3	560	140	230
θ_4	500	140	150
θ_6	600	140	420
θ_7	520	140	500
θ_8	600	140	530
θ_{3D1}	85	140	90
θ_{3D2}	100	140	100
θ_{3D3}	370	140	150
θ_{3D4}	555	140	190
θ_{3D5}	570	140	240
θ_{3D6}	675	140	450
θ_{3D7}	1080	140	490

Table 6.3: Comparison of streak spacing obtained from DNS, RNSAI and OP for 3D turbulent channel flow. The DNS results are at a wall-normal distance of $z^+ = 5.6$ wall units.

On the basis of above results the following conclusions can be summarised:

1. The shape of the mean scalar profile significantly changes the streak spacing even when the vortex structure of the velocity field is invariant.
2. As OP theory only provides a qualitative match, it needs a major modification in order to get a better quantitative agreement.

In light of the above discussions Chernyshenko and Baig [11] (see the Appendix) proposed a new Generalized optimal perturbation theory. This theory overcomes the inherent deficiencies of the OP and provides theoretical predictions which are in good agreement with DNS results.

6.5 Passive scalar streaks in a flow with potential velocity fluctuations

If we consider the equation (6.1) for the scalar concentration, we see that the previous simulation mentioned above have been performed with the velocity distribution **u**(x,y,z,t) obtained by simultaneously solving the momentum equations in a turbulent channel flow. Therefore, the flowfield contained all the organised vortices existing in turbulent flows. In order to check whether there is any need of organised vortices for generation of streaks, numerical simulations were performed with $\mathbf{u} = U(z)\mathbf{i} + \nabla\phi(x,y,z,t)$ with random ϕ. For this configuration only spanwise vorticity is present and as the perturbations are potential, there should be no organised vortices present in the flow.

The random perturbation velocity potential can be expressed as

$$\phi(x,y,z,t) = \sum_{k_x,k_y} C_{(k_x,k_y,t)} e^{\imath 2\pi\alpha_{(k_x,k_y,t)}} e^{\imath(k_x x+k_y y)} f_{k_x,k_y}(z) \tag{6.4}$$

The wavenumbers can be expressed as $k_x = \frac{2\pi k}{L_x}$ and $k_y = \frac{2\pi l}{L_y}$ where k and l are number of Fourier modes in x and y directions, respectively. As $\mathbf{u} = \nabla\phi$ is solenoidal, hence ϕ should satisfy the Laplace equation.

$$\nabla^2\phi = \sum_{k_x,k_y} C_{(k_x,k_y,t)} e^{\imath 2\pi\alpha_{(k_x,k_y,t)}} (-(k_x^2+k_y^2) f_{k_x,k_y}(z) + f''_{k_x,k_y}(z)) e^{\imath(k_x x+k_y y)} = 0 \tag{6.5}$$

The solution of the above equation gives $f_{k_x,k_y}(z) = e^{\pm\sqrt{k_x^2+k_y^2}z}$. As the walls are at $z = \pm 1$, ϕ can be expressed as

$$\phi = \sum_{k_x,k_y} C_{(k_x,k_y,t)} e^{\iota 2\pi\alpha_{(k_x,k_y,t)}} e^{\iota(k_x x+k_y y)} \left(e^{\sqrt{k_x^2+k_y^2}(z+1)} + e^{-\sqrt{k_x^2+k_y^2}(z+1)}\right) \tag{6.6}$$

This gives normal potential velocity distribution as

$$w = \frac{\partial\phi}{\partial z} = \sum_{k_x,k_y} C_{(k_x,k_y,t)} e^{\iota 2\pi\alpha_{(k_x,k_y,t)}} e^{\iota(k_x x+k_y y)} \left(e^{\sqrt{k_x^2+k_y^2}(z+1)}\sqrt{k_x^2+k_y^2} + e^{-\sqrt{k_x^2+k_y^2}(z+1)}\sqrt{k_x^2+k_y^2}\right) \tag{6.7}$$

As $w = 0$ at $z = -1$ but not at $z = 1$, it shows that at the bottom wall the impermeability condition is satisfied while the potential flow is being generated by random boundary conditions at the upper wall. Further ϕ is normalized by w at $z = 1$ to get the new wall-normal function

$$f_{k_x,k_y}(z) = e^{\sqrt{k_x^2+k_y^2}(z-1)} + e^{-\sqrt{k_x^2+k_y^2}(z+3)} \tag{6.8}$$

On leaving the imaginary parts in eqn. (6.5) we get

$$\phi(x,y,z,t) = \sum_{k_x,k_y} \left(C_{(k_x,k_y,t)} cos(2\pi\alpha_{(k_x,k_y,t)}) cos(k_x x + k_y y) - C_{(k_x,k_y,t)} sin(2\pi\alpha_{(k_x,k_y,t)}) sin(k_x x + k_y y)\right) f_{k_x,k_y}(z) \tag{6.9}$$

Further differentiation of the potential function gives us the potential velocities. In order to obtain a random potential flow field, we have to generate random coefficients $C_{k_x,k_y,t}$ and $\alpha_{k_x,k_y,t}$ in time for all the wavenumbers, using a random number generator. For this purpose use has been made of a random number generator based on uniform deviates. The amplitude A regulates the strength of the potential velocity perturbations. The relationship is given as

$$\alpha_{k_x,k_y} = random(seed) - 0.5$$

$$C_{k_x,k_y} = A * random(seed1)$$

These random coefficients (for all the wavenumbers) are generated at time intervals τ and spline interpolation [42] is performed to get values in between. The mean scalar concentration is chosen to be same as the mean velocity distribution, $\Theta(z) = U(z)$ which is in turn given by the Reynolds-Tiederman profile [68] as given in eqn.(5.6).

6.5.1 Results

The numerical simulation was performed in channel geometry of $L_x = 6$, $L_y = 3$ and $L_z = 2$ using 128*128*160 grid points for the Reynolds number $Re_\tau = 360$. The numbers k and l of the Fourier modes used to generate potential velocity fluctuations are 16 in streamwise direction and 16 in the spanwise direction. The characteristic time scale $\tau = 0.05$ has been used to generate potential velocity field. The amplitude $A = 0.0004$ has been kept small such that the flow-field is properly resolved by the grid points used in the simulation. The wall-normal velocity perturbations that are generated at the upper wall attenuate in strength significantly as we proceed towards the bottom wall but still they possess sufficient strength to cause lift-up of slow-moving fluid in order to generate streaks at the lower walls. The wall-normal velocity w perturbations corresponding to time $t = 1.5$ at $z^+ = 5.6$ (see Figure 6.32) at the top and bottom wall exemplify the same by showing energetic small eddies at the top wall and much weakened larger structures near the bottom wall.

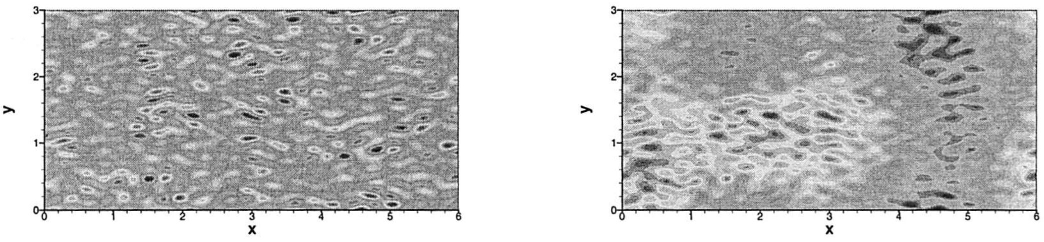

(a) At top wall

(b) At bottom wall

Figure 6.32: Wall-normal velocity w fluctuations at the top and bottom wall of the channel at $t = 1.5$

Figure 6.33(a) shows the initial growth of the scalar streaks near the bottom wall at $z^+ = 5.6$ corresponding to time $t = 0.5$. As time progresses, these scalar streaks get elongated and the same can be seen in Figure 6.33(b) at time $t = 1.5$. As evident from the figures the streak spacing is comparable to that that in Figure 6.6(a), which shows the velocity streaks in turbulent flow with the same mean profile and at the same Reynolds number. Figure 6.34 show the temporal variation of instantaneous velocity component w at a point on the central plane of the channel.

In order to find out the effect of characteristic time scale of potential velocity perturbations on the streak spacing, another simulation has been performed with the characteristic time scale now reduced to $\tau = 0.01$. For this case, the amplitude A was taken to be constant for each wavenumber while the real and imaginary parts of the random complex-valued coefficients $C_{(k_x,k_y,t)}$ were generated independently using random numbers based on uniform deviates distributed in (0, 1) square

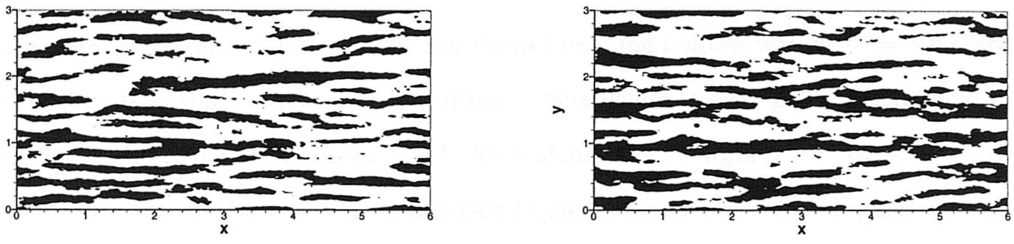

(a) At t=0.5

(b) At t=1.5

Figure 6.33: Scalar streaks at the bottom wall at $z^+ = 5.6$ for two time instants for characteristic time scale $\tau = 0.05$.

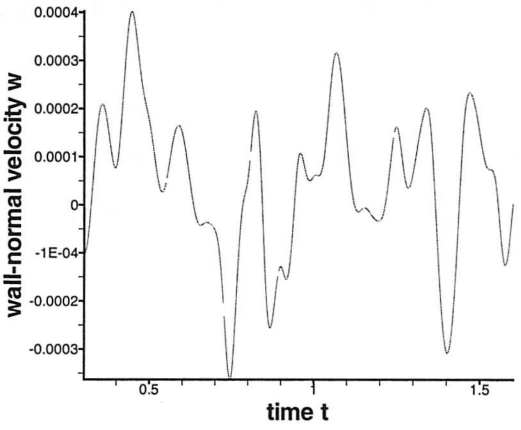

Figure 6.34: Temporal variation of wall-normal velocity component w at a point on the central plane of the channel

domain. Also, in this case we took $\alpha_{(k_x,k_y,t)} = 0$. The amplitude was increased to $A = 0.0008$ but the number of Fourier modes used to generate potential velocity field were retained as 16 in homogeneous directions. The simulation was run till time t=1.5 and a similar behaviour regarding attenuation of wall-normal velocity perturbations from top to bottom wall was observed. Figure 6.35(a) shows the initial growth of the scalar streaks near the bottom wall at $z^+ = 5.6$ corresponding to time $t = 0.5$. With further increase of time, these scalar streaks get elongated and the same can be seen in Figure 6.35(b) at time $t = 1.5$. As evident from the figures the streak spacing is quite similar to that observed for velocity streaks (see Figure 6.6(a) at same Re). Figure 6.36 shows the temporal variation of instantaneous velocity component w at a point on the central plane of the channel.

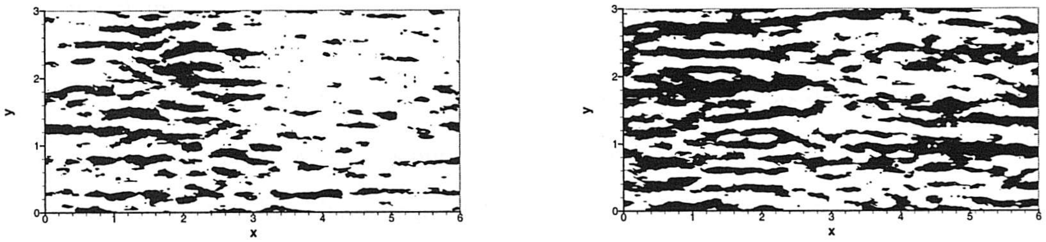

(a) At t=0.5

(b) At t=1.5

Figure 6.35: Scalar streaks at the bottom wall at $z^+ = 5.6$ at two time instants for characteristic time scale $\tau = 0.01$

In the numerical experiments performed above, with the scalar concentration being advected by the velocity of the carrier phase taken as the sum of mean turbulent profile and random potential perturbations, the appearance of scalar streaks clearly proves that organised vortices are not needed for formation of streaks.

6.6 Generalized Optimal perturbation theory

Generalized optimal perturbation (GOP) theory is a modification of OP theory and in it the solution norm being maximised differs from the solution norm used to formulate the restriction on the initial condition. As it was found by Butler and Farrell [7] that optimal perturbations for plane

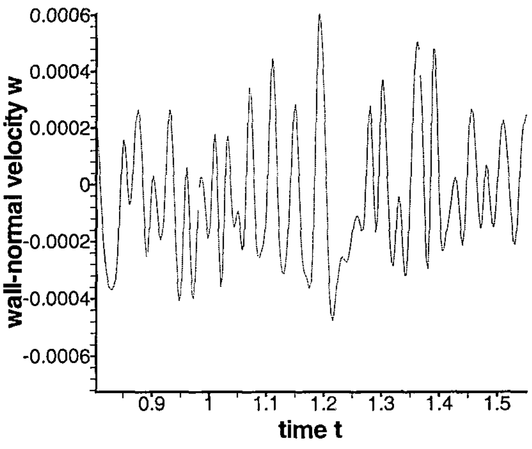

Figure 6.36: Temporal variation of wall-normal velocity component w at a point on the central plane of the channel

channel flows are independent of the longitudinal coordinate x, it was decided to develop a GOP code which has no streamwise dependence i.e. $\partial/\partial x = 0$ by modifying the original OP code (modifications performed by Prof. Sergei Chernyshenko). The solution norm was the mean energy density of the longitudinal velocity component at a given distance z from the wall:

$$||\mathbf{u}||_z^2 = \lim_{a,b\to\infty} \frac{1}{ab} \int_{x,y=0}^{x=a,y=b} u^2(x,y,z)dxdy \tag{6.11}$$

Here $\mathbf{u} = (u,v,w)$. This approach gives the streak spacing as a function of distance $|z - z_{wall}|$ to the wall and not as a single value. This norm cannot be used for imposing the restriction on the initial distribution, as it does not limit the cross-flow component. Therefore, another norm has to be prescribed for doing the same. So GOP can be formulated as: to find $\mathbf{u}_0'$ at which the solution norm $||\mathbf{u}||_s$ reaches its maximum over all $t > 0$ and over all possible $\mathbf{u}_0'$ such that the initial condition norm $||\mathbf{u}_0'||_\mathbf{i} = \mathbf{1}$. As we are solving the linearized Navier-Stokes equations, $\mathbf{u}'$ can be expressed as $\mathbf{u}' = A(t)\mathbf{u}_0'$, where $A(t)$ is a non-normal linear operator. Furthermore, assuming norms can be related to scalar products by the relation $||\mathbf{u}'||_i^2 = (\mathbf{u}',\mathbf{u}')_i$ and $||\mathbf{u}'||_s^2 = (\mathbf{u}',\mathbf{u}')_s$ the maximal problem can be cast in variational form whose functional is

$$F = (A(t)\mathbf{u}_0', A(t)\mathbf{u}_0')_s + \kappa((\mathbf{u}_0',\mathbf{u}_0')_i - 1) \tag{6.12}$$

Here κ is the Lagrange multiplier for the fixed norm of initial conditions. During the numerical implementation, the velocity $\mathbf{u}_0'$ is represented as a vector γ of finite dimension, and so the scalar products can be written as $(A(t)\mathbf{u}_0', A(t)\mathbf{u}_0')_s = \gamma^* E_t \gamma$ and $(\mathbf{u}_0',\mathbf{u}_0')_i = \gamma^* E_0 \gamma$. The $*$ denotes transposition of the vector. Hence the above equation can be transformed to the Euler-Lagrange equation

$$E_t\gamma + \kappa E_0\gamma = 0 \tag{6.13}$$

Here the eigenvalues κ correspond to the ratio of the square of the norm $||.||_s$ of the solution at time t to the square of the initial condition norm $||.||_i$. The initial condition norm $||.||_i$ was taken as the cross-flow perturbation energy density averaged over the entire channel

$$||\mathbf{u}||_c^2 = \lim_{a,b\to\infty} \frac{1}{ab}\int_{x,y,z=0,0,-1}^{x,y,z=a,b,1} (v^2+w^2)\,dxdydz \tag{6.14}$$

By using the continuity equation, a cross-flow stream function ψ can be introduced of the form $\psi = \psi_\beta(t,z)e^{\imath\beta y}$ where the amplitude ψ_β is always real. Then the velocity perturbations can be expressed as $u' = \imath u_\beta(t,z)e^{\imath\beta y}$, $v' = \imath v_\beta(t,z)e^{\imath\beta y}$ and $w' = w_\beta(t,z)e^{\imath\beta y}$. Then the three functions $u_\beta(t,z)$, $v_\beta(t,z)$ and $w_\beta(t,z)$ determine the solution $\mathbf{u}_\beta$. The solution and initial norms can now be expressed as $||\mathbf{u}_\beta||_y^2 = |u_\beta(t,z)|^2$ and $||\mathbf{u}_\beta||_c^2 = \int_{-1}^{1}(v_\beta^2 + w_\beta^2)dz$, respectively. The variational problem now consists in maximising $u_\beta(t,z)$ for given t, β and z by varying the initial distribution of $v_\beta(z)$ and $w_\beta(z)$ but keeping $||\mathbf{u}_\beta||_c^2 = 1$. The solution to the GOP problem is then obtained by maximising over all β and all $t > 0$ for a fixed wall-normal distance z. The value of β then provides the most probable streak spacing $\lambda^+ = 2\pi Re/\beta$ at a fixed wall-normal distance from the wall.

The methodology that is used to solve the governing linearised Navier-Stokes equations is very similar to that explained in subsection 2.5.1 with the energy norm now replaced by the definitions given above. The global optimal of the Lagrange multiplier $\kappa(t,\beta,z)$ now provides the measure of the most probable streak spacing. The major advantage of GOP theory over OP theory is that it provides a variation of streak spacing with distance from the wall, while OP theory just gives a constant streak spacing for all the wall-normal distances. The results of GOP theory showing variation of streak spacing l^+ with wall-normal distance are compared with DNS results of streak spacing at three wall-normal distances ($z^+ = 5.6$, $z^+ = 22.3$ and $z^+ = 39.2$) for the new mean scalar profiles $\Theta_{3D1},\ldots,\Theta_{3D7}$ and can be seen from Figure 7 in the paper by Chernyshenko and Baig [11] which has been included in the Appendix A. From the Figure, it is apparent that the GOP gives considerably much better agreement than OP for all the mean scalar profiles and even if there is disagreement for few cases, the qualitative trend is picked up very well for streak spacing variation with wall-normal distance.

Though GOP theory is a small modification technically of the OP theory and also both theories support the idea that the streak formation mechanism is the Stuart's lift-up mechanism, there is a major difference between the two regarding the selection mechanism of the streak spacing. In OP theory [7] the streak spacing is determined by the eddy turnover time which constrains the growth of the perturbations which in turn is regulated by nonlinear effects and has to be ascertained either numerically or experimentally. In contrast, the streak spacing selection mechanism in GOP theory is linear and just depends on the inherent properties of the Stuart's [60] lift-up mechanism alone.

Chapter 7

DISCUSSION AND CONCLUSIONS

7.1 Physical mechanism for streak spacing

The results for streak spacing from DNS of 3D turbulent channels flows with passive scalars clearly elucidate that for a fixed vortex structure we can get scalar streak spacing that varies by an order of magnitude and is very much dependent on the mean scalar profile. Moreover, we have seen that the results from the OP theory qualitatively show a similar behaviour and only on making a modification to the OP theory, we get a good quantitative match [11]. Hence the physical mechanism of the selection of a certain streak spacing can be described in terms of optimal perturbations. As is known from OP theory, an optimal perturbation consists of longitudinal vortices of a fixed initial energy and zero initial longitudinal velocity. Now as time progresses these cross-flow perturbations (or longitudinal vortices for $k_x = 0$ Fourier mode) decay in time, while there is a substantial growth in amplitude of longitudinal velocity perturbations u'. This growth is brought about by the linear coupling term $w\frac{dU}{dz}$ of the linearized Navier-Stokes equations, especially by the wall-normal velocity component w of the optimal vortex. For small spanwise wavelengths or smaller diameter vortices, the effect of viscosity is more strong and these vortices decay out faster before lift-up mechanism can act on the wall-region fluid. For very large spanwise wavelengths of the longitudinal vortices almost all the kinetic energy is concentrated in the spanwise velocity component, hence there is a weak lift-up effect which results in small amplitude of the streaks. This clearly points that there is a optimum wavelength for which maximum amplitude of streaks is observed.

Based on the above physical mechanism, the streak scale mechanism can be formulated as: Streaks are generated due to wall-normal motions advecting the low-speed momentum fluid away from the wall to high-speed momentum fluid region. The streak spacing is determined by the balance between the viscous diffusion, which constraints the minimal streak spacing, and reduction in wall-normal velocity component of perturbations as the wavelength increases which constraints the maximum streak spacing.

7.2 Origin of structures in turbulence

The theme of the present study causes one to ask the question, what constitutes the primary structure in turbulent shear flows: Is it organised vortices or is it streaks? From the results of the present study we know that streaks emerge from chaotic motion through the GOP with no involvement of organised vortices; it is possible that organised vortices are created by the streaks. Such vortex generation by streaks is most likely to involve lifting-up of streaks and nonlinearity to play a role as has been shown by Waleffe et. al. [67] and Schoppa and Hussain [50]. These organised vortices are then most likely to inherit the same spacing from streaks as we know that the linearised Navier-Stokes equations favour longitudinal vortices of much larger spacing [67]. This is also evident from the results of Kim and Lim [31] that when they switched off the non-linear terms in their DNS simulations they recorded a substantial increase in vortex spacing.

Based on the above discussion there can possibly be two regeneration cycles of coherent structures in developed turbulent flows. One of the cycle can be a closed regeneration cycle having no primary organised structure i.e. organised vortices produce streaks and streaks in turn produce vortices and the spatially random process is repeated cyclically. Another cycle can be certain primary structures (like streaks) appear directly from chaotic background and they in turn produce other structures (such as organised vortices) which subsequently by nonlinear interactions with each other again generate a chaotic background flow. The results of this study favour the second concept due to the appearance of streaks as primary structures from a chaotic background flow.

7.3 Conclusions

Though we have discussed conclusions at the end of each chapter, here we aim to provide a succinct summary of conclusions:

1. Our numerical experiments in quasi-2D decaying turbulence show that streaks can form even in case when there is no feedback from the streaky longitudinal flow profile, to the cross-flow vortex structure.
2. The passive scalar streak spacing varies significantly even when the vortical structure generated by the velocity field is fixed. This clearly demonstrates that organised vortices play no role in the development of streaks (either velocity or scalar concentration streaks.)
3. Vortex regeneration theories which assume the streak spacing being equal to twice the vortex spacing, like, for example, RNSAI, cannot explain this fact.
4. The scalar streak spacing strongly depends on the mean profile of the scalar and this behaviour is only described by OP theory, though in many cases the the theoretical prediction of streak spacing by OP differs considerably from DNS results.
5. Scalar streaks can be generated in a random potential velocity field with a mean turbulent velocity profile, thereby strongly corroborating the fact that organized vortices play no significant role and it is the lift-up mechanism [60] which is responsible for formation of streaks as well as their cross-flow spacing.
6. The modification of OP to GOP theory results in development of a theory whose predictions are in good agreement with the DNS results of scalar streak spacings.

7.4 Suggestions for future work

As in our 3D DNS simulation the size of the computational box in spanwise direction was only 1080 wall units, it became a problem to perform comparison with GOP predictions for scalar mean profiles exhibiting a large spanwise streak spacings. So we would like to propose that another DNS of 3D turbulent channel flows should be performed in a much bigger computational box so that comparison of theoretical predictions from GOP theory with DNS results can be performed even for scalar profiles which have large spanwise streak spacing. Moreover, the basic scalar mean profiles that should be used must be Chebyshev polynomials, so that practically any new mean profile could be represented as a linear combination of them, without incurring the difficulties associated with ill-posed problems which need regularization of the coefficient matrix [17].

As has been stated earlier in the chapter, up till now the question of possible regeneration cycles is not clear. So we propose that future work should be performed with the intention of discovering organised vortices in an unstructured velocity field by supplying an initial condition of mean flow with random potential perturbations (so that no coherent vortices are present) to which a streaky velocity profile has been added. If in the ensuing numerical simulation there is the process of vortex generation by streaks, it would provide a proof that streaks are the primary structures and other organised structures follow from it and hence provide support to the idea of linear regeneration cycle. This numerical experiment will also be able to explain the numerous observations of vortices correlating with streaks but now in the context that streaks generate the vortices instead of the current perception that organised vortices are responsible for streaks.

Another possible area which can be further investigated is generation of passive scalar streaks in a flow with potential fluctuations. There are at least three factors which can affect significantly the scalar streak spacing. Specifically one can examine the effect of characteristics time scale of the random potential perturbations on the scalar streak spacing in more detail. Besides this simulations pertaining to variation of the mean scalar profile can also be performed in order to see their effect on the scalar streak spacing. The third crucial factor is the number of Fourier modes used in generation of random potential velocity field.

Bibliography

[1] M.S. Acarlar and C.R. Smith. A study of hairpin vortices in a laminar boundary layer. *J. Fluid Mech.*, 175:1–83, 1987.

[2] N. Aubry, P. Holmes, J.L. Lumley, and E. Stone. The dynamics of coherent structures in wall region of turbulent boundary layer. *J. Fluid Mech.*, 192:115–173, 1988.

[3] R.F. Blackwelder and H. Eckelmann. Streamwise vortices associated with the bursting phenomenon. *J. Fluid Mech.*, 94:577–594, 1979.

[4] J.W. Brooke and T. J. Hanratty. Origin of turbulence producing eddies in a channel flow. *Phys. of Fluids A*, 5:1011–1021, 1993.

[5] G.L. Brown and A.S.W Thomas. Large structure in a turbulent boundary layer. *Phys. of Fluids*, 20:5243, 1977.

[6] K. M. Butler and B. F. Farrell. Three-dimensional optimal perturbations in viscous shear flow. *Phys. of Fluids*, 4:1637–1650, 1992.

[7] K. M. Butler and B. F. Farrell. Optimal perturbations and streak spacing in wall-bounded turbulent shear flows. *Phys. of Fluids A*, 5:774–777, 1993.

[8] B. J. Cantwell. Organized motion in turbulent flow. *Ann. Rev. of Fluid Mechanics*, 13:457–515, 1981.

[9] C. Canuto, M. Y. Hussaini, A. Quarteroni, and T. Zang. *Spectral methods in fluid dynamics.* Springer-Verlag, 1988.

[10] J. R. Chasnov. On the decay of two dimensional homogeneous turbulence. *Phys. of Fluids*, 9:171–180, 1997.

[11] S.I. Chernyshenko and M. F. Baig. The mechanism of streak formation in near-wall turbulence. *submitted to J. of Fluid Mechanics*, 2003.

[12] E.R. Corino and R.S. Brodkey. A visual investigation of the wall region in turbulent flow. *J. Fluid Mech.*, 37:1–30, 1969.

[13] A.D.D. Craik. Wave-induced longitudinal-vortex instability in shear flows. *J. Fluid Mech.*, 125:37, 1982.

[14] B.F. Farrell. Optimal excitation of perturbations in viscous shear flow. *Phys. of Fluids*, 31:2093–2102, 1988.

[15] U. Frisch and P.L. Sulem. *Phys. of Fluids*, 27:1921–1927, 1984.

[16] J. M. Hamilton, J. Kim, and F. Waleffe. Regeneration mechanisms of near-wall turbulence structures. *J. Fluid Mech.*, 232:317–348, 1995.

[17] P.C. Hansen. *Rank-Deficient and Discrete Ill-Posed Problems*. SIAM, Philadelphia, 1998.

[18] M. R. Head and P. Bandyopadhyay. New aspects of the boundary layer structure. *J. Fluid Mech.*, 107:297–338, 1981.

[19] Z. Hu, C. L. Morfey, and N. D. Sandham. Aeroacoustics of plane turbulent flows,. Technical Report AFM-01/02, University of Southampton, 2001.

[20] Z. Hu and N. D. Sandham. Dns databases for turbulent couette and poiseuille flow. Technical Report Tech. Rep. 01/04, SES, University of Southampton, 2001.

[21] Z. W. Hu and N. D. Sandham. Large-domain simulations of couette and poiseuille flow. In *Proc. 2nd Inter. Symposium on Turbulent and Shear Flow Phenomena*, Stockholm, 2001.

[22] P. S. Jang, D. J. Benney, and R. L. Gran. On the origin of streamwise vortices in a turbulent boundary layer. *J. Fluid Mech.*, 169:109–123, 1986.

[23] J. Jeong, F. Hussain, W. Schoppa, and J. Kim. Coherent structures near the wall in a turbulent channel flow. *J. Fluid Mech.*, 332:185–214, 1997.

[24] J. Jimenez. Some open computational problems in wall-bounded turbulence. In C. Dopazo et. al., editor, *Advances in Turbulence VIII*, page 637, Barcelona, 2000. CIMNE. Proceedings of the Eighth European Conference.

[25] J. Jimenez and P. Moin. The minimal flow unit in a near-wall turbulence. *J. Fluid Mech.*, 225:213–240, 1991.

[26] J. Jimenez and P. Orlandi. The roll-up of a vortex layer near a wall. *J. Fluid Mech.*, 248:297, 1993.

[27] J. Jimenez and A. Pinelli. The autonomous cycle of near-wall turbulence. *J. Fluid Mech.*, 389:335–359, 1999.

[28] A.V. Johansson, J.V. Her, and J.H Haritonidis. On the generation of high amplitude wall-pressure peaks in turbulent boundary layers and spots. *J. Fluid Mech.*, 175:119–142, 1987.

[29] N. Kasagi, J. Tomita, and A. Kuroda. Direct numerical simulation of passive scalar field in a turbulent channel flow. *Journal of Heat Transfer*, 114(9):598–606, 1992.

[30] H.T. Kim, S.J. Kline, and W.C. Reynolds. The production of turbulence near a smooth wall in a turbulent boundary layer. *J. Fluid Mech.*, 50:133–160, 1971.

[31] J. Kim and J. Lim. A linear process in wall-bounded turbulent shear flows. *Phys. of Fluids*, 12(9):1885–1888, 2000.

[32] J. Kim and P. Moin. Transport of passive scalars in a turbulent channel flow. In J.C. et. al. Andre, editor, *Turbulent shear flows 6*, pages 85–96, Heidelberg, 1989. Springer-Verlag.

[33] J. Kim, P. Moin, and R. Moser. Turbulence in channel flow at low reynolds number. *J. Fluid Mech.*, 177:133–160, 1987.

[34] L. Kleiser and U. Schumann. Treatment of incompressibility and boundary conditions in 3d numerical spectral simulations of plane channel flows. In E.H. Hirschel, editor, *Proc. 3rd GAMM Conf. on Numerical Methods in Fluid Mechanics*, pages 165–173. Vieweg, 1980.

[35] S.J. Kline and P.W. Runstadler. Some preliminary results of visual studies of the wall layers of the turbulent boundary layers. *Trans. ASME Series E*, 2, 1959.

[36] R.H. Kraichnan. Inertial ranges in two-dimensional turbulence. *Phys. of Fluids*, 10:1417–1423, 1967.

[37] B.K. Martin, X.L. Wu, W.I. Goldburg, and M.A. Rutgers. Spectra of decaying turbulence in a soap film. *Physical Review Letters*, 80(18):3964–3967, 1998.

[38] N.V. Nikitin and S.I. Chernyshenko. On the nature of the organised structures in turbulent near-wall flows. *Fluid Dynamics*, 32(1):18–23, 1997. Translated from Izvestiya Rossiiskoi Akademii Nauk, Mekhanika Zhidkosti i Gaza, No. 1, pp. 24–30, 1997.

[39] P. Orlandi and J. Jimenez. On the generation of turbulent wall friction. *Phys. of Fluids*, 6:634–641, 1994.

[40] S.S. Panchev. *Random functions and Turbulence*. Pergamon Press, New York, 1971.

[41] A. E. Perry and M. S. Chong. On the mechanisms of wall turbulence. *J. Fluid Mech.*, 119:173–217, 1982.

[42] W.H. Press, S.A. Teukolsky, W.T. Vellerling, and B.P. Flannery. *Numerical Recipes in Fortran.* Cambridge University Press, Cambridge, 1992.

[43] S.C. Reddy and D.S. Henningson. Energy growth in viscous channel flows. *J. Fluid Mech.*, 252:209–238, 1993.

[44] S.K. Robinson. Coherent motions in the turbulent boundary layer. *Ann. Rev. Fluid Mech.*, (23):601–639, 1991.

[45] S.K. Robinson. Kinematics of turbulent boundary layer structure,. Technical Report TM 103859, NASA, 1991.

[46] M.A. Rutgers. Forced 2d turbulence: Experimental evidence of simultaneous inverse energy and forward enstrophy cascades. *Physical Review Letters*, 81(11):2244–2247, 1998.

[47] N.D. Sandham and R.J.A. Howard. Direct simulation of turbulence using massively parallel computers. In D.R. Emerson, A. Ecer, J. Periaux, N. Satofuka, and P. Fox, editors, *Parallel Computational Fluid Dynamics*. North-Holland, 1998.

[48] W. Schoppa and A.K.M.F. Hussain. Formation of near-wall streamwise vortices by streak instability. Technical Report 98-3000, AIAA, 1998. 29th AIAA Fluid Dynamics Conf., Albuquerque, NM, U.S.A.

[49] W. Schoppa and F. Hussain. Genesis and dynamics of coherent structures in near-wall turbulence: A new look. In R.L. Panton, editor, *Self-sustaining mechanism of wall turbulence*. Southampton: Computational Mechanics, 1997.

[50] W. Schoppa and F. Hussain. Coherent structure generation in near-wall turbulence. *J. Fluid Mech.*, 453:57–108, 2002.

[51] F.A Schraub and S.J. Kline. A study of the turbulent boundary layer with and without longitudinal pressure gradients. Technical Report MD-12, Mech. Engrg. Dept., Stanford University, 1965.

[52] C.R. Smith and S.P. Metzler. The characteristics of low-speed streaks in the near-wall region of a turbulent boundary layer. *J. Fluid Mech.*, 129:27–54, 1983.

[53] C.R. Smith and J.D.A Walker. Turbulent wall layer vortices. In S. Green, editor, *Fluid Vortices*. Springer-Verlag, 1994.

[54] C.R. Smith and J.D.A Walker. Sustaining mechanisms of turbulent boundary layers: The role of vortex development and interactions. In R.L. Panton, editor, *Self-sustaining mechanisms of wall turbulence*. Southampton: Computational Mechanics, 1997.

[55] C.R. Smith, J.D.A. Walker, A.H. Haidari, and U. Sobrun. On the dynamics of near-wall turbulence. *Phil. Trans. of the Royal Soc. of London A*, 336:131–175, 1991.

[56] L.M. Smith and V. Yakhot. *Physical Review Letters*, 71:352–354, 1993.

[57] P.R. Spalart. Direct sumulation of a turbulent boundary layer up to $re_\theta = 1410$. *J. Fluid Mech.*, 187:61–98, 1988.

[58] P.R. Spalart, R.D. Moser, and M. M. Rogers. Spectral methods for the navier-stokes equations with one infinite and two periodic directions. *J. of Computational Physics*, 96(2):297–324, 1991.

[59] K.R. Sreenivasan. A unified view of the origin and morphology of the turbulent boundary layer structure. In H.W. Liepmann and R. Narasimha, editors, *Proc. IUTAM Symp. on Turbulence Management and Relaminarisation*, pages 37–61. Springer, 1988.

[60] J.T. Stuart. The production of inrense shear layers by stretching and convection. Technical Report 514, NATO AGARD Report, 1965.

[61] J. D. Swearingen and R. F. Blackwelder. The growth and breakdown of streamwise vortices in the presence of a wall. *J. Fluid Mech.*, 182:225, 1987.

[62] T. Theodorsen. Mechanism of turbulence. In *In Proc. 2nd Midwestern Conf. on Fluid Mechanics*, page Bulletin No. 149. OSU, Ohio, 1952.

[63] A.N. Tikhonov, A.V. Goncharskii, V.V. Stepanov, and A.G. Yagoda. *Numerical Methods for the Solutions of Ill-Posed Problems.* Kluwer, Dordrecht, 1995.

[64] A. A. Townsend. *The structure of turbulent shear flow.* Second Edition, Cambridge University Press, 1956.

[65] F. Waleffe. Hydrodynamic stability and turbulence: beyond transients to a self-sustaining process. *Studies in Appl. Math.*, 95:319–343, 1995.

[66] F. Waleffe. Homotopy of exact coherent structures in plane shear flows. *Phys. of Fluids*, 15:1517–1534, 2003.

[67] F. Waleffe and J. Kim. How streamwise rolls and streaks self-sustain in a shear flow. In R.L. Panton, editor, *Self-Sustaining Mechanism of Wall Turbulence*, pages 309–331. Southampton: Computational Mechanics, 1997.

[68] F. Waleffe, J. Kim, and J. M. Hamilton. On the origin of streaks in turbulent boundary layers. In F. Durst, R. Friedrich, B. E. Launder, F. W. Schmidt, U. Schumann, and J.H. Whitelaw, editors, *Turbulent Shear Flows 8*, pages 37–49. Springer, 1993.

[69] W.W. Willmarth. Structure of turbulence in boundary layers. In *Advances in Applied Mechanics*, pages 159–254. 1975.

[70] J. Zhou, R. J. Adrian, and S. Balachandar. Mechanisms for generating coherent packets of hairpin vortices in channel flow. *J. Fluid Mech.*, 387:353–396, 1999.

[71] J. Zhou, R.J. Adrian, and S. Balachandar. Autogeneration of near-wall vortical structures in a channel flow. *Phys. of Fluids*, 8:288, 1996.

Appendix A

The mechanism of streak formation in near-wall turbulence

The mechanism of streak formation in near-wall turbulence

By S. I. CHERNYSHENKO AND M. F. BAIG

School of Engineering Sciences, University of Southampton, Southampton, SO17 1BJ, UK

(Received ?? and in revised form ??)

It is demonstrated that the lift-up mechanism responsible for formation of streaks in near-wall turbulent flows is also responsible for their cross-flow spacing, with organised vortices playing no significant part in the selection of streak spacing.

A generalisation of the optimal perturbation approach is proposed in which the solution norm being maximised differs from the solution norm used to formulate the restriction on the initial condition. Using the solution norm equal to the averaged perturbation energy at a given distance to the wall, the dependence of the streak spacing on the distance to the wall is obtained. The approach emphasises the fact that the optimal perturbation theory does predict the streaks but it does not predict streamwise vortices. Numerical calculations were performed of turbulent channel flow with several passive scalars. Streaks of scalar concentration were observed. Although the vortical structure of the flow is the same, the scalar streak spacing varies by an order of magnitude depending on the mean profile of the scalar concentration in agreement with the predictions of generalised optimal perturbation theory, thereby clearly demonstrating that streak spacing is independent of vortices and supporting the theory. Calculations of scalar concentration were also performed with the velocity of the carrier phase taken as the sum of mean turbulent profile and random potential perturbation. Such velocity field has no organised vortices. Nonetheless scalar streaks were observed.

1. Introduction

1.1. *Streaks*

Turbulent flows are not entirely chaotic. Smoke visualisation of a turbulent boundary layer can look similar to the picture in figure 1 (the picture plane is parallel to the wall). The observed pattern is neither completely ordered nor quite chaotic. One can clearly see, for example, the difference between the horizontal (which is along the mean flow) and vertical (which is parallel to the wall and perpendicular to the mean flow, and which is often called spanwise) directions. In fact, one sees here some objects elongated in the direction of the mean flow. This is an example of organised structures. It is possible, although not easy, to give a mathematical definition of organised structures, using, for example, conditional averaging. However, for the purpose of the present paper it is sufficient that, once having a good look at them, one can recognise them and distinguish them from other structures. A variety of organised structures is observed in turbulent flows. The structures shown in figure 1 are the subject of the present paper. These structures are called streaks, or, more specifically, near-wall streaks.

Streaks observed with the help of smoke visualisation are just that, streaks of smoke. Experimental measurements and numerical calculations show that from kinematic viewpoint streaks are regions of slow fluid motion. In fact, figure 1 shows the visualisation

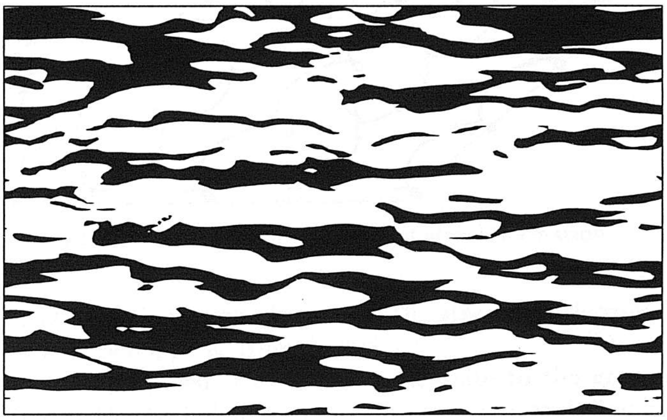

FIGURE 1. Steaks in near-wall turbulent flow at $y^+ = 5.6$ from the wall.

of the instantaneous longitudinal velocity at the fixed distance from the wall $y^+ = 5.6$, with dark areas corresponding to lower velocity. The velocity distribution was obtained by direct numerical simulation undertaken in the course of the present study. Streaks are universal, they are always observed in near-wall turbulent flows and their characteristic dimensions are always the same if expressed in wall units and measured immediately at the wall: the length is about 1000 and the spanwise period about 100. To be more accurate, the dimensions depend on the distance to the wall (Smith & Metzler 1983). As the wall distance increases the streak spacing increases, but streaks become less and less discernible.

In direct numerical simulation of turbulent flow it is possible to observe the effect of removing specific terms from the Navier–Stokes equations. This is an important method of investigating the mechanism of turbulence (see Jiménez, Pinelli & Uhlmann 2000). It is well-known now that streaks disappear if the term $v\partial u/\partial y$ is removed, were u and v are the longitudinal and wall-normal velocity components and y is the wall-normal coordinate. Moreover, u can be represented as a sum of the averaged velocity U and a fluctuation, and numerical experiments show (Kim & Lim 2000) that it is the $v\partial U/\partial y$ term which is responsible for formation of streaks. In other words, the regions of slow fluid motion appear because there are wall-normal motions advecting the slow-moving near-wall fluid into the region away from the wall. The lift-up mechanism of streak formation was first described by Stuart (1965). Figure 2 illustrates it. Rows of vortices elongated in the direction of the mean flow and rotating in alternating directions capture the fluid and advect it from the wall and to the wall in alternating stripes. The fluid advected from the wall is moving slower than on average at this distance from the wall, while fluid advected to the wall is moving faster. This creates the wavy longitudinal velocity profile at a fixed distance from the wall shown in figure 2. The same vortices advect smoke creating streaks similar to figure 1.

Near-wall streaks are very important. Numerical experiments show that if streaks are somehow suppressed the turbulence intensity is reduced significantly. Convex velocity profiles are much more stable than profiles with inflection points in the sense that perturbations of velocity profiles with inflection points grow much faster. The mean velocity profile is convex while the streak velocity profiles have inflection points. It was also sug-

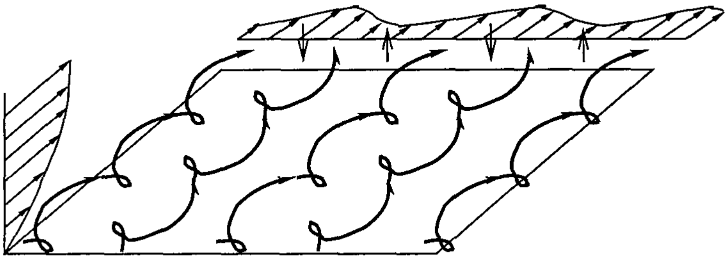

FIGURE 2. Lift-up mechanism of streak formation

gested that transient growth of perturbations of the streaky background flow may be of even more importance (Schoppa & Hussain 2002)

Anyway, it is generally agreed that streaks contribute to the generation of the turbulence energy. Then, the turbulence energy regeneration cycle includes formation of streaks, instability growth at their inflection points or transient growth, and, finally, breakdown of streaks when the perturbations become large. However, there is no generally accepted view on the mechanism of streak formation, and numerous competing theories and conceptual models exist. Some of them can be found in the book edited by Panton (1997). Other references are Jang, Benney & Gran (1986); Sreenivasan (1988); Brooke & Hanratty (1993); Butler & Farrell (1993); Waleffe, Kim & Hamilton (1993); Smith & Walker (1994); Hamilton, Kim & Waleffe (1995); Nikitin & Chernyshenko (1997); Schoppa & Hussain (1998).

Figure 2 implies that the distance between streaks is equal to the period of the vortices. Accordingly, almost all the theories aiming at predicting streak spacing describe in fact mechanisms of vortex formation and predict the vortex spacing. The situation is further complicated by the fact that experiments and numerical calculations give no clear evidence of significant vortices with spanwise dimensions corresponding to streaks. According to Robinson (1991) in the vicinity of streaks there are longitudinal vortices of the length of about one fifth of streak length. On the other hand, it is also known that the spanwise autocorrelation function for the wall-normal velocity has a minimum at $\Delta z^+ \approx 25$ (see, for example, the data in the database of Moser *et al.* (1999) or Hu & Sandham (2001*a*)†) and not at half the streak spacing ($\approx 100/2 = 50$) as implied by figure 2. The uncertainty concerning the numerical and experimental observations of longitudinal vortices of the same spacing as streaks is a serious problem for the majority of the theories of streak formation.

1.2. *Streaks and vortices*

Further introduction can be considerably simplified if we state briefly one of our recent results (Baig & Chernyshenko 2003, see also section 3, which gives full description of the calculations and extensive comparisons with the theory).

The mechanism of formation of streaks of smoke is the same as that of velocity streaks. Indeed, the equation for smoke concentration θ contains the term $v\partial\theta/\partial y$ similar to the term $v\partial u/\partial y$ responsible for the velocity streaks and lacks only the term $\partial p/\partial x$ which anyway is known not to contribute to streak formation (see the passive scalar calculations of Kim & Moin (1989) and Kasagi, Tomita & Kuroda (1992)). We have calculated the spanwise period of streaks of smoke modelled as passive scalar, for different profiles of mean scalar concentration in direct numerical simulation of a turbulent channel flow.

---

† Available online at http://www.tam.uiuc.edu/faculty/moser/channel/ and http://www.afm.ses.soton.ac.uk/~zhi/channeldata/Poiseuille/ respectively

Several scalars were assumed to be present simultaneously in the flow and calculated in a single run. It turns out that the streak spacing for different scalars differs by an order of magnitude depending on the profile of the mean concentration. The velocity and vorticity fields are independent of the scalar concentration, of course. In other words, exactly the same vortices can produce very different streaks. This disproves all theories which predict streak spacing by predicting vortex spacing and assuming them to be equal‡. The only remaining theory is the application of optimal perturbations to predicting streak spacing (Butler & Farrell 1993). It has to be noted that this theory is presented in the Butler & Farrell (1993) paper in such a way that its ability to qualitatively explain our numerical result is far from obvious. In fact, only a generalised optimal perturbation theory (section 2) makes it clear that optimal perturbations can explain the formation of streaks without an implication that the vortex structure of the real flow is similar to the vortex structure of the optimal perturbation creating streaks. We will proceed now with an outline of the idea of optimal perturbations as applied to turbulent flows by Butler & Farrell (1993), leaving other theories aside.

1.3. *Background to optimal perturbation theory*

The optimal perturbation theory is based on the linearised Navier–Stokes equations, while turbulent flow is a non-linear phenomenon. However, application of linear theories to the description of structures observed in nonlinear phenomena can make sense. For example, a horizontal fluid layer at rest heated from below looses it stability if heating is sufficiently strong. Small perturbations grow exponentially in accordance with linear theory until their amplitude becomes so large that non-linear effects become significant. Naturally, the structures in the non-linear flow, that is convective rolls or cells, are not governed by linearised equations. Nevertheless, it often happens that the shape and dimensions of these nonlinear structures are close to the shape and dimensions of the perturbations having the fastest growth rate according to the linearised theory. Therefore, it is quite reasonable to take the mean (and, therefore, not containing any structures) velocity distribution in the turbulent flow and to try to determine what kind of structures will grow the fastest from small perturbations of this velocity distribution governed by linearised equations. It is also possible to take the laminar velocity profile but since we are interested in the developed turbulent flow the mean turbulent profile is a better choice.

This simple idea meets, however, with a certain difficulty. In the case of the plane channel flow it turns out that within a linear theory all perturbations decay, even at such Reynolds numbers when the flow is turbulent and streaks are well developed. The optimal perturbation theory, developed initially for studying the stability of steady flows (see the review by Trefethen, Trefethen, Reddy & Driscoll (1993)) helps to overcome this difficulty. Substituting $\boldsymbol{u} = \boldsymbol{U} + \boldsymbol{u}'$, $\boldsymbol{u}' \ll 1$ into the Navier–Stokes and continuity equations

$$\frac{\partial \boldsymbol{u}}{\partial t} + \boldsymbol{u} \cdot \nabla \boldsymbol{u} = -\nabla p + \frac{1}{\mathrm{Re}} \nabla^2 \boldsymbol{u}, \qquad \nabla \boldsymbol{u} = 0 \tag{1.1}$$

and neglecting quadratic terms gives the linearised Navier–Stokes equations for $\boldsymbol{u}'$

$$\frac{\partial \boldsymbol{u}'}{\partial t} + \boldsymbol{U} \cdot \nabla \boldsymbol{u}' + \boldsymbol{u}' \cdot \nabla \boldsymbol{U} = -\nabla p' + \frac{1}{\mathrm{Re}} \nabla^2 \boldsymbol{u}', \qquad \nabla \boldsymbol{u}' = 0. \tag{1.2}$$

Assuming $\boldsymbol{u}' = e^{\sigma t} \tilde{\boldsymbol{u}}(x)$ gives an eigenproblem

$$\sigma \tilde{\boldsymbol{u}} + \boldsymbol{U} \cdot \nabla \tilde{\boldsymbol{u}} + \tilde{\boldsymbol{u}} \cdot \nabla \boldsymbol{U} = -\nabla \tilde{p} + \frac{1}{\mathrm{Re}} \nabla^2 \tilde{\boldsymbol{u}}, \qquad \nabla \tilde{\boldsymbol{u}} = 0.$$

---

‡ Note that among others this disproves our own theory (Nikitin & Chernyshenko 1997), too.

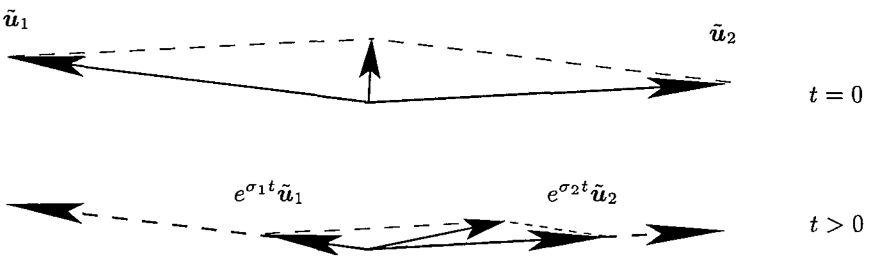

FIGURE 3. Transient growth

This eigenproblem has infinite number of solutions, but all of them decay, that is the real part of σ is always negative. However, in spite of this, the solution of linearised Navier–Stokes equations can exhibit a transient growth. For example, let us assume that for two eigensolutions $\sigma_1 < \sigma_2 < 0$ and that $u' = \tilde{u}_1 + \tilde{u}_2$ at $t = 0$. Then $u' = e^{\sigma_1 t}\tilde{u}_1 + e^{\sigma_2 t}\tilde{u}_2 \to 0$ as $t \to \infty$. It can happen, however, that $\tilde{u}_1 \approx -\tilde{u}_2$. Then $u' \approx (e^{\sigma_1 t} - e^{\sigma_2 t})\tilde{u}_1$. If $\sigma_1 \neq \sigma_2$ then at $t > 0$ the difference between the exponentials is not equal to zero because the exponentials decay with different rate. Therefore, u' may grow. Figure 3 shows how an initially small vector equal to the sum of two almost opposite vectors grows initially when one of the summands decays faster than the other. Eventually the sum will tend to zero anyway, of course.

From figure 3 it is clear that such transient growth is possible only if vectors $\tilde{u}_1$ and $\tilde{u}_2$ are non-orthogonal. To speak about orthogonality of the eigensolutions one needs a dot, or scalar product. Eigensolutions are functions, and their scalar product is usually defined as

$$(u_1, u_2) = \int u_1 u_2 \, dx,$$

where the integral is taken over the entire flow field, suitably normalised if necessary. In the general case the eigenfunctions of the linearised Navier–Stokes operator are non-orthogonal. The scalar product also makes it possible to measure u': the norm $||u'|| = \sqrt{(u', u')}$ is just the square root of the kinetic energy of the perturbation. The optimal perturbation is the perturbation whose energy grows by a maximum factor prior to decay. The exact formulation of the optimal perturbation problem is: find the initial condition $u'_{|t=0} = u'_0$ and the corresponding u' that $||u'_0|| = 1$ and the $\max_{t>0} ||u'||$ is the greatest possible. There exists quite extensive literature on the subject, see papers by Butler & Farrell (1992), Trefethen *et al.* (1993) and Criminale, Jackson & Lasseigne (1995) and references therein.

The solution of this problem shows that in practically interesting cases the energy of the initial perturbation can grow by a factor of several hundreds or even more. Naturally, this is very important for the transition to turbulence. As far as the streaks are concerned, the following result was obtained. Butler & Farrell (1993) assumed U to be the mean velocity in turbulent flow in a plane channel. They calculated the optimal perturbations for the Reynolds number based on the dynamic velocity and the channel half-width $Re = 180$ (this corresponds to the Reynolds number based on the maximal velocity and the channel width $Re_{max} \approx 6480$). The structure of the optimal perturbation involved strong streaks. The perturbation energy grew significantly (by a factor of 235), but the streak spacing was much greater ($l^+ = 540$) than in reality (at the wall $l^+ \approx 100$). The time needed for the energy to attain the maximum value turned out to be much greater that the characteristic time scale of small-scale turbulent fluctuations. Then they suggested an assumption that in reality the perturbation exists only over a limited time equal to the so-called eddy turnover time $t_e = q^2/\epsilon$, which is the ratio of the characteristic turbulent velocity, defined as $q^2 = \langle u_i u_i \rangle$, to the dissipation rate, $\epsilon = \langle \nu u_{i,j} u_{i,j} \rangle$. After this time the perturbation is assumed to be destroyed by turbulent fluctuations. Here and throughout the paper angular brackets $\langle . \rangle$ denote averaging. The eddy turnover time depends on the distance to the wall, and Butler & Farrell (1993) proposed to take its value at the center of the streak. With this correction the streak spacing was found to be close to the experiment. Further discussion is continued in the concluding section.

1.4. *The structure of the paper*

Section 2 describes the generalised optimal perturbation theory developed in the present study. This theory makes it possible to calculate streak spacing as a function of the distance to the wall and without limiting the life time of the perturbation. Also, the generalised optimal perturbation emphasises the fact that there is no reason to believe that longitudinal vortices characteristic of optimal perturbation solutions can be observed in reality. Section 3 describes numerical calculations performed specifically in order to demonstrate that streak spacing may vary considerably (by an order of magnitude) with vortices in the flow being fixed. This calculations provided material for extensive comparisons with the theory. Section 3 also demonstrates that streaks may appear even when there are no organised vortices in the flow, by calculating the scalar concentration for the case when the velocity distribution of the carrier phase is a sum of a mean velocity profile and a potential perturbation. Discussion and conclusion section addresses the implications of the obtained results in the wider field of turbulence theory. The method of calculating the generalised optimal perturbations is described in the Appendix.

Certain readers may be interested in understanding the results of the present study without going through the more mathematical parts of the paper. For this reason the paper is structured so that the more complicated parts are isolated within certain subsections. To avoid these subsections, the reader may now proceed through the subsection 2.1, have a look at the comparison in figures 4 and 6 and then go to subsection 2.5. Similarly, in section 3 subsection 3.2 can be skipped. Full strength of the obtained results can of course be perceived only by reading the entire paper.

2. Generalised optimal perturbations

2.1. *The idea.*

The above argument leading to limiting the evolution time of the optimal perturbation by the eddy turnover time is far from perfect. Waleffe & Kim (1997) point out that this simply transforms the length-scale selection problem into the time-scale selection problem. Anyway, an initial value problem is not directly relevant for a developed turbulent flow. Rather, one can argue that the linearised Navier–Stokes equations form an important part of the full nonlinear Navier–Stokes equations, so that the structures favoured by the linearised Navier–Stokes equations can be expected to be observed in the solution of the full Navier–Stokes equations. The optimal perturbation is then just a simple (and certainly not the only; consider for example the pseudo-spectra approach (Trefethen *et al.* 1993) or forced response studies (Jovanović & Bamieh 2001)) way to determine which structures are favoured by the linearised Navier–Stokes equations. Since developed turbulent flow exists for a very long time, limiting the evolution time of the optimal perturbation cannot be justified.

On the other hand, there is another explanation why, without eddy-turnover-time adjustment, the standard optimal perturbation theory does not predict the correct streak spacing. It is well known that streaks are an essentially near-wall feature. The streak spacing increases and streak strength decreases with the distance from the wall. The energy norm used by Butler and Farrell is equivalent to some kind of averaging across the channel. A solution with very strong streaks localised near the walls and very weak in other parts of the flow domain can have quite a small energy norm as compared to a solution of moderate amplitude but occupying a considerable part of the flow domain. Therefore, this norm favours large-scale solutions and may ignore solutions with strongest streaks. To improve on this, we suggest the use of a different norm, which would emphasise the flow parameters at a given distance from the wall. For example, such a norm used in the present study is just the mean energy density of the longitudinal velocity component at a given value of the wall-normal coordinate y.

$$||\boldsymbol{u}||_y^2 = \lim_{a,b\to\infty} \frac{1}{ab} \int_{x,z=0}^{x=a,z=b} u^2(x,y,z)\, dx\, dz. \tag{2.1}$$

In this paper we consider a plane channel flow. The longitudinal, wall-normal, and spanwise coordinates and perturbation velocity components are denoted x, y, z, and u, v, w respectively, so that $\boldsymbol{u} = (u, v, w)$. Importantly, in contrast to other theories, our approach gives the streak spacing not as a single value but as a function of the distance $|y - y_{\mathrm{wall}}|$ to the wall which can be compared with the corresponding function obtained experimentally or numerically.

The norm (2.1) cannot be used for imposing the restriction on the possible initial distribution, since it does not limit the cross-flow component. It also does not limit the longitudinal velocity at other y. Hence, it would not limit the maximum growth. Therefore, another norm has to be used for this purpose. Accordingly, we formulate a generalised optimal perturbation problem: to find $\boldsymbol{u}_0'$ at which the solution norm $||\boldsymbol{u}'||_s$ reaches its maximum over all $t > 0$ and over all possible $\boldsymbol{u}_0'$ such that the initial condition norm $||\boldsymbol{u}_0'||_i = 1$.

If $||.||_i$ and $||.||_s$ coincide then the generalised optimal perturbation problem reduces to the optimal perturbation problem in its usual formulation. The norms $||.||_i$ and $||.||_s$ should be tailored to the specific problem in question and can differ from those used in the present study.

Since (1.2) is linear, the dependence of $\boldsymbol{u}'$ on $\boldsymbol{u}_0'$ can be expressed as $\boldsymbol{u}' = A(t)\boldsymbol{u}_0'$, where $A(t)$ is a linear operator depending on time t. Finding the optimal perturbation can be done in two steps, first maximising $||\boldsymbol{u}'(t)||_s$ over $\boldsymbol{u}_0'$ with t fixed and then maximising the result over $t > 0$. Assuming that scalar products $(.,.)_i$, $(.,.)_s$ can be defined such that $||\boldsymbol{u}'||_i^2 = (\boldsymbol{u}', \boldsymbol{u}')_i$, $||\boldsymbol{u}'||_s^2 = (\boldsymbol{u}', \boldsymbol{u}')_s$ maximising over $\boldsymbol{u}_0'$ reduces to the variational problem whose functional is

$$F = (A(t)\boldsymbol{u}_0', A(t)\boldsymbol{u}_0')_s + \lambda((\boldsymbol{u}_0', \boldsymbol{u}_0')_i - 1). \tag{2.2}$$

Here, λ is the Lagrange multiplier for the fixed norm of initial conditions.

If, in the numerical implementation, the velocity $\boldsymbol{u}_0'$ is represented (say, by Galerkin approximation or by a grid function) as a vector γ of finite dimension, then one can introduce matrices E_t and E_0 such that $(A(t)\boldsymbol{u}_0', A(t)\boldsymbol{u}_0')_s = \gamma^* E_t \gamma$ and $(\boldsymbol{u}_0', \boldsymbol{u}_0')_i = \gamma^* E_0 \gamma$. Here, * denotes transposition. Then the Euler-Lagrange equation for (2.2) is

$$E_t\gamma + \lambda E_0 \gamma = 0. \tag{2.3}$$

This is a generalised eigenproblem whose (necessary real) eigenvalues λ are the ratios of the square of the norm $||.||_s$ of the solution at time t to the square of the norm $||.||_i$ of the initial condition. The notation here is chosen to coincide with notation in equation (22) in Butler & Farrell (1992) in order to emphasise the similarity. Because of this similarity, many optimal perturbation codes can be easily modified for solving the generalised optimal perturbation problem.

2.2. *Plane channel.*

To test this approach, generalised optimal perturbations were calculated for a channel flow with additional assumptions that the entire flow is independent of x and that $u = 0$ at $t = 0$. This simplification is justified since the optimal perturbations for channel flows found so far possess these features. The cross-flow perturbation energy density averaged over the entire channel

$$||\boldsymbol{u}||_c^2 = \lim_{a,b\to\infty} \frac{1}{ab} \int_{x,y,z=0,-1,0}^{x,y,z=a,+1,b} (v^2 + w^2)\, dx\, dy\, dz \tag{2.4}$$

was used as the initial condition norm $||.||_i$. We assume that the channel walls are at $y = \pm 1$. This choice of $||.||_i$ and $||.||_s$ is not the only one which is reasonable, of course†. The mean velocity distribution of the turbulent flow was approximated with the Reynolds-Tiederman profile used also by Butler & Farrell (1993).

The Mathematica package was used for calculating explicitly eigensolutions of the linearised Navier–Stokes equations and for prototyping the more efficient Fortran code. The code was validated by reproducing the results of Butler & Farrell (1993), and then, by small modification, it was adjusted for solving the generalised problem. More detail is given in the Appendix. In figure 4 the spanwise period of the global generalised optimal as a function of the distance to the wall is compared with twice the value of the spanwise distance to the minimum of the two-point longitudinal velocity correlation, as obtained from direct numerical simulation by Hu & Sandham (2001*b*) (see also Hu, Morfey & Sandham 2003)). Both quantities represent the streak spacing l^+. Here and throughout the paper the Reynolds number is based on the friction velocity and the channel half-width. For $y^+ < 50$ the streak spacing curves predicted by generalised optimal perturbation for the two values of the Reynolds number Re overlap while, in contrast, direct numerical simulation results for Re = 180 and Re = 360 coincide only quite close to the wall. This may happen because in direct numerical simulation results there are no streaks away from the walls while the present study is limited to 'streaky' perturbations independent of x. Therefore, far from the wall only a qualitative comparison makes sense. It is interesting to note that both the theoretical and numerical curves have similar inflections near the center of the channel. Further comparisons are also characterised by such qualitative similarity even where there is no quantitative agreement. The generalised optimal perturbation gives the correct order of magnitude for the streak spacing and correct qualitative behaviour as a function to the distance to the wall. For comparison, the optimal perturbation without eddy-turnover-time adjustment gives $l^+ = 540$ independent of y^+ for Re = 180 (Butler & Farrell 1993). Even with the eddy-turnover-time adjustment ordinary optimal perturbations give constant streak spacing. One more advantage of generalised optimal perturbation is that the calculations are more straightforward than when the eddy turnover time is to be found for the optimal perturbation using experimental or numerical data.

---

† Strictly speaking these norms apply to different functional spaces due to the difference between the zero elements of these spaces. However, this subtle detail is of no importance in the context of the present study.

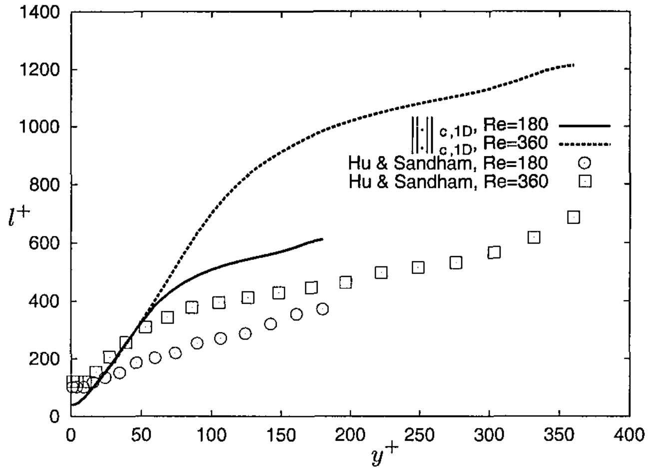

FIGURE 4. Streak spacing l^+ as a function of the distance to the wall. Curves are the wavelength of the generalised optimal perturbation with $||.||_s = ||.||_y$ and $||.||_i = ||.||_c$, points are twice the value of the spanwise distance to the minimum of the two-point longitudinal velocity correlation as obtained in direct numerical simulation by Hu & Sandham (2001*b*).

To analyse the selectivity of the generalised optimal perturbation theory, let us consider the solution of the variational problem (2.2) in the special case when, as in the present study, $||.||_s = ||.||_y$ and the perturbations are independent of x. Then from the continuity equation it follows that a cross-flow stream function ψ can be introduced so that $v' = -\partial\psi/\partial z, w' = \partial\psi/\partial y$. Let $\psi = \psi_\beta(t,y)e^{i\beta z}$. Without loss of generality ψ_β can be assumed to be real-valued. Then $v' = -i\beta\psi_\beta e^{i\beta z} = iv_\beta e^{i\beta z}$ and $w' = (\partial\psi_\beta/\partial y)e^{i\beta z} = w_\beta e^{i\beta z}$ where v_β and w_β are also real-valued. Since with $\partial/\partial x = 0$ the equation for u' involves v' but not w' it is natural to take $u' = iu_\beta e^{i\beta z}$ with real-valued u_β. Then the three functions $u_\beta(t,y)$, $v_\beta(t,y)$, and $w_\beta(t,y)$ determine the solution which we will denote $\boldsymbol{u}_\beta$.

The solution of the linearised Navier–Stokes equations is a superposition of solutions of the type $\boldsymbol{u}_\beta$. Solutions with different β are orthogonal with respect to a scalar product corresponding to (2.1). Therefore, solutions for each β can be studied separately. Similarly to $||.||_y$ and $||.||_c$ we introduce $||\boldsymbol{u}_\beta||^2_{y,1D} = |u_\beta(t,y)|^2$ and $||\boldsymbol{u}_\beta||^2_{c,1D} = \int_{-1}^{+1}(v_\beta^2 + w_\beta^2)\,dy$ respectively. Naturally, the continuity equation imposes a relation between v_β and w_β which can be used to obtain an equivalent alternative formulation. The variational problem now consists in maximising $u_\beta(t,y)$ for given t, β and y by varying the initial (at $t = 0$) distribution of $v_\beta(y)$ and $w_\beta(y)$ but keeping $||\boldsymbol{u}_{\beta 0}||_{c,1D} = 1$. With $\boldsymbol{u}_\beta = A_{1D}(t,\beta)\boldsymbol{u}_{\beta 0}$ and scalar products $(.,.)_{c,1D}$, $(.,.)_{y,1D}$ defined such that $||\boldsymbol{u}_\beta||^2_{c,1D} = (\boldsymbol{u}_\beta, \boldsymbol{u}_\beta)_{c,1D}$, $||\boldsymbol{u}_\beta||^2_{y,1D} = (\boldsymbol{u}_\beta, \boldsymbol{u}_\beta)_{y,1D}$, the variational problem consists in maximising

$$F_\beta = (A_{1D}(t)\boldsymbol{u}_{\beta 0}, A_{1D}(t)\boldsymbol{u}_{\beta 0})_{y,1D} + \lambda(t,y,\beta)((\boldsymbol{u}_{\beta 0}, \boldsymbol{u}_{\beta 0})_{c,1D} - 1). \qquad (2.5)$$

Here, as in (2.2), $\lambda(t,y,\beta)$ is the Lagrange multiplier. Similar to (2.2) and (2.3) the Euler-Lagrange equation for (2.5) may be reduced to

$$E_{t,\beta}\gamma + \lambda E_{0,\beta}\gamma = 0. \qquad (2.6)$$

Solving the variational problem with the functional (2.5) gives $\lambda(t,y,\beta)$. The solution to the generalised optimal perturbation problem is then obtained by maximising $\lambda(t,y,\beta)$ over all β and all $t > 0$. The value of β gives then the most probable streak spacing

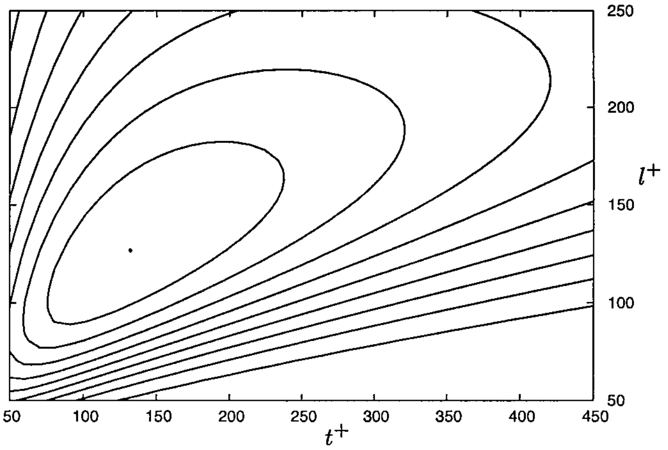

FIGURE 5. Contours of constant $\sqrt{\lambda}$ drawn at every 10% of its maximum value: Re = 360, $y^+ = 20$, $\lambda_{max} = 437$.

$l^+ = 2\pi \operatorname{Re}/\beta$ at this distance to the wall. The results in figure 4 were obtained in this way.

The selectivity of the generalised optimal perturbation mechanism depends on how sharp is the maximum of $\lambda(t, y, \beta)$. Figure 5 shows the isolines of $\sqrt{\lambda(t, y, \beta)}$ at $y^+ = 20$ for Re = 360. (Note that since the walls are at $y = \pm 1$ and Re is based on the dynamic velocity, $y^+ = \operatorname{Re}|y \pm 1|$.) The global optimal corresponds to the maximum $\lambda(t, y, \beta)$ value, which is equal to 437 and which is attained at $t^+ = 130$ and $l^+ = 125$. (The specific values are given only for other researchers to be able to verify our numerical results. These values depend on the distance to the wall $y^+ = 20$ which is chosen arbitrarily for illustration purposes only.) Assuming that λ is analogous to the probability density of l^+ one can conclude that the average streak spacing should be greater than the most probable streak spacing, and that the streak spacing variance can be large, as it is indeed observed in experiments by Smith & Metzler (1983).

2.3. *Relation to a Green function.*

Due to the linearity of the problem maximising u_β is equivalent to maximising $|u_\beta|$. Since $u_\beta(t, y)$ is a linear functional of the initial distribution $(v_{\beta 0}, w_{\beta 0})$, it can be represented via the Green function $\boldsymbol{G}(t, \beta, y, \eta) = (G_v(t, \beta, y, \eta), G_w(t, \beta, y, \eta))$ as

$$u_\beta(t, y) = \int_{-1}^{+1} \left(G_v(t, \beta, y, \eta) v_{\beta 0}(\eta) + G_w(t, \beta, y, \eta) w_{\beta 0}(\eta)\right) d\eta. \tag{2.7}$$

Since this is an L_2 scalar product of (G_v, G_w) and (v_β, w_β), $u_\beta(t, y)$ is maximised when these vectors are parallel, that is when $(v_{\beta 0}(\eta), w_{\beta 0}(\eta)) = \text{const} \cdot (G_v(t, \beta, y, \eta), G_w(t, \beta, y, \eta))$. The constant can be found from the requirement that the initial condition should have a unit initial condition norm: $||\boldsymbol{u}_{\beta 0}||^2_{c,1D} = \int_{-1}^{+1}(v^2_{\beta 0} + w^2_{\beta 0})\, dy = 1$. Hence, the solution to the variational problem with functional (2.5) is

$$(v_{\beta 0}(\eta), w_{\beta 0}(\eta)) = \frac{\boldsymbol{G}(t, \beta, y, \eta)}{\sqrt{\int_{-1}^{+1}\left(G_v(0, \beta, y, \eta)^2 + G_w(0, \beta, y, \eta)^2\right) d\eta}},$$

and the Lagrange multiplier $\lambda(t, y, \beta)$ is the square of the L_2 norm of the Green function:

$$\lambda(t, y, \beta) = \int_{-1}^{+1} \left(G_v(t, \beta, y, \eta)^2 + G_w(t, \beta, y, \eta)^2\right) d\eta. \tag{2.8}$$

Therefore, with $||.||_{y,1D}$ and $||.||_{c,1D}$ used solving eigenproblem (2.6) gives the Green function and, vice-versa, the Green function can be used as the solution to the eigenproblem. Notice that since any initial condition which is orthogonal to the Green function results in zero $u_\beta(t,y)$, there is only one non-zero eigenvalue. This can be used for developing an efficient numerical solver for the eigenproblem in question.

2.4. *Improving the initial norm*

In a turbulent flow the mean energy of the cross-flow motion strongly depends on the distance to the wall. Therefore, initial conditions with energy distribution close to experimentally observed should be considered as more probable, and the initial norm is the natural tool for taking this into account. This can be done by using the norm

$$||\boldsymbol{u}_\beta||_{c',1D} = \int_{-1}^{+1} \left(\frac{v_\beta^2}{\langle v^2 \rangle} + \frac{w_\beta^2}{\langle w^2 \rangle} \right) dy$$

instead of $||.||_{c,1D}$. Here, $\langle v^2\rangle(y)$ and $\langle w^2\rangle(y)$ are the normal Reynolds stresses which can be taken from experiment or direct numerical simulation. Intuitively, as compared to $||(v_{\beta 0}, w_{\beta 0})||_{c,1D} = 1$, the restriction $||(v_{\beta 0}, w_{\beta 0})||_{c',1D} = 1$ allows greater values of $v_{\beta 0}$ and $w_{\beta 0}$ where $\langle v^2\rangle$ and $\langle w^2\rangle$ are large and requires smaller values of $v_{\beta 0}$ and $w_{\beta 0}$ where $\langle v^2\rangle$ and $\langle w^2\rangle$ are small. In addition, it has a neat form with initial optimal perturbation energy weighted with the turbulent energy of the real flow.

An alternative argument in favour of $||.||_{c',1D}$ can be obtained by considering a statistical ensemble of random initial conditions $(\hat{v}_{\beta 0}(y), \hat{w}_{\beta 0}(y))$ with zero means, which correspond to solutions $\hat{u}_\beta(t,y)$. As it is natural for a linearised problem, the mean value of $\hat{u}_\beta(t,y)$ is also zero. Then, using (2.7) gives the following expression for the variance of $\hat{u}_\beta(t,y)$:

$$\begin{aligned} \langle \hat{u}_\beta(t,y)^2 \rangle = \int_{-1}^{+1}\int_{-1}^{+1} & (G_v(t,\beta,y,\eta_1)G_v(t,\beta,y,\eta_2)\langle \hat{v}_{\beta 0}(\eta_1)\hat{v}_{\beta 0}(\eta_2)\rangle \\ & +2G_v(t,\beta,y,\eta_1)G_w(t,\beta,y,\eta_2)\langle \hat{v}_{\beta 0}(\eta_1)\hat{w}_{\beta 0}(\eta_2)\rangle \\ & +G_w(t,\beta,y,\eta_1)G_w(t,\beta,y,\eta_2)\langle \hat{w}_{\beta 0}(\eta_1)\hat{w}_{\beta 0}(\eta_2)\rangle)\, d\eta_1\, d\eta_2. \end{aligned} \tag{2.9}$$

Here one can notice the similarity with the analysis of Jovanović & Bamieh (2001), and, indeed, the link between transient growth and response to external excitations is well known (Trefethen *et al.* 1993).

If we assume (rather crudely) that the characteristic correlation lengths are small and independent of y and that the cross-correlation $\langle \hat{v}_{\beta 0}\hat{w}_{\beta 0}\rangle$ is negligible then the variance reduces to

$$\langle \hat{u}_\beta(t,y)^2 \rangle = \text{const} \int_{-1}^{+1} (G_v^2(t,\beta,y,\eta)\langle \hat{v}_{\beta 0}^2(\eta)\rangle + G_w^2(t,\beta,y,\eta)\langle \hat{w}_{\beta 0}^2(\eta)\rangle)\, d\eta. \tag{2.10}$$

On the other hand, as it is easy to verify with simple algebraic transformations, with $||.||_{c',1D}$ used instead of $||.||_{c,1D}$ equation (2.8) becomes

$$\lambda(t,y,\beta) = \int_{-1}^{+1} (G_v^2(t,\beta,y,\eta)\langle v^2(\eta)\rangle + G_w^2(t,\beta,y,\eta)\langle w^2(\eta)\rangle)\, d\eta.$$

Assuming further that $(\langle \hat{v}_{\beta 0}^2\rangle, \langle \hat{w}_{\beta 0}^2\rangle) = \text{const}(\langle v^2\rangle, \langle w^2\rangle)$ one can conclude that $\lambda(t,y,\beta)$ and the variance $\langle \hat{u}_\beta(t,y)^2\rangle$ are maximised at the same t and β.

These two empirical arguments in favour of $||.||_{c',1D}$ justify an attempt to use it. Notice also that $\langle v^2\rangle$ and $\langle w^2\rangle$ here are functions of y only and they do not contain explicit information on the spanwise length scale.

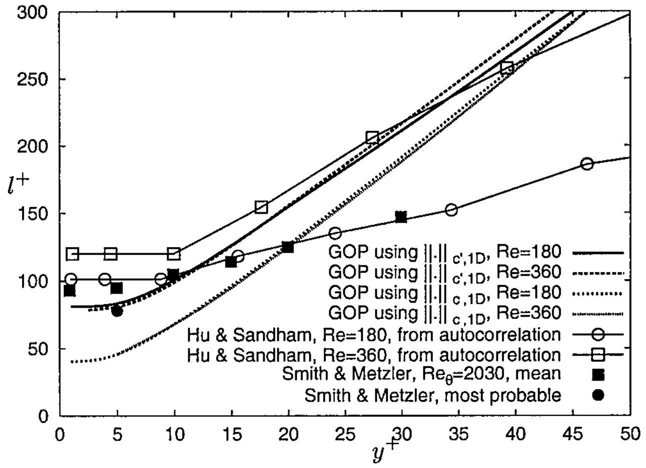

FIGURE 6. Streak spacing as a function of the distance to the wall.

Figure 6 shows the comparison of the generalised optimal perturbation results obtained using the two initial norms. The normal Reynolds stresses $\langle v^2\rangle$ and $\langle w^2\rangle$ were taken from the direct numerical simulation results of Hu & Sandham (2001*b*). The Smith & Metzler (1983) measurements were performed in a boundary layer, with the Reynolds number Re_θ based on the momentum thickness and the upstream velocity. If the dynamic velocity were used their Reynolds number would be roughly about 100, and if in addition the boundary layer thickness were used instead of the momentum thickness then it would be roughly about 1000. For channel flow the Reynolds number is based on the dynamic velocity and the channel half-width. When $||.||_{c',1D}$ is used the agreement in magnitude with direct numerical simulation of Hu & Sandham (2001*b*) and experiment of Smith & Metzler (1983) is somewhat better. Note that the optimal perturbation agrees better with the most probable value of the streak spacing, as it can be expected. Qualitatively the generalised optimal perturbation results and the numerical results differ in that in the range of figure 6 the generalised optimal perturbation results for the two values of the Reynolds number almost overlap while numerical results depend on Re. However, as far as dependence on the wall distance is concerned, the generalised optimal perturbation reproduces both the independence of l^+ of y^+ in the near vicinity of the wall and the increase in l^+ with y^+ further away from the wall. Overall the comparison seems to be favourable for generalised optimal perturbation theory. Calculating generalised optimal perturbation with sufficient accuracy for small values of y^+ and large Re is computationally intensive. For this reason, the generalised optimal perturbation curves for Re = 180 start at $y^+ = 1$. For Re = 360 the curves start at $y^+ = 2.5$ for $||.||_{c',1D}$ case and at $y^+ = 5$ for $||.||_{c,1D}$ case.

2.5. *Generalised optimal perturbation for longitudinal vortices*

Generalised optimal perturbation with a norm tailored so as to distinguish streaks shows that there exist such initial conditions of unit magnitude that the corresponding solution of the linearised Navier–Stokes equations will exhibit streaks of much greater than unit magnitude. This gives a reason to expect that streaks of this spacing will indeed be observed in a real flow. Thus found, the generalised optimal perturbation has the structure similar to figure 2, that is apart from streaks it involves also longitudinal vortices. However, and very importantly, the magnitude of these vortices is not large. By the very idea of generalised optimal perturbation, in order to determine what kind of longitudinal vortices will be observed in the real flow the solution norm should be tailored so as to distinguish longitudinal vortices. The simplest such norm is just the kinetic energy of the cross-flow motion, with additional assumption of the flow being independent of longitudinal coordinate needed in order to emphasise the longitudinal vortices. However, an attempt to find the corresponding generalised optimal perturbation immediately reveals the well-known fact that longitudinal vortices have no transient growth. The reason for this is that all x-independent eigensolutions of the linearised problem are orthogonal with respect to the cross-flow energy norm. Technically, one can find the longitudinal-vortex-tailored generalised optimal perturbation but it is just the slowest-decaying vortex. Hence, there is no reason to believe that such vortices will be observed in the real flow. Of course the longitudinal vortices of the generalised optimal perturbation based on the streak-tailored solution norm $||.||_y$ decay even faster. Since the magnitude of longitudinal vortices is not large they will not dominate the flow. This means that optimal perturbation theory predicts streaks but does not predict longitudinal vortices. This is equally true for optimal perturbations of Butler and Farrell. The generalised optimal perturbation approach just makes this fact very obvious.

Within the linearised Navier–Stokes equations framework, the preferential longitudinal vortex spacing is the spacing between the slowest-decaying vortices. Such vortices have a period of approximately $2\pi/1.2$ times the channel half-width independently of the Reynolds number (see for example Waleffe & Kim 1997), which is much larger then the characteristic spanwise scale in the near-wall region of a real flow. Naturally, since these vortices are only decaying, the nonlinear effects may well prevail in real flow as far as vortices are concerned.

If the restriction $\partial/\partial x = 0$ is not imposed one can expect the possibility of transient growth even with respect to the norm tailored to vortices. It would be very interesting to calculate the vortical structures using generalised optimal perturbation approach with the norm tailored to non-longitudinal, that is general, vortices, and compare the result with experimental and numerical observations. In doing this the solution norm should be chosen with certain care in order that strong streaks would not obscure other possible organised structures. Anyway, whatever vortical structures can be revealed by such other generalised optimal perturbation solutions they need not be directly related to streaks. Numerical calculations of the following section aim to establish to what degree the streaks are linked to the vortical structures of the real flow and to provide further material for comparisons with the generalised optimal perturbation theory.

3. Passive scalar streaks.

3.1. *Scalar streaks in turbulent flow.*

According to the optimal perturbation theory the streak spacing depends on the mean velocity profile, since it enters the formulation of the optimal perturbation problem. Therefore, if it can be demonstrated that variation of the mean profile strongly affects the streak spacing even when the vortical structure is held fixed then that will be a strong argument in favour of the optimal perturbation theory. However, the change of mean velocity profile will invariably affect the vortex structure of the flow. Instead it is possible to consider a passive scalar. If the mean profile of scalar is similar to the mean profile of the longitudinal velocity then figure 2 implies that the same lift-up mechanism will create streaks of scalar with the same spacing as the spacing of velocity streaks and longitudinal vortices. Streaks of scalar were found in direct numerical simulations by Kim

& Moin (1989), but in their calculations the mean scalar profiles were similar to the mean velocity profile, and the scalar streaks spacing was close to the velocity streak spacing. Kasagi, Tomita & Kuroda (1992) also report close correlation between fluctuations of streamwise velocity and temperature.

We assume that the Schmidt number for each scalar is equal to unity. Then passive scalar θ_i is governed by the equation

$$\frac{\partial \theta_i}{\partial t} + \boldsymbol{u} \cdot \nabla \theta_i = S_i(y) + \frac{1}{Re} \nabla^2 \theta_i, \tag{3.1}$$

where $S_i(y)$ is the source term for the passive scalar. Prescribing different $S_i(y)$ one can obtain different mean profiles for θ_i. Calculations with different mean scalar profiles can be performed simultaneously, and each solution will correspond to exactly the same vortex structure. This allows to isolate the influence of the shape of the mean profile on the streak spacing.

We have modified the pseudo-spectral channel code of Sandham & Howard (1998) in order to solve an arbitrary number of passive-scalar equations. All calculations were performed at Re $= 360$ in a computational box of the size $L_x \times L_y \times L_z = 6 \times 2 \times 3$ using $64 \times 64 \times 160$ modes (Chebyshev in wall-normal and complex-valued Fourier in homogeneous directions).

Streaks are not exactly regular, and different definitions of streak spacing are possible. The velocity auto-correlation function $R_{uu}(\Delta) = \langle u(t,x,y,z)u(t,x,y,z+\Delta)\rangle$ has a maximum at $\Delta = 0$ and reaches a minimum at a certain value $\Delta_{\min}$. Streak spacing can be defined as $2\Delta_{\min}$. Similarly, the auto-correlation function for the passive scalar can be used for determining the scalar streak spacing. Note that both $R_{uu}(\Delta)$ and $\Delta_{\min}$ depend on y but are independent of t, x, and z.

3.2. *Linear combinations of the passive scalar solutions*

Since the equations for the scalar are linear, a linear combination of several solutions is a solution. Then, if

$$\theta = \sum_{i=1}^{i=n} A_i \theta_i \tag{3.2}$$

then

$$R_{\theta\theta}(\Delta) = \sum_{i=1,j=1}^{i=n,j=n} A_i A_j R_{\theta_i \theta_j}(\Delta). \tag{3.3}$$

Note that the mean profile of the scalar is

$$\Theta = \langle \theta \rangle = \sum_{i=1}^{i=n} A_i \langle \theta_i \rangle = \sum_{i=1}^{i=n} A_i \Theta_i.$$

Therefore, by solving simultaneously several passive-scalar equations with different source terms and calculating the cross-correlations $R_{\theta_i \theta_j}(\Delta)$ it is then quite easy to calculate the auto-correlation function and, hence, the streak spacing, for any linear combination determined by the vector of coefficients A_i. To check this concept, one of the calculated scalars was a linear combination of the rest, so that its auto-correlation function was calculated both directly and by the method described above, and the results coincided. We also compared the streak spacing as calculated from the auto-correlation function with the streak spacing as it, although rather approximately, was obtained from visualisation, and again found that our linear-combination approach works.

Technically, it was easier to modify the code in such a way that instead of prescribing the source terms S_i it was possible to prescribe directly the mean scalar profiles $\Theta_i(y) = \langle\theta_i\rangle$. Solutions for seven scalar mean profiles were calculated simultaneously, with one, as mentioned, being a linear combination of others for validation purposes. Therefore, the results were obtained for six independent basic profiles. For completeness, the best choice of the basic profiles would be a sufficiently large number of, say, Chebyshev polynomials, so that practically any mean profile could be represented as a linear combination of them. However, the required computer resources would be too large. We compromised by taking three profiles of the shape more or less close to what seemed to be of possible interest and three other profiles as trigonometric functions, to allow for further adjustments. The profiles were defined via their derivatives with respect to y, because these derivatives are needed for optimal perturbation theory. Introducing two auxiliary functions,

$$g(y, Re) = 0.5(1 + (\frac{0.525}{3}\,\mathrm{Re}(1 + y^2 - 2y^4)(1 - e^{(-(1-|y|)\mathrm{Re}/37)})^2)^{0.5} - 0.5$$

($g(y, Re)$ corresponds to the Reynolds-Tiederman profile, as in Waleffe *et al.* (1993)), and

$$h(y, d, w) = 150(e^{-(-1+d-y)^2/w^2} - e^{-(-1+d+y)^2/w^2}),$$

the derivatives of the basic mean profiles are

$$\begin{aligned}
\Theta_1' &= -y \times Re/(1 + g(y)),\\
\Theta_2' &= h(y, 0.20, 0.150),\\
\Theta_3' &= h(y, 0.10, 0.075),\\
\Theta_4' &= \sin(1 \times \pi(1 + y)/2),\\
\Theta_5' &= \sin(3 \times \pi(1 + y)/2),\\
\Theta_6' &= \sin(5 \times \pi(1 + y)/2).
\end{aligned}$$

Cross-correlations were calculated for solutions corresponding to these six profiles. Results of the calculations showed the existence of scalar streaks and moderate variation in their spacing.

For checking to which extent the streak spacing can be varied by varying the mean scalar profile, the following method was used. Ideally, one can try to find such a vector $(A_1, \ldots, A_6)$ that the autocorrelation function (3.3) has a minimum at or as close as possible to a desired value of $\Delta = \Delta_0$. Then, varying this value would vary the streak spacing. Such a problem, however, is too difficult. Instead, we first normalise the auto-correlation function (3.3) of the linear combination (3.2) by imposing a restriction that it is equal to unity at $\Delta = 0$:

$$R_{\theta\theta}(0) = \sum_{i=1,j=1}^{i=6,j=6} A_i A_j R_{\theta_i\theta_j}(0) = 1. \tag{3.4}$$

Then we require this normalised auto-correlation function to be as small as possible at $\Delta = \Delta_0$. We expect that this function will then have a minimum not too far away from that value, so that the streak spacing can be controlled by Δ_0. This idea, while working in many cases, for certain values of Δ_0 resulted in an ill-conditioned problem. The reason for this is simple. Imagine that the basic profiles are not linearly independent. Then, if $\sum_{i=1}^{i=6} A_i^0\Theta_i = 0$ then adding vector $\mathbf{A}^0$ multiplied by an arbitrary constant C to the solution $\mathbf{A}$ of our minimisation problem will change nothing. Therefore, the solution is not unique and the problem is ill-posed. Notice that C may be very large so that the sum $C\mathbf{A}^0 + \mathbf{A}$ may be large, too. In practice in our case the basic profiles are not linearly dependent but, on one hand they are not orthogonal, and on the other hand,

ID	$2\Delta_0$	r	A_1	A_2	A_3	A_4	A_5	A_6
A	16.87	0.1	-0.9452	0.03027	0.3191	0.003794	-0.03407	-0.05132
B	101.2	0.1	-0.9841	0.1426	0.04708	-0.0007388	-0.08993	-0.03150
C	270.0	0.01	-0.3198	-0.1153	0.7649	-0.1601	0.5173	0.07813
D	320.6	0.001	0.1415	-0.07865	-0.07077	0.3237	-0.8607	-0.3522
E	438.8	0.1	-0.07543	-0.8645	0.4305	0.02091	-0.1787	0.1709
F	776.2	0.0025	-0.03643	-0.03295	0.002782	-0.2214	0.9641	0.1380
G	1063	0.001	-0.006337	-0.02004	0.005644	-0.1841	0.9090	-0.3733

random numerical errors are present. Together, it sometimes leads to very large vectors **A** determined mostly by the numerical errors, with erratic behaviour of the resulting auto-correlation function. The obvious solution to this problem is to use some kind of Tikhonov regularisation (Tikhonov *et al.* 1990). Specifically, we require the normalised auto-correlation function to be as small as possible at a given $\Delta = \Delta_0$ but the vector **A** to be not large.

This leads to a minimisation problem for the functional

$$\sum_{i=1,j=1}^{i=6,j=6} A_i A_j \left(R_{\theta_i\theta_j}(\Delta_0) + r\delta_{i,j}\right) - \mu \left(\sum_{i=1,j=1}^{i=6,j=6} A_i A_j R_{\theta_i\theta_j}(0) - 1\right) \to \min,$$

were r is the regularisation parameter, which should be reasonably small, δ_{ij} is the Kronecker delta, and μ is the Lagrange multiplier for the restriction (3.4). This, in turn, can in a standard way be reduced to a linear eigenvalue problem. This method was used to obtain passive-scalar solutions with quite large and quite small streak spacing. Naturally, for linear combinations obtained in this way, the minimum of the auto-correlation function does not exactly coincide with Δ_0, but in practice Δ_0 and $\Delta_{\min}$ turn out to be close within a reasonable range of Δ_0.

The table gives the values of the parameters used and the obtained eigenvectors. Of six eigensolutions we always choose the one giving the smallest value of $R_{\theta\theta}(\Delta_0)$. The cross-correlations depend on the distance to the wall. The results in the table were obtained with $R_{\theta\theta}$ being calculated at the distance $y^+ = 19.6$ from the wall. Here *ID* is the profile identifier. The A_i values in this table determine the profiles uniquely.

3.3. *Passive scalar results*

Figure 7 summarises the results for each profile.

The calculations were performed in a box of the size $6 \times 2 \times 3$, in other words, the solutions are double-periodic with period 6 in the main flow direction and with period 3 in the transverse direction, with distance between the walls equal to 2. The Reynolds number was Re $= 360$. The mean pressure gradient was -1, and, correspondingly, the mean wall shear stress was equal to unity. Accordingly, one wall unit was equal to $1/360$. Wall units are used in figure 7 since streak spacing is normally expressed in wall units. The improved initial condition norm was used.

Each row corresponds to the mean scalar profile shown in the last column, with the mean scalar Θ plotted along the abscissa axis. The first column shows the streak spacing l^+ as the function of the distance y^+ to the wall, as obtained from direct numerical simulation (DNS), from generalised optimal perturbation theory (GOP) and from optimal perturbation theory with eddy turnover time (OPETT) of Butler and Farrell. In direct numerical simulation the streak spacing was defined as twice the distance to the minimum

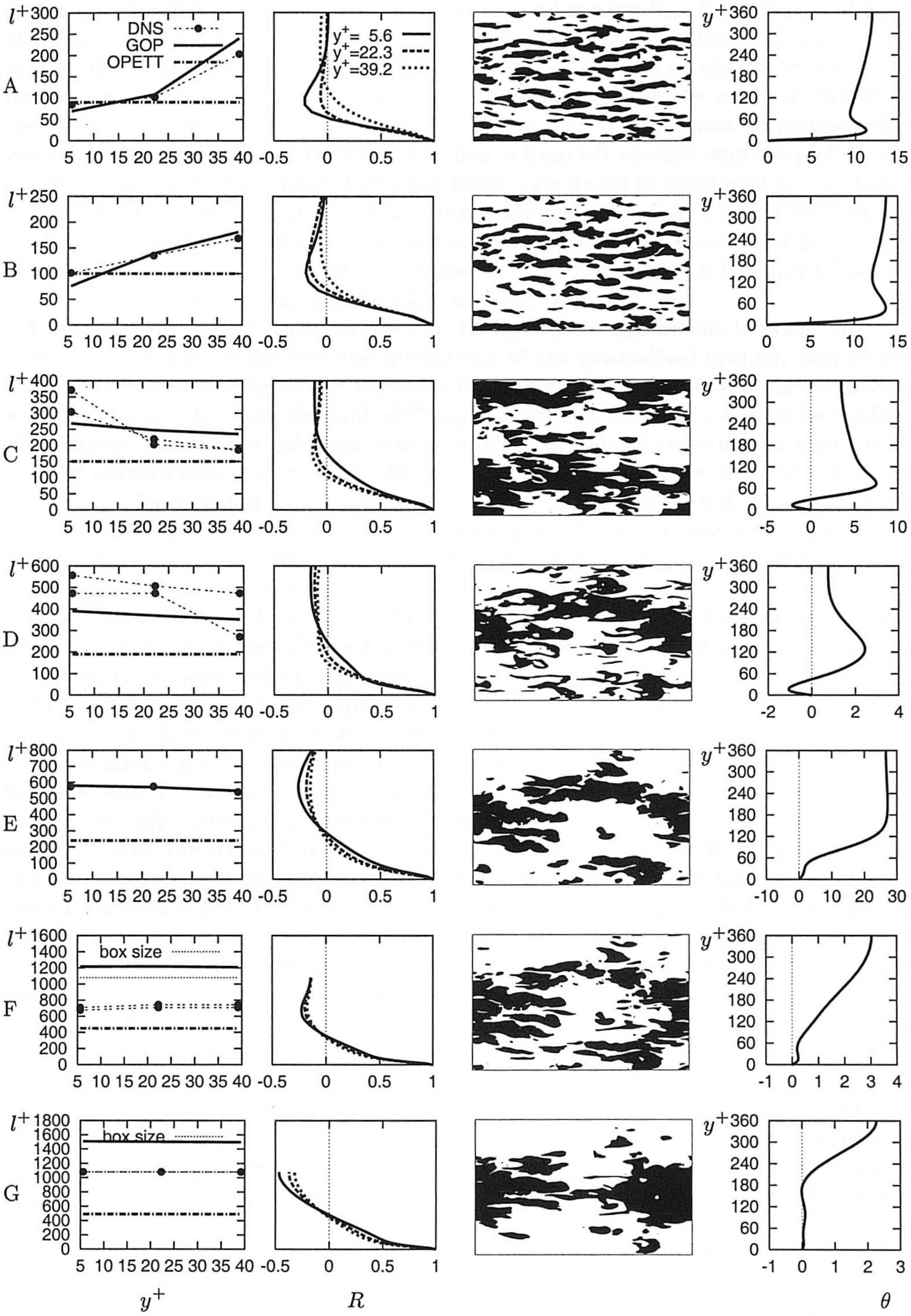

FIGURE 7. Instantaneous visualisations and relations between the streak spacing l^+, wall distance y^+, autocorrelation R, and mean scalar Θ for profiles A-G.

of the autocorrelation function. The autocorrelation function $R_{\theta\theta}(\Delta)$ is plotted along the abscissa axis in the second column of pictures, for three values of the wall distance. The scale of the ordinate axis is such that the smallest value of $R_{\theta\theta}$ on the curve is level with the corresponding DNS point on the left of it. For example, in the first row this level is just below 100 for the solid curve with $y^+ = 5.6$. The third column of pictures shows instantaneous visualisation of streaks. The flow is from left to right, and the picture plane is parallel to the channel walls. The black areas correspond to regions in $y^+ = 5.6$ plane where the instantaneous values of θ were below the threshold values which were adjusted so that visually the area of dark region was approximately the same in all pictures. For profiles A-G the thresholds values were respectively $15, 16, 4.5, 5, 3.6, 0.7,$ and 1.5 per cent of the scalar minimal instantaneous value in that plane.

For Profiles A and B (two top rows in the figure) the agreement between direct numerical simulation results and the predictions of the generalised optimal perturbation theory is quite good. Note that while for both profiles the streak spacing l^+ increases with the distance y^+ from the wall, d^2l^+/dy^{+2} is greater for profile A than for profile B. Generalised optimal perturbation results exhibit the same behaviour. In contrast, the optimal perturbation theory with eddy turnover time predicts the same streak spacing for all y^+. The visualisation shows streaky structures in both A and B cases. It should be noted that as the distance to the wall increases, streaks become less apparent (less elongated). The visualisation for greater y^+ are not shown here since this behaviour is well known for velocity streaks (Smith & Metzler (1983)).

In contrast to A and B, for profiles C and D the streak spacing decreases as y^+ increases. This behaviour also is reproduced by generalised optimal perturbation, but the quantitative agreement is less good. Note the shape of the auto-correlation curves: in these cases it is difficult to determine the location of the minimum of the auto-correlation function. The direct numerical simulation data shown were obtained by time-averaging. The averaging time T_{av} was repeatedly increased until the variation of auto-correlation function with T_{av} fell to within about 3% in the worst case. However, where the lowest part of the auto-correlation curve is almost flat, even a small variation in $R_{\theta\theta}(\Delta)$ can result in large variation of the location of the minimum. To illustrate the uncertainty caused by this effect, each plot in the first column shows in fact the direct numerical simulation results for two values of T_{av}, but in cases A, B, E, and G they overlap, and in case F they are quite close. In cases C and D, however, the uncertainty in direct numerical simulation results is of the same order of magnitude as the deviation of these results from generalised optimal perturbation predictions. In case E the minimum of the auto-correlation function is quite clear, and the agreement between direct numerical simulation and generalised optimal perturbation is again quite good.

In cases F and D the agreement is affected by the finite size of the computational box. The maximum streak spacing which could be obtained in our direct numerical simulation is equal to the box size that is 1080 wall units. In both cases generalised optimal perturbation theory predicts streak spacing greater than this value, and, of course, if the possible perturbations were limited to wavelengths not greater than the box size then generalised optimal perturbation would give just the box size as the optimal perturbation. Nevertheless, in case F the direct numerical simulation result is below 1080. It should be noted of course that the insufficient box size affects the results not only by limiting the maximum possible wavelength but also by distorting the spectrum in the vicinity of the box size, which can explain the discrepancy. However, there is also another possibility. The streak visualisations clearly shows that as the streak spacing increases from profile A to profile G the streaks become less and less discernible. On the other hand, the generalised optimal perturbation considered here are limited to perturbations

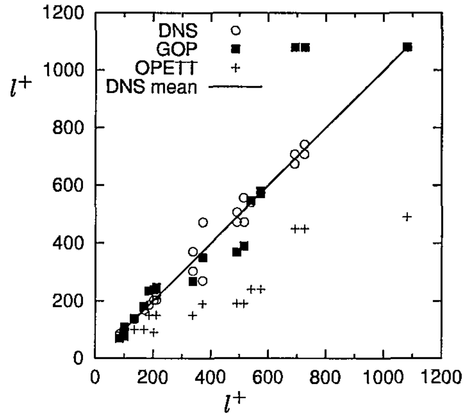

FIGURE 8. Overall comparison of predicted vs calculated streak spacing

independent of x, that is elongated streaks. Therefore, there is a possibility that removing the limitation of $\partial/\partial x = 0$ for generalised optimal perturbations may further improve the agreement.

Overall quality of generalised optimal perturbation predictions as compared with optimal perturbation with eddy turnover time can be judged by figure 8. The abscissa of each plotted point is the mean of the two values of streak spacing obtained from direct numerical simulation for the same scalar profile while the ordinate is the value obtained theoretically or in a specific calculation. For the three cases when generalised optimal perturbation predicts spacing greater than the size of the computational domain this prediction was reduced to this size when plotting in figure 8. It is interesting to note that results of optimal perturbations with eddy turnover time, while being less accurate than generalised optimal perturbation, still correlate with the direct numerical simulation results.

Another important point to be noticed from figure 8 is the behaviour of the direct numerical simulation results as such and in the first place large variation of streaks spacing. Even limited to profiles A,B, and C (the profiles resulting in clearly manifested streaks) the variation (from 85 to more than 300) of the streak spacing is well beyond what could be considered as compatible with the idea that these different streaks are caused by the same organised vortex structure. The only remaining possibility is that the lift-up mechanism itself possesses the scale-selecting properties, as is indeed suggested by the generalised optimal perturbation theory, while the vortex motion can be unstructured. Calculations described in the following subsection were aimed at strengthening this result.

3.4. *Scalar streaks in a flow with potential velocity fluctuations.*

In the equation (3.1) for the scalar concentration the velocity distribution $\boldsymbol{u}(t, x, y, z)$ was the velocity distribution from simultaneously running direct numerical simulation of turbulent flow in a channel. Therefore, the flow field contained all the organised vortices existing in turbulent flows. In order to check if the presence of organised vortices is in any way needed for streak generation, numerical calculations were performed with $\boldsymbol{u} = U(y)\mathrm{e}_x + \nabla\phi(t, x, y, z)$ with random ϕ. In this case the vorticity in the flow is strictly spanwise, and the perturbations are potential, therefore, such a flow field can hardly be considered as containing any organised vortices. Mean scalar concentration was chosen to coincide with the mean velocity distribution, $\Theta(y) = U(y)$, and the Reynolds number Re= 360. The perturbation velocity distribution was solenoidal, so that ϕ satisfied the Laplace equation. At the bottom wall the impermeability condition was imposed,

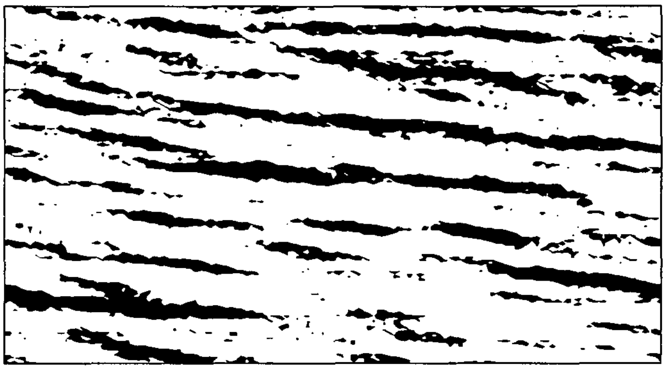

FIGURE 9. Scalar streaks in flow with potential velocity fluctuations

$\partial\phi/\partial y = 0$. The potential was taken as

$$\phi = 0.0008\,\mathrm{Real} \sum_{k=1,l=1}^{k=32,l=32} (P_{kl}(t) + iQ_{kl}(t))e^{i(k_x x + k_z z)} \left(e^{\sqrt{k_x^2+k_z^2}(y-1)} + e^{-\sqrt{k_x^2+k_z^2}(y+3)}\right)$$

where $k_x = 2\pi k/L_x$ and $k_z = 2\pi l/L_z$ with $L_x = 6$ and $L_z = 3$ as before.

The coefficients $P_{kl}(t)$ and $Q_{kl}(t)$ were generated as random numbers uniformly distributed in the interval $(-0.5, 0.5)$ at time intervals $\tau = 0.05$ and spline-interpolated in between. Figure 9 shows the scalar streaks at $y^+ = 8.4$

Streaks are clearly seen and the streak spacing is not too far from that in figure 1, which shows the velocity streaks in turbulent flow with the same mean profile and at the same Reynolds number.

4. Discussion and conclusions

In the present study the streak spacing was defined via the spanwise autocorrelation function. Alternative definitions are possible. For example, several observers can be asked to identify independently the streaks in flow visualisation. It turns out that results obtained by different observers are consistent (Smith & Metzler 1983). It is then possible to determine the probability density distribution for streak spacing and calculate the mean and the most probable streak spacing. Streak spacings obtained in these three ways differ. A theory of such an approximate nature as generalised optimal perturbation theory may be expected to deviate from experiments at least as far as the deviation between these three possible streak spacing. However, whatever the definition of streak spacing is used its qualitative dependence on various parameters should be expected to be the same. In view of this one has to conclude that the figures 6, 7, and 8 present a decisive evidence in favour of the generalised optimal perturbation theory.

Naturally, there is no direct equivalence between optimal perturbations and turbulent flows. The relationship between them consists in the following. The full Navier–Stokes equations (1.1) governing the developed turbulent flow can be rewritten by collecting all the terms present in the linearised Navier–Stokes equations in the left hand side and moving the rest to the right hand side. In order to make this right hand side smaller on average the linearisation should be performed about the mean velocity of turbulent flow rather than about the velocity of steady laminar flow. If terms in the right hand side are denoted $\boldsymbol{F}(t,x,y,z)$, the Navier–Stokes equations then take the form

$$\frac{\partial \boldsymbol{u}'}{\partial t} + \boldsymbol{U}\cdot\nabla\boldsymbol{u}' + \boldsymbol{u}'\cdot\nabla\boldsymbol{U} + \nabla p' - \frac{1}{\mathrm{Re}}\nabla^2\boldsymbol{u}' = \boldsymbol{F}, \qquad \nabla\boldsymbol{u}' = 0. \tag{4.1}$$

This is, in fact, the linearised Navier–Stokes equations with forcing $\boldsymbol{F}$.

If now one solves this equation with $\boldsymbol{F}$ taken from the Navier–Stokes solution (and with the appropriate initial conditions) then, of course, the Navier–Stokes solution will be reproduced and it will contain streaks. This does not give any new information. If, however, it is demonstrated that the same streaks will appear in the solution of (4.1) for almost arbitrary, within reasonable limits, random forcing than it means that the mechanism of streak generation is in fact described by the left hand side of (4.1). Optimal perturbation theory considers initial value problem for the linearised Navier–Stokes equations. The forced response problem (4.1) is reduced to the initial value problem if $\boldsymbol{F}(t,x,y,z) = \delta(t)(\boldsymbol{u}_0'(x,y,z))$. Inversely, the solution to the random forcing problem can be obtained from the solution to the initial value problem by simple quadrature. More details on this relationship with respect to optimal perturbations can be found in Trefethen *et al.* (1993). This relationship means that the generalised optimal perturbations can be considered simply as an efficient way of investigating the properties of the left-hand side of (4.1) with respect to the specific flow feature determined by the choice of the solution norm of the generalised optimal perturbation.

Tailoring the solution norm of the generalised optimal perturbation to longitudinal vortices gives immediately that the left hand side of (4.1), that is the linearised part of the Navier–Stokes equations, does not predict such vortices (see subsection 2.5). However, it does predict streaks. Therefore, organised vortices are not directly needed and are not directly responsible for streaks. This conclusion, following from generalised optimal perturbation theory, is convincingly supported by large variation of streak spacing for fixed vortex structure obtained in subsection 3.3 and by the streak formation in a flow without any organised vortices, as in subsection 3.4.

The physical mechanism of the selection of a certain streak spacing of an optimal perturbation can be described in the following way. An optimal perturbation consists of longitudinal vortices of a fixed initial energy and zero initial longitudinal velocity. The longitudinal vortices decay with time, while longitudinal velocity perturbation grow to quite large amplitude before starting to decay. This growth is caused by the wall-normal velocity component of the optimal vortex, which lifts up the slowly moving fluid from the wall and advects the fast-moving fluids to the wall in alternating stripes. For perturbations of quite small spanwise wavelength, viscosity causes faster decay of longitudinal vortices and smooths out the non-uniformity in longitudinal velocity. Because of this, for very small wavelengths the streak amplitude is small. For very large spanwise wavelengths almost all kinetic energy of the longitudinal vortex is concentrated in the spanwise velocity component, while the lift-up effect is proportional to the wall-normal velocity component. Because of this, for very large wavelengths the streak amplitude is also small and, hence, there is a maximum in between. It may seem that the reference to longitudinal vortices contradicts the conclusion that organised vortices are not involved in the streak scale selection. However, any chaotic cross-flow velocity field may be represented as a Fourier integral in the spanwise direction, that is as a superposition of vortices, and the mechanism described just explains why there is a wavelength for which the corresponding part of the Fourier decomposition is the most efficient in producing streaks. Obviously, the possibility of representing a chaotic field as a superposition of non-chaotic modes does not mean that the chaotic field has an inherent structure. In a form directly applicable to turbulent flow and not only to perturbations governed by linearised Navier–Stokes equations used in the generalised optimal perturbation theory the streak scale selection mechanism can be formulated in the following way. Streaks appear due to wall-normal motions advecting the slowly-moving fluid away from the wall. The streak spacing is determined by the balance between viscous diffusion, which strengthens as the streak spacing decreases, and vanishing of the wall-normal component of perturbations as the streak spacing increases.

Generalised optimal perturbation determines the structure most favoured by the linearised Navier–Stokes equations. Whether this structure will dominate also the solution of the full nonlinear Navier–Stokes equations depends on its strength characterised by the absolute value of λ. There is a certain difficulty in interpreting specific values of λ in the case of generalised optimal perturbation due to the difference between the initial norm and solution norm. A correlation between λ and the degree to which streaks were pronounced in figure 7 was indeed observed but further research in this direction is desirable.

Technically, the generalised optimal perturbation theory is a small modification of the optimal perturbation theory of Butler & Farrell (1993) since the required calculations are very similar. However, as far as the mechanisms of turbulence are concerned, the difference is significant. While the mechanism of streak formation is the same Stuart's lift-up mechanism in both theories, the mechanisms of selection of the streak spacing are different. In Butler & Farrell (1993) theory the streak spacing is determined by the non-linear breakdown of streaks. The eddy turnover time which is needed for obtaining quantitative results is also determined by nonlinear effects and has to be taken from experiment. In contrast, within generalised optimal perturbation theory the streak spacing selection mechanism is linear and relies on the selective properties of the lift-up mechanism alone.

While streaks emerge from disorganised chaotic motion without organised vortices being involved, the chaotic motion itself is generated in a process which can involve organised vortices. Moreover, the streaks may turn out to be the source of the organised vortices. This is of course only a guess but some further arguments can be put forward in favour of it. Organised vortices, if produced by, say, streaks instability, are likely to inherit the same spacing from streaks. Such vortex production by streaks is likely to require nonlinearity to play a role, since, as we can see from the generalised optimal perturbation theory, linear effects alone favour longitudinal vortices of much greater spacing (see subsection 2.5). If this is true then switching off the non-linear terms should lead to an increase in vortex spacing, as it indeed was observed by Kim & Lim (2000) but should not affect strongly the streak spacing until much later times when the solution will approach the steady flow. However, Kim & Lim (2000) do not give data on longitudinal velocity.

The presence of a variety of organised structures, including vortices, in near-wall turbulent flows appears to be a well established fact. It is more complicated to prove by numerical or experimental observations the existence of a relationship between organised vortices and streaks. An observation that characteristic spacing between organised vortices is equal to the streak spacing could provide such a proof. However we have already mentioned that, for example, the wall-normal velocity has characteristic spanwise wavelength only about half of the streak spacing. The process of vortex generation by streaks could of course explain observations of vortices correlating with streaks. However, identification of such vortices by an observer is subjective. Being under impression of the widely accepted relation between streaks and vortices (figure 2) and in view of the solid evidence of the existence of streaks (figure 1) an observer can wishfully pick up organised vortices where in fact there are none in a chaotic picture of the distribution of, say, vorticity or pressure, or of any other criteria used for the purpose. In view of the results of the present study it seems reasonable to cautiously re-examine the available evidence of the existence of organised vortices associated with streaks, with more emphasis on objective techniques. It might well be instructive to apply the techniques used for discovering organised vortices to an unstructured reference velocity field similar to the mean flow plus random potential perturbations of subsection 3.4, may be with added coherent streaks.

There are two possible concepts of the origin of structure in developed turbulent flows. One obvious idea implies the existence of a closed cycle of regeneration of organised structures, in which, say, organised vortices produce streaks and streaks in turn produce vortices and so on. The cycle may include more types of structures than these two. In this concept none of the structures is primary. Another, also quite obvious, possibility is that certain primary structures appear directly from a chaotic unstructured background. They can produce other structures and so on until the last structure in the chain is dissipated by viscosity or destroyed by the chaotic motion. The results of the present paper favour this second possibility and indicate that at least streaks are such a primary structure. Naturally, more complicated concepts, say, with several independent cycles and/or chains are also possible.

The generalised optimal perturbation theory and the physical mechanism of streak generation from unstructured chaotic background revealed by this theory are the main results of the present study.

This research was supported in part by the EPSRC grant GR/R27785 on 'Mechanism of longitudinal vortices in near-wall turbulent flow'. The authors would like to thank Dr. Z. W. Hu for providing the direct numerical simulation data for the plots in electronic form. This research and the presentation of the results benefited from discussions with Profs. N. D. Sandham, I. P. Castro, J. Kim, and many other researchers who cannot be listed here. M. F. Baig acknowledges the support via studentship from the School of Engineering Sciences of the University of Southampton.

5. Appendix

The specific results of the present study were obtained by the methodology which became possible with development of computerised algebraic systems capable of exporting its formulae into a highly efficient algorithmic language. Technically, the entire generalised optimal perturbation study was first performed with Mathematica system, starting from analytic transformations of the Navier–Stokes equations followed by numerical calculations and preliminary analysis of the results. Then, in order to achieve higher numerical accuracy and to allow systematic calculations of a number of cases within a reasonable time, the Mathematica notebooks where used as a prototype for the Fortran code, with large parts of the notebooks simply exported into Fortran. Physically, Mathematica notebooks are just computer files which can be interpreted by Mathematica. From the researcher viewpoint, Mathematica notebooks are hybrids between formula notes, interactive algebraic manipulation system, numerical code, and visualisation tool. A notebook can be worked with in a manner remotely similar to working with a scrap paper, but it can also be run as a code. Describing in a journal paper the research performed in this way presents certain difficulties. Mathematica allows to work with analytic expressions far too long to be printed. On the other hand, the Fortran code inherits these long expressions and tends to be just a calculation by these formulae combined with the use of standard library subroutines corresponding to Mathematica commands, as for example the command/subroutine for calculating numerically definite integrals. Then the Fortran code does not contain much of a numerical method to talk about. Nevertheless, the method of obtaining the results presented in a journal paper should be reported at least to an extent sufficient for independent reproduction of the results. This is the goal of this Appendix. We will limit ourselves to the calculation of the Green function $\boldsymbol{G}$, since the rest is fairly simple.

5.1. *General outline*

Substituting $u' = iu_\beta(t,y)e^{i\beta z}$, $v' = iv_\beta(t,y)e^{i\beta z}$, $w' = w_\beta(t,y)e^{i\beta z}$ and $p' = ip_\beta(t,y)e^{i\beta z}$ into the linearised Navier–Stokes equations (1.2) gives

$$\frac{\partial u_\beta}{\partial t} + v_\beta U'(y) = \frac{1}{\mathrm{Re}}\left(\frac{\partial^2 u_\beta}{\partial y^2} - \beta^2 u_\beta\right), \tag{5.1}$$

$$\frac{\partial v_\beta}{\partial t} = -\frac{\partial p_\beta}{\partial y} + \frac{1}{\mathrm{Re}}\left(\frac{\partial^2 v_\beta}{\partial y^2} - \beta^2 v_\beta\right), \tag{5.2}$$

$$\frac{\partial w_\beta}{\partial t} = \beta p_\beta + \frac{1}{\mathrm{Re}}\left(\frac{\partial^2 w_\beta}{\partial y^2} - \beta^2 w_\beta\right). \tag{5.3}$$

The boundary conditions are $u_\beta = v_\beta = w_\beta = 0$ at $y = \pm 1$.

The initial conditions are $t = 0$, $u_\beta = 0$, $v_\beta = u_{\beta 0}(y)$ and $w_\beta = w_{\beta 0}(y)$.

The problem is to find functions $G_v(t,\beta,y,\eta)$ and $G_w(t,\beta,y,\eta)$ such that (2.7) is valid, that is such that

$$u_\beta(t,y) = \int_{-1}^{+1} \left(G_v(t,\beta,y,\eta)v_{\beta 0}(\eta) + G_w(t,\beta,y,\eta)w_{\beta 0}(\eta)\right)\, d\eta.$$

Introducing the stream function $\psi_\beta(t,y)$ such that $v_\beta = -\beta\psi_\beta$, and $w_\beta = \partial\psi_\beta/\partial y$ reduces (5.2) and (5.3) to a single equation.

Separating variables gives solutions of the form $e^{-\lambda_k t/\mathrm{Re}} f_k(y)$. There is an infinite set of such solutions and corresponding values of $\lambda = \lambda_k$, $k = 1, \ldots, \infty$, satisfying all the boundary conditions. For each solution $v_\beta = -\beta f_k = v_k$, $w_\beta = f_k' = w_k$.

Functions

$$E_m(z) = \sin(\pi m(y+1)/2)$$

form a full orthonormal (in L_2) basis so that for each $f_k(y)$ there are coefficients

$$B_{km} = \int_{-1}^{+1} f_k(y)U'(y)E_m(y)\, dy$$

such that

$$f_k(y)U'(y) = \sum_m B_{km}E_m(y).$$

Substituting $v = v_k$ into (5.1) one then obtains

$$u_k = -\beta T_k(t)E_k(y),$$

where

$$T_k(t) = \mathrm{Re}\,\frac{e^{-(k^2\pi^2/4+\beta^2)t/\mathrm{Re}} - e^{-\lambda_k t/\mathrm{Re}}}{(k^2\pi^2/4 + \beta^2 - \lambda_k)}.$$

As it is shown in the following subsection, suitably normalised vectors (v_k, w_k) form a full orthonormal basis in the sense that

$$\int_{-1}^{+1} (v_k v_l + w_k w_l)\, dy = \delta_{kl}, \tag{5.4}$$

where δ_{kl} is the Kronecker delta and that if

$$\gamma_k = \int_{-1}^{+1} (v_{\beta 0} v_k + w_{\beta 0} w_k)\, dy \tag{5.5}$$

then

$$(v_{\beta 0}, w_{\beta 0}) = \sum_k \gamma_k (v_k, w_k). \tag{5.6}$$

Therefore,

$$u_\beta = \sum_k \gamma_k u_k = -\beta \sum_k \gamma_k T_k(t) E_k(y). \tag{5.7}$$

At this point it is possible just to look for γ_k, $k = 1, \ldots$ which maximise u_β^2 with the restriction $\sum_k \gamma_k^2 = 1$. This would lead to an eigenvalue problem, the solution to which is equivalent to calculating the Green function (see subsection 2.3). Alternatively, substituting (5.5) into (5.7) and comparing with (2.7) gives

$$(G_v, G_w) = -\beta \sum_{k,m} B_{km} T_m(t) E_m(y)(v_k, w_k).$$

The entire idea of this solution is quite standard, and the specific algebraic transformations leading to the above formulae can be performed on paper without computerised algebraic system, even though in our study we used Mathematica throughout. However, calculating $f_k(y)$ and B_{km} is more complicated.

5.2. *Eigenfunctions f_k and coefficients B_{km}*

The equation for f_k can be obtained by simple substitutions from Navier–Stokes equations. It has the form:

$$f_k^{(\mathrm{iv})}(y) - 2\beta^2 f_k''(y) + \beta^4 f_k(y) = \lambda_k(\beta^2 f_k(y) - f_k''(y)). \tag{5.8}$$

The boundary conditions are $f(-1) = f'(-1) = f(1) = f'(-1) = 0$. This is a self-adjoint positively determined eigenvalue problem. Therefore (Kamke 1983), its eigenfunctions are orthogonal and form a full basis in a functional space with the scalar product defined as

$$(g, h) = \int_{-1}^{+1} g(y)(\beta^2 h(y) - h''(y))\, dy.$$

For functions satisfying the boundary conditions integration by parts leads to

$$(g, h) = \int_{-1}^{+1} (\beta^2 g(y) h(y) + g'(y) h'(y))\, dy.$$

This immediately gives (5.4-5.6).

Equation (5.8) can be solved analytically using Mathematica. This gives the general solution as a sum of four independent solutions each multiplied by an arbitrary coefficient. Then the requirement that the solution should satisfy four boundary conditions gives a homogeneous system of four equations for these coefficients. The eigenvalues λ_k can then be found from the requirement that the determinant of this system is equal to zero.

This approach leads to very complicated expressions, which are difficult to handle even with Mathematica. Another approach consists in finding a solution satisfying only three of the boundary conditions. Then the eigenvalues λ_k can be sought from the fourth boundary condition. This approach does not guarantee, however, that all the eigenvalues will be found. Also, λ_k has to be determined numerically, and the solutions can turn into infinity at certain values of λ_k thus making the numerical calculations difficult. After some experimenting it was found that satisfactory results can be obtained by considering two solutions of (5.8), $f_s(y)$ and $f_a(y)$, satisfying the boundary conditions

$$f_s(-1) = f_s(1), \quad f_s'(-1) = f_s'(1) = 0,$$

$$f_a(-1) = -f_a(1), \quad f_a'(-1) = f_a'(1) = 0,$$

and having, with suitable normalisation, the form

$$f_s = \frac{e^{z\beta}\left(-1+e^{2\beta}\right)\beta\cos(z\,\nu_k) + e^{\beta}\left(1+e^{2\,z\,\beta}\right)\nu_k\sin(\nu_k)}{e^{z\beta}\left(1+e^{2\beta}\right)\sqrt{\beta^2+{\nu_k}^2}},$$

$$f_a = \frac{e^{\beta}\left(-1+e^{2\,z\,\beta}\right)\nu_k\cos(\nu_k) - e^{z\beta}\left(1+e^{2\beta}\right)\beta\sin(z\,\nu)}{e^{z\beta}\left(1+e^{2\beta}\right)\sqrt{\beta^2+{\nu_k}^2}},$$

where $\nu_k = \sqrt{\lambda_k - \beta^2}$.

Each of these functions gives eigenvalues as solutions to $f_s(1) = 0$ and $f_a(1) = 0$. To obtain different eigenvalues, iterative numerical procedure was started from different initial approximations. For f_s the initial approximations were $\nu_k = 0.7\pi, 1.7\pi, 2.7\pi, \ldots$ and for f_a the initial approximations were $\nu_k = 1.3\pi, 2.3\pi, 3.3\pi, \ldots$. To check that the obtained system was full, several test functions were expanded into a series using the obtained basis, and the sum of the series was compared to the test function itself.

To exploit the full advantage of the Mathematica's ability to perform algebraic manipulations, the coefficients B_{km} were calculated in the following way. We represent B_{km} in the form

$$B_{km} = \int_{-1}^{+1} \left(f_k(y)(U'(y) - yU'(1))E_m(y)\right) dy + U'(1)\int_{-1}^{+1} f_k(y)yE_m(y)\,dy.$$

The second integral here can be calculated analytically in a general form (that is with λ_k and β as symbols in f_k and elsewhere). The result is just a huge explicit expression. The first integral is calculated by expanding $f_k(y)$ in $E_m(y)$: $f_k(y) = \sum_m f_{km}E_m(y)$ again analytically in a general form, so that $f_k(y) = \sum_m f_{km}E_m(y)$, expanding $U'(y) - yU'(1)$ in $E_m(y)$ numerically so that $U'(y) - yU'(1) = \sum_m U_m E_m(y)$, and calculating

$$\Pi_{klm} = \int_{-1}^{1} E_k(z)E_l(z)E_m(z)\,dz$$

again analytically. Then

$$B_{km} = \sum_{l,n} f_{kl}U_n\Pi_{lnm} + U'(1)\int_{-1}^{+1} f_k(y)yE_m(y)\,dy.$$

The advantage of this approach is that all the components here are calculated only once for all values of β and λ_k either because the calculations are symbolic or because β and λ_k are not involved in the numerical part. Separating $yU'(1)$ also greatly accelerates convergence.

Exporting large expressions to Fortran may result in the loss of accuracy due to rounding errors. In the present study this was checked by performing the calculations in Fortran with single and double precision and comparing the results. Rounding errors turned out to be large but that was corrected simply by rearranging the expressions involved.

REFERENCES

BAIG, M. F. & CHERNYSHENKO, S. I. 2003 Streak and coherent vortices in near-wall turbulence. *Submitted to Phys. Fluids* .

BROOKE, J. W. & HANRATTY, T. J. 1993 Origin of turbulence producing eddies in a channel flow. *Phys. of Fluids A* **5**, 1011–1021.

BUTLER, K. M. & FARRELL, B. F. 1992 Three-dimensional optimal perturbations in viscous shear flow. *Phys. of Fluids A* **4** (8), 1637–1650.

BUTLER, K. M. & FARRELL, B. F. 1993 Optimal perturbations and streak spacing in wall-bounded turbulent shear flows. *Phys. of Fluids A* **5**, 774–777.

CRIMINALE, W. O., JACKSON, T. L. & LASSEIGNE, D. G. 1995 The initial-value problem for viscous channel flows. *Tech. Rep.* 95-6. NASA CR-195034 ICASE, Institute for Computer Applications in Science and Engineering, Mail Stop 132C, NASA Langley Research Center Hampton, VA, available at http://www.icase.edu/.

HAMILTON, J. M., KIM, J. & WALEFFE, F. 1995 Regeneration mechanisms of near-wall turbulence structures. *J. Fluid Mech.* **232**, 317–348.

HU, Z. & SANDHAM, N. D. 2001*a* DNS databases for turbulent Couette and Poiseuille flow. *Tech. Rep.* 01/04. AFM Research group, SES, University of Southampton.

HU, Z. W., MORFEY, C. L. & SANDHAM, N. D. 2003 Sound radiation in turbulent channel flows. *J. Fluid. Mech.* **475**, 269–302.

HU, Z. W. & SANDHAM, N. D. 2001*b* Large-domain simulations of Couette and Poiseille flow. In *Proc. 2nd Inter. Symposium on Turbulent and Shear Flow Phenomena*. Stockholm.

JANG, P. S., BENNEY, D. J. & GRAN, R. L. 1986 On the origin of streamwise vortices in a turbulent boundary layer. *J. Fluid Mech.* **169**, 109–123.

JIMÉNEZ, J., PINELLI, A. & UHLMANN, M. 2000 Control of turbulent wall flows. School of Aeronautics — Universidad Politécnica de Madrid. *ERCOFTAG Bulletin* (44), 7–14.

JOVANOVIĆ, M. & BAMIEH, B. 2001 Modeling flow statistics using the linearized Navier-Stokes equations. In *Proceedings of the 40th IEEE Conference on Decision and Control*, pp. 4944–4949.

KAMKE, E. 1983 *Differentialgleichungen: Lösungsmethoden und Lösungen, Bd. 1: Gewöhnliche Differentialgleichungen*. Stuttgart: Teubner.

KASAGI, N., TOMITA, Y. & KURODA, A. 1992 Direct numerical simulation of passive scalar field in a turbulent channel flow. *Transactions of the ASME. Journal of Heat Transfer* **114**, 598–606.

KIM, J. & LIM, J. 2000 A linear process in wall-bounded turbulent shear flows. *Phys. of Fluids* **12** (9), 1885–1888.

KIM, J. & MOIN, P. 1989 Transport of passive scalars in a turbulent channel flow. In *Turbulent Shear Flows 6* (ed. J.-C. A. et al.), pp. 85–96. Berlin, Heidelberg: Springer Verlag.

MOSER, R. D., KIM, J. & MANSOUR, N. N. 1999 Direct numerical simulation of turbulent channel flow up to $\mathrm{Re}_\tau = 590$. *Phys. Fluids* **11** (4), 943–945.

NIKITIN, N. V. & CHERNYSHENKO, S. I. 1997 On the nature of the organised structures in turbulent near-wall flows. *Fluid Dynamics* **32** (1), 18–23, [Translated from Izvestiya Rossiiskoi Akademii Nauk, Mekhanika Zhidkosti i Gaza, No. 1, pp. 24–30, 1997].

PANTON, R. L., ed. 1997 *Self-Sustaining Mechanism of Wall Turbulence*. Southampton: Computational Mechanics Publication.

ROBINSON, S. 1991 Coherent motions in the turbulent boundary layer. *Ann. Rev. Fluid Mech.* **23**, 601–639.

SANDHAM, N. D. & HOWARD, R. J. A. 1998 Direct simulation of turbulence using massively parallel computers. In *Parallel Computational Fluid Dynamics. Recent Developments and Advances Using Parallel Computers* (ed. D. R. Emerson, A. Ecer, J. Peraux & P.Fox), pp. 23–32. Elservier.

SCHOPPA, W. & HUSSAIN, A. K. M. F. 1998 Formation of near-wall streamwise vortices by streak instability. *Tech. Rep.* 98-3000. AIAA, 29th AIAA Fluid Dynamics Conf., Albuquerque, NM, U.S.A.

SCHOPPA, W. & HUSSAIN, F. 2002 Coherent structure generation in near-wall turbulence. *Journal of Fluid Mechanics* **453**, 57–108.

SMITH, C. R. & METZLER, S. P. 1983 The characteristics of low-speed streaks in the near-wall region of a turbulent boundary layer. *J. Fluid Mech.* **129**, 27–54.

SMITH, C. R. & WALKER, J. D. A. 1994 Turbulent wall layer vortices. In *Fluid Vortices* (ed. S. Green). Springer-Verlag.

SREENIVASAN, K. R. 1988 A unified view of the origin and morphology of the turbulent boundary layer structure. In *Proc. IUTAM Symp. on Turbulence Management and Relaminarisation* (ed. H. W. Liepmann & R. Narasimha), pp. 37–61. Springer.

STUART, J. T. 1965 The production of intense shear layers by vortex stretching and convection. *NATO AGARD report* **514**, 1–29.

TIKHONOV, A. N., GONCHARSKII, A. V., STEPANOV, V. V. & YAGODA, A. G. 1990 *Numerical methods for ill-posed problems.* Moscow: Nauka, [In Russian].

TREFETHEN, L. N., TREFETHEN, A. E., REDDY, S. C. & DRISCOLL, T. A. 1993 Hydrodynamics stability without eigenvalues. *Science* **261**, 578–584.

WALEFFE, F. & KIM, J. 1997 How streamwise rolls and streaks self-sustain in a shear flow. In *Self-Sustaining Mechanism of Wall Turbulence* (ed. R. L. Panton), pp. 309–331. Southampton: Computational Mechanics Publication.

WALEFFE, F., KIM, J. & HAMILTON, J. 1993 On the origin of streaks in turbulent boundary layers. In *Turbulent Shear Flows 8* (ed. F. Durst, R. Friedrich, B. E. Launder, F. W. Schmidt, U. Schumann & J. Whitelaw), pp. 37–49. Springer.